Investigation of Designed Peptides for the Disruption of Bacterial and Mammalian Amyloid Systems

Sarah Nick

A dissertation

submitted in partial fulfillment of the

requirements for the degree of

Doctor of Philosophy

University of Washington

2024

Reading Committee:

Valerie Daggett, Chair

James Bryers

Buddy Ratner

Matthew Parsek

Program Authorized to Offer Degree:

Bioengineering

University of Washington

Abstract

Investigation of Designed Peptides for the Disruption of Bacterial and Mammalian Amyloid Systems

Sarah Nick

Chair of the Supervisory Committee:

Valerie Daggett

Department of Bioengineering

Amyloid proteins are associated with an increasing number of human diseases. In amyloid systems, soluble proteins experience conformational changes that trigger aggregation into toxic soluble oligomers, then protofibrils, and eventually into insoluble amyloid fibrils. Synthetic α-sheet peptides inhibit amyloid formation by adopting a complementary conformation to the native protein structure and by binding toxic oligomers, including the β-amyloid peptide (Aβ) involved in Alzheimer's Disease (AD). These α-sheet peptides not only inhibit amyloid fibrilization in mammalian amyloid diseases but also in bacteria, which produce functional amyloid proteins as part of their biofilm extracellular matrix. Here, we demonstrate that co-administration of α-sheet peptides with various antibiotics increases biofilm antibiotic susceptibility in both gram-negative and -positive bacteria. Additionally, the peptides are incorporated into a functionalized gauze for

biofilm inhibition at a wound site and tethered to titanium dental implants to prevent oral biofilm infection. Next, the effects of the α-sheet peptides on Aβ in the context of AD were further examined. An increased rate of phagocytosis of Aβ oligomers in multiple cell lines was observed when cells were treated with α-sheet peptides. The α-sheet peptides were then administered alongside Aβ oligomers to transgenic mice that overexpress human tau. Intracranial injections of Aβ oligomers resulted in long-term behavioral impairments in the mice, whereas the peptide injections appeared to be safe and to reduce the anxiety induced by the intracranial injection of Aβ oligomers. In this dissertation, synthetic α-sheet peptides are first presented as novel amyloid inhibitors with proposed biomaterial applications for biofilm prevention. Finally, the peptides are investigated in the context of AD with implications for further elucidation of the disease mechanisms.

Table of Contents

List of Figures

List of Tables

Acknowledgements

The author would like to thank Dr. Valerie Daggett and Dr. James Bryers for mentorship throughout her graduate career, as well as Dr. Buddy Ratner and Dr. Matthew Parsek for service on the supervisory committee. She is also grateful to Dr. Tatum Prosswimmer for helpful discussions and practical instruction as well as her friendship. Additional thanks to the many lab members in the Daggett and Bryers groups who have provided assistance and camaraderie over the years, namely Louis Chen, Patrick Gerber, Dr. Thomas Hady, Dr. Nathan Chan, Quentin Phillips, Paul Goo, Dr. Dylan Shea, Anthony Heng, Carter Rowell, and Isiac Orr. Thank you as well to collaborators at the Roskamp Institute, namely Dr. Daniel Paris. The author would also like to thank the Department of Bioengineering for providing administrative support, as well as the NIH National Center for Advancing Translational Sciences through the Clinical and Translational Science Awards Program (CTSA) for financial support. Finally, the author would like to thank her parents, Jerry and Jennifer, her sister Sophie, and her fiancé Thomas for their support and love and for inspiring her with their work ethic and commitment to science and medicine.

Chapter 1. Introduction

1.1 Introduction to Amyloid

Amyloid proteins are associated with over 40 human diseases, with many disorders becoming increasingly prevalent [1]. In amyloid diseases, soluble proteins experience conformational changes that trigger aggregation into toxic soluble oligomers, then protofibrils, and eventually precipitation of insoluble amyloid fibrils. Amyloid oligomers are non-covalently bound groups of monomers that display greater toxicity than either the monomeric or full-length fibril forms [2]. In some amyloid diseases, the oligomer causes cellular damage before mature fibrils are formed, making these toxic intermediates potential therapeutic targets. Amyloid fibrils also have impressive material properties including high deformation, resistance, and elasticity. As such, many organisms, including bacteria, utilize amyloid functionally.

Amyloid proteins have non-branching, rigid fibrils with a high β-sheet content, a distinct protein sequence, and form insoluble deposits from the aggregation of proteins [3]. Amyloid proteins display a cross-β diffraction pattern in X-ray diffraction analysis and can be detected with extrinsic dyes including Congo Red and Thioflavin T (ThT) [3]. Mature amyloid fibrils have a rigid structure due to the high number of β-sheets and their stability is primarily attributed to intermolecular interactions [2]. Their β-sheets are perpendicular to the fibril axis and van der Waals interactions between the side chains promote hydrogen bonding parallel to the fibril axis (**Figure 1.1**).

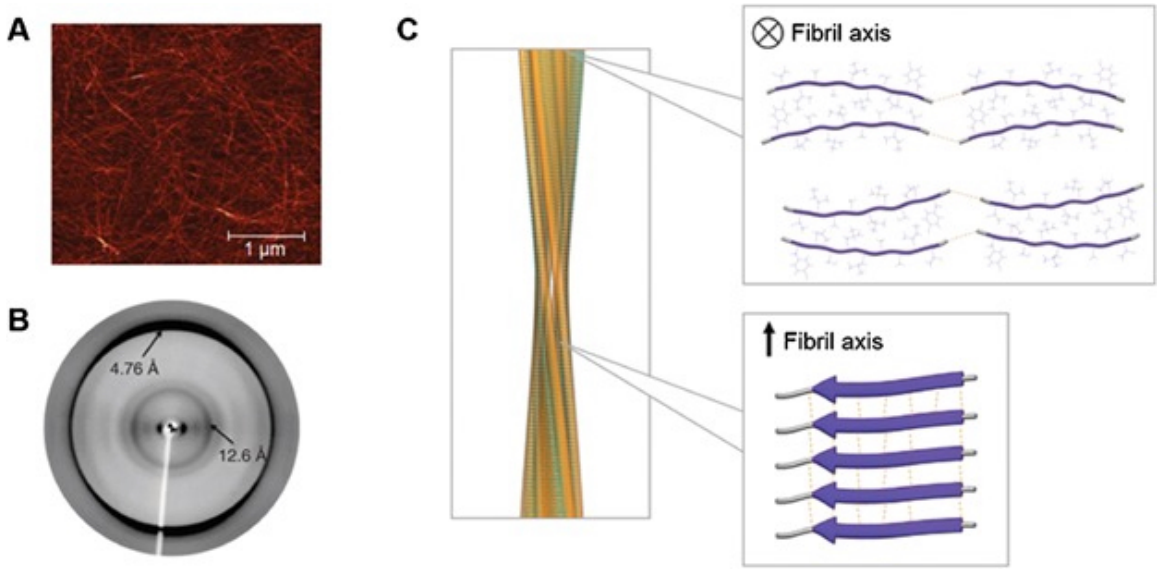

Figure 1.1: Amyloid fibril morphology. A) Atomic force microscopy (AFM) of *Staphylococcus aureus* amyloid fibrils. **B)** A standard "cross-β" X-ray diffraction pattern as seen for amyloid fibrils. **C)** Atomic models showing the secondary, tertiary, and quaternary structure of amyloid. Figure from Bleem and Daggett, 2017 [2].

1.2 α-Sheet Structure

Amyloid aggregation follows a nucleation-dependent mechanism and aggregation has three phases: lag, exponential, and plateau [4]. During the lag phase, a protein changes conformation to an aggregation competent monomer. An aggregation nucleus then forms, ending the lag phase. Next, the exponential phase is characterized by rapid oligomerization. This results in the formation of β-sheet heavy fibrils and ultimately the plateau phase where fibrils are deposited into the surrounding environment (**Figure 1.2**) [4]. Studies have shown that the insoluble, amyloid fibrils are stable and non-toxic while the intermediate, soluble oligomers are toxic. The A11 antibody binds the oligomeric form of multiple amyloid species, suggesting a shared and specific structure for the toxic oligomers [5].

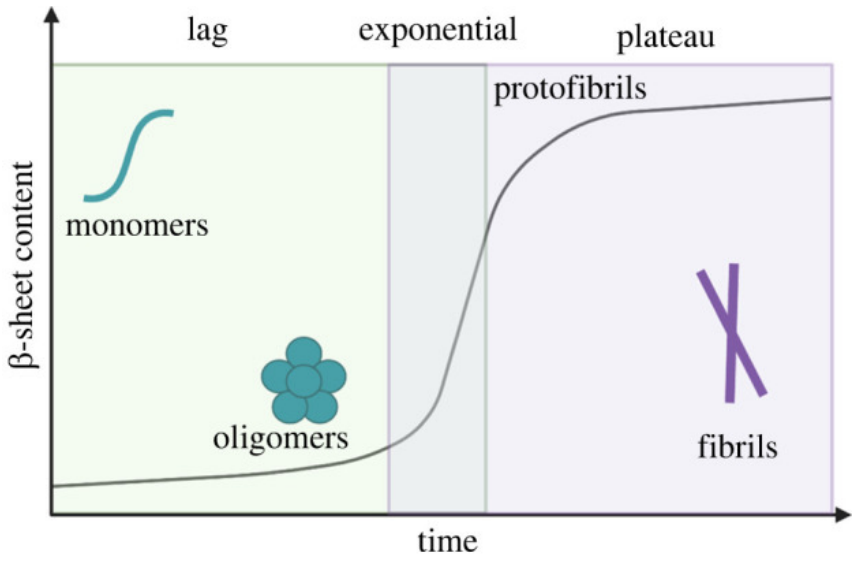

Figure 1.2: Schematic of the amyloid aggregation pathway. During the lag phase, amyloid-competent monomers and oligomers form sequentially. Then, during the exponential phase, the amyloid protein undergoes a structural change into β-sheet protofibrils. During the plateau, fibrils rearrange to the ordered cross-β-sheet structure. Figure from Prosswimmer and Daggett, 2022 [5].

Due to this shared binding by the A11 antibody, the Daggett lab conducted Molecular dynamics (MD) simulations of multiple unrelated amyloidogenic proteins to study the conformational changes of the aggregation course under known amyloidogenic conditions. These studies revealed a non-standard secondary structure, now referred to as α-sheet. α-Sheet structure is stabilized by hydrogen bonding between individual strands. Elongated strands form due to the sequential alternation between α_L and α_R backbone dihedral angles. α-Sheet is unique because of main chain carbonyl alignment on one side of the sheet and NH alignment on the other side, creating a strong molecular dipole across the sheet. Subsequently, the Daggett lab designed and engineered *de novo* hairpin peptides, with α-sheet structure, that adopt a complementary conformation to the observed native α-sheet structure [6, 7]. These designed α-sheet peptides inhibit the aggregation and toxicity of multiple mammalian amyloid species as well as bacterial amyloid, including *Staphylococcus aureus*, *Escherichia coli*, and *Streptococcus mutans* [8-10].

1.3 Functional Bacterial Amyloid

Both gram-negative and gram-positive bacteria use amyloid proteins as structural scaffolding in their biofilm extracellular matrix (ECM). Recent studies suggest that many multi-drug resistance bacteria use amyloid fibrils as a mechanism of virulence through facilitation of bacterial aggregation and biofilm formation [11-13]. In gram-negative *E. coli*, the amyloid proteins are called curli and they are the major proteinaceous component of the ECM. Curli are assembled at the bacterial cell surface and promote adhesion to surfaces and aggravate the host inflammatory response [14]. At least six proteins are dedicated to curli formation and they are encoded by the *csgBA* and *csgDEFG* operons [14]. The *csgBA* operon encodes both CsgA, the major structural subunit, and CsgB, the nucleator protein. CsgA and CsgB are the same size, with 30% sequence identity. In the absence of CsgB, curli are not assembled and CsgA is secreted from the cell and not polymerized [14]. Curli assembly also requires four accessory proteins which are encoded by the *csgDEFG* operon. Curli formation is a highly regulated and directed process, in stark contrast to mammalian amyloid which is largely an off-pathway folding event. Bacteria use a range of methods to prevent self-toxicity from amyloid oligomers. For example, in *E. coli*, polymerization of the protein subunits into mature fibrils only occurs once they have reached the cell surface [14].

The gram-positive species *S. aureus* also produces amyloid proteins called phenol soluble modulins (PSMs). *S. aureus* expresses four α-PSMs, two β-PSMs, and one γ-PSM [15]. PSMs are surfactant-like peptides that can modulate biofilm disassembly through amyloid-like aggregation [16]. While soluble PSMs promote biofilm disassembly, PSM fibers actually improve biofilm stability [16]. PSM amyloid fibrils have also been shown to promote resistance to various biofilm dispersion agents including Proteinase K, DNAse, and Dispersin [16]. Research addressing functional bacterial amyloids is of growing interest with emerging work on *Streptococcus mutans*,

Bacillus subtilis, *Pseudomonas aeruginosa*, *Staphylococcus epidermidis*, *Klebsiella pneumoniae*, *Streptomyces coelicolor*, and more. As such, research has also focused on amyloids as targets to promote biofilm dispersal. A number of amyloid inhibitors have been identified including anti-amyloid peptides, proteins, pilicides and curlicides, molecular tweezers, and polyphenols [15]. Some inhibitors have been successful at reducing biofilm formation but many are limited because they show species-specific effects, show cross reactivity with human amyloids, or increase the antibiotic resistance of the biofilm [15].

1.3.1 Designed Peptides and Bacterial Amyloid Inhibition

Amyloids are a major protein component of many bacterial biofilms and are thus a target for anti-biofilm strategies. In previous work in *S. aureus* and *E. coli*, the Daggett group's synthetic α-sheet peptides successfully inhibited the *in vitro* amyloid aggregation of PSMα1 and CsgA (for *S. aureus* and *E. coli,* respectively) [8, 9]. The peptides also showed bacterial amyloid inhibition in Thioflavin T (ThT) assays as indicated by reduced β-sheet content. These studies also demonstrated a significant reduction in biofilm density for bacteria incubated with the α-sheet peptides [8, 9]. *In vitro* biofilm experiments also showed that, although the total number of cells stayed the same, the number of planktonic cells increased. This suggests that the peptides inhibit biofilm formation and force more cells into the planktonic state without causing cell death. This is critical in preventing conferred resistance to the peptides over time as has occurred with traditional antibiotics. Finally, as will be elaborated on in **Chapter 2**, the peptides increase the antibiotic susceptibility of both gram-negative and gram-positive bacteria to a broad spectrum of antibiotics.

1.4 Hospital Acquired Infections

Hospital acquired infections (HAIs) are the most common adverse healthcare event. In the United States, there are more than 680,000 HAIs each year and one in 31 hospital patients has an HAI at any given time [17, 18]. The estimated cost of treating HAIs in the US is $28-45 billion annually [19]. These infections lead to longer hospital stays, chronic inflammation, impaired wound healing, acquired antibiotic resistance, sepsis, and death. There are several risk factors for HAIs including invasive procedures, severe illness, failure to follow best practices for prevention, and improper antibiotic use. The majority of HAIs are biofilm mediated, and many infections are caused by antibiotic resistant bacteria [20]. Approximately 65% of all infections and 80% of chronic and recurring microbial infections are associated with biofilm formation on an implanted device including prosthetic heart valves, orthopedic implants, intravascular catheters, cardiac pace makers, urinary catheters, and contact lenses [21].

1.4.1 Medical Biofilms

Biofilms form when bacteria adhere to a surface, replicate, and then begin to produce a three-dimensional extracellular polysaccharide (EPS) matrix that solidifies the structure. Within this matrix, channels form for the delivery of nutrients and export of waste products from the biofilm structure. Mature biofilms then shed cells that can travel between biofilms or establish new ones (**Figure 1.3**). Biofilm associated microorganisms are significantly less susceptible to antibiotics and to host defenses. Biofilm associated bacteria are 10-1000 times more resistant to antibiotics than bacteria in the planktonic form and sublethal antibiotic doses can enhance biofilm formation [22]. Biofilms have several defense mechanisms against antibiotics. First, the EPS can act as a physical barrier to slow diffusion of drugs or bind to the antibiotic, with many antibiotics

becoming deactivated at the biofilm surface [23]. Next, if an antibiotic penetrates the biofilm surface, the microenvironment of the biofilm can be challenging to the drug. This environment is often anaerobic and pH changes and low oxygen levels can reduce the efficacy of common antibiotics [23]. Third, biofilms often contain "persister cells" which evade antibiotics by entering a dormant-like state where they are resistant to extreme conditions. These cells then return to a standard state and re-start division once released from the biofilm [22]. Finally, biofilms not only evade antibiotic treatment but also promote resistance through communication strategies such as quorum sensing which allows for the transfer of genetic elements, including antibiotic resistance information.

All medical devices are susceptible to infection and biofilms can form on hard surfaces such as implants or on soft surfaces such as bandages. Biofilm diagnosis, particularly on medical devices, is often difficult and can require sampling the device surface through invasive surgeries. When a culture is successfully grown, mixed cultures from polymicrobial infections can make it challenging to identify a proper antibiotic regimen. The most common bacteria on device-associated infections are *Staphylococcus epidermidis* and *Staphylococcus aureus*, with *S. epidermidis* accounting for about 80% of medical device infections [24]. However, multidrug resistant bacteria including *Escherichia coli*, *Klebsiella pneumoniae*, *Acinetobacter baumannii* and *Pseudomonas aeruginosa*, are increasingly problematic, particularly as related to catheter-associated urinary tract infections [25].

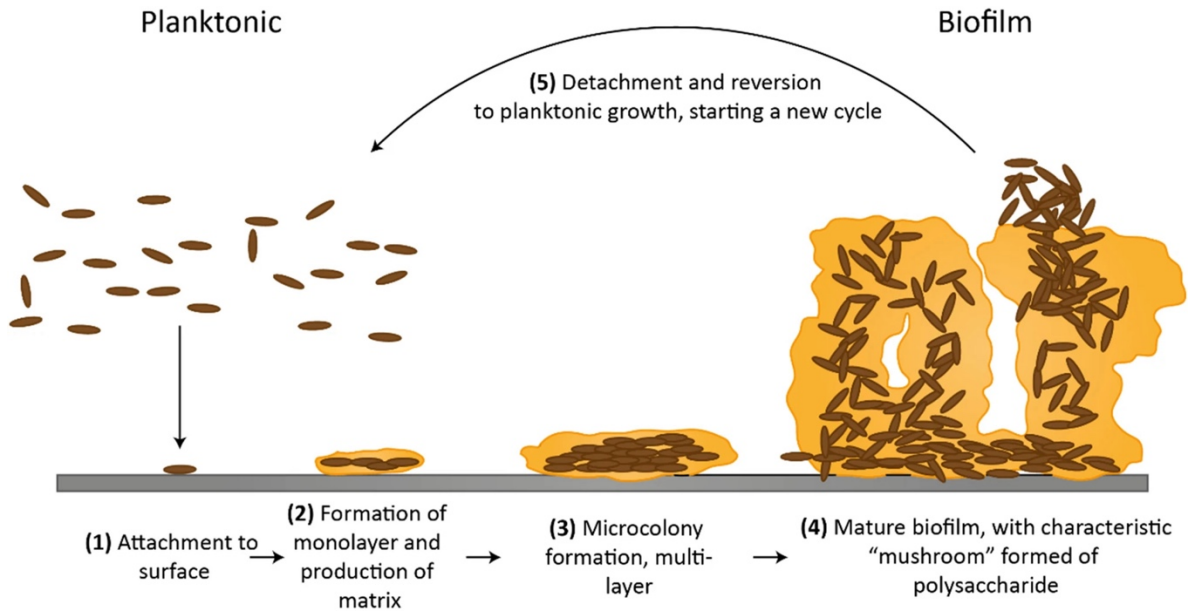

Figure 1.3: Stages of biofilm formation on a surface. Planktonic cells adhere to a surface within seconds. First colonizers then attach and begin rapid cell growth and division. Cells then begin to produce a robust extracellular matrix. Finally, second colonizers join, and microbes disperse from the mature biofilm. Image from Giorgi et al. [26].

1.4.2 Biomaterials for Biofilm Prevention

Biomedical devices are susceptible to protein fouling. Protein fouling occurs when an implanted device causes a host response and a film made of proteins and glycoproteins forms on the surface. Many of these proteins help bind colonizing bacteria. This phenomenon occurs for all materials including glass, ceramic, titanium, and polyurethane. The host response to biomaterials occurs in several overlapping stages: blood-material interactions, acute inflammation, chronic inflammation, foreign body reaction, and fibrous encapsulation [21]. The body's first defense against bacterial infection is the innate immune response of neutrophils, macrophages, and dendritic cells. However, many bacteria have the ability to evade these defenses and can even be toxic to immune cells [21]. Thus, biocompatible materials should be inert, limit the host foreign body response, and prevent biofilm formation [27].

Biofilms are often treated through physical, mechanical, or biological removal from devices. For example, a mechanical approach uses a high-powered spray for debridement of a

surgical site or a dental biofilm. However, the recurring nature of biofilm related infections exacerbates the difficulty of treatment. For this reason, many strategies instead focus on biofilm prevention. The most common prevention technique is device surface modification through the coating or elution of a drug. One such strategy is through mechanical designs like adding an antibiotic fill or skin cuff to a catheter. Many materials also utilize tethered antibacterial agents such as silver coatings or synthetic antibiotics. However, coatings have limited success as they are only toxic to the first wave of bacteria and become ineffective as dead cell layers accumulate. As such, some materials instead release soluble toxic agents like chlorhexidine or antibiotics. Success here, though, is limited only to the period of release. Additionally, controlled release strategies raise concerns of increased resistance as sub-lethal antibiotic doses can enhance biofilm formation and accelerate resistance. This document describes work towards two anti-biofilm strategies: release (**Chapter 2** and **Chapter 3**) and tethering of synthetic α-sheet peptides (**Chapter 4**).

1.5 Mammalian Amyloid Systems- Alzheimer's Disease

Alzheimer's Disease (AD) is the 6th leading cause of death in the United States and currently affects over 50 million people worldwide, with this number predicted to only grow in the coming years [28]. AD is characterized by neuronal death and progressive cognitive decline caused by the extracellular accumulation of amyloid plaques and the intracellular formation of neurofibrillary tangles in the brain. Monomeric β-amyloid peptide (Aβ) is involved in multiple biological functions including memory, learning, and neuroprotection [29-32] and the accumulation of Aβ outside of neurons is a hallmark of AD. However, there is evidence that the toxic soluble oligomers, not the amyloid burden, are associated with disease progression and that damage begins prior to amyloid plaque deposition [33-37]. Along with the accumulation of Aβ

plaques, progression of AD is characterized by tau hyperphosphorylation. In AD brains, hyperphosphorylated tau form fibrils in neuronal cell bodies, referred to as neurofibrillary tangles (NTFs), leading to cell damage and inflammation.

1.5.1 Designed Peptides and Alzheimer's Disease

The α-sheet peptides have previously demonstrated amyloid inhibition in multiple mammalian systems, including against the 42-amino Aβ peptide in the context of AD. As described, during amyloidogenesis, Aβ forms toxic, soluble oligomers before the deposition of mature fibrils [38, 39]. The synthetic α-sheet peptides specifically bind the toxic Aβ oligomers and inhibit Aβ aggregation *in vitro* and in two animal models [38]. Incubation of the toxic Aβ oligomers with the α-sheet peptides caused a 96% reduction in aggregation *in vitro* [38]. The peptides also protect against toxicity in cells and co-incubation with Aβ oligomers led to recovered cell viability [38]. The peptides were also tested in transgenic APPsw mice that express human Aβ and caused a dose-dependent reduction in detectable oligomers with reductions of up to 79% in coronal brain sections. When the peptides were injected intracranially into the right hemisphere of the mice, reductions of 40% of Aβ oligomers were seen as compared to the control left hemisphere. In a transgenic *C. elegans* model, the peptides significantly delayed paralysis due to the effect of Aβ toxicity [38].

1.5.2 β-Amyloid and the Immune System

Microglia are the primary immune cells of the central nervous system (CNS). Microglia function primarily as phagocytes in the CNS and are involved in tissue maintenance, injury response, and defense against pathogens [40]. Sustained inflammation in AD results in chronic

microglial cell activation and increase cytokine release. In healthy humans, microglia can degrade and phagocytose Aβ aggregates but in AD, if Aβ levels are significantly elevated, chronic microglial activation causes a sustained pro-inflammatory response that exacerbates disease pathology [41]. It was hypothesized that the previously observed α-sheet peptide mediated reduction in toxic Aβ oligomers is caused by the peptides altering the rate by which toxic Aβ oligomers are phagocytosed, as the peptides do not directly impact Aβ production [17]. This hypothesis is investigated in **Chapter 5**.

1.6 Overview of Chapters

This dissertation is comprised of studies of synthetic α-sheet peptides and amyloid inhibition in two parts. First, **Chapters 2-4** focus on the inhibition of functional bacterial amyloid and prevention of biofilm formation through the development of novel biomaterials. Second, **Chapters 5-6** center on the investigation of the peptides in the context of Alzheimer's Disease.

Medical biofilms are a significant and growing problem as the usage of biomedical devices rises and bacteria become increasingly resistant to existing antibiotic treatments. Many bacteria use functional amyloids in their biofilm ECM as structural support and to help resist dispersion. The Daggett lab has developed synthetic α-sheet peptides that inhibit amyloid formation and reduce biofilm density in multiple bacterial species. In **Chapter 2**, we tested the effect of peptide and antibiotic co-administration on the antibiotic susceptibility of clinical strains of *S. aureus* and *E. coli*. Two peptides and five antibiotics were used to examine the differences between peptides with the same sequence but opposite chirality and to determine how the peptides affect antibiotic resistance to antibiotics with various mechanisms of action. Both peptides increased antibiotic susceptibility with varying effects on the gram-negative and gram-positive species. In **Chapter 3**,

the peptides were incorporated into a layer-by-layer functionalized gauzed for controlled release at a wound site. Chitosan and alginate were chosen for alternating layers due to their natural antibacterial and hemostatic properties and biocompatibility. Biofilm inhibition was then demonstrated using a broth culture assay against two clinical bacterial isolates. Finally, in **Chapter 4**, a polydopamine based coating with α-sheet peptide attachment was developed for titanium dental implants and demonstrated efficacy of the peptides against biofilms formed by the oral pathogen *S. mutans.* Together, this work presents a promising new approach to biofilm inhibition and antibiotic susceptibility with two potential applications for high-need medical biofilm prevention.

As the world population ages, the prevalence and economic and social burden of Alzheimer's Disease continues to rise. Synthetic α-sheet peptides specifically bind the toxic Aβ oligomers, inhibit Aβ aggregation, and protect against toxicity in cells. In **Chapter 5**, we investigated the effect of multiple monomer and dimer APs on phagocytosis of *E. coli* bioparticles and toxic Aβ oligomers by macrophages and microglial cells. We demonstrate that administration of seven APs increases phagocytosis of Aβ oligomers by both cell types. Additionally, an engineered HEK293 cell line was used to investigate the mechanism of increased Aβ uptake. Finally, in **Chapter 6**, the α-sheet peptides were administered alongside Aβ oligomers to transgenic mice that overexpress human protein tau. The intracranial injections of Aβ oligomers resulted in long-term behavioral impairments in the mice, whereas the peptide injections appeared to be safe and to reduce the anxiety induced by the intracranial injection of Aβ oligomers.

Chapter 2. Designed De Novo α-Sheet Peptides Destabilize Bacterial Biofilms and Increase the Susceptibility of *E. coli* and *S. aureus* to Antibiotics*

*Text and figures from *International Journal of Molecular Science* DOI: 10.3390/ijms25137024

2.1 Abstract

Biofilm-associated microbes are 10-1000 times less susceptible to antibiotics. An emerging treatment strategy is to target biofilm structural components to weaken the extracellular matrix without introducing selective pressure. Biofilm-associated bacteria, including *Escherichia coli* and *Staphylococcus aureus*, generate amyloid fibrils to reinforce their extracellular matrix. Previously, *de novo* synthetic α-sheet peptides designed *in silico* were shown to inhibit amyloid formation in multiple bacterial species, leading to destabilization of their biofilms. Here, we investigated the impact of inhibiting amyloid formation on antibiotic susceptibility. We hypothesized that combined administration of antibiotics and α-sheet peptides would destabilize biofilm formation and increase antibiotic susceptibility. Two α-sheet peptides, AP90 and AP401, with the same sequence but inverse chirality at every amino acid were tested: AP90 is L-amino acid dominant while AP401 is D-amino acid dominant. For *E. coli*, both peptides increased antibiotic susceptibility and decreased the biofilm colony forming units when administered with five different antibiotics, and AP401 caused a greater increase in all cases. For *S. aureus*, increased biofilm antibiotic susceptibility was also observed for both peptides, but AP90 outperformed AP401. Comparison of the peptide effects demonstrates how chirality influences biofilm targeting of gram-negative *E. coli* and gram-positive *S. aureus*. The observed increase in antibiotic susceptibility highlights the role amyloid fibrils play in the reduced susceptibility of bacterial biofilms to specific antibiotics. Thus, the co-administration of α-sheet peptides and existing antibiotics represents a promising strategy for the treatment of biofilm infections.

Graphical Abstract:

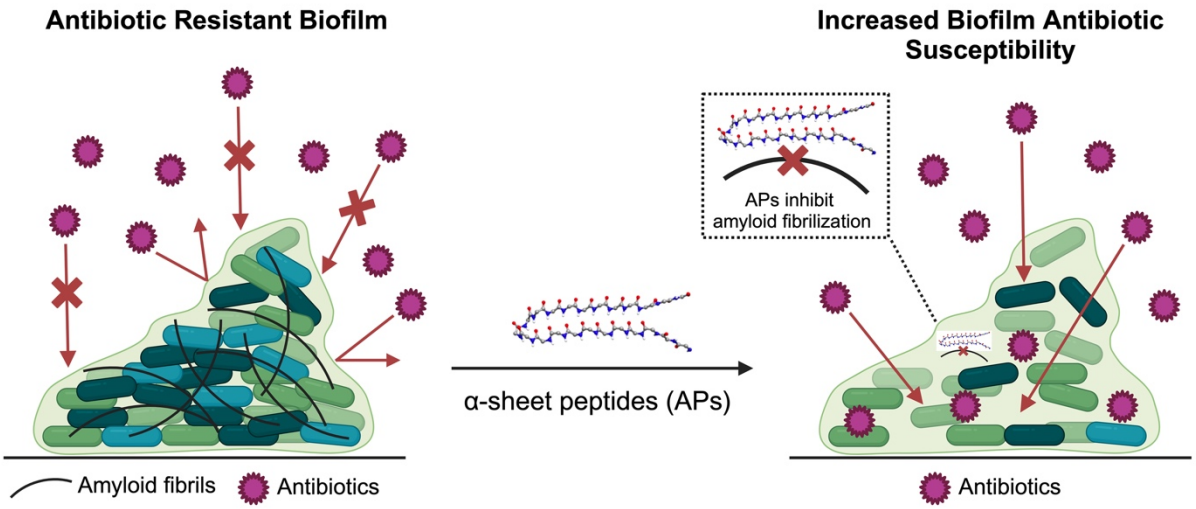

2.2 Introduction

Amyloidogenic proteins are implicated in over 50 mammalian diseases and are considered inherently pathogenic [1, 5, 6, 38, 42-46]. Notably, many bacteria utilize mature amyloid fibrils, termed "functional amyloid," as a structural scaffold in their extracellular biofilm to protect cells from the surrounding environment [8, 9, 16, 47-49]. In both cases, the soluble, oligomeric intermediates that form prior to stable fibrils are the primary toxic species, while insoluble fibrils are nontoxic [1, 5, 6, 38, 39, 42-46, 50-52]. Toxic oligomers adopt a nonstandard secondary structure, α-sheet, that has been observed and characterized in several amyloid proteins in both mammals and bacteria, including the amyloid-β peptide (Alzheimer's Disease), islet amylin polypeptide (type 2 diabetes), CsgA (*Escherichia coli*) and PSMα1 (*Staphylococcus aureus*) [5-8, 10, 38, 53, 54]. α-Sheet structure is unique in that each residue is locally helical, but alternation between right- and left-handed conformations results in the formation of an elongated strand [5, 53, 55]. The conserved nonstandard intermediate structure represents a unique target for inhibiting amyloid formation in the context of both mammalian disease and biofilm-associated infection.

Biofilms are microbe-generated, surface-associated extracellular matrices (ECMs) composed of cells and secreted insoluble extracellular molecules (proteins, polysaccharides, and extracellular DNA) that facilitate cell communication and protect cells from the surrounding environment (i.e., host immune response and antibiotics) [49]. Biofilm cells are significantly less susceptible to antibiotics than free-floating, or planktonic, cells and this reduced antibiotic sensitivity is implicated in the rise of multidrug resistant bacteria and nosocomial infections [56, 57].

Nosocomial infections afflict approximately 15% of all hospitalized patients, and these infections often result in prolonged hospital stays, significant financial burden, and disability in both developed and developing countries [58]. Multidrug resistant bacteria are implicated in at least 14% of all nosocomial infections in the United States, and this number continues to rise [59, 60]. Increased resistance is accompanied by a sharp decline in the development of new antibiotics, which has resulted in a global healthcare crisis [61]. Antibiotic resistance is caused in part by the overuse and misuse of antibiotics, as selective pressure can accelerate conferred resistance [62]. Additionally, some bacterial growth conditions, such as biofilm formation, reduce antibiotic susceptibility. Bacteria within a biofilm are 10-1000 less susceptible to antibiotics due to numerous complex mechanisms including the structural barrier provided by the extracellular matrix (ECM), ECM-sequestered antibiotic-degrading enzymes, and phenotypic/metabolic changes in sessile bacteria orchestrated by cell-to-cell communication [22, 57, 63, 64]. Additionally, cells present in the nutrient-lacking biofilm can exhibit lower growth rates and reduced metabolic activity, contributing to reduced antibiotic susceptibility [57]. Biofilms can foster “persister” cells that can often lead to recalcitrance and reestablishment of infection, and they are thought to have a significant role in acquired resistance [57].

Escherichia coli (*E. coli*) and *Staphylococcus aureus* (*S. aureus*) are robust biofilm-forming bacteria that are often implicated in drug-resistant nosocomial infections. Uropathogenic *E. coli* (UPEC) alone account for approximately 50% of all hospital-acquired infections [65]. Although antibiotic resistance varies between isolates, UPEC strains have exhibited resistance to a wide range of antibiotics including fluoroquinolones, amoxicillin, cephalosporin, and ampicillin [65]. Many *S. aureus* strains have also demonstrated clinical resistance to a vast majority of antibiotics including aminoglycosides, penicillins, tetracyclines, all β-lactam antibiotics, and more [56, 66].

To date, many anti-biofilm efforts have focused on the destabilization of the 3-dimensional structure of the biofilm ECM, prompting bacteria to return to the planktonic state and resulting in increased sensitivity of the treated biofilm to antibiotics. Biofilm dispersal can be achieved using various matrix-degrading enzymes such as proteases, deoxyribonucleases, and glycoside hydrolases [67-69]. Other strategies employ anti-biofilm peptides, peptide mimetic graphene quantum dots, or oligosaccharides against specific protein or extracellular DNA targets in the extracellular polymeric substance [70-72]. While these techniques can render biofilms more susceptible to antibiotic treatment, some biofilms have shown resistance to various dispersion agents. Further, small molecule agents can be degraded by bacteria or can rapidly diffuse away from biofilms. Thus, the identification of new extracellular targets, such as amyloid proteins, and the development of novel inhibition or dispersion methods is desirable.

The reduced antibiotic susceptibility of many *E. coli* and *S. aureus* species is partially attributed to the use of mature amyloid fibrils as structural biofilm scaffolds and to mediate dispersion of chemical or mechanical agents [8, 9, 16, 47-49]. *E. coli*, a gram-negative bacterium, produces amyloid fibrils known as curli in its biofilms [47, 73]. Curli biogenesis involves seven

genes that are transcribed by two separate operons, *csgBAC* and *csgDEFG* [47]. CsgA and CsgB form the amyloid fibrils, and CsgC, CsgD, CsgE, CsgF, and CsgG are involved either in the secretion-assembly machinery or function to activate transcription of the *csgBAC* operon [47]. This complex machinery has evolved to tightly regulate curli biogenesis and to protect the cell from self-toxicity associated with the accumulation of intracellular aggregates [47]. The toxicity risk is minimized by secreting precursors to the growing curli fibers outside of the cell thereby restricting amyloid formation to the cell surface alone.

In *S. aureus*, a gram-positive bacterium, phenol soluble modulins (PSMs) aggregate to form amyloid fibrils that fortify the biofilm matrix [8, 16, 48]. PSMs are surfactant-like peptides that, in the monomeric form, are responsible for the promotion of biofilm disassembly [16]. However, during biofilm assembly, PSMα3 forms small aggregates capable of seeding fibrilization that then undergo secondary nucleation by PSMα1, PSMα3 and PSMβ1, with PSMα1 being the dominant component of the mature fibrils [48]. Notably, mutant strains lacking the machinery to produce PSMs are more susceptible to biofilm degradation [16]. Although the mechanisms of amyloid formation in *S. aureus* are not fully characterized, the regulation of PSM aggregation has a clear and significant role in biofilm assembly and disassembly [16].

As previously mentioned, nonstandard α-sheet structure was identified in the oligomeric intermediates of both CsgA and PSMα1 [8, 9]. To characterize this structure, a [5, 53, 74] library of *de novo* hairpin peptides composed of alternating L- and D-chirality amino acids that adopt stable α-sheet structure was produced to specifically target and bind to α-sheet oligomers [5-10, 38, 53, 54]. These α-sheet peptides are denoted “AP” for “Alternating Peptide,” which indicates alternating L- and D-amino acid templating. Notably, APs inhibit fibrilization and oligomer-associated toxicity of amyloid proteins regardless of their native structure [6-10, 38, 54]. Further,

APs exhibit no specificity toward the monomeric and fibrillar forms of amyloid species, supporting the significance of α-sheet structure in binding and inhibition [38, 75].

Previous studies demonstrate that by inhibiting amyloid fibrilization, APs can weaken bacterial biofilms and significantly reduce biofilm cell density in various bacteria, including *E. coli* and *S. aureus* [8, 9]. These findings are visually supported by electron microscopy experiments that depict complete, or near complete, inhibition of biofilm and amyloid formation by APs in multiple bacteria [8-10]. Pertinent to the studies presented here, α-sheet peptides inhibited the aggregation and amyloid formation of PSMα1 *in vitro* [8]. Inhibition of CsgA fibrilization was also observed *in vitro* when excess CsgA was co-incubated with α-sheet peptides [9]. Immunoblotting was also performed on endpoint samples: CsgA without peptide was almost entirely converted to insoluble fibrils while CsgA co-incubated with α-sheet peptides resulted in an increased concentration of soluble CsgA [9]. Interestingly, amyloid and biofilm inhibition by APs does not cause cell death, eliminating the concern of selective pressure leading to acquired resistance [9]. Instead, amyloid inhibition facilitates a shift in cells from the biofilm to the planktonic state, rendering them more susceptible to antibiotics [9]. In a previous paper, we showed that AP401 significantly increased the susceptibility of uropathogenic *E. coli* to gentamicin [9]. Here, we expand on our previous work to investigate the ability of AP90 and AP401, two 23-residue α-sheet peptides with identical sequences but opposite chirality at each residue, to increase the susceptibility of *E. coli* and *S. aureus* to a wide range of antibiotics. *E. coli* and *S. aureus* were selected as representative gram-negative and gram-positive species, respectively, and peptide concentrations were chosen based on efficacy in preliminary work. Our goal here is to evaluate the effect of co-administration of the α-sheet peptides with a range of antibiotics on biofilm susceptibility.

2.3 Results

2.3.1 E. coli *UTI89 and* S. aureus *MN8 show low biofilm antibiotic susceptibility*

All experiments used either *E. coli* strain UTI89 [76] or *S. aureus* strain MN8 [8], both of which are derived from clinical isolates. UTI89 and MN8 were selected as clinically relevant representative gram-negative and -positive bacteria, respectively. UTI89 is a well-characterized uropathogenic *E. coli* (UPEC) strain from cystitis and is considered a prototype UPEC isolate [77]. MN8 is a toxic shock strain isolated from the urogenital tract.

We first conducted experiments to quantify the susceptibility of mature *E. coli* UTI89 and *S. aureus* MN8 biofilms to five antibiotics: amoxicillin (an amino-penicillin effective against many uropathogenic *E. coli* and *Staphylococcus* species [78]), ciprofloxacin (a broad spectrum fluroquinolone active against both gram-positive and gram-negative bacteria [79]), erythromycin (a macrolide primarily effective against gram-positive bacteria [80]), gentamicin (an aminoglycoside primarily effective against gram-negative bacteria [81]), and vancomycin (a tricyclic glycopeptide used against gram-positive bacteria [82]). These antibiotics were selected to cover a range of antibiotic classes and to target both gram-negative and -positive bacteria. A diverse panel of antibiotics was to chosen to demonstrate that any effects of the peptides on antibiotic susceptibility are not antibiotic specific. We tested four concentrations per antibiotic (100 μg/mL, 300 μg/mL, 500 μg/mL, and 1 mg/mL) and compared the total colony forming units (CFUs) to the non-antibiotic control condition to measure the decrease in CFUs upon antibiotic addition after 24 (*S. aureus*) or 48 (*E. coli*) total hours. The percentage decrease for each antibiotic condition was calculated from the UTI89 or MN8 CFUs for the non-antibiotic control and the CFUs with antibiotics: % decrease = $((CFU_{control} - CFU_{abx\ condition}) / (CFU_{control})) \times 100\%$. Low biofilm antibiotic susceptibility was observed for both bacteria (**Table 2.1**).

		Antibiotic Concentration (µg/mL)			
		100	300	500	1000*
***E. coli* UTI89**	Amoxicillin	39	78	88	56
	Ciprofloxacin	44	70	79	60
	Erythromycin	47	40	42	48
	Gentamicin	99	99.9	99.99	99.99
	Vancomycin	38	43	47	53
***S. aureus* MN8**	Amoxicillin	48	31	26	18
	Ciprofloxacin	40	54	72	81
	Erythromycin	11	45	37	51
	Gentamicin	45	53	59	63
	Vancomycin	59	88	86	87

Table 2.1: CFU Percentage Reductions of UTI89 and MN8 Biofilms to Five Antibiotics Indicate Multidrug Resistance. CFU percent reductions for addition of antibiotics to UTI89 and MN8 biofilms were determined for CFUs measured after 48 (UTI89) or 24 (MN8) hours. The percentage decrease for each antibiotic condition was calculated from the UTI89 or MN8 CFUs for the non-antibiotic control and the CFUs with antibiotics: percentage decrease = (($CFU_{control}$ - $CFU_{abx\ condition}$) / ($CFU_{control}$)) x 100%. *Some antibiotics (amoxicillin, ciprofloxacin and erythromycin) are not fully soluble in media at concentrations of 500 µg/mL and 1000 µg/mL.

E. coli exhibited the highest susceptibility to gentamicin at each of the tested concentrations (4-log or 99.99% CFU reduction at 1,000 µg/mL) and showed very little susceptibility to the other antibiotics (**Table 2.1**). We predicted that erythromycin and vancomycin would have minimal effect on *E. coli*, as they are primarily effective against gram-positive bacteria. However, the lack of effect by ciprofloxacin and amoxicillin indicates that UTI89 biofilms exhibit reduced antibiotic susceptibility to multiple drugs.

S. aureus exhibited the highest susceptibility to vancomycin at each concentration, although a CFU reduction of 1-log or greater was not observed for any antibiotic combination (**Table 2.1**). The highest CFU reduction (88%) was observed at 300 µg/mL, with similar reductions

of 86 and 87% observed for 500 or 1,000 μg/mL respectively. Ciprofloxacin was also effective against *S. aureus*, resulting in an 81% reduction at 1,000 μg/mL (**Table 2.1**). *S. aureus* was minimally susceptible to amoxicillin, erythromycin, and gentamicin with the highest percentage CFU reduction of only 63% for 1000 μg/mL gentamicin (**Table 2.1**). As gentamicin is primarily effective against gram-negative bacteria, we expected it to have little effect against *S. aureus*. However, the lack of susceptibility to amoxicillin and erythromycin indicates that the MN8 biofilms are multidrug resistant. Additionally, the decline in CFU percentage reduction at higher concentrations for some antibiotics (amoxicillin, ciprofloxacin, and erythromycin) is attributed to the fact that they were not fully soluble in the media at concentrations above 500 μg/mL.

Based on these results, an antibiotic concentration of 300 μg/mL was used for the following studies incorporating our α-sheet peptides. This concentration was selected because a reduction in biofilm formation was observed for all antibiotics and both bacterial species at this concentration. Additionally, this antibiotic concentration falls within the range of known minimum biofilm inhibitory concentrations (bMICs) for uropathogenic *E. coli* and methicillin susceptible *S. aureus* (MSSA) for the five antibiotics tested [83-92]. Rafaque et al. measured the bMICs for 155 uropathogenic *E. coli* strains and reported a range of 128-2048 μg/mL for ciprofloxacin and 64-1024 μg/mL for gentamicin [83]. For MSSA strains, bMICs reported by Pettit et al. were >128 μg/mL for ciprofloxacin and >2048 μg/mL for gentamicin and vancomycin [86, 87]. Similarly, Mandell et al. observed bMICs for MSSA isolates ranging from 10-1000 μg/mL for gentamicin and 50-1000 for vancomycin [86]. The range of bMICs reported in the literature reflects the variation in biofilm antibiotic susceptibility between strains. However, all reports indicate reduced biofilm antibiotic susceptibility as observed with the *E. coli* strain UTI89 and the *S. aureus* strain MN8 in this study.

2.3.2 α-Sheet peptides inhibit amyloid formation and reduce biofilm density

UTI89 and MN8 biofilms were then grown with α-sheet peptides (no antibiotics) to determine their effect on amyloid formation and biofilm density. The amyloid dye Thioflavin T (ThT) was used an indicator of amyloid fibril content as it fluoresces upon binding β-sheet fibrils [93]. As ThT also binds nonspecifically to the bacterial cell surface [8], UTI89 experiments included a non-amyloid forming control mutant strain, UTI89 ΔcsgA, as an estimate of nonspecific ThT fluorescence.

For UTI89 experiments, a significant reduction in ThT fluorescence was observed for all peptide conditions (**Figure 2.1A**). The 100 μM AP90 and AP401 conditions had the largest reductions of 67% and 70%, for AP90 and AP401 respectively, as compared to the UTI89 control ($p<0.0001$; this p-value indicates that the differences are statistically significant where $p<0.05$ is the cutoff for determined statistical significance). This reduction was comparable to that of the UTI89 Δ*csgA* control, indicating complete inhibition of amyloid fibrilization. The difference in ThT reduction between the 100 μM peptide conditions and the UTI89 Δ*csgA* control was not statistically significant. Critically, the addition of peptides at either concentration did not cause a significant reduction in biofilm ThT fluorescence for the UTI89 Δ*csgA* control (**Supplementary Figure 2.1A**). As the UTI89 Δ*csgA* strain does not form amyloid, it was expected that the peptides would not affect the baseline ThT fluorescence. For MN8 experiments, a significant reduction in ThT fluorescence was also observed for all peptide conditions (**Figure 2.1C**). The 100 μM AP401 condition showed the greatest reduction with a 29% fluorescence reduction as compared to the MN8 control ($p<0.0001$).

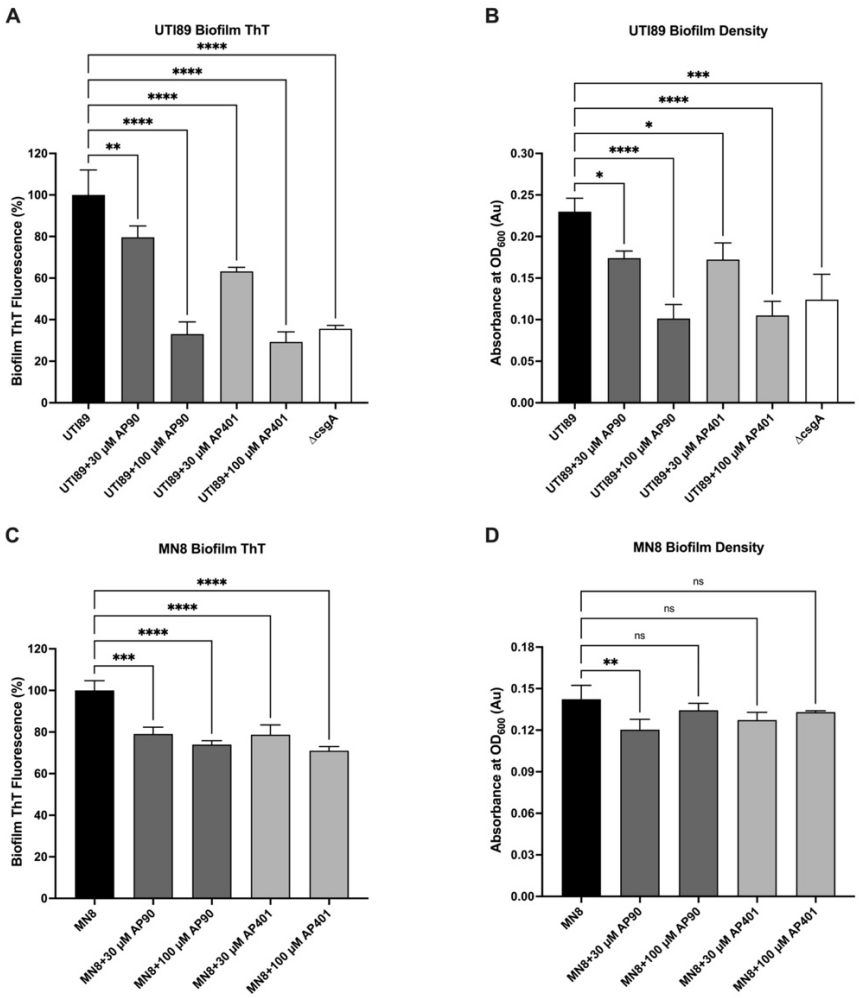

Figure 2.1: ThT and biofilm density graphs indicate amyloid inhibition. Both α-sheet peptides inhibited amyloid formation as indicated by reduced ThT fluorescence. Biofilm ThT fluorescence values are reported as percent of the average UTI89 or MN8 peptide-free control fluorescence. For UTI89 **A)**, 100 µM AP401 caused the greatest reduction in fluorescence of 70% as compared to the UTI89 control (*p<0.0001*). Reductions in biofilm formation as quantified by biofilm density measurements (OD_{600}) were also observed for both peptides and bacteria. For UTI89 **B)**, 100 µM AP90 and AP401 reduced biofilm formation to the level of the control UTI89 Δ*csgA* strain. For ThT fluorescence for MN8 **C)**, the 100 µM AP401 condition caused the greatest reduction of 29% as compared to the MN8 control (p<*0.0001*). For MN8 biofilm density **D)**, the 30 µM AP90 condition significantly reduced biofilm formation. All values are mean ± SD for three replicates.

The optical density (OD_{600}) was quantified as a measure of the mass of the biofilms. For UTI89, all peptide conditions caused a significant reduction in biofilm density (**Figure 2.1B**). The 100 µM AP90 and AP401 conditions caused a 56% and 54% reduction in biofilm density (*p<0.0001*), for AP90 and AP401 respectively, as compared to the UTI89 control. This is

comparable to the reduction seen for UTI89 Δ*csgA*. For MN8, a small, yet statistically significant reduction in biofilm density was observed only for the 30 μM AP401 condition (*p=0.008*) (**Figure 2.1D**). These data indicate that the α-sheet peptides inhibit amyloid formation as indicated by ThT fluorescence, and that this inhibition correlates to a reduction in biofilm material as measured by optical density. This conclusion is supported by previous studies conducted with PSMα1 and α-sheet peptides *in vitro* in which the α-sheet peptides inhibited the aggregation and amyloid fibril formation of PSMα1 [8]. Furthermore, the mechanism of action of the α-sheet peptides is the same in both bacterial systems via binding to the α-sheet oligomers of PSMα1 and CsgA to prevent amyloid formation.

Varied efficacy by the two peptides as well as a concentration-dependent response was observed for both bacterial strains. The density of cells in the planktonic state and in the PBS rinse were also quantified with OD measurements (**Figure 2.2A** and **Figure 2.2B**). As shown in **Figure 2.1B and 2.1E**, the addition of the peptides caused a reduction in biofilm mass. Concomitantly, addition of the peptides caused an increase in the planktonic cell density such that the total density did not decrease, as previously shown for UTI89 [9]. Next, the addition of the peptides did not cause a reduction in the total cell density for the UTI89 Δ*csgA* control (**Supplementary Figure 2.1B**). Finally, UTI89 and MN8 growth curves were performed with growth measured by CFUs in the presence of peptide (**Figure 2.2C** and **Figure 2.2D**). The peptides did not affect the growth rates of UTI89, UTI89 Δ*csgA*, or MN8 in the presence of 100 μM AP90 or AP401 as compared to cells grown in an equal volume of water. This indicates that the peptides did not affect cell growth, only the formation of mature amyloid.

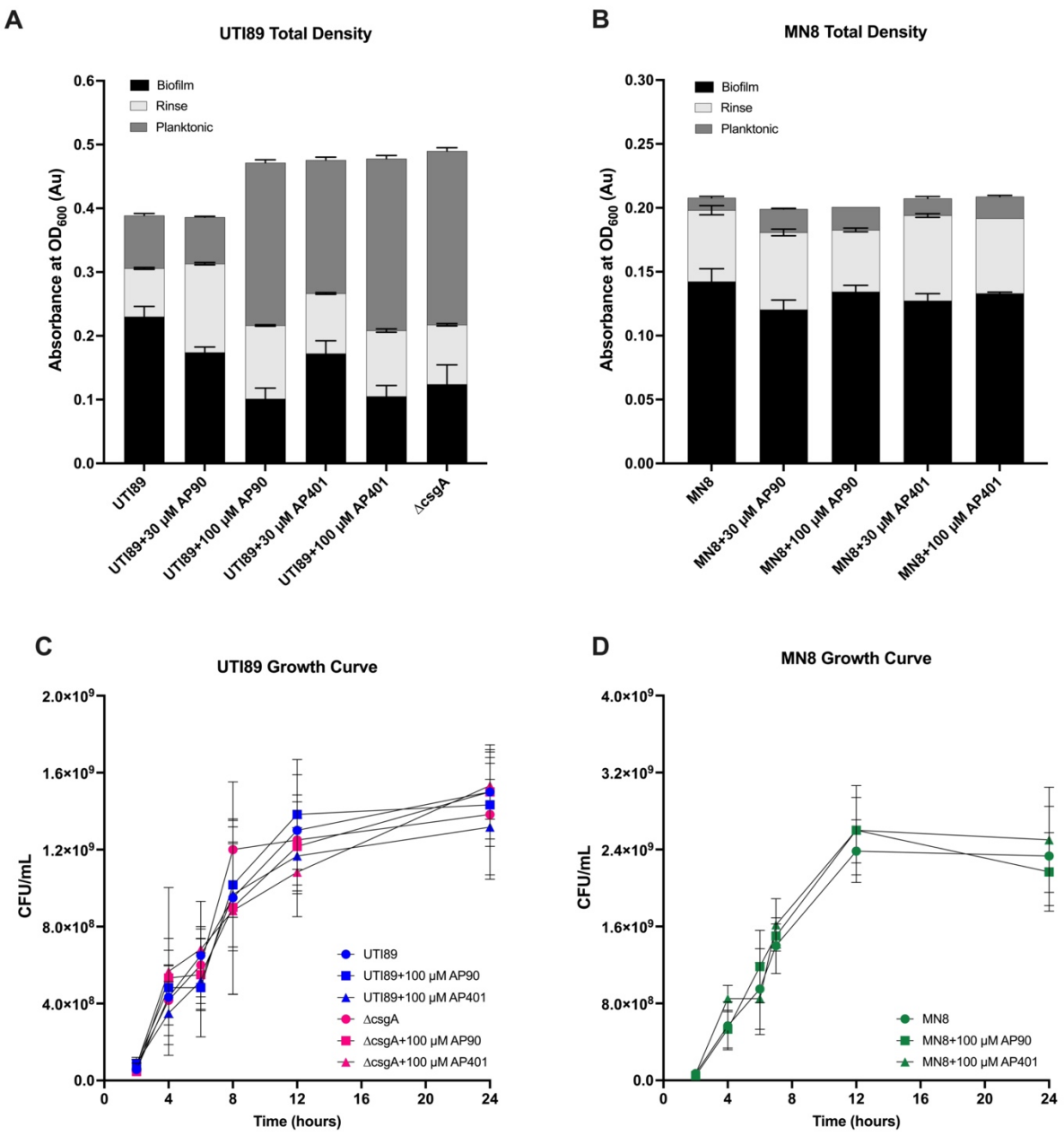

Figure 2.2: α-Sheet peptides do not cause cell death or affect bacterial growth rate. A) For UTI89, the peptides caused a reduction in biofilm density but an increase in planktonic cell density, such that there is not a reduction in overall density. The same effect on overall density is observed for MN8 **B)** where the total density remains constant with the addition of peptides. All values are mean and standard deviation for three replicates. Growth curves for **C)** UTI89 and UTI89 Δ*csgA* strain and **D)** MN8 in the presence of α-sheet peptides at 100 µM showed that the peptides had no effect on growth rate. All values are mean ± SD for three replicates.

2.3.3 Curli fibril inhibition by AP90 and AP401 render E. coli *more susceptible to antibiotics*

After establishing the susceptibility of mature biofilms to the antibiotics (**Table 2.1**) and determining the effect of the α-sheet peptides on curli fibril and biofilm inhibition (**Figure 2.1**), we tested the effect of the co-administration of the α-sheet peptide inhibitors and antibiotics on antibiotic susceptibility. For each *E. coli* antibiotic condition, we compared the susceptibility of the UTI89 strain to the non-amyloid forming control mutant strain, UTI89 Δ*csgA*. Because our hypothesis is contingent on the idea that curli fortifies the biofilm and reduces antibiotic susceptibility, we predicted that the CsgA knockout strain, UTI89 Δ*csgA*, would be more susceptible than UTI89 to each antibiotic without α-sheet peptide treatment. This was the case for all antibiotics tested except for amoxicillin where a comparable effect was observed (**Figure 2.3 A-E**).

Comparing the antibiotic susceptibility of wild-type UT189 treated with α-sheet peptides to the antibiotic susceptibility of UTI89 Δ*csgA* also confirmed the extent of curli inhibition. Notably, in cases where UTI89 Δ*csgA* is not more susceptible to an antibiotic than UTI89 treated with a-sheet peptides, we can deduce that biofilm fortification by curli does not play a significant role in *E. coli* antibiotic resistance. In these cases, we would not predict that our peptides would have a large effect on antibiotic susceptibility. For each peptide and antibiotic combination, we presented the CFU counts (**Figure 2.3** and **Figure 2.4**) as these values demonstrate the magnitude of the effect of the peptides and the antibiotics. The percentage decrease for each antibiotic condition was calculated from the UTI89 or MN8 CFUs for the non-antibiotic control and the CFUs with antibiotics as previously defined. Our findings are discussed below and summarized in **Table 2.2**.

UTI89 Susceptibility: Amoxicillin

For the non-antibiotic conditions, addition of both peptides significantly reduced biofilm CFUs as compared to the UTI89 strain with AP401 showing a reduction equal to that of the UTI89 Δ*csgA* control strain (*p<0.0001* for all) (**Figure 2.3A**). For the antibiotic conditions, AP401 caused a non-significant reduction in biofilm formation (**Figure 2.3A**). UTI89 and UTI89 Δ*csgA* exhibited a 77% and 72% reduction in CFUs, respectively, when exposed to 300 μg/mL amoxicillin, suggesting that curli formation does not have a significant effect on biofilm susceptibility to this antibiotic (**Figure 2.3A**). We therefore predicted that our designed peptides would not have a large effect on clearance by amoxicillin. Interestingly, the CFU reduction of UTI89 increased to 92% when incubated with AP401 (**Figure 2.3A**). This indicates that UTI89 is more susceptible to amoxicillin with co-administration of AP401. In contrast, AP90 had no effect on UTI89 susceptibility to amoxicillin.

UTI89 Susceptibility: Ciprofloxacin

For the non-antibiotic conditions, addition of each peptide caused a statistically significant reduction in biofilm CFUs, with AP401 causing a greater reduction (*p=0.0020* for AP90 and *p<0.0001* for AP401) (**Figure 2.3B**). A significant CFU reduction was again observed for both α-sheet peptides as compared to the UTI89 strain for ciprofloxacin-treated conditions (*p<0.0001*) (**Fig 2.3B**). Ciprofloxacin applied to UTI89 biofilms resulted in a 44% reduction in CFUs as compared to the non-antibiotic UTI89 condition (**Figure 2.3B**). UTI89 Δ*csgA* exhibited a 95% CFU reduction upon ciprofloxacin treatment, indicating that amyloid incorporation into UTI89 biofilms has a critical role in establishing susceptibility to the antibiotic (**Figure 2.3B**). When

grown with AP90 and AP401, the UTI89 CFU reduction from the UTI89 non-antibiotic control increased to 91% and 96%, respectively (**Figure 2.3B**). α-Sheet peptide inhibition of curli formation made UTI89 more susceptible to ciprofloxacin, and AP401 increased susceptibility to that of the non-amyloid forming control strain, UTI89 Δ*csgA*.

UTI89 Susceptibility: Erythromycin

For the erythromycin conditions, AP401 significantly reduced biofilm CFUs to the level of the UTI89 Δ*csgA* control strain (*p=0.028*) (**Figure 2.3C**). Erythromycin caused a 44% CFU reduction to UTI89 biofilms and an 82% CFU reduction to UTI89 Δ*csgA* (**Figure 2.3C**). When grown with AP90 or AP401, UTI89 CFU reductions increased to 72% and 79%, respectively (**Figure 2.3C**). These CFU reduction values are relatively low even with significant amyloid inhibition by AP90 and AP401 as seen in **Figure 2.1A**, but this was expected since erythromycin is not active against gram-negative bacterial species.

UTI89 Susceptibility: Gentamicin

Application of gentamicin caused the greatest reduction in UTI89 biofilm CFUs of the five antibiotics tested. As previously demonstrated for the non-antibiotic conditions, addition of both peptides caused a statistically significant reduction in biofilm CFUs and biofilm OD_{600} (**Figure 2.1B**) as compared to UTI89 (*p<0.0001*) (**Figure 2.3D**). Exposure to gentamicin reduced UTI89 biofilm CFUs in the case of both peptides. The observed effect was comparable to that of the UTI89 ΔcsgA strain that does not form amyloid fibrils. Of note, there was no statistically significant difference between the peptide conditions and the UTI89 Δ*csgA* strain, even in cases where the peptide conditions caused a CFU reduction beyond that of the knockout strain. These

data indicate that amyloid formation contributes significantly to UTI89 biofilm gentamicin susceptibility (**Figure 2.3D**). Both AP90 and AP401 rendered UTI89 more susceptible to gentamicin, resulting in 99.99% CFU reductions as compared to the UTI89 non-antibiotic condition for both peptides (**Figure 2.3D**).

UTI89 Susceptibility: Vancomycin

For the vancomycin conditions, both peptides significantly reduced biofilm formation as compared to UTI89 (*p=0.0019* for AP90 and *p=0.0002* for AP401) and reduced biofilm formation to levels comparable to UTI89 ΔcsgA (**Figure 2.3E**). Vancomycin exposure led to a 32% reduction of CFUs in UTI89 biofilms and 86% reduction in UTI89 Δ*csgA* biofilms (**Figure 2.3E**). Although vancomycin is primarily used against gram-positive bacterial species, the discrepancy in CFU reduction between UTI89 and UTI89 Δ*csgA* suggests that curli inhibition may result in increased vancomycin susceptibility. Indeed, AP90 and AP401 increased UTI89 CFU reductions to 85% and 93%, respectively (**Figure 2.3E**). Incubation of UTI89 with AP401 resulted in a 60% greater biofilm reduction by vancomycin than with no peptide. These data are notable in that they demonstrate that amyloid fibril inhibition can improve susceptibility to a wide range of antibiotics, independent of the antibiotic's specific mechanism of action.

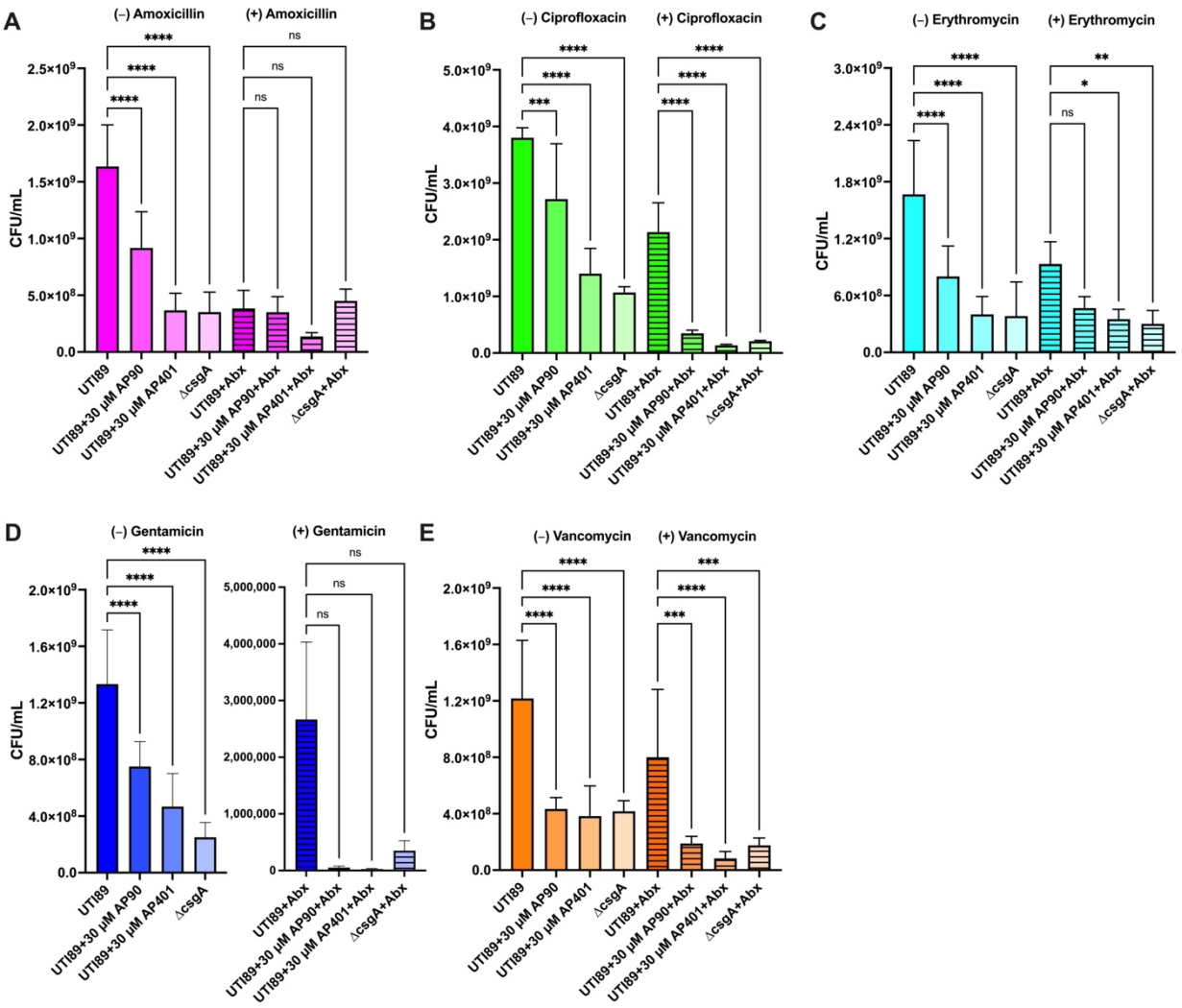

Figure 2.3: α-Sheet peptides increase biofilm antibiotic susceptibility of UTI89. Both synthetic α-sheet peptides inhibited biofilm formation for the non-antibiotic and antibiotic conditions for the *E. coli* strain UTI89. Biofilm formation was quantified as CFU/mL for UTI89 biofilms without (plain bars) and with antibiotics (striped bars) after 48 hours. Antibiotics at 300 μg/mL were added after 42 hours of growth and biofilm formation was measured for **A)** amoxicillin, **B)** ciprofloxacin, **C)** erythromycin, **D)** gentamicin, and **E)** vancomycin. Values are mean ± SD for three replicates and p-values are indicated as follows: *ns* = not significant; * $p < 0.05$; ** $p < 0.01$, *** $p < 0.001$, **** $p < 0.0001$. There is not a statistically significant reduction in CFUs between the peptide conditions and the Δ*csgA* control for all non-antibiotic and antibiotic conditions.

2.3.4 AP90 and AP401 increase S. aureus *biofilm susceptibility to antibiotics*

MN8 Susceptibility: Amoxicillin

For the non-antibiotic conditions, both peptides caused a significant reduction in biofilm formation as compared to the MN8 *S. aureus* strain alone, and AP90 had a larger effect than AP401 ($p=0.0038$ for AP90 and $p=0.04$ for AP401) (**Figure 2.4A**). A significant reduction was also seen for both peptides for the antibiotic conditions ($p<0.0001$ for AP90 and $p=0.001$ for AP401) (**Figure 2.4A**). When applied to mature MN8 biofilms, amoxicillin caused a 24% reduction in total CFUs (**Figure 2.4A**). Incubation with both AP90 and AP401 increased MN8 susceptibility to the antibiotic, resulting in a 68% and 59% CFU reduction, respectively (**Figure 2.4A**). Although the peptides increased antibiotic susceptibility, the magnitude of the change likely indicates that the MN8 biofilm susceptibility to amoxicillin is largely independent of amyloid formation in the biofilm.

MN8 Susceptibility: Ciprofloxacin

For the non-antibiotic conditions, both peptides caused a reduction in biofilm formation, with a larger effect observed with AP90 ($p=0.0016$) (**Figure 2.4B**). For the ciprofloxacin conditions, only AP90 caused a reduction in CFU formation (**Figure 2.4B**). The addition of ciprofloxacin caused a 64% reduction in CFUs for the MN8 control while the AP90 and AP401 conditions resulted in 80% and 53% reductions, respectively (**Figure 2.4B**). The increase in CFU reduction with AP90 indicates that amyloid formation contributed to but was not the primary factor in biofilm susceptibility to ciprofloxacin. Additionally, the difference in CFU change between AP90 and AP401 suggests that peptide chirality played a role in efficacy.

MN8 Susceptibility: Erythromycin

The addition of erythromycin to mature MN8 biofilms caused a 61% reduction in biofilm CFUs (**Figure 2.4C**). For the non-antibiotic conditions, only AP90 caused a significant reduction in CFUs (*p=0.0012*) (**Figure 2.4C**). For the antibiotic conditions, both peptides caused a significant reduction in CFUs (*p=0.02* and *p=0.035* for AP90 and AP401, respectively) with reductions of 89% for AP90 and 87% for AP401 (**Figure 2.4C**). These increases in CFU reduction suggest that amyloid formation is a factor in the reduced MN8 biofilm susceptibility to erythromycin.

MN8 Susceptibility: Gentamicin

Gentamicin was predicted to have a minimal effect on *S. aureus* as it targets aerobic gram-negative bacteria by passing through the gram-negative membrane [50]. Both peptides caused a moderate reduction in biofilm formation as compared to the MN8 strain with gentamicin only (*p=0.04* for both peptides) (**Figure 2.4D**). When applied to mature MN8 biofilms, gentamicin reduced CFUs 37% (**Figure 2.4D**). Incubation with AP90 and AP401 increased MN8 susceptibility, corresponding to a 63% reduction in biofilm CFUs for both peptides (**Figure 2.4D**).

MN8 Susceptibility: Vancomycin

For the non-antibiotic conditions, both peptides caused a significant reduction in CFUs (*p=0.001* and *p=0.0042* for AP90 and AP401, respectively) (**Figure 2.4E**). For the vancomycin conditions, incubation with AP90 and AP401 led to a non-significant reduction in biofilm CFUs (**Figure 2.4E**). Vancomycin reduced MN8 biofilm CFUs by 91%, and AP90 and AP401 successfully increased susceptibility further, corresponding to CFU reductions of 96% and 93%, respectively (**Figure 2.4E**). These data confirm that MN8 amyloid formation reduced biofilm

susceptibility to vancomycin and that the amyloid inhibiting peptides improved antibiotic susceptibility.

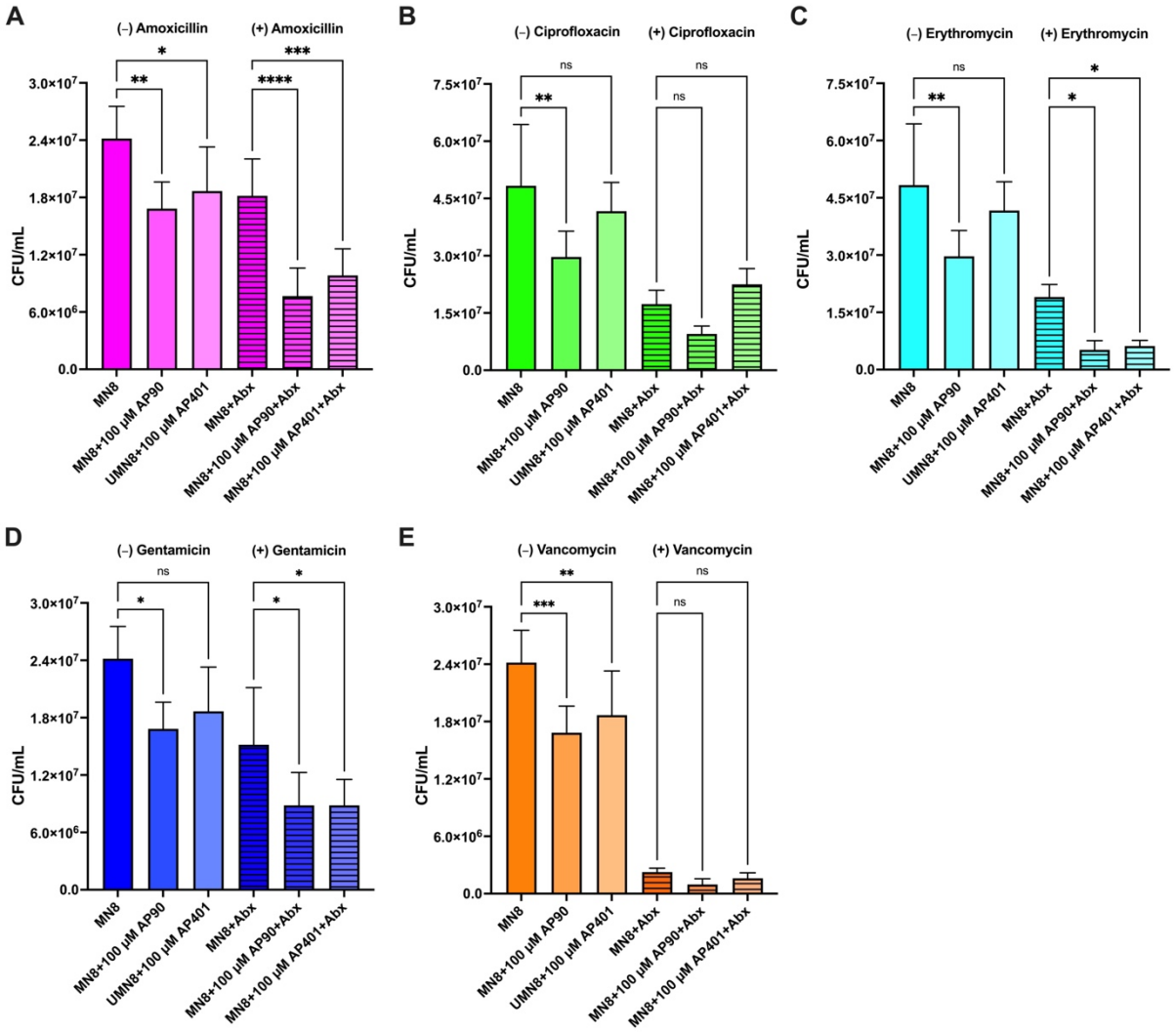

Figure 2.4: α-Sheet peptides increase biofilm antibiotic susceptibility of MN8. The α-sheet peptides inhibited *S. aureus* biofilm formation for the non-antibiotic and antibiotic conditions to varying extents. Biofilm formation was quantified as CFU/mL for MN8 biofilms without (plain bars) and with antibiotics (striped bars) after 24 hours of growth. Antibiotics at 300 µg/mL were added after 18 hours of growth and biofilm formation was measured for **A)** amoxicillin, **B)** ciprofloxacin, **C)** erythromycin, **D)** gentamicin, and **E)** vancomycin. Values are mean ± SD for three replicates and p-values are indicated as follows: *ns* = not significant; * $p < 0.05$; ** $p < 0.01$, *** $p < 0.001$, **** $p < 0.0001$.

2.4 Discussion

Increased rates of antibiotic resistance pose a global threat, thus there exists a significant need to develop novel methodologies to target microbial infections, particularly those that are biofilm-associated. The ongoing emergence of multidrug resistant strains and the use of some drugs only as antibiotics of last resort disincentives the development of novel antibiotics. Approaches like the strategy presented here are advantageous as they may facilitate the continued use of existing antibiotics for treatment. Here, we present a strategy to increase the susceptibility of amyloid-forming bacteria to antibiotics without introducing selective pressure as caused by bactericidal compounds and reducing the risk of acquired resistance. We have previously shown that α-sheet peptides inhibit curli fibril formation, increase *E. coli* susceptibility to gentamicin, and improve macrophage clearance [9]. The findings reported here expand on our previous research by demonstrating that α-sheet peptides reduce biofilm cell density as reported by CFU quantification (**Figure 2.3** and **Figure 2.4**) and OD_{600} (**Figure 2.1B** and **Figure 2.1E**), and are effective at increasing antibiotic susceptibility of both gram-negative (*E. coli*) and gram-positive (*S. aureus*) bacterial species to multiple classes of antibiotics (**Table 2.2**) with varying mechanisms of action. The results reported here suggest that our peptides may be effective against additional amyloid-producing bacteria.

		Increased Susceptibility?	
		AP90+abx	AP401+abx
***E. coli* UTI89**	Amoxicillin	✓	✓✓✓
	Ciprofloxacin	✓✓✓	✓✓✓
	Erythromycin	✓	✓
	Gentamicin	✓✓✓✓ ✓	✓✓✓✓✓
	Vancomycin	✓✓	✓✓✓
***S. aureus* MN8**	Amoxicillin	✓	✓
	Ciprofloxacin	✓	✓
	Erythromycin	✓✓	✓✓
	Gentamicin	✓	✓
	Vancomycin	✓✓✓✓	✓✓✓

Table 2.2: Summary of susceptibility results for UTI89 and MN8 co-administration of α-sheet peptides AP90 or AP401 with five antibiotics. All peptide and antibiotic combinations increased biofilm antibiotic susceptibility, although to varying extents. Check marks indicate an increase in antibiotic susceptibility as determined by CFU percentage decrease from the UTI89 or MN8 non-antibiotic control where ✓= 50-80% reduction, ✓✓= 81-90% reduction, ✓✓✓= 91-95% reduction, ✓✓✓✓= 96-99% reduction, and ✓✓✓✓✓= >99% reduction.

Although our α-sheet peptides proved effective at increasing antibiotic susceptibility of clinically derived strains of both *E. coli* and *S. aureus*, there were key differences in the response of the bacteria to amyloid inhibition by APs. A higher peptide concentration was required to achieve a significant increase in *S. aureus* antibiotic susceptibility (100 μM vs. 30 μM in *E. coli*), and the observed differences likely arise because *E. coli* is a gram-negative bacterium while *S. aureus* is gram-positive. Gram-positive bacterial species are encompassed by thick layers of peptidoglycan, while gram-negative species have much thinner peptidoglycan cell walls surrounded by an outer membrane containing lipopolysaccharide [94]. Variations in the cell surface may differentially affect the ability for the *de novo* α-sheet peptides to access the growing

amyloid located on the cell surface. The observed differences may also be due to variations in the amount of amyloid precursor secreted by and incorporated into the biofilm of *E. coli* and *S. aureus*.

We also observed discrepancies in the relative potency of AP90 and AP401 in the two species. Previously, we found that AP401 is a more potent inhibitor of curli formation than its structural isomer, AP90. AP90 and AP401 have the same amino acid sequence, but every amino acid has the opposite chirality, and we hypothesized that the potency of AP401 in *E. coli* was due to the presence of D-amino acids in the hairpin turn resulting in increased stability to proteases. The results presented here suggest that AP401 is not only a more potent inhibitor of curli formation, but that this elevated inhibition also translates to a larger effect on antibiotic susceptibility. Interestingly, there was a smaller potency difference between AP90 and AP401 in *S. aureus* with AP90 causing a greater effect for four antibiotics. D-amino acids are frequently incorporated into gram-positive cell walls which are composed of thick peptidoglycan layers [95]. Because *S. aureus* utilizes D-amino acids in its cell wall, the bacteria may also produce proteases that are designed to cleave the peptide bond between D-amino acids. Therefore, AP401 may not be more stable than AP90 to proteases in *S. aureus*, as is hypothesized to be the case in *E. coli*.

Our designed peptides improved bacterial susceptibility to varying extents for each antibiotic. These observed variations can be attributed both to the differences between the mechanism of action of each antibiotic, as well as to the mechanism that governs the bacterial susceptibility to the antibiotic. AP90 and AP401 are amyloid inhibitors, and our hypothesis is contingent on biofilm amyloid formation having a significant effect on antibiotic susceptibility. However, AP90 and AP401 may not have any effect on a bacterium's susceptibility if the mechanism of reduced susceptibility is unrelated to biofilm fortification by amyloid fibrils. The largest increase in antibiotic susceptibility upon peptide administration was seen with gentamicin

for *E. coli* and vancomycin for *S. aureus*, indicating that amyloid formation was contributing significantly to antibiotic susceptibility in these cases.

Previous studies have identified several other compounds with anti-amyloid activity against bacterial biofilms, including peptides, proteins, curlicides, graphene quantum dots, and polyphenols [73, 96-98]. However, in some cases, such as for the plant flavonoids luteolin, myricetin and quercetin, biofilm inhibition was seen in some bacteria (*E. coli* and *S. aureus*) while an increase or no change in biofilm formation was observed in other bacteria (*Pseudomonas aeruginosa*) [99]. Additionally, while some compounds have successfully inhibited biofilm formation, most compounds have not been tested with antibiotics, or have even been shown to increase antibiotic resistance. In one study, the anti-amyloidogenic polyphenol epigallocatechin gallate (EGCG) caused reduced susceptibility of *S. aureus* to vancomycin, oxacillin, and ampicillin [100]. Another study found that in some conditions, EGCG administration promoted biofilm formation in *P. aeruginosa* and increased antibiotic resistance to tobramycin [101]. A third study reported that co-administration of EGCG and tobramycin had a moderate effect on wildtype *P. aeruginosa* biofilm minimum bactericidal eradication concentrations but a larger effect when the functional amyloid fibril Fap was overexpressed [102]. Thus, it is critical to test the efficacy of potential bacterial amyloid inhibitors in combination with antibiotics, as done in this study.

2.5 Materials and Methods

2.5.1 Peptide Synthesis

Synthetic α-sheet peptide inhibitors were designed *in silico* as previously described [6, 8, 9, 54]**,** using backbone dihedral angle constraints derived from MD simulations [103, 104] and

synthesized as described by Bleem et al. [9]. Briefly, peptides contain two α-strands of seven residues each, with amino acids alternating sequentially between L-conformation and D-conformation in each of the strands. The α-strands are connected by a five residue turn comprised of all L-amino acids (AP90) or all D-amino acids (AP401), which gives the peptide a hairpin shape. Finally, the tail of each strand consists of a Gly and an Arg residue, followed by acetyl and amide caps at the N- and C-terminus, respectively. Peptides were assembled by solid phase peptide synthesis on Rink amide resin with Fmoc chemistry and HBTU activation. Peptides were cleaved from the resin and side chain deprotected by TFA/TIPS/H2O (95:2.5:2.5) and precipitated by cold ether. Crude peptides were purified to >95% by RP-HPLC using 5 μM C12 or C18 100 Å columns (Phenomenex; Torrance, CA) and atomic masses were confirmed by electrospray mass spectrometry on a Bruker Esquire Ion Trap (Bruker; Billerica, MA). Sequences for the two α-sheet designs described in this study (AP90 and AP401) are listed in **Table 2.3**. All peptides were lyophilized after purification and stored at -20 or -80°C until use.

Peptide Sequences			
Name[a]	**Sequence**[b]	**Description**	**Source**
AP90	Ac-RGEmNlSwMNEYSGWtMnLkMGR-NH2	α-sheet monomer	Hopping et al., 2014
AP401	Ac-rGeMnLsWmneysGwTmNlKmGr-NH2	α-sheet monomer	Bleem et al., 2017
***E. coli* Strains**			
UTI89		UPEC strain; cystitis isolate	Mulvey et al., 2001
UTI89 ΔcsgA		UPEC strain; cystitis isolate with chromosomal deletion of *csgA* gene	Cegelski et al., 2009
***S. aureus* Strain**			
MN8		Clinically relevant strain; toxic shock isolate, urogenital tract	Schwartz et al., 2012

Table 2.3: Peptide sequences and bacterial strain descriptions. [a] "AP" refers to "Alternating Peptide", which indicates alternating L- and D- amino acid templating. [b] L- amino acids are displayed in all upper case; D-amino acids are displayed in lower case and underlined.

2.5.2 E. coli Biofilm Growth

A uropathogenic clinical isolate strain, UTI89 [76], and a control strain with a chromosomal deletion of the *csgA* gene, UTI89 Δ*csgA* [73], were used for all *E. coli* experiments. Overnight cultures were grown in 25 g/L Luria Broth (LB; Miller, Thermo Fisher Scientific; Waltham, MA) for 16-18 hours at 37°C with shaking (180 rpm). Cultures were then "refreshed" by replacing 5 mL of culture with 5 mL fresh LB medium and grown for an additional three hours

to ensure bacteria were in the exponential phase. Overnight cultures were then diluted to an optical density (OD_{600}) of 0.1 (~$8x10^7$ cells/mL) in YESCA broth supplemented with 4% DMSO (Corning; Glendale, AZ), medium known to promote increased curli formation [105]. Lyophilized peptide stock was dissolved in water and concentrations were determined by Nanodrop™ (Thermo Fisher Scientific; Waltham, MA). Diluted bacteria culture (180 µL) was plated with 20 µL peptide (or water, in the case of controls) and aliquoted in triplicate into wells of a sterile, clear 48-well polystyrene plate (Corning; Glendale, AZ). The final peptide concentration was 0, 30 µM (1.2 pg/CFU), or 100 µM (4 pg/CFU). Plates were covered, sealed in a plastic bag, and statically grown at 26°C for 48 hours.

2.5.3 S. aureus Biofilm Growth

S. aureus MN8 (clinical isolate; urogenital tract; [106]) was grown for 16-18 hours in 10 g/L trypticase soy broth (TSB; Becton, Dickinson and Company; Sparks, MD) at 37°C with shaking (180 rpm). Overnight cultures were "refreshed" by replacing 5 mL of culture with 5 mL of fresh TSB medium and grown for an additional six hours. Cells were then spun down and re-suspended in peptone-NaCl-glucose (PNG) media (Thermo Fisher Scientific; Waltham, MA) [16]. Resuspended cells were diluted to an optical density of 0.1 (OD_{600}). Peptides were prepared as described above. Diluted bacteria culture (180 µL) was plated with 20 µL peptide (or water, in the case of controls) and aliquoted in triplicate into wells of a sterile, clear 48-well polystyrene plate (Corning; Glendale, AZ). The final peptide concentration was 0, 30 µM (1.2 pg/CFU), or 100 µM (4 pg/CFU). Plates were covered, sealed in a plastic bag, and grown at 37°C for 24 hours with shaking (250 rpm).

2.5.4 Thioflavin T (ThT) Assay, Biofilm, and Total Density Measurements

After 24 or 48 hours of growth for *S. aureus* or *E. coli* respectively, planktonic cells and medium were removed, and biofilms were rinsed once with 250 µL PBS. Planktonic cells were spun down and resuspended in PBS, and the optical density of both planktonic and rinse samples was determined at 600 nm to estimate "planktonic" and "rinse" cell densities. The PBS rinse solution was removed from the wells and biofilms were resuspended in 200 µL of 20 µM ThT in PBS (Sigma- Aldrich; St. Louis, MO). Biofilms were homogenized by vigorous pipetting (30x per well), 3 minutes of sonication, and 1 minute on a plate shaker. 100 µL of each biofilm suspension was then transferred to a black-walled, clear-bottom 96 well plate for measurements in a plate reader (PerkinElmer; Waltham, MA). ThT fluorescence was measured at 438/495 nm as a proxy for amyloid formation, and biofilm absorbance was measured at 600 nm to estimate bacterial cell density. Fluorescence measurements were corrected for nonspecific fluorescence by subtracting the background intensity of identical samples without bacteria. Biofilm ThT fluorescence values are reported as percent of the average MN8 or UTI89 peptide-free control fluorescence. All values are mean and standard deviation for three replicates.

2.5.5 Growth Curves

Overnight cultures of UTI89 and UTI89 ΔcsgA were grown in 25 g/L Luria Broth (LB; Miller, Thermo Fisher Scientific; Waltham, MA) for 16-18 hours at 37°C with shaking (180 rpm). Overnight cultures of MN8 were grown in 10 g/L TSB. For each condition, 30 µL of the overnight was added to 3 mL of fresh LB or TSB medium supplemented with water or 100 µM AP90 or AP401 (final concentration) and grown at 37°C with shaking (180 rpm). At each time point (2, 4, 6, 7 or 8, 12, and 24 hours), 200 µL of media was removed, spun down, and resuspended in an

equal volume of PBS (Sigma- Aldrich; St. Louis, MO). The samples were then ultra-sonicated for 5 seconds on ice and diluted in tenfold increments. The serial dilutions were then plated on agar plates (LB agar or TSB agar) using the drop plate method [107]. Six replicates were plated per condition. Colonies were grown for 16 hours at 37°C and CFUs were counted. Total CFUs of the suspensions were calculated using the dilution number and the number of CFUs counted in that dilution.

2.5.6 Antibiotic Susceptibility

Biofilms were grown according to the methods described above. Five antibiotics were tested: amoxicillin (MP Biomedicals: Solon, OH), ciprofloxacin hydrochloride (MP Biomedicals: Solon, OH), erythromycin (Thermo Fisher Scientific; Waltham, MA), gentamicin sulfate (Thermo Fisher Scientific; Waltham, MA), and vancomycin hydrochloride (Thermo Fisher Scientific; Waltham, MA). Antibiotics were dissolved in YESCA (*E. coli*) or PNG medium (*S. aureus*) at a concentration of 900 µg/mL. 100 µL of antibiotic or control (YESCA/PNG media) was added to each well after 42 (*E. coli*) or 18 (*S. aureus*) hours of incubation without disturbing the biofilm for a final well concentration of 300 µg/mL. Following 6 additional hours of biofilm growth (48 or 24 hours total), planktonic cells were removed and discarded. The biofilms were rinsed with 250 µL PBS (Sigma Aldrich; St. Louis, MO), and the rinse was discarded. Biofilms were homogenized in 200 µL PBS by vigorous pipetting (30x per well), and the biofilm suspensions were transferred to an Eppendorf tube. The biofilm suspensions were then ultra-sonicated for 5 seconds on ice and diluted in tenfold increments. The serial dilutions were then plated on agar plates (LB agar or TSB agar) using the drop plate method [107]. Six replicates were plated per condition. Colonies were grown for 16 hours at 37°C and CFUs were counted. Total CFUs of the biofilm suspensions were

calculated using the dilution number and the number of CFUs counted in that dilution. The percentage decrease for each antibiotic condition was calculated from the UTI89 or MN8 CFUs for the non-antibiotic control and the CFUs with antibiotics: percentage decrease = (($CFU_{control}$ - $CFU_{abx\ condition}$) / ($CFU_{control}$)) x 100%.

2.5.7 Statistics

All statistical significance values reported are One-Way ANOVA with post-hoc comparisons as shown, and a Bonferroni multiple comparison correction performed in GraphPad Prism. A single asterisk indicates a p-value less than 0.05, which is the cutoff to be considered statistically significant. Two asterisks indicate greater significance, with a p-value less than 0.01. Three asterisks indicate a p-value less than 0.001. Four asterisks indicate a p-value less than 0.0001.

2.6 Supplementary Information

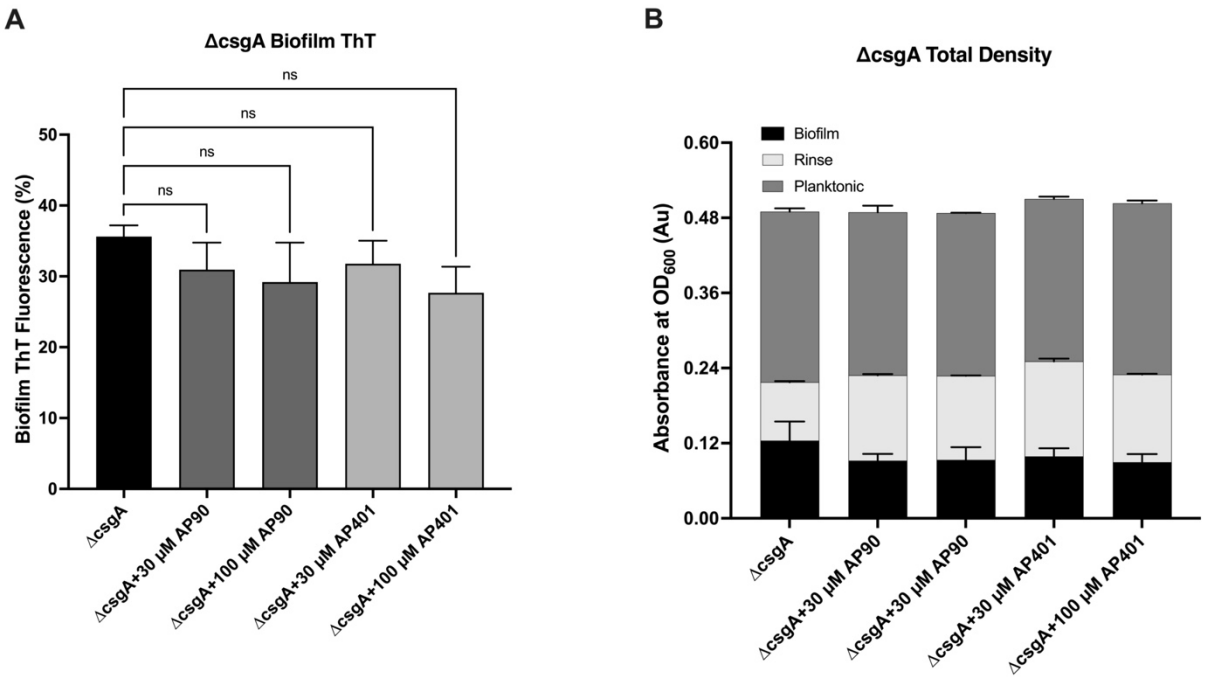

SI Figure 2.1: Peptides do not affect growth of UTI89 Δ*csgA* control. **A)** Addition of the peptides to the UTI89 Δ*csgA* control did not cause a reduction in ThT fluorescence as the strain does not produce amyloid. Addition of the peptides also did not cause a decrease in the total cell density of the UTI89 and MN8 strains. **B)** For the UTI89 Δ*csgA* control, addition of peptides did not reduce biofilm or planktonic cell density. All values are mean ± SD for three replicates.

Chapter 3. Layer-by-Layer Functionalized Gauze with Designed α-Sheet Peptides Inhibits *E. coli* and *S. aureus* Biofilm Formation*

*Text and figures under review at the *Journal of Biomedical Materials Research: Part A*

3.1 Abstract

Microbial biofilms on wounds lead to longer hospital stays, mechanical debridement, and higher mortality. Amyloid fibrils stabilize the bacterial biofilm's extracellular matrix (ECM) and represent a potential anti-biofilm target. As previously reported, *de novo* α-sheet peptides inhibit amyloid fibrillization and reduce biofilm formation in several bacterial species. Alginate (ALG) and chitosan (CH) are widely used in wound dressings due to their adhesive and antimicrobial activity. Here, we describe a layer-by-layer (LbL) functionalized gauze with alternating layers of ALG and CH loaded with α-sheet peptides for controlled release and biofilm inhibition at a wound site. Material analysis indicated successful LbL polyelectrolyte deposition and peptide incorporation. The LbL gauze facilitated controlled peptide release for 72 hours with an initial burst delivery and demonstrated good biocompatibility with no toxicity towards human fibroblasts. The LbL gauze was assessed against *Escherichia coli* biofilms and reduced colony forming units (CFUs) of adherent bacteria by 81% and 96% as compared to the plain gauze for non-antibiotic and antibiotic (+gentamicin) conditions, respectively. A similar reduction in biofilm formation and increase in antibiotic susceptibility was observed for tests with *Staphylococcus aureus* and vancomycin. Thus, LbL gauze with incorporated α-sheet peptides demonstrated anti-biofilm properties for both gram-negative and gram-positive bacteria and presents an alternative wound dressing for the prevention of biofilm-associated infections.

3.2 Introduction

The skin is the largest organ in the human body and plays a vital role in defending the body against physical, chemical, and biological agents [108]. Bacteria and the skin microbiota exist on both healthy skin and wounds, but the disruption of healthy skin can lead to increased numbers of pathogenic bacteria, infection, and ultimately biofilm formation. When the epithelial barrier is broken, wounds become susceptible to bacterial infection from endogenous or exogenous sources due to impairment to the innate immune system and the disruption of hemostasis [109]. Infections thrive as the wound provides a humid, nutrient rich, and warm environment for bacteria. Wound infection begins with contamination, followed by colonization where replicating bacteria can trigger a local host response, and then ultimately infection when multiplying microorganisms enter the host tissue [110].

While all wound infections are potentially serious, biofilm formation exacerbates the infection and impairs healing. Biofilms are communities of microorganisms attached to surfaces and each other via an extracellular matrix (ECM) of proteins, exopolysaccharides, and nucleic acids. Biofilms grow on both soft tissues, packaging materials, and on bandages; a mature biofilm can form on a wound bed within 24 hours [111]. Biofilm development follows three stages: attachment of microbes to the wound surface, ECM production and formation of microcolonies, and maturation and dissemination of the adherent microbial cells [109]. Clinically relevant infections occur when the infectious burden exceeds 10^5 bacteria. Wound biofilms lead to longer and more expensive hospital stays, the need for mechanical or chemical debridement, delayed healing, and higher morality [112]. Despite advances in wound management and the use of topical antibiotics, infections from both gram-negative and gram-positive species are one of the leading

causes of mortality [112]. An ideal wound dressing would prevent infection and promote an environment conducive to healing.

The challenge of treating wound biofilms is compounded by the growing threat of antibiotic-resistant infections. Antibiotic resistance is an emerging public health crisis, with increased failure of even the antibiotics of last resort. The development of resistant strains is paired with the slowed pace of development of new antibiotics. Additionally, chronic wounds with biofilm infections do not respond to currently available topical or systemic antibiotics [113]. Biofilms are 10-1000 times less susceptible to antibiotics and sublethal antibiotic doses can enhance biofilm formation [114]. Chronic wounds can require long-term treatment, which increases the risks of antibiotic resistance. Due to the difficulty of treating established biofilms, we need therapeutic strategies to inhibit biofilm infection and improve the efficacy of existing antibiotics.

Many bacteria, including *Escherichia coli* and *Staphylococcus aureus*, produce amyloid fibrils in their ECM as part of biofilm formation [2, 5, 11]. Amyloid fibrils are β-sheet rich structures formed when normally soluble peptides and proteins aggregate into insoluble structures [2]. *E. coli* form amyloid fibers called curli, which are assembled at the cell surface and promote biofilm formation by providing structural stability [14]. *S. aureus* also produce amyloid as part of the biofilm ECM in the form of small peptides called phenol soluble modulins (PSMs) [16]. In a fibril, β-sheet state, PSMs both stabilize the biofilm and promote resistance to a range of dispersion agents [16]. Of note, mutant *S. aureus* strains that lack the machinery to produce PSMs are more susceptible to biofilm degradation, indicating a role of the amyloid proteins in biofilm assembly and resistance [16].

As such, bacterial amyloid structures are an attractive drug target for disrupting biofilm. Before amyloid fibril formation, soluble monomers experience a conformational change which causes aggregation into toxic, soluble oligomeric intermediates [114]. Previous research by the Daggett group suggests that these oligomeric intermediates share a common backbone structure: a novel secondary structure called an "α-sheet." α-Sheets are like β-sheets but are characterized by the alignment of main chain carbonyl groups on one side of the α-strand. Identification of these α-sheets led to the development of synthetic peptides with a stable, monomeric α-sheet structure [6, 7]. These peptides are denoted "AP" for "Alternating Peptide" due to the alternating L- and D-amino acid templating. These APs inhibit assembly of bacterial amyloid in *S. aureus* and *E. coli*, two of the most common bacteria that cause wound infections [9, 114-116]. The APs not only prevent amyloid fibrilization but also reduce biofilm formation. Critically, the APs inhibit biofilm formation, thus keeping microbial cells in a planktonic form without killing cells, which reduces the possibility of resistance developing over time. By inhibiting amyloid formation, these APs also increase the biofilm antibiotic susceptibility of clinical isolates of *S. aureus* and *E. coli* [116]. Thus, α-sheet inhibitor peptides are a novel approach to destabilizing the biofilm ECM and disrupting wound-associated biofilm formation.

There are many wound dressings currently available, the most basic being cotton or wool bandages with no functionality beyond physically shielding the wound. While traditional dressings simply protect the wound from additional physical damage, functionalized dressings can be therapeutic or prevent infection by incorporating active agents and antimicrobials. One technique for functionalized gauze preparation is layer-by-layer (LbL) assembly. Electrostatic LbL assembly is a common technique based on the successive deposition of oppositely charged polymers onto a surface. The deposition cycle creates a bilayer that can be repeated as desired, allowing for a highly

tunable technique [117-119]. In LbL assembly, film construction is driven by the excess charge, alternating between positive and negative, after each polyelectrolyte adsorption. By controlling the number of deposition cycle and the types of polyelectrolytes, the user can control the thickness and roughness of the film. Successful LbL coating also requires a minimal initial surface charge on the substrate. In a general LbL assembly, a charged substrate, in this case the cotton gauze, is immersed in a solution of an oppositely charged polyelectrolyte to add the first monolayer. A washing cycle is then performed to remove any unbound material, and the coated substrate is then submerged in the second polyelectrolyte solution to deposit a second layer. The substrate is again rinsed and subsequent layers are added as desired (**Figure 3.1A**).

Cross-linking is often used in conjunction with LbL to convert layers to a surface hydrogel that can be used to trap bioactive agents, such as the APs. The release of the peptides by diffusion from the hydrogel can then be tuned to the desired release profile. This LbL technique is advantageous because the coating can be fabricated directly on the material of interest. LbL techniques are flexible and allow for preparation of conformal coatings on uneven surfaces [118]. Additionally, it is an inexpensive, relatively fast, and simple technique that does not require exotic equipment or complicated chemical reactions.

Two popular polyelectrolyte choices for LbL assembly are chitosan (CH) and alginate (ALG). CH and ALG are both biodegradable, nontoxic, and biocompatible polymers [120, 121]. CH is extensively used in wound dressings due to demonstrated mucoadhesive properties, cationic nature, and antibacterial and hemostatic properties. CH is positively charged and can interact with negatively charged residues on the surface of bacteria. This can cause cell surface modifications that alter cell wall permeability and inhibit normal cellular metabolism. CH is also able to induce macrophage activation by interaction of the acetylated residues with mannose receptors [122-125].

ALG is also nontoxic, hemostatic, and biocompatible with many cell types [126, 127]. It has been studied for various biomaterials applications, including extensively as a wound dressing. ALGs comprise two monomeric units, guluronic acid and mannuronic acid. High mannuronic content ALGs may induce cytokine production by human monocytes, a process very useful in chronic wound healing [128].

This paper adapts a previously established LbL method from Gomes et al [119, 125, 129] for deposition of alternating layers of CH and ALG on cotton gauze with incorporation of novel APs for biofilm prevention (**Figure 3.1B**). Before layering, a negative charge is imparted on the cotton sample with a solution of sodium bromide (NaBr) and (2,2,6,6-Tetramethylpiperidin-1-yl)oxyl (TEMPO) [119, 130, 131]. A calcium wash is employed after the final alginate layer as calcium and alginate form a hydrogel for AP peptide incorporation; once deployed, the hydrogel allows for controlled peptide diffusion from the gauze over time.

We have developed a LbL functionalized gauze with alternating layers of ALG and CH and loaded with α-sheet peptides for controlled release at the wound site to prevent biofilm formation and increase antibiotic susceptibility. First, the LbL gauze method and peptide incorporation were verified by scanning electron microscopy (SEM), Attenuated Total Reflection-Fourier Transform Infrared Spectroscopy (ATR-FTIR), and X-ray photoelectron spectroscopy (XPS). The peptide absorption and release kinetics were then optimized for 72 hours of sustained release following an initial burst of peptide. Finally, the cytotoxicity of the material was assessed, and the anti-biofilm activity of the gauze was tested against *E. coli* and *S. aureus*.

3.3 Results

3.3.1 Scanning Electron Microscopy (SEM)

SEM provides information about the sample including the external morphology and orientation of materials. First, the plain and LbL gauze were imaged at 2000x to determine if the layering process caused any larger structural changes to the gauze (**Figure 3.1C-D**). No significant differences were observed in the morphology of the plain and LbL (CT5) gauze. Additionally, the cotton fibers of the plain gauze appeared smooth and uniform in texture and orientation (**Figure 3.1C**). However, morphological changes to the CT5 gauze indicated LbL coating on the strands, although the fibers appeared undamaged and remained uniform in orientation and size (**Figure 3.1D**). Further evidence of the coating was visible in micrographs of the plain (**Figure 3.1E**) and CT5 gauze (**Figure 3.1F**) taken at 5000x, where the coating appeared relatively uniform in thickness over the fibers.

3.3.2. Attenuated Total Reflection-Fourier Transform Infrared Spectroscopy (ATR-FTIR)

ATR-FTIR was performed to ensure that each layer was added as expected and to confirm peptide incorporation. The depth of penetration in ATR-FTIR spectroscopy is typically on the order of a few micrometers, making ATR particularly suitable for the analysis of thin films, coatings, and surface layers of materials. Specifically, the ATR accessory measures the changes in an internally reflected IR beam when the beam encounters the gauze sample. Spectra were collected for plain cotton gauze (denoted C), gauze+TEMPO (CT), gauze with 1-5 layers of chitosan/alginate (CT1-CT5), and gauze with all 5 layers and AP incorporation (CT5+AP). As expected, the spectra differed at key wavelengths (**Figure 3.2** and **Table 3.1**; additional spectra provided in **Supplementary Figure 3.1**).

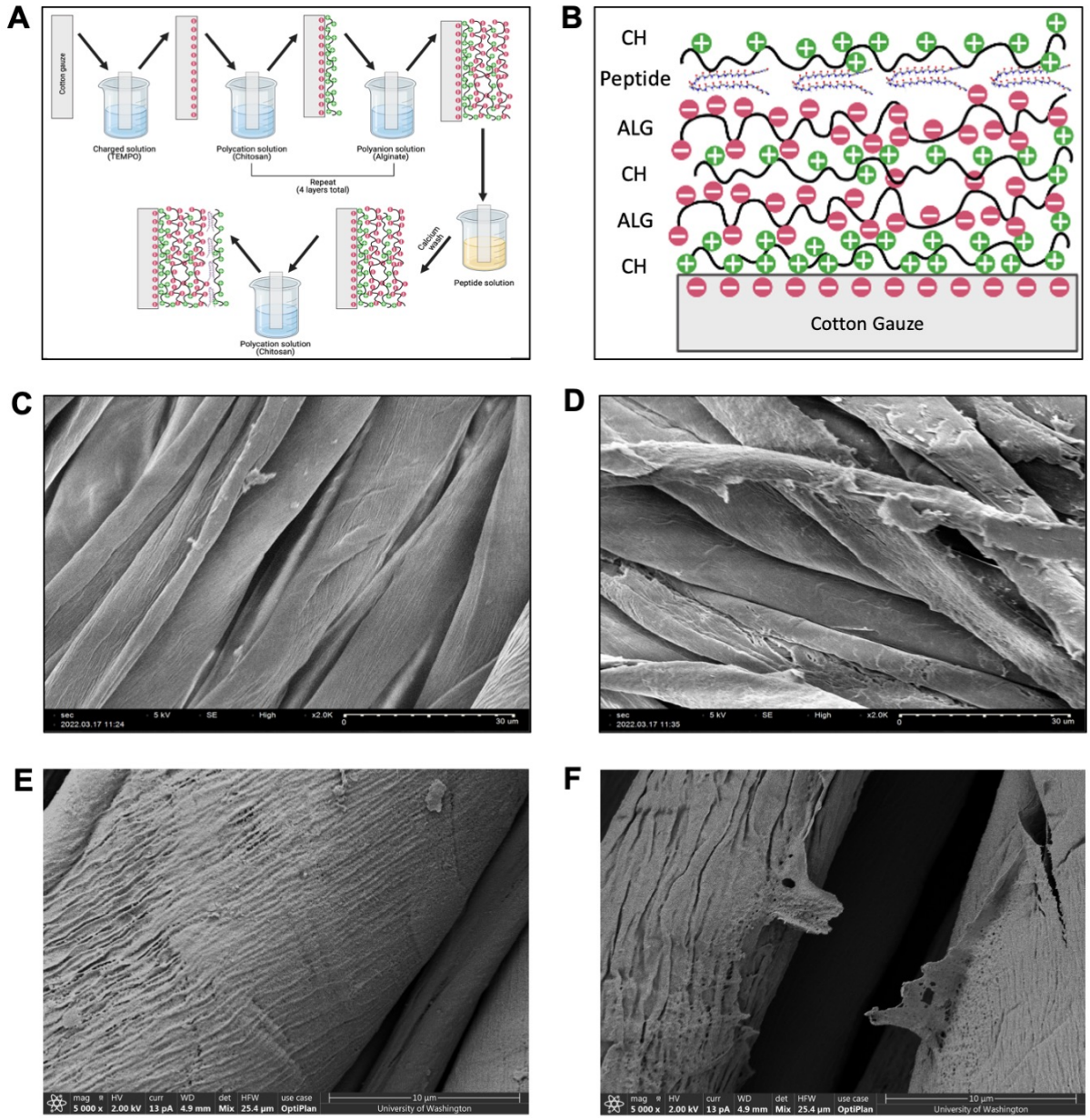

Figure 3.1: Schematic and SEM images of the layer-by-layer assembly method. A) The general workflow for LbL preparation begins with cotton gauze, followed by addition of a charged layer, repeated CH and ALG deposition, and finally peptide incorporation. **B)** The diagram of complete LbL gauze depicts five alternating layers of CH and ALG and peptide incorporated into an ALG hydrogel between the fourth and fifth layers. SEM images for plain and CT5 gauze show evidence of coating. **C)** Plain gauze at 2000x and **D)** CT5 gauze at 2000x revealed no fibril damage from the LbL coating. Morphological differences between **E)** Control gauze at 5000x and **F)** CT5 gauze at 5000x demonstrated successful polyelectrolyte deposition.

Key wavelengths were selected to examine the TEMPO mediated oxygenation and CH and ALG layering as shown in **Figure 3.2**. At 1,000-1,200 cm^{-1}, a characteristic cellulose peak, the primary component of cotton, was seen [119, 132]. At 1,600 cm^{-1}, as highlighted in the **Figure 3.2** inset, there was a variation in peak intensity that was attributed to the TEMPO-mediated oxidation. The peak at 1600 cm^{-1} was attributed to the ionized form of the carboxylate group, specifically to the asymmetric stretching of the COO^- ion [119, 132]. Under TEMPO-mediated oxidation conditions, carboxylate groups were converted to the ionized form, causing the peak observed in the **Figure 3.2** inset, and imparting a negative surface charge on the cotton. However, variation between the CT5 and CT5+AP spectrum around this wavelength, and particularly at 1,558 and 1,637 cm^{-1}, were attributed to the amide group of the peptide. This indicated successful incorporation of the α-sheet peptide.

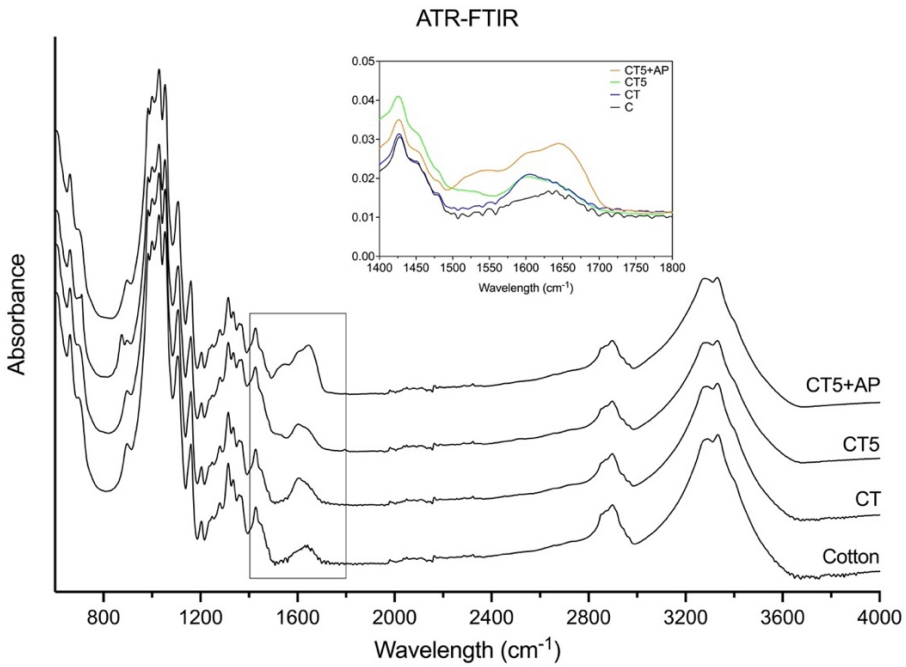

Figure 3.2: ATR-FTIR spectra for plain cotton, CT, CT5, and CT5+AP gauze samples. The spectra indicated TEMPO-mediated oxygenation, ALG and CH addition, and peptide incorporation. The inset shows differences in the peaks at the 1,400 to 1,800 cm^{-1} wavelengths, highlighting the effect of TEMPO, the polyelectrolytes, and the peptide on the spectra. Each spectrum is an average of three measurements taken on different places on a single sample (standard deviation not shown to reduce noise).

At 1,400 and 1,600 cm^{-1}, there were characteristic bands for ALG [119, 120, 133, 134]. When CH was the outer layer, the amine groups extending into the solution became deprotonated upon washing and drying and the peak was less evident. Variations in peak intensities, indicating alternating deposition of CH and ALG, were further evident in the full spectra available in the supplementary information (**Supplementary Figure 3.1**). At 1,700 cm^{-1} there was a characteristic peak for chitosan, corresponding to the amino group. At 2,800-2,980 cm^{-1}, there was an additional band related to the chemical structure of cellulose from the C-H bond [119, 132]. Finally, at 3,100-3,550 cm^{-1}, there was evidence of hydrogen bonded OH, a characteristic band related to the chemical structure of cellulose [119, 132].

Wavelength (cm^{-1})	Significance
1,000-1,200	Characteristic cellulose peaks
1,400 and 1,600	Characteristic band of ALG
1,600	TEMPO-mediated oxidation
1,600-1,800	Asymmetrical COO- stretching (cellulose)
1,500-1,700	Amino group (characteristic peaks of chitosan)
1,558 and 1,637	Peptide signal- NH amide group of peptide
2,800-2,980	C-H band (cellulose)
3,300	Hydrogen bonded OH (cellulose)- should become less evident as layers added

Table 3.1: Key Wavelengths and interpretations for ATR-FTIR Spectra.

3.3.3 X-ray Photoelectron Spectroscopy (XPS)

XPS was performed to further characterize the material and observe peptide incorporation. XPS is a complementary surface analysis technique that gives information about the elemental composition of a material's surface as well as the chemical and electronic state of the atoms in a material, information not provided by ATR-FTIR. Specifically, for the gauze functionalization analysis, XPS quantified the extent of protonation of amine groups through examination of the nitrogen 1s narrow scan with an average depth of analysis of 10 nm. For these experiments, a

composite analysis and High-resolution spectra for nitrogen and carbon were performed. **Table 3.2** summarizes the composite scans for each layer from plain gauze (C) through layered gauze with peptide (CT5+AP). From these scans, the percentage atomic composition as determined by the area under the peak for each element was calculated as a measure of the elemental surface composition (**Table 3.2**, all spectra shown in **Supplementary Figure 3.2**). As layers were added to the gauze, the percentage of carbon composition decreased as the cellulose was covered. At the same time, the nitrogen percentage increased as layers of CH were added. Specifically, samples with CH as the final layer (CT1, CT3, and CT5) had a higher nitrogen composition. Sodium was also present in the samples with alginate as a top layer. Finally, there was a small percentage of calcium present from the washes performed after the fourth layer.

Percentage Atomic Composition						
	O 1s	**C 1s**	**N 1s**	**Ca 2p**	**Na 1s**	**S 2p**
C	23.2	75.2	0.2	0.9	x	0.41
CT	33.9	65.6	0.1	0.4	x	x
CT1	31.4	66.4	2.3	x	x	x
CT2	32.4	64.9	1.6	0.5	0.6	x
CT3	31.5	64.8	3.6	x	x	x
CT4	33.5	62.4	2.7	x	1.4	x
CT5	34.4	60.4	3.3	1.8	x	x
CT5+AP	31.1	62.1	6.0	0.8	x	x

Table 3.2: XPS Composition Analysis. Total atomic composition analysis for plain cotton gauze through CT5+AP gauze presented as a percentage. Gauze samples are abbreviated as follows: plain cotton gauze (denoted C), gauze + TEMPO (CT), gauze with 1-5 layers of chitosan/alginate (CT1-CT5), and gauze with all 5 layers and AP incorporation (CT5+AP).

In addition to the composite spectra, high-resolution scans for carbon and nitrogen were collected and summarized in **Table 3.3** with select spectra in **Figure 3.3** (all spectra included in **Supplementary Figures 3.3** and **3.4**). First, addition of the TEMPO soak shifted the distribution of carbon peaks (**Table 3.3**). TEMPO selectively oxidized the primary hydroxyl groups and left

secondary groups untouched as indicated by the shift in distribution of the carbon peaks (**Table 3.3**). Next, the addition of CH and ALG introduced nitrogen peaks. When CH was the outermost layer (CT1, CT3 and CT5), the amine groups extending into the solution during fabrication became deprotonated (neutral) upon washing and drying in air [134]. When ALG was the outermost layer (CT2 and CT4), the amine groups of the underlying CH layer were protonated to a larger degree due to the interaction with the deprotonated carboxylate groups of ALG [134]. Thus, a higher amount of protonated amine was expected with ALG as the outermost layer. Correspondingly, the percentage changes of the two nitrogen peaks increased and decreased as expected with subsequent polyelectrolyte deposition. Finally, for the CT5+AP sample, there was a shift in the nitrogen peak distribution due to the addition of the peptide amine groups (**Table 3.3**).

Percentage Atomic Composition						
	N 1s	**N 1s**	**C 1s (C-C, C-H)**	**C 1s (C-O, C-N)**	**C 1s (C=O)**	**C 1s**
Binding Energy (eV)	**399.8**	**401.97**	**285**	**286.6**	**288.1**	**289.24**
C	100	x	54.2	33.0	12.8	x
CT	x	x	30.1	51.3	18.6	x
CT1	78.6	21.4	27.7	55.7	16.6	x
CT2	70.4	29.7	28.4	51.3	16.4	3.9
CT3	60.6	39.4	26.9	51.5	17.5	4.2
CT4	56.2	43.8	25.4	53.1	17.5	4.0
CT5	84.5	15.6	25.5	49.6	18.6	6.3
CT5+AP	71.8	28.2	24.4	46.2	29.4	x

Table 3.3: High-Resolution XPS Spectra for C and N. High resolution XPS spectra for carbon and nitrogen as quantified by the percentage atomic composition for plain cotton gauze thorough CT5+AP gauze. Gauze samples are abbreviated as follows: plain cotton gauze (denoted C), gauze + TEMPO (CT), gauze with 1-5 layers of chitosan/alginate (CT1-CT5), and gauze with all 5 layers and AP incorporation (CT5+AP).

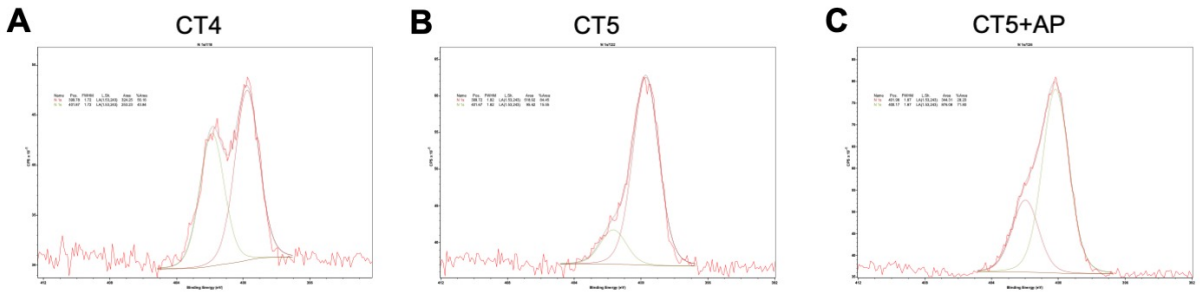

Figure 3.3: Representative graphs for the XPS high-resolution nitrogen scans for **A)** CT4, **B)** CT5, and **C)** CT5+AP gauze displaying shifts in the nitrogen peaks caused by ALG and CH outer layers and peptide addition.

3.3.4 Peptide Absorption and Release

After four alternating layers of chitosan and alginate, the gauze was submerged in a solution of APs in water. AP absorption by the gauze was monitored for 24 hours by periodic sampling of the solution peptide concentration using a Nanodrop™ instrument (Thermo Fisher Scientific; Waltham, MA). Rapid absorption, around 150 µg, was observed over the first hour. Although the gauze was left in solution for 24 hours, absorption plateaued after 4 hours with about 250 µg of total peptide absorbed (**Figure 3.4A**).

The peptide release profile was tuned such that the gauze provided 72 hours of release of approximately 250 µg of peptide. The gauze demonstrated a burst release of peptide over the first 6 hours, releasing an average of 177 µg or 68% of the absorbed peptide (**Figure 3.4B**). The release profile then flattened with the remaining peptide released at a more gradual rate. After 72 hours, 92% of the absorbed peptide had been released (**Figure 3.4B**).

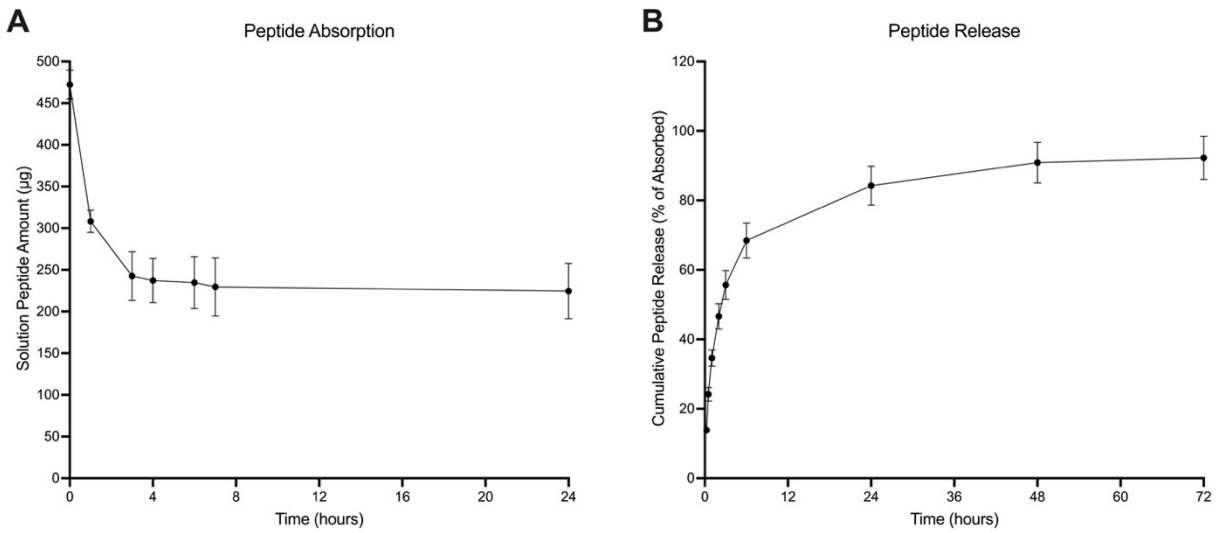

Figure 3.4: Optimization of peptide absorption and release kinetics. **A)** Peptide absorption was measured by periodic measurement of the solution concentration. An average of ~250 µg of peptide was absorbed per 1x1 cm^2 gauze sample over 24 hours. **B)** Cumulative peptide release as calculated as percentage of peptide absorbed. The peptide was released with a burst release phase over the first 6 hours followed by continued release for 72 hours. Values are mean ± SD for three replicates.

3.3.5 MTT Cytocompatibility

Cytocompatibility of the LbL gauze was evaluated using a 3-(4,5-dimethylthiazol-2-yl)-2,5-diphenyltetrazolium bromide (MTT) viability assay (Sigma Aldrich; USA) with human fibroblasts. The MTT assay measures cellular metabolic activity as an indication of mammalian cell viability and cytotoxicity [135]. This colorimetric assay is based on the reduction of MTT to purple formazan crystals by metabolically active cells. The formazan crystals are then solubilized, and the colored solution is quantified by absorbance reading at 570 nm where a darker solution indicates a greater number of viable cells. The cytotoxicity assay was performed using human fibroblasts (ATCC® CRL-2522™) cultured in complete growth medium at 37°C and 5% humidified CO_2. Cells were grown in the absence of gauze, or in the presence of control, CT5, or CT5+AP gauze for 24 hours and cell viability is presented as percentage of the no-gauze control. For a negative control, cells were grown in the presence of 5% Tween 20. For the Tween condition,

cells showed <1% viability as compared to the control, indicating almost complete cell death (*p<0.0001*) (**Figure 3.5**). For the gauze conditions, not one of the gauzes displayed toxicity, with 100% cell viability for the CT5+AP condition (**Figure 3.5**).

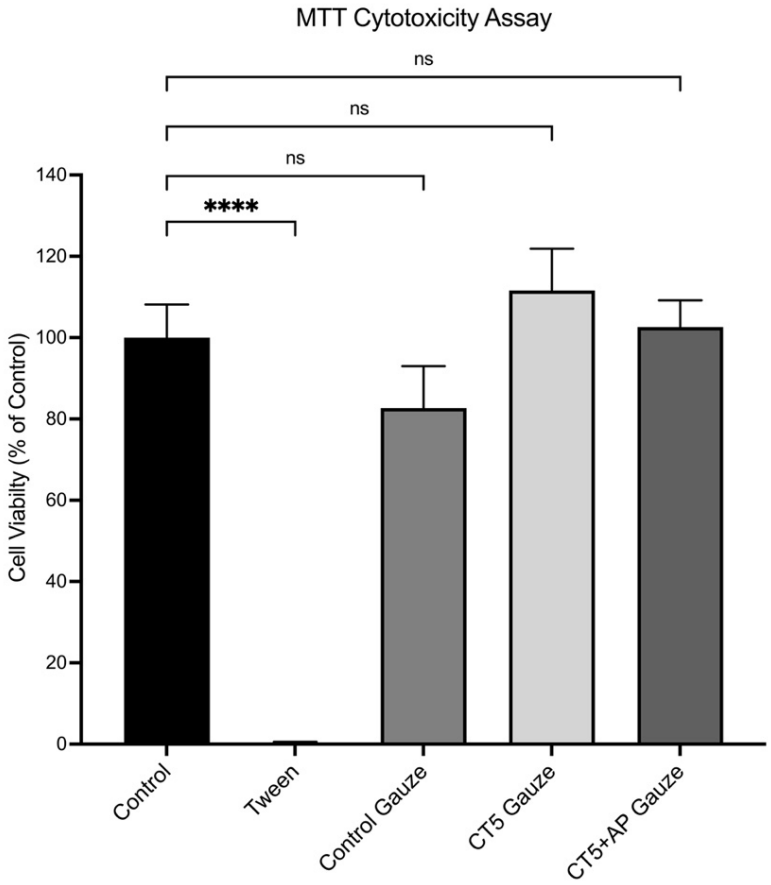

Figure 3.5: MTT Cytotoxicity Assay. The viability of human fibroblasts after exposure to C, CT5, and CT5+AP gauze for 24 hours. Cell viability was assessed using an MTT assay and absorbance values are expressed as a percentage of the no-gauze control. The C, CT5, and CT5+AP gauzes were not toxic to the cells. Values are mean ± SD for three replicates and p-values are indicated as follows from a one-way ANOVA with post-hoc comparisons and Tukey correction: ns = not significant and **** indicates *p<0.0001* as compared to the control.

3.3.6 E. coli *Biofilm Challenge*

The anti-biofilm property of the gauze against gram-negative *E. coli* was assessed through measurement of colony forming units (CFUs) of adherent bacteria after gauze submersion in a bacterial suspension [107, 136, 137]. For the non-antibiotic conditions, both the CT5 gauze and the CT5+AP gauze significantly reduced adherent bacteria as compared to the control (*p<0.0001)* (**Figure 3.6A**). Additionally, there was a significant difference between the CT5 gauze and the CT5+AP gauze (*p=0.0152*), with the CT5 gauze reducing CFUs by 63% and the CT5+AP gauze by 81% as compared to the plain gauze control. For the antibiotic conditions, both the CT5 gauze and the CT5+AP gauze significantly decreased CFUs as compared to the control (*p=0.0418* and *p=0.0147* for CT5 and CT5+AP, respectively) (**Figure 3.6B**). The CT5 gauze caused a 75% reduction while the CT5+AP gauze caused a 96% reduction in CFUs compared to the control. Additionally, the fold reduction upon antibiotic addition was calculated by dividing the plain gauze CFUs without antibiotics by the CFUs for each antibiotic gauze condition. While the control gauze reduced the CFUs only 30.7-fold, the CT5 gauze caused a 121-fold reduction, and the CT5+AP gauze led to a 694-fold reduction with antibiotics (**Figure 3.6C**).

The anti-biofilm properties of the gauze were further assessed with SEM imaging where adherent bacteria were observed with representative micrographs presented at 2000x and 5000x magnification. As indicated by the broth culture assay, there was significantly greater visible biofilm formation on the control gauze than on the CT5+AP gauze. Robust biofilm structures and curli fibrils were viewed on the plain cotton gauze (**Figure 3.6D**) whereas the CT5 and the CT5+AP gauze contained only isolated bacterial clumps (**Figure 3.6E-F**). The CT5+AP gauze specifically demonstrated a reduction in bacteria quantity, with only small bacterial clusters, as well as evidence of remaining LbL coating in some images.

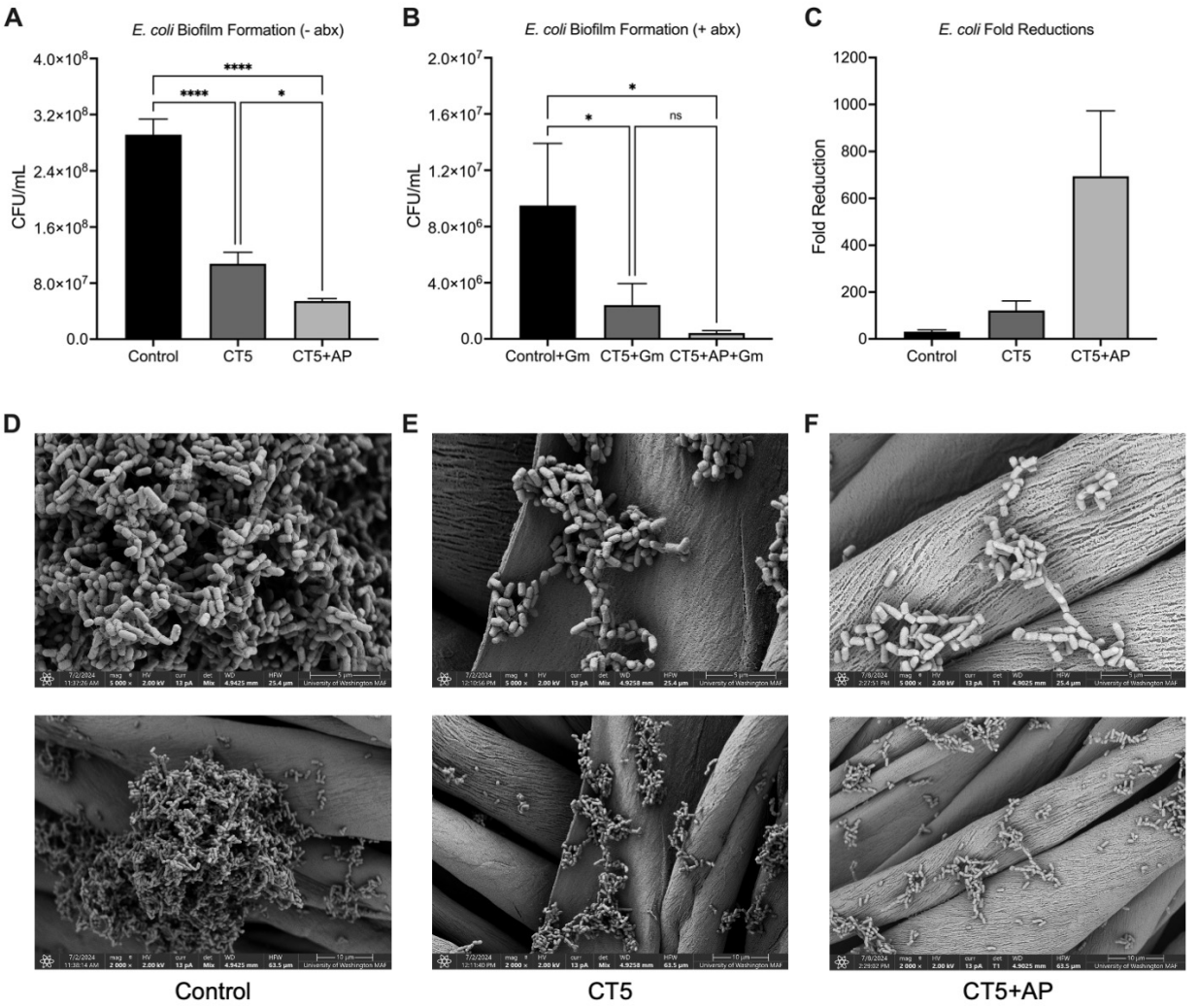

Figure 3.6: Inhibition of *E. coli* biofilm formation. The anti-biofilm activity of the gauze samples was assessed against *E. coli* in a broth culture assay. **A)** For the non-antibiotic conditions, the CT5 and CT5+AP gauzes caused a significant reduction in adherent bacteria as compared to the control gauze (*p<0.0001* for both). **B)** For the antibiotic conditions, both CT5 and CT5+AP gauzes significantly reduced biofilm formation (*p=0.0418* and *p=0.0147* for CT5 and CT5+AP, respectively). **C)** The CT5+AP gauze increased biofilm susceptibility to gentamicin as determined by fold reduction calculations. Fold reductions were calculated from biofilm CFU values after 48 hours as control gauze CFU in the absence of antibiotics divided by the condition CFU in the presence of antibiotics. SEM micrographs of the gauze samples with *E. coli* at 5000x (top) and 2000x (bottom) for **D)** plain cotton, **E)** CT5, and **F)** CT5+AP gauze. Large biofilm structures were visible on the plain cotton gauze with only smaller clumps on the CT5 and CT5+AP gauze. Values are mean ± SD for three replicates and are p-values are indicated as follows from a one-way ANOVA with post-hoc comparisons and Tukey correction: ns = not significant, * *p<0.05*, ** *p<0.01*, *** *p<0.001*, and **** *p<0.0001*.

3.3.7 S. aureus *Biofilm Challenge*

The anti-biofilm action of the gauze was then tested against the gram-positive pathogen *S. aureus*. The CT5+AP gauze significantly decreased the CFUs of adherent bacteria as compared to the control gauze (*p=0.0111*) (**Figure 3.7A**), causing a 75% reduction in CFUs as compared to the control. For the antibiotic conditions, the CT5+AP gauze again significantly reduced the CFUs of adherent bacteria as compared to the control and CT5 gauze (*p=0.0131* and *p=0.0174* for control and CT5 gauze, respectively) (**Figure 3.7B**), with CT5+AP decreasing CFUs by 75% as compared to the control gauze. Fold reduction calculations yielded only a 2.7 and 2.9-fold reduction in CFUs for the control and CT5 gauzes respectively, suggesting high biofilm resistance of this *S. aureus* strain to vancomycin (**Figure 3.7C**). However, the CT5+AP condition reduced CFUs by 11.2-fold, indicating increased biofilm susceptibility to vancomycin when administered with the peptide gauze.

For the SEM analysis, robust *S. aureus* biofilm structures were visible on the plain gauze (**Figure 3.7D**). For the CT5 gauze, there was evidence of significant bacteria, although it appeared in more isolated colonies and not in large biofilm structures (**Figure 3.7E**). Finally, only isolated bacteria in a reduced quantity were visible on the CT5+AP gauze fibers and no biofilm structures were observed (**Figure 3.7F**). For both the *E. coli* and *S. aureus* tests, neither the CT5 nor the CT5-AP appeared to alter the size or shape of the individual bacteria.

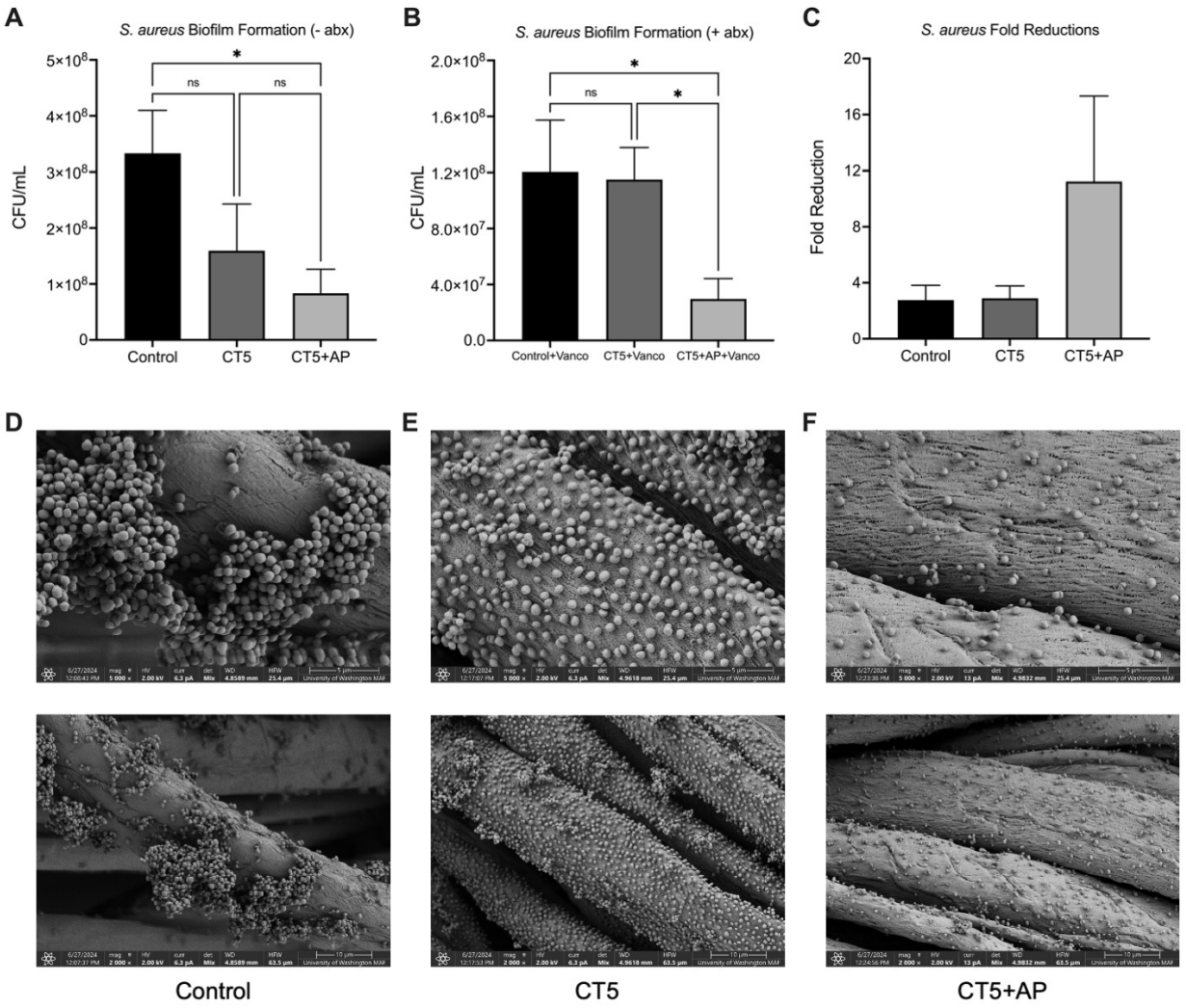

Figure 3.7: Inhibition of *S. aureus* biofilm formation. The gauze was also assessed against *S. aureus* biofilms. **A)** For the non-antibiotic conditions and the **B)** antibiotic conditions, the CT5+AP gauze reduced biofilm formation by 75% as compared to the control gauze. **C)** Fold reductions were calculated from biofilm CFU values after 48 hours as control gauze CFU in the absence of antibiotics divided by the condition CFU in the presence of antibiotics. The CT5+AP gauze increased biofilm susceptibility to vancomycin as compared to the control and CT5 gauze as determined by fold reduction. SEM micrographs of the gauze samples with *S. aureus* at 5000x (top) and 2000x (bottom) for **D)** plain cotton, **E)** CT5, and **F)** CT5+AP gauze showing reduced biofilm formation for the functionalized gauze with peptides. Values are mean ± SD for three replicates and p-values are indicated as follows from a one-way ANOVA with post-hoc comparisons and Tukey correction: ns = not significant, * $p<0.05$, ** $p<0.01$, *** $p<0.001$, and **** $p<0.0001$.

3.4 Discussion

Biofilm formation at wound sites critically impairs healing and often requires systemic antibiotic treatment. However, biofilm infections can require up to 1000 times the systemic antibiotics dose of a planktonic infection while sub-lethal antibiotic doses can structurally alter the biofilm, exacerbate biofilm formation, and lead to acquired antibiotic resistance [138-140]. This study developed a layer-by-layer functionalized gauze with alternating layers of CH and ALG and incorporated peptides. The gauze was formulated to inhibit biofilm infections at a wound site through controlled delivery of α-sheet peptides from the gauze. We have previously demonstrated biofilm inhibition with peptide delivery in solution in an *in vitro* biofilm assay [116]. This paper assessed anti-biofilm activity when APs were incorporated into a biomaterial with the goal of inhibiting biofilm formation in both gram-negative and gram-positive bacteria and increasing the antibiotic susceptibility of the biofilm.

Beyond basic cotton bandages, advanced wound dressings include synthetic polymer films, polymeric hydrogels, auto- and allografts, polymeric foams, sponges, and hydrogels [110]. Despite the range of existing dressings, there are limitations to current treatment options. Many conventional dressings cover the wound surface and absorb tissue exudates but do not necessarily promote an antimicrobial environment and biofilm-associated infection remains common. In particular, existing therapies that incorporate traditional antibiotics for delivery at the wound site do not address increasing antibiotic resistance and the rise of multi-drug resistant bacterial strains [141].

Alternative approaches to the treatment and prevention of wound infection, primarily silver and silver adjuncts and iodine-containing compounds, are available but have demonstrated mixed outcomes [142, 143]. High concentrations of ionic silver seem effective at treating biofilms *in*

vitro, and planktonic microorganisms *in vitro* and *in vivo* [144]. However, ionic silver is toxic to macrophages and fibroblasts in high concentrations and can subsequently impair healing [145, 146]. Thus, ionic silver containing dressings may not be recommended for long-term use [147] which is critical as over 78% of chronic non-healing wounds have been shown to contain biofilms [148]. While there are reports of bacterial resistance to silver-containing antimicrobial agents [149-151], there is less concern regarding the development of resistance because silver causes cell death via multiple mechanisms. Next, iodine-containing compounds are also widely used as antimicrobial agents. Iodine formulations, such as cadexomer iodine, an iodine within a starch lattice that is formed into a microbead, have demonstrated both bactericidal action and healing properties through effective exudate management [152]. Limitations of iodine formulations include concerns of toxicity, particularly when used over larger wound areas, as well as reports of transient pain upon application, and the development of a contact allergy [142, 145]. Finally, special consideration must be used for patients with thyroid disorders [145, 153]. Increasing concerns of bacterial resistance to traditional antibiotics and toxicity profiles to alternatives like silver mandate new antibacterial targets for wound dressings. Thus, prevention of biofilm formation through inhibition of amyloid proteins in the biofilm ECM is an exciting new approach.

CH and ALG are widely used in wound treatments as they are biodegradable, nontoxic, hemostatic, and biocompatible polymers. Previous LbL gauze studies showed that five alternating layers (CH, ALG, CH, ALG, CH) had a significant coating effect as well as antimicrobial action [119, 125, 154]. Methods with up to 10 layers were tested in this study with no significant difference in peptide incorporation observed so five layers was chosen for the final formulation.

The LbL methodology was first assessed using SEM imaging (**Figure 3.1C-F**). Changes in the morphology of the cotton fibers indicated the presence of the LbL coating but the

functionalization did not appear to damage or disorder the fibers. Images taken at 2000x confirmed that the LbL method did not cause macro scale damage to the gauze or affect the random orientation of the individual fibers (**Figure 3.1C-D**). Similarly, images taken at 5000x did not indicate any fibril realignment but showed morphological changes indicative of successful coating with visual estimates of bilayer thickness matching previous reports (**Figure 3.1E-F**) [125].

ATR-FTIR was used to assess if an initial charged surface was forming on the gauze and to confirm CH and ALG deposition on the gauze (**Figure 3.2**). The spectra indicated a successful initial surface charge and clear evidence of TEMPO-mediate oxidation on the cotton gauze. TEMPO can catalytically oxidize primary and secondary alcohols under aqueous conditions but when used with NaBr the oxidation is selective to only primary hydroxyl groups. A cellulose molecular chain is composed of repeating D-glucose units, each of which has three hydroxyl groups, with the C6 hydroxyl being the most reactive [119, 130, 131]. This oxidation selectively converts the carboxyl group to the carboxylate ion form (COO-) imparting a negative surface charge on the cotton. Next, visualization of signature CH and ALG peaks verified successful additive polyelectrolyte layers. Depression in the cellulose signal as layers were added also indicated successful LbL formulation. Peptide incorporation was confirmed from a peak corresponding to the amide group of the peptide (**Figure 3.2**). One limitation of ATR-FTIR in examining surface functionalization are overlapping peaks. For example, at 1,700 cm^{-1} there was a characteristic peak for chitosan, corresponding to the amino group, and at 1,600 cm^{-1}, there was signal from an alginate band [119, 120, 133, 134]. While both bands likely contributed to the signal peaks around this wavelength, they were also partially obscured by the larger cellulose peak from 1,400-1,600 cm^{-1}.

Additionally, since ATR-FTIR penetration is typically only 0.5-5 μM, each spectrum does not just represent the outermost layer but instead a combined spectra for the cotton surface and multiple coating layers. As such, XPS was employed as it probes only the outermost 2-10 nm of a solid surface for a more specific examination of each layer. Again, these results verified the successful charge addition to the gauze as well as successive polyelectrolyte deposition. There was no S 2p signal detected in the CT5+AP sample from the AP with a cysteine residue (**Table 3.2**). XPS probes only the outermost surface, in this case the final CH layer. The estimated thickness of one layer of polyelectrolyte deposition is 150-250 nm [125] while the penetration depth of XPS is only 2-10 nm, so it is not unexpected that there is no measurable S 2p signal from the incorporated peptide.

After the material verification, the peptide absorption and release kinetics were determined (**Figure 3.4**). Each 1x1 cm^2 gauze piece absorbed about 250 μg of peptide over 24 hours. Based on previous biofilm inhibition studies with the α-sheet peptides, concentrations of 15.5 and 51.5 μg of peptide per 1x1 cm^2 significantly inhibited biofilm formation for *E. coli* and *S. aureus* respectively [8, 9]. Thus, the concentrations absorbed by the gauze should provide sufficient, sustained peptide concentrations for biofilm inhibition by the LbL gauze. The release profile (**Figure 3.4B**) indicated that the gauze delivered almost all available peptide in the first 72 hours with more than half of the peptide delivered in the first 6 hours, satisfying the desired release rate. A high initial release of peptide to the wound site is advantageous as the wound is at greatest risk for infection the first 24 hours. The goal was sustained release for 2-3 days based on a recommended schedule for changing hydrogel type wound dressings in a hospital setting. Thus, the calcium gelation successfully trapped the peptide and allowed for diffusion out of the material on the desired time scale.

Materials developed for biological use need to demonstrate biocompatibility and it is critical to evaluate cytotoxicity *in vitro* before any continuing studies *in vivo*. CH and ALG are highly biocompatible and the LbL gauze has previously demonstrated *in vitro* compatibility [125]. Additionally, the APs were previously demonstrated to be nontoxic and did not elicit an immune response *in vitro* and in *vivo* so no toxicity was expected [155]. The MTT assay measured the cytotoxicity of the material against the relevant cell type of human fibroblasts (**Figure 3.5**). Both the functionalized gauze (CT5) with and without peptide (CT5+AP) demonstrated no toxicity with cell viabilities greater than that of the no gauze control while the negative control caused almost 100% cell toxicity. Thus, it was concluded that the gauze, functionalization components, and incorporated peptide did not cause a drop in cell viability.

Finally, the anti-biofilm activity of the material was assessed using an *in vitro* broth culture assay. For *E. coli*, both the CT5 gauze and the CT5+AP gauze significantly prevented the growth of adherent bacteria and increased antibiotic susceptibility (**Figure 3.6**). Additionally, the CT5+AP gauze significantly reduced CFUs of adherent bacteria as compared to the CT5 gauze. It was not unexpected that the CT5 gauze alone was antibacterial as CH and ALG both have known antimicrobial properties and promote wound healing [120, 127, 132]. The CT5+AP gauze also caused a significant increase in biofilm antibiotic susceptibility, increasing from 30-fold for the control to 694-fold for the CT5+AP. This indicates that amyloid formation within the biofilm ECM contributes to the gentamicin resistance.

For *S. aureus*, biofilm inhibition was observed from the CT5+AP gauze for both the non-antibiotic and antibiotic conditions (**Figure 3.7**). Previously, this *S. aureus* strain demonstrated significant biofilm resistance to a range of antibiotics [116]. Thus, the increase in biofilm antibiotic susceptibility, even from 2.7 to 11.2-fold, is a significant result. Gentamicin and vancomycin were

chosen as representative antibiotics for treatment of gram-negative and gram-positive bacteria [156]. However, the APs previously demonstrated similar susceptibility increases to additional antibiotics (amoxicillin, ciprofloxacin, and erythromycin) [116], suggesting the efficacy of the CT5+AP gauze and other antibiotic combinations at preventing biofilm formation. With the escalating antibiotic resistance crisis, it is critical to maximize the efficacy of existing antibiotics.

Biofilm formation in wounds indicates significant infection, requires intensive treatment, and delays healing. Preventing biofilm formation is critical due to the difficulty of biofilm clearance and lack of antibiotic susceptibility. The APs target amyloid proteins in the biofilm ECM, inhibiting biofilm formation, and rendering the biofilms more susceptible to antibiotics (**Figures 3.6C** and **3.7C**). The α-sheet peptides do not kill bacterial cells and thus may prevent the development of acquired resistance. Critically, most colonized wounds are polymicrobial [157] which can complicate treatment. In chronic wounds, microbial colonization typically begins with gram-positive bacteria, predominantly *S. aureus*. Then, in more advanced phases of infection, gram-negative species like *E. coli* dominant and enter deep tissue layers [110]. Ideally, a wound defense strategy would prevent against infection from multiple strains of bacteria, both gram-positive and -negative. Thus, treatments such as the APs that target multiple bacterial species are highly advantageous. Other species like *Pseudomonas aeruginosa*, *Salmonella*, *Klebsiella, Streptomyces,* and *Bacillus subtilis* form amyloid in their extracellular matrix and represent additional potential peptide targets.

Finally, the CT5 gauze itself functions as both as a drug delivery vehicle and a biofilm inhibitor. LbL functionalization with CH and ALG is a simple and biocompatible technique with tunable properties and the potential to incorporate other bioactive agents like the APs. These experiments demonstrated inhibition of biofilm formation of gram-negative and gram-positive

bacteria *in vitro* and a wound bandage that facilitated increased antibiotic susceptibility for resistant biofilm infections.

3.5 Conclusion

A biocompatible, LbL functionalized gauze loaded with synthetic α-sheet peptides represents a novel way to combat wound biofilm formation. ATR-FTIR, XPS, and SEM analysis demonstrated successful LbL deposition on charged cotton gauze and evidence of peptide incorporation. Immersion in a calcium solution caused ALG gel formation containing the α-sheet peptides and facilitated sustained peptide release over 72 hours. Cytocompatibility tests revealed no toxicity of the functionalized gauze with peptides towards human fibroblasts. Finally, in a measure of biofilm formation, the CT5+AP gauze significantly reduced adherent bacteria on the gauze and increased antibiotic biofilm antibiotic susceptibility for *E. coli* and *S. aureus.* The functionalized gauze is presented as a novel dressing to prevent critical biofilm infections through inhibition of amyloid proteins in the bacterial extracellular matrix.

3.6 Materials and Methods

3.6.1 Peptide Synthesis

Synthetic α-sheet peptide inhibitors were designed *in silico* as previously described [6, 8, 9, 54], using backbone dihedral angle constraints derived from MD simulations [103, 158] and synthesized as previously described by Bleem, et al [9]. Briefly, peptides contain two α-strands of seven residues each, with amino acids alternating sequentially between L-conformation and D-conformation in each of the strands. The α-strands are connected by a five residue turn comprised of all L-amino acids, which gives the peptide a hairpin shape. Finally, the tail of each strand

consists of a Gly and an Arg residue, followed by acetyl and amide caps at the N- and C-terminus, respectively. Peptides were assembled by solid phase peptide synthesis on Rink amide resin with Fmoc chemistry and HBTU activation using the Liberty Blue Microwave Peptide Synthesizer (CEM Corporation; Charlotte, NC). Peptides were cleaved from the resin and side chain deprotected by TFA/TIPS/H2O (95:2.5:2.5) and precipitated by cold ether. Crude peptides were purified to >95% by RP-HPLC using 5 μM C12 or C18 130 Å columns (Waters Corporation; Milford, MA) and atomic masses were confirmed by electrospray mass spectrometry on a Bruker Esquire Ion Trap (Bruker; Billerica, MA). Sequences for the two α-sheet designs described in this study (AP401 and AP526) are listed in **Supplementary Table 3.1**. AP401 was used for all experiments except for ATR-FTIR and XPS where AP526 were used. AP401 and AP526 have the same sequence with the exception of one amino acid where a leucine is substituted for a cysteine in AP526. Thus, AP526 is better for identification via the thiol group for ATR-FTIR and XPS analysis. All peptides were lyophilized after purification and stored at -20 or -80°C until use.

3.6.2 Layer-by-Layer Gauze Functionalization

For the layer-by-layer (LbL) gauze functionalization, a dip coating method was adapted from Gomes, et al [119, 125, 129, 154, 159]. All chemicals were analytical grade and used as obtained: (2,2,6,6- tetramethylpiperidin-1-yl)oxyl designated by TEMPO (Sigma Aldrich; USA), Sodium Bromide (NaBr) (Sigma Aldrich; USA), Sodium Hypochlorite Solution (NaClO) (Sigma Aldrich; USA), acetic acid, sodium chloride, calcium carbonate ($CaCO_3$), hydrochloric acid (HCl), sodium hydroxide (NaOH). Cotton gauze (James Heal; Sterling, VA) samples of 1x1 cm^2 was charged by immersion in a TEMPO+NaBr+NaClO 5%, pH=10.5 solution for 30 minutes with moderate stirring, followed by rinsing with deionized water [130, 131, 160]. The cotton gauze was

then alternately immersed in alginate and chitosan solutions for 5 minutes each. Between each polyelectrolyte exposure, the samples were rinsed with deionized water. The chitosan solution was made by dissolving 1 mg/mL of 5%, CH (low molecular weight, 50–190 kDa and 80% degree of deacetylation) (Sigma Aldrich; USA) in 0.1 M acetic acid [119]. The alginate solution was made by dissolving 1 mg/mL alginic acid sodium salt (Sigma Aldrich; USA) in 0.5 M sodium chloride [119]. The pH of each solution was adjusted to 5 as it is an intermediate between the pK_a of CH and ALG [161]. The charged gauze was functionalized with four layers (cotton gauze/CH/ALG/CH/ALG) and then immersed in a 250 μg/mL solution of α-sheet peptides. Gauze substrates were left in the peptide solution for 24 hours and peptide absorption into the gauze was measured over time with a Nanodrop™ instrument (Thermo Fisher Scientific; Waltham, MA). Control CT5 gauze (no peptide) were submerged in water only. After 24 hours, the samples were rinsed with a 5% wt/vol $CaCO_3$ solution to form an ALG hydrogel, [119] then rinsed with water. A final CH layer was then added, and the gauze was dried overnight at room temperature. Gauze samples were sterilized with 1 hour of UV exposure (30 minutes per side) before antibacterial or cytotoxicity testing.

3.6.3 Scanning Electron Microscopy (SEM)

SEM was performed on the samples to assess the effect of layer-by-layer deposition on gauze morphology. Gauze samples were prepared with layer-by-layer functionalization and prepared for SEM imaging by drying in the critical point dryer (CPD). Dried samples were then stored in a sealed bag with a desiccant until use. Samples were sputter coated for 180 seconds with gold/palladium and then imaged on a scanning electron microscope (FEI SEM XL Siron or Apreo

2) at 2 kV with a 5 mm working distance. Gauze samples were imaged from the top view in three spots at various magnifications.

3.4.4 Attenuated Total Reflection (ATR)-Fourier Transform Infrared Spectroscopy (FTIR)

Gauze samples were analyzed by ATR-FTIR to determine differences in the functional groups present between the plain gauze and each successive layer and to determine if peptides were incorporated into the gauze. Gauze samples were analyzed in absorption mode using a Bruker FTIR Spectrometer with a diamond ATR accessory. Before the first sample, the chamber was purged to eliminate the CO_2 signal and prior to each sample a background spectrum was taken. For each sample, the gauze was placed on the diamond stage and secured using a pressure clamp and the stage was cleaned with isopropyl alcohol and allowed to dry. Each spectrum was taken at a resolution of 4 cm^{-1} from 4000 to 600 cm^{-1} with 64 scans per spectrum. Three measurements were taken in varying spots on each gauze to demonstrate even chemical composition. For each sample, the three spectra were averaged and the mean for select layers was plotted in **Figure 3.2** with all spectra included in **Supplementary Figure 3.1**.

3.6.5 XPS

All XPS spectra were taken on a Kratos Axis-Ultra DLD spectrometer. This instrument has a monochromatized Al Kα X-ray and a low energy electron flood gun for charge neutralization. X-ray spot size for these acquisitions was on the order of 700 x 300 μm. Pressure in the analytical chamber during spectral acquisition was less than 5 x 10^{-9} Torr. Pass energy for survey and detailed spectra (composition) was 80 eV. Pass energy for the high-resolution spectra was 20 eV. The take-off angle (the angle between the sample normal and the input axis of the energy analyzer) was 0^o

(0-degree take-off angle ~ 100 Å sampling depth). The Kratos Vision2 software program was used to determine peak areas and to calculate the elemental compositions from peak areas. CasaXPS™ software was used to peak fit the high-resolution spectra. For the high-resolution spectra, a Shirley background was used, and all binding energies were referenced to the C ls C-C bonds at 285.0 eV. All composition spectra are included in **Supplementary Figure 3.2** and all high-resolution spectra are in **Supplementary Figures 3.3** and **3.4**.

3.6.6 Peptide Release Kinetics

A series of trials were carried out to quantitate the release kinetics of α-sheet peptides added to the gauze. To determine the release kinetics, 1x1 cm^2 gauze samples were submerged in 1 mL of PBS in a 24-well polypropylene plate (Corning; Glendale, AZ) and kept covered at room temperature. At each sampling time point (0.25, 0.5, 1, 2, 4, 8, 24, 48, and 72 hours), the gauze was moved to a new well with fresh PBS. The concentration of peptide released was then determined using the Bradford method (Coomassie (Bradford) Protein Assay, Thermo Scientific; Rockford, IL). When Coomassie dye binds a protein, there is a shift in the absorption maximum from 465 to 595 nm as well as a color change from blue to brown [159, 162, 163]. The amount of absorption is proportional to the amount of protein present. For each time point, 1 mL of Coomassie Reagent was added to each well, incubated at room temperature for 10 minutes, and the absorbance was read at 595 nm using a plate reader (PerkinElmer; Waltham, MA). A standard curve of the reference protein Bovine Serum Albumin (BSA) was created to determine peptide concentration from absorbance values as recommended. Coomassie color response is nonlinear with increasing protein concentration and a quadratic fit was used (**Supplementary Figure 3.5**).

3.6.7 MTT Cytocompatibility

Cytocompatibility of the gauze was evaluated using a 3-(4,5-dimethylthiazol-2-yl)-2,5-diphenyltetrazolium bromide (MTT) viability assay (Sigma Aldrich; USA). The MTT assay measures mammalian cellular metabolic activity as an indication of cell viability and cytotoxicity [135]. The colorimetric assay is based on the reduction of MTT to purple formazan crystals by metabolically active cells. The formazan crystals are then solubilized and the colored solution is quantified by absorbance reading at 570 nm where a darker solution indicates a greater number of viable cells. The cytotoxicity assay was performed using human fibroblasts (ATCC® CRL-2522™) (ATCC; Manassas, VA) cultured in complete growth medium and grown at 37°C and 5% humidified CO_2. As previously reported [164, 165], fibroblasts at a density of $3x10^5$ cells/well were inoculated in Eagle's Minimum Essential Medium (EMEM) (ATCC; Manassas, VA) supplemented with 10% fetal bovine serum (FBS) (Thermo Scientific; Rockford, IL), 100 units/mL penicillin (Sigma Aldrich; USA), and 100 µg/mL streptomycin (Sigma Aldrich; USA) in a 48-well plate tissue culture treated plate (Corning; Glendale, AZ). Cells were incubated for 72 hours until 70% confluency. Fresh growth medium was then added to the wells and a 0.5x0.5 cm^2 gauze sample (CT5 and CT5+AP) was added to select culture wells. Cells with media only were grown as a positive control and cells with 5% Tween 20 in media were grown as a negative control. The cells and gauze were incubated together for 24 hours. After 24 hours, the media and gauze samples were removed and 200 µL of 1 mg/mL MTT in PBS was added to each well and incubated for 4 hours at 37 °C. After 4 hours, 200 µL of lysis buffer (20% SDS, 50% DMF, 1% glacial acetic acid, and 0.2% HCl) was added to each well and the plate was left covered at room temperature for 24 hours. The absorbance was then read at 570 nm using a plate reader (PerkinElmer; Waltham,

MA). Cell viability was expressed as the percentage of viable cells for the control, cells only well, with all experiments performed in triplicate.

3.6.8 Broth Culture Biofilm Assay- E. coli *and* S. aureus

A broth culture assay was performed to measure the anti-biofilm activity of the LbL gauze as previously described [136, 137, 141]. A uropathogenic *E. coli* clinical isolate, UTI89 [76], was used as a representative gram-negative pathogen and a *S. aureus* clinical isolate from the urogenital tract, MN8 [106], was used as a representative gram-positive pathogen. Overnight cultures were grown in Luria Broth for *E. coli* (LB; 25 g/L Miller, Thermo Fisher Scientific; Waltham, MA) or trypticase soy broth (TSB; 10 g/L, Becton, Dickinson and Company; Sparks, MD) for *S. aureus* for 16-18 hours at 37°C with shaking (180 rpm). Cultures were then "refreshed" by replacing 5 mL of original culture suspension with 5 mL fresh media and grown for an additional three (*E. coli*) or six (*S. aureus*) hours to ensure bacteria were in the exponential growth phase. Overnight cultures were then diluted to an optical density (OD_{600}) of 0.1 (~$8x10^7$ cells/mL) in yeast extract-Casamino Acids (YESCA) broth supplemented with 4% dimethyl sulfoxide (DMSO) (Corning; Glendale, AZ) for *E. coli* or peptone-NaCl-glucose (PNG) media (Thermo Fisher Scientific; Waltham, MA) for *S. aureus*, media known to promote increased curli formation [16, 105].

The gauze (C, CT5, and CT5+AP) was cut into 1x1 cm^2 samples, placed in triplicate in the wells of a non-tissue culture treated 24-well polystyrene plate (Corning; Glendale, AZ), and seeded with 1 mL of the bacterial suspension. For the *E. coli* tests, the plates were incubated at 26°C without shaking. After 42 hours, gentamicin (Thermo Fisher Scientific; Waltham, MA) or YESCA media was added to each well for a final well antibiotic concentration of 300 µg/mL and incubated for 6 more hours. For the *S. aureus* tests, the plates were incubated at 37°C and shaken at 200

RPM. After 18 hours, vancomycin (Thermo Fisher Scientific; Waltham, MA) or PNG media was added to each well for a final well antibiotic concentration of 300 μg/mL and incubated for 6 more hours. After 24- or 48-hours total for *S. aureus* or *E. coli* plates respectively, the media was removed from each well. Each gauze sample was gently placed in 1 mL of fresh PBS to remove non-adherent bacteria. The gauze was then placed in an Eppendorf tube with 1 mL of fresh PBS and sonicated gently for 30 seconds to remove adherent bacteria. The bacteria in PBS was then diluted in tenfold increments and the serial dilutions were plated on agar plates (TSB agar or LB agar for *S. aureus* or *E. coli*, respectively) using the drop plate method [107]. Six replicates were plated per condition. Colonies were grown for 16 hours at 37°C and CFUs were determined. Total CFUs of the biofilm suspensions were calculated using the dilution number and the number of CFUs counted in that dilution. CFU fold reductions were calculated by dividing the mean CFUs of the control (plain gauze) by each antibiotic gauze condition (C, CT5, or CT5+AP).

3.6.9 SEM with Bacteria

Gauze samples (1x1 cm^2) were incubated with bacteria as previously described for 24 (*S. aureus*) or 48 (*E. coli*) hours. However, after the first PBS rinse, samples were fixed with 2.5% glutaraldehyde (25%, EM grade, Ted Pella Inc.; Redding, CA) for two hours. After fixation, samples were rinsed three times with PBS solution for 15 minutes each. Samples were then dehydrated by submersion in a series of ethanol solutions of 25, 50, 70, and 100% ethanol for 15 minutes each. The samples were stored in 100% ethanol at 4°C. Samples were prepared for SEM imaging by drying in the critical point dryer (CPD). Dried samples were then stored in a sealed bag with a desiccant until use. Samples were sputter coated for 180 seconds with gold/palladium and then imaged on a scanning electron microscope (FEI SEM XL Siron or Apreo 2) at 5 kV with

a 5 mm working distance. Gauze samples were imaged from the top view in three spots at varying magnification.

3.6.10 Statistical Analysis

All statistical significance values reported are One-Way ANOVA with post-hoc comparisons as shown, and a Tukey multiple comparison correction performed in GraphPad Prism version 10.1.0. A single asterisk indicates a p-value less than 0.05, which was considered the cutoff to be considered statistically significant. Two asterisks indicate a p-value less than 0.01. Three asterisks indicate a p-value less than 0.001. Four asterisks indicate a p-value less than 0.0001.

3.7 Supplementary Information

Peptide Sequences			
Name[a]	**Sequence**[b]	**Description**	**Source**
AP401	Ac-rGeMnLsWmneysGwTmNlKmGr-NH2	α-sheet monomer	Bleem et al., 2017
AP526	Ac-rGeMnLsWmneysGwTmNcKmGr-NH2	α-sheet monomer; addition of cysteine	This work
***E. coli* Strain**			
UTI89		Uropathogenic *E. coli* (UPEC) strain; cystitis isolate	Mulvey et al., 2001
***S. aureus* Strain**			
MN8		Clinically relevant strain; toxic shock isolate from the urogenital tract	Schwartz et al., 2012

SI Table 3.1: Peptide Sequences and Bacterial Strains. [a] "AP" refers to "Alternating Peptide", which indicates alternating L- and D- amino acid templating. [b] L- amino acids are displayed in all upper case; D-amino acids are displayed in lower case and underlined.

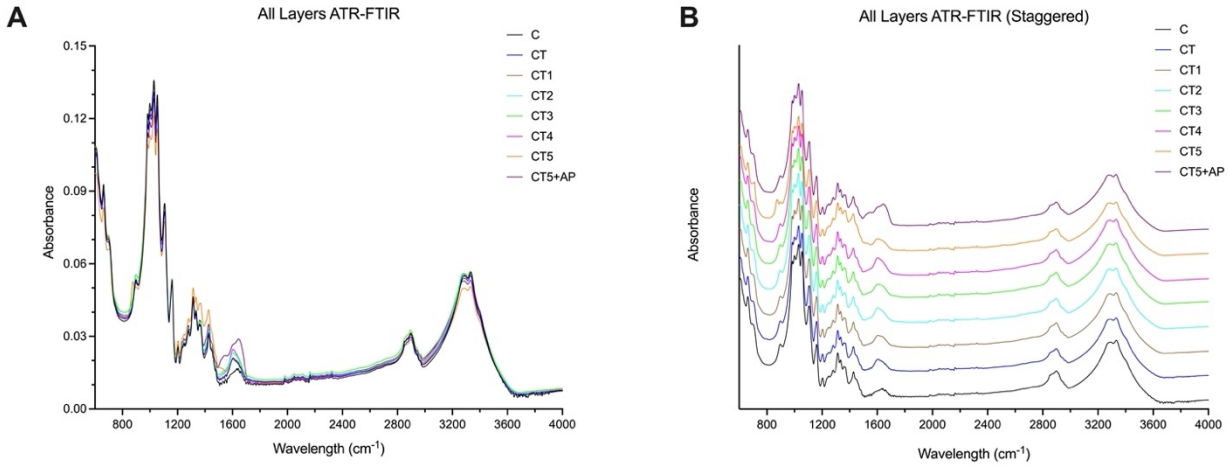

SI Figure 3.1: ATR-FTIR spectra for all gauze samples from plain cotton (C) to CT5+AP. **A)** Spectra are shown with measured absorbance values. **B)** Spectra are offset for better visualization of individual measurements.

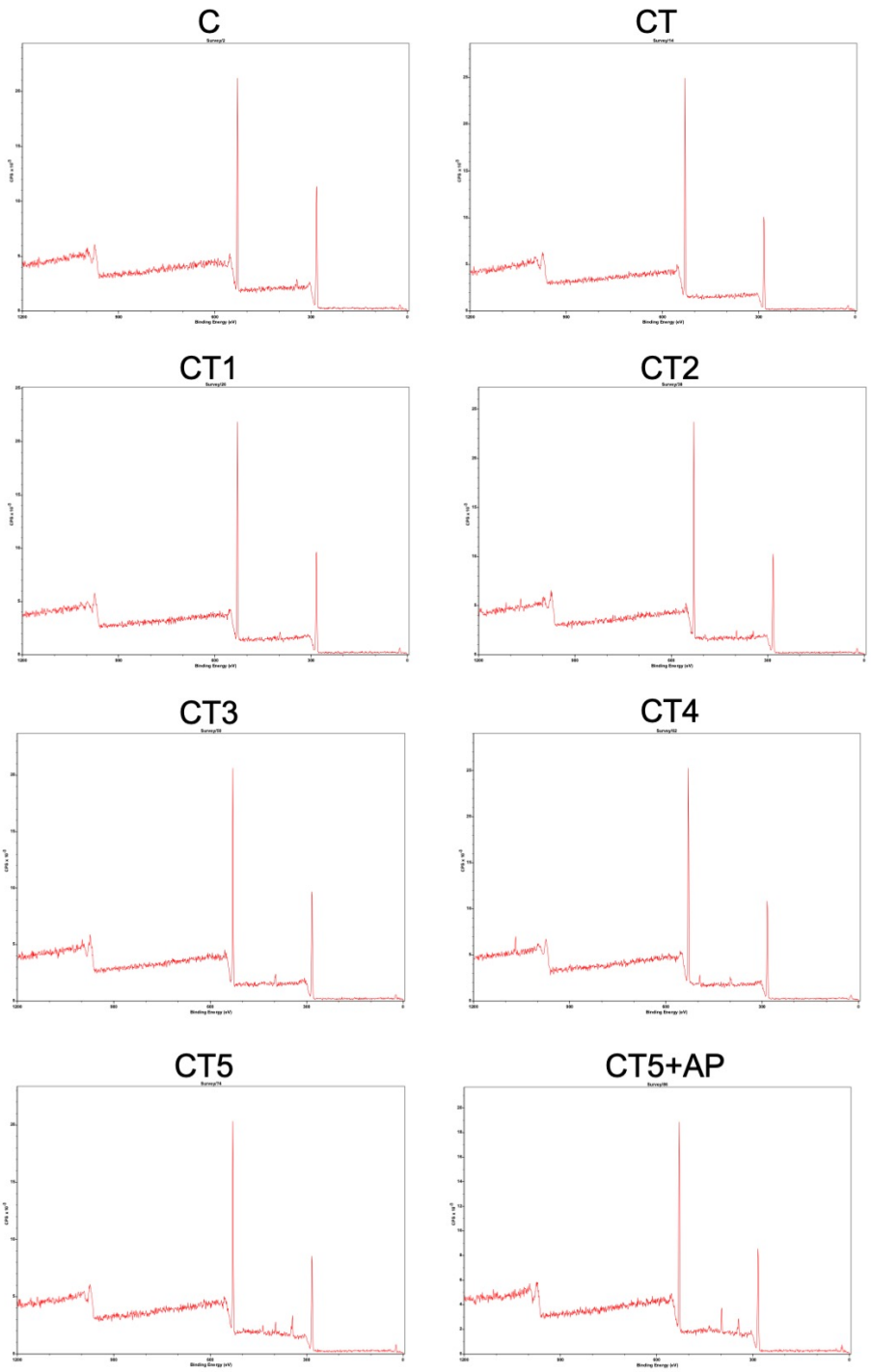

SI Figure 3.2: All spectra for the XPS composition analysis of plain cotton (C) to CT5+AP gauze. Areas under the peaks were analyzed to determine percentage atomic composition for each sample.

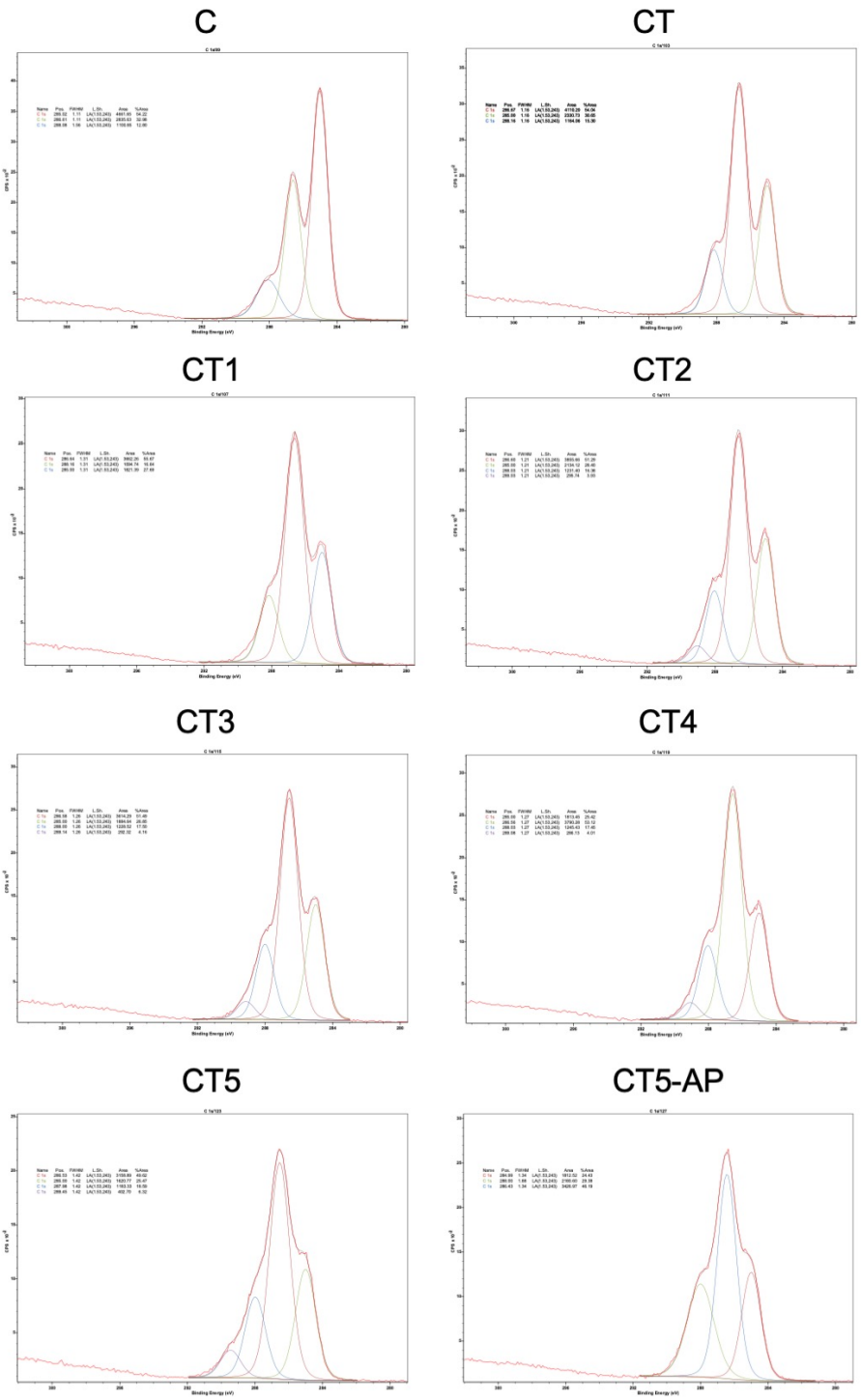

SI Figure 3.3: All spectra for the XPS high-resolution carbon analysis of plain cotton (C) to CT5+AP gauze. Areas under the peaks were analyzed to determine percentage atomic composition for each sample.

SI Figure 3.4: All spectra for the XPS high-resolution nitrogen analysis of plain cotton (C) to CT5+AP gauze. Areas under the peaks were analyzed to determine percentage atomic composition for each sample.

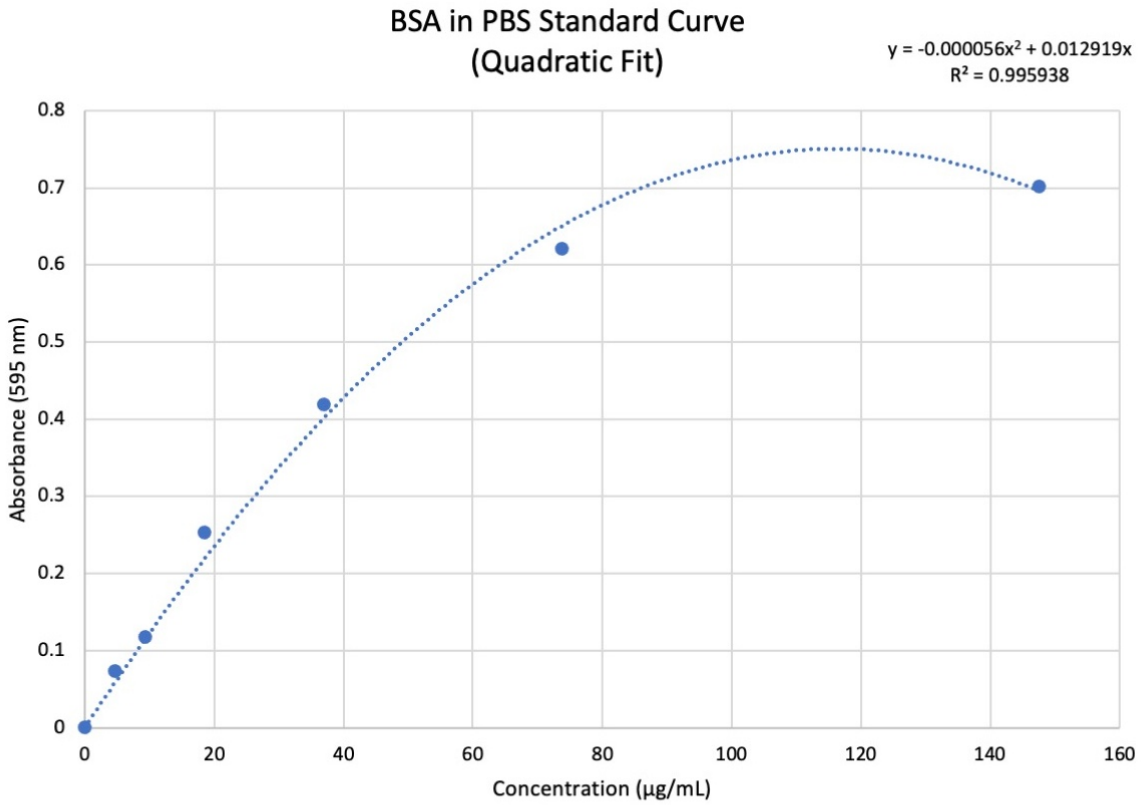

SI Figure 3.5: BSA Calibration Curve. Peptide release was measured using a Coomassie stain and calibration from absorbance to concentration with a quadratic curve of best fit. BSA samples of known concentration were used as a known protein standard as recommended by kit manufacturers.

Chapter 4. Investigation of α-Sheet Peptides for Oral Biofilm Prevention

4.1 Abstract

Oral biofilms have greater resistance to antimicrobial agents and increased virulence as compared to their planktonic counterparts [166]. Dental caries, or cavities, is the second most prevalent human disease and begins with microbiological shifts within the complex oral microbiome [167]. Many proteins contribute to the bacterial extracellular matrix, but functional amyloid structures are an attractive drug target as they are hypothesized to reinforce the biofilm and resist dispersion by chemical and mechanical agents. *De novo* α-sheet peptides inhibit amyloid formation in *Streptococcus mutans* [10], a gram-positive bacterium, that is the primary contributor to cavity formation. Here, two monomer peptides and two dimer peptides were tested against *S. mutans* with AP510 dimer demonstrating significant amyloid and biofilm inhibition. Next, dental implants are a successful therapy but up to 11% of implants fail, with many of these failures caused by infection [168]. Thus, this work presents a polydopamine based coating for oral implants for the localized delivery of α-sheet peptides and oral biofilm inhibition. The α-sheet peptides demonstrated a high coupling efficiency with a dimer peptide. The covalently bound peptide showed some inhibition of *S. mutans* amyloid formation, presenting a new method to inhibit *S. mutans* dental biofilm formation.

4.2 Introduction

All surfaces in the oral cavity are colonized by bacteria and teeth provide a non-shedding surface for microbial colonization. Over 700 bacterial species have been detected in the human mouth and saliva contains 10^8-10^9 bacteria per milliliter [169]. Teeth are a non-shedding surface

where bacteria readily adhere to form a surface-attached biofilm in both healthy and diseased conditions [170]. Dental biofilms are similar to those formed on tissue surfaces or artificial implants, and feature an extracellular matrix (ECM) of polysaccharides, proteins, and DNA [169]. Biofilm formation and persistence are governed by complicated physical, chemical, and biological processes [171]. Oral cavity bacterial attachment on dentine and enamel begins with recognition of salivary pellicle receptors [172]. Next, extracellular polymeric substance (EPS) forms on bacterial surfaces and the salivary pellicle presents binding sites for microorganisms [172]. The EPS increases biofilm stability and structural integrity, providing protection to the bacteria [171].

Many proteins are incorporated into the biofilm secreted extracellular matrix (ECM). However, functional amyloid structures are an attractive drug target as they are produced by several pathogenic bacteria and promote ECM stabilization and virulence. As described, amyloid fibril formation is preceded by the aggregation of soluble monomers into toxic, soluble oligomeric intermediates [74]. These oligomeric transient intermediates share a non-standard secondary backbone structure called an "α-sheet" [38, 74]. Identification of these α-sheets has led to the development of synthetic peptides with a stable, monomeric α-sheet structure [6, 7]. *De novo* α-sheet peptides interrupt biofilm formation and impair biofilm-associated infection in both gram negative and positive bacterial species [10, 114, 115].

Streptococcus mutans is a gram-positive bacterium primarily responsible for cavity formation. This species is an acidophile that binds to the salivary pellicle, a layer of glycoproteins coating tooth surfaces. After initial adhesion, bacteria form a biofilm termed a dental plaque [170], most often involving *S. mutans* [173]. Recent Thioflavin T (ThT) fluorescence measurements, Congo-Red birefringence, and Transmission Electron Microscopy imaging of multiple *S. mutans* biofilm-associated proteins suggest they are amyloidogenic [174, 175]. The Daggett group has

shown that *S. mutans* may share an intermediate α-sheet structured species in the pathway to amyloid formation and that synthetic α-sheet peptides inhibited fibril formation in a physiologically relevant setting [10]. Significantly, Paranjapye and Daggett, showed that three α-sheet peptides (AP90, AP407, and AP510) inhibited amyloid fibril formation in *S. mutans* as indicated by decreased ThT fluorescence [10].

Oral biofilms are a virulence factor for many infections, including dental caries (cavities), secondary caries, gingivitis, periodontitis, and peri-implantitis [166]. Dental caries is the second most prevalent human disease, accounting for 5-10% of public health expenditures [167]. Bacteria from a dental biofilm can spread to other tissue via the bloodstream, especially during tooth extractions and oral surgery. Secondary caries occur after a filling has been in place for some period of time and is a primary reason for restoration failures. Nearly half of clinical restorations fail within ten years [176]. Dental implants are a successful therapy for edentulism, but 5-11% of implants fail and must be removed, with ~10% of these failures caused by infection [168]. Implant infection, or peri-implantitis, leads to chronic inflammation, loss of the supporting bone structure, and implant failure. Approximately 25% of dental implants develop peri-implantitis within 11 years of implant placement [177].

Oral biofilms have increased resistance to antimicrobials and greater virulence than planktonic bacteria as the ECM protects biofilm-associated bacteria from exogenous compounds. Additionally, the oral cavity poses unique complexities including the rapid clearance of saliva which can prevent antibacterial agents from achieving a minimum inhibitory concentration over a sufficient time. Peri-implantitis treatments include root debridement, local delivery of antimicrobials, and regenerative surgery to reestablish the bone-implant interface [168]. However, these procedures are limited as they only deliver antibiotics to the gingival interface and not into

deep interfacial defects. Existing techniques that scratch or roughen the implant surface using scaling probes can also lead to increased plaque re-accumulation [168]. Clearly, new strategies and materials are needed to reduce and eliminate bacterial colonization at oral implant interfaces.

A range of bio- and nanomaterial-based approaches have been proposed to prevent and treat secondary caries and peri-implantitis. Nanomaterials made of silver, copper oxide, zinc oxide, titanium oxide, and graphene as well as nanoparticles made of quaternary ammonium polyethyleneimine, chitosan, and silica have been tested. Additionally, nanomaterials have been used for drug delivery, either as a carrier or with a specific affinity for tooth surfaces. For example, silver conjugated chitosan nanoparticles have been used as a coating material for titanium dental implants [178]. “Smart” drug delivery systems have also been tested, where drug release is triggered by an environmental stimulus such as pH, glucose, or bacterial products [166]. Composite or bioactive resins and adhesive systems have also been explored. Composite resins are used in clinical restoration due to their aesthetic effects. While the mechanical properties and wear resistance of dental composites have improved over time, fewer strides have been made to increase antibacterial properties, other than the addition of antibiotics and silver to adhesive systems [176, 179, 180].

Titanium and titanium alloy are commonly used as dental implants because of their biocompatibility, strength, corrosion resistance, small density, and good osseointegration [181, 182]. However, titanium has poor bioactivity and antibacterial properties, which can contribute to loose fixation with bone tissues and postoperative infection [182]. Additionally, titanium can undergo leaching and microbial-mediated corrosion [177]. Modification of an implant surface may promote quicker stabilization and integration of implants into the bone. Existing calcium phosphate coatings have been successful but suffer inconsistencies with coating quality, coating

failures, and susceptibility to bacterial colonization [181, 182]. Commercially available coatings were primarily designed to be osteoconductive and not necessarily antimicrobial. One emerging approach is the use of biocompatible and biodegradable implant coatings. These coatings promote the uniform delivery of antimicrobials at the implant-bone interface, discouraging initial bacterial attachment and growth during early healing and osseointegration. Local antimicrobial delivery has been explored for orthopedic implants, but coatings for dental applications must be adapted due to differences in the infectious nature of the oral cavity. The controlled delivery of antimicrobials from coatings is needed after as implant failures are highest during the first few months after implantation [183, 184]. An ideal coating should be antibacterial, biodegradable, biocompatible, and promote bioactive properties such as wound healing and osseointegration.

A polydopamine (PDA) coating is a simple and inexpensive technique for modifying surfaces. PDA surfaces are able to self-polymerize, form thin films, and support attachment of additional macromolecules such as peptides [185-187]. Dopamine is a biomolecule found in high concentrations in mussel adhesive proteins [187]. It contains a catechol and amine functional groups and polymerizes at alkaline pHs to form a thin, adherent PDA film on most material surfaces. These films are subsequently reactive towards amine and thiol groups that can be used to covalently attached biomolecules to the surface [187]. Dopamine polymerization occurs when catechol groups are oxidized to quinones that then react with amines and other catechols/quinones to form an adherent polymer film [185]. PDA coated surfaces can then be utilized for secondary molecule attachment. Under oxidizing conditions, the catechol groups react with amines or thiols via a Michael addition or Schiff base reaction (**Figure 4.1**) [185]. PDA coatings have been successfully demonstrated on titanium surfaces and allow for straightforward peptide conjugation [185-187].

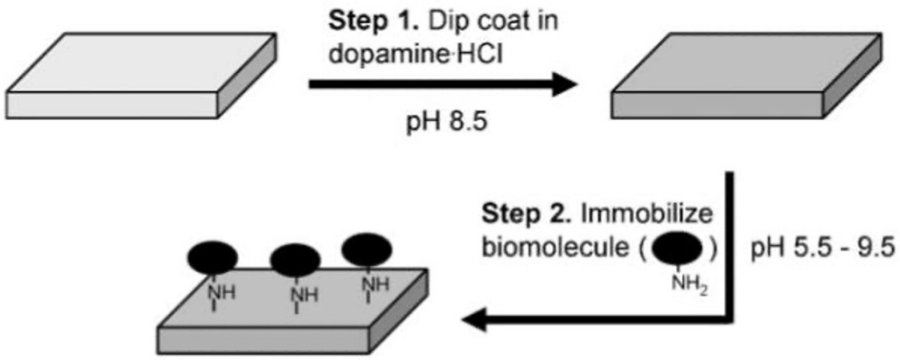

Figure 4.1: Schematic of polydopamine coating and biomolecule immobilization. Biomolecules are added through a reaction between amines and the polydopamine surface. Schematic from Lee et al. [187].

This work investigates the prevention of *S. mutans* oral using synthetic α-sheet peptides. Both monomer and dimer α-sheet peptides were tested in an *S. mutans* assay *in vitro* to determine the effect on amyloid formation and biofilm inhibition. Materials were then prepared with PDA coatings and assessed for α-sheet peptide coupling efficiency. Finally, the efficacy of the PDA-tethered peptides was assessed against amyloid and biofilm inhibition. This aim presents the foundational studies for the development of a biocompatible coating for oral implants to present synthetic α-sheet peptides and prevent oral biofilms.

4.3 Results

4.3.1 S. mutans *Growth Curve*

Streptococcus mutans strain UA159 [UAB577], a human isolate strain acquired from a child with active caries, was used for all experiments. First, a growth curve of planktonic *S. mutans* in BHI medium supplemented with sucrose and Oxyrase® (subsequently referred to as "BHI+" medium) was performed to characterize the growth kinetics (**Figure 4.2**). *S. mutans* grown in

suspended batch culture demonstrated logarithmic growth for the first 4 hours, followed by a stationary phase of limited growth up to 12 hours, and then a decline phase for the remainder of the time surveyed. This matches the predicted behavior of the bacteria under these growth conditions: BHI+ medium and incubation at 37°C without shaking. These conditions were thus used for all subsequent studies.

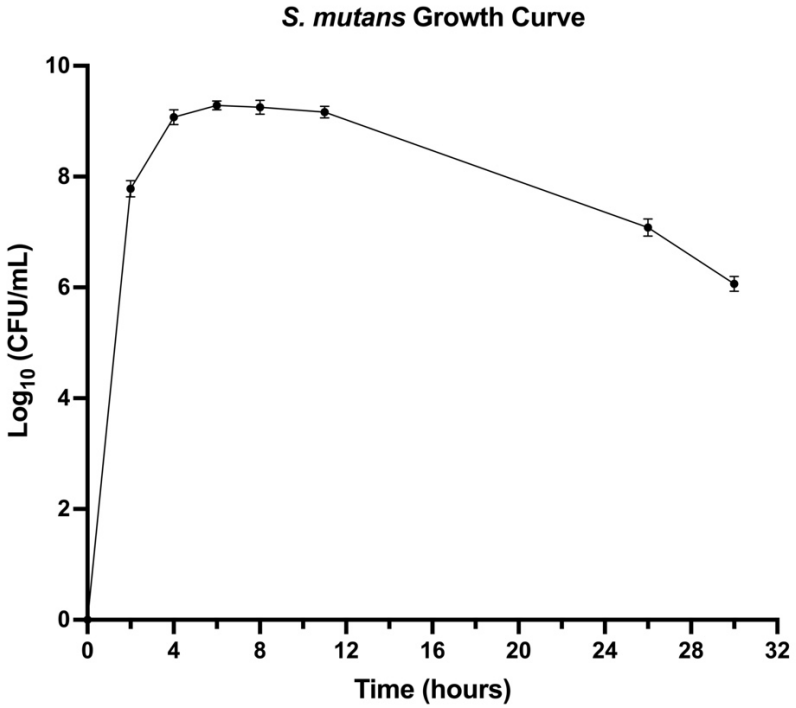

Figure 4.2: Growth curve of *S. mutans* in a suspended batch culture showing logarithmic growth over the first 4 hours, followed by the stationary phase until 12 hours, and then a decline phase. All values are mean ± SD for three replicates.

4.3.2 Dimer APs Inhibit S. mutans *Amyloid and Biofilm Formation*

After establishing growth conditions for *S. mutans*, four α-sheet peptides, two monomer peptides and two dimer peptides, were tested for prevention of amyloid fibrillization and biofilm formation. First, AP90 and AP401 monomer were tested due to previous efficacy in amyloid and biofilm inhibition in gram-negative and -positive species [116]. AP90 demonstrated statistically significant reduction of amyloid formation as indicated by ThT fluorescence at all peptide

concentrations (20-76 µM) (**Figure 4.3A**). The greatest amyloid inhibition was seen at 76 µM at 31% (*p<0.0002*). AP90 did not cause a significant reduction in biofilm formation as indicated by absorbance measurements, although a trend for biofilm inhibition was seen at higher concentrations (6% at 76 µM) (**Figure 4.3B**). As seen previously with *E. coli* and *S. aureus,* the total cell density did not decrease significantly with the addition of peptides (**Figure 4.3C**).

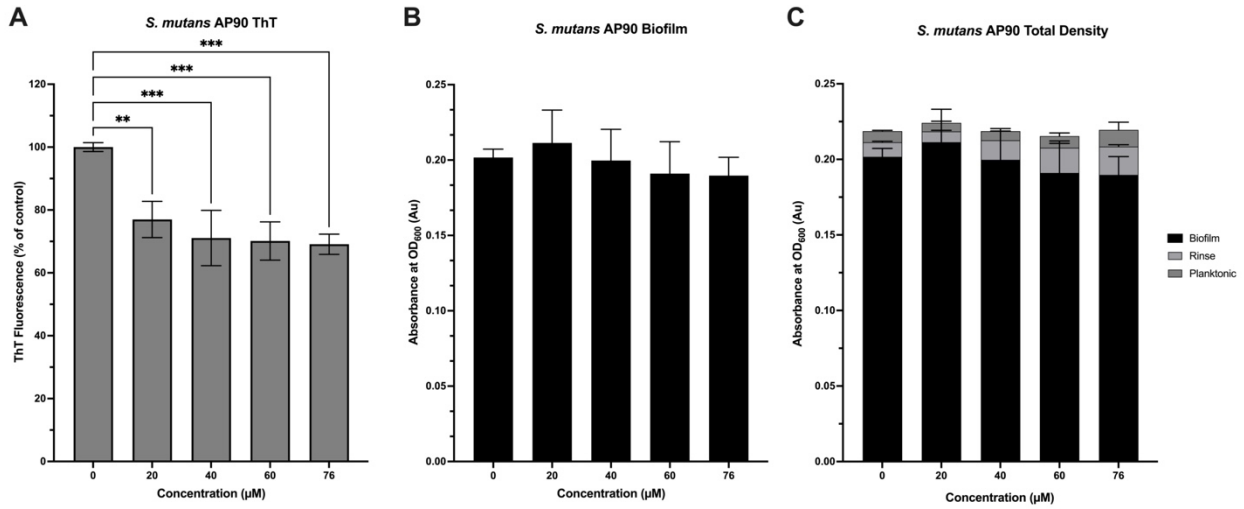

Figure 4.3: AP90 significantly inhibits *S. mutans* amyloid formation. A) AP90 caused a significant reduction in ThT fluorescence at all concentrations tested with the 76 µM condition causing the greatest reduction of 31%. **B)** Addition of AP90 did not cause a significant reduction in biofilm formation as indicated by absorbance values. **C)** AP90 did not have a significant effect on the total number of bacterial cells as indicated by absorbance values for the biofilm, rinse, and planktonic conditions. All values are mean ± SD for three replicates.

AP90 and AP401 have the same amino acid sequence but every amino acid has the opposite chirality. AP401 was subsequently tested for inhibition of amyloid and biofilm formation by *S. mutans*. A significant decrease in ThT fluorescence was not observed at any peptide concentration, although the greatest effect was seen at 80 µM with a 6% reduction in fluorescence (**Figure 4.4A**). Similarly, AP401 did not affect the biofilm formation (**Figure 4.4B**) or the total number of cells (**Figure 4.4C**) at any concentration.

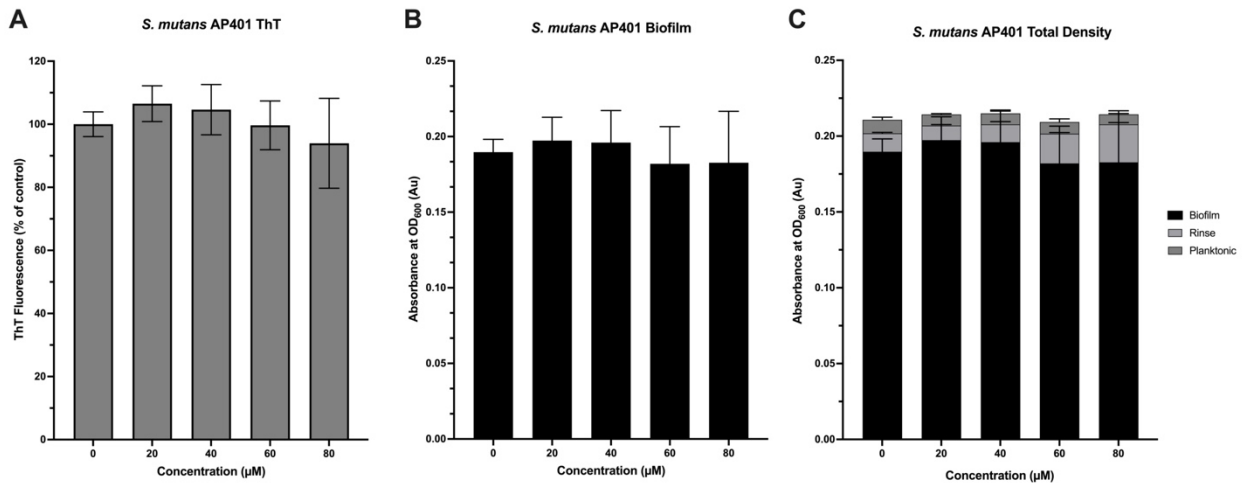

Figure 4.4: AP401 does not affect *S. mutans* amyloid or biofilm formation. A) Addition of AP401 did not cause a significant reduction in ThT fluorescence, although a trend for reduced fluorescence was seen at higher concentrations. No significant effect of AP401 was seen on **B)** biofilm density or **C)** total cell density for *S. mutans* at any peptide concentration. All values are mean ± SD for three replicates.

After testing two monomer peptides, the efficacy of the mixed dimer forms of AP510 and AP520 were assessed against *S. mutans* amyloid inhibition and biofilm formation. AP510 or AP520 mixed dimer (AP510md or AP520md) refers to peptides dimerized using a DMSO reaction without additional purification such that the final peptide solution is a mixture of the monomer and dimer forms of the peptide. Both peptides significantly inhibited amyloid formation as indicated by ThT fluorescence (**Figure 4.5A**). Specifically, AP510md caused as 45% reduction in fluorescence as compared to the control ($p<0.0001$). A significant reduction in biofilm formation was also observed for both mixed dimer peptides (**Figure 4.5B**) with AP520md causing a greater reduction of 15.9% ($p=0.0085$). A reduction in the total number of cells was also observed with decreased absorbance values for the planktonic and rinse samples for the two peptide conditions (**Figure 4.5C**).

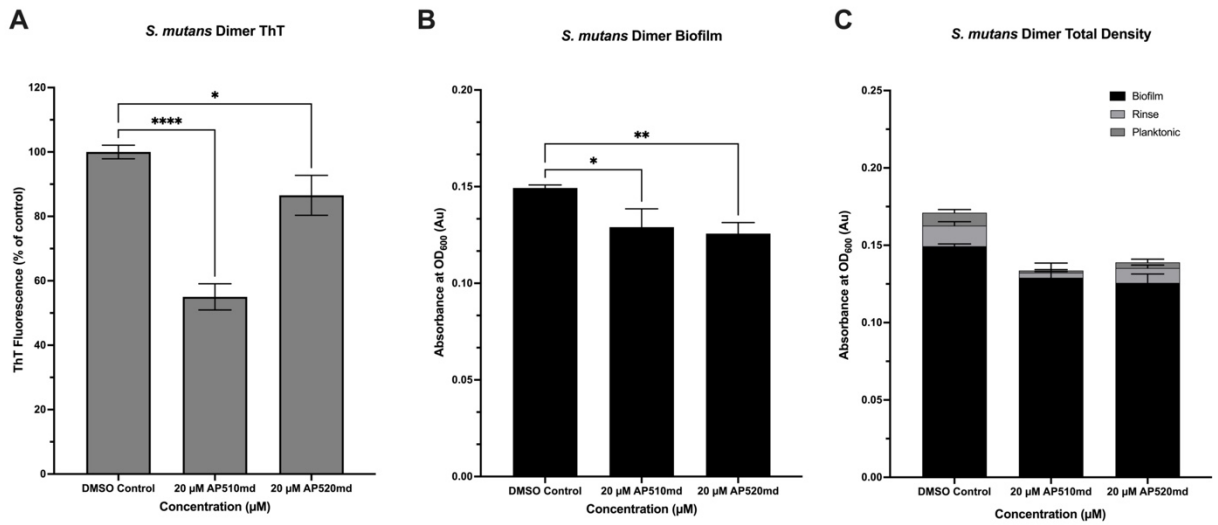

Figure 4.5: Dimer peptides significantly inhibit *S. mutans* amyloid and biofilm formation. A) Both mixed dimer peptides caused a significant reduction in ThT fluorescence as compared to the control, with AP510md causing at 45% reduction. **B)** Addition of the peptides also caused a significant reduction in biofilm formation. **C)** A decrease in total cell density was observed for the peptide conditions due to decreased cells in the rinse and planktonic samples. All values are mean ± SD for three replicates.

4.3.3 PDA Preparation Tests

The PDA coating and peptide coupling protocol was first tested with 96 well polystyrene plates. The coupling efficiency of AP510 mixed dimer and monomer were tested using two methods. In the first method, peptides were applied to a PDA coated surface and incubated at 26°C for four hours, followed by incubation overnight at 4°C. In the second method, the peptides were coupled at 25°C for two hours and then used immediately for biofilm assays. The coupling efficiency for both methods and AP510 mixed dimer and monomer are summarized in **Figure 4.6A**. No difference in coupling efficiency was observed between the coupling methods for either peptide form. However, significantly higher coupling efficiency was measured for the mixed dimer form, at around 95%, as compared to the monomer, at only 12%. The total concentration and concentration per well of the mixed dimer and monomer form were also calculated (**Figure 4.6B**), again emphasizing greater coupling efficiency for the mixed dimer form.

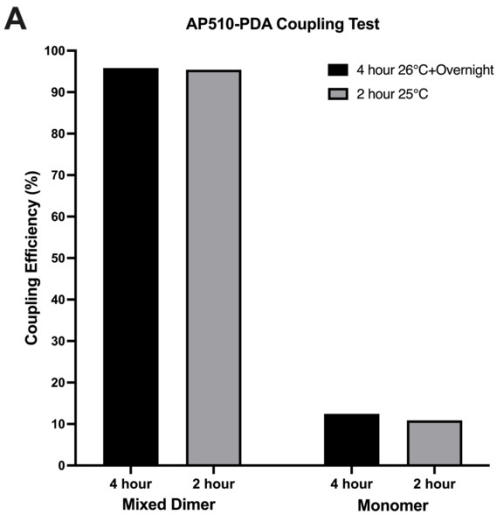

B

AP510-PDA Coupling Efficiency

		% Coupling	Plate (μM)	Plate (monomer μM)	μmol/well
4 hour	Tethered Mixed Dimer	95.83	119.78	239.56	0.0120
	Tethered Monomer	12.44	31.09	31.09	0.0016
2 hour	Tethered Mixed Dimer	95.41	119.26	238.52	0.0119
	Tethered Monomer	10.88	27.19	27.19	0.0014
	Solution Mixed Dimer		125	250	0.0030
	Solution Monomer		250	250	0.0030

Figure 4.6: Test of AP510 coupling efficiency to PDA coated surface. A) Two coupling methods, 4 hours at 26°C followed by overnight at 4°C or 2 hours at 26°C only, were tested to determine AP510 coupling efficiency. No differences in coupling efficiency were measured between the two methods. **B)** The coupling efficiency of AP510 heterodimer and AP510 monomer were tested with PDA coating on polystyrene plates. The AP510 heterodimer showed significantly higher coupling efficiency than the monomer.

4.3.4 PDA Preparation Tests

Finally, PDA-tethered AP510md was assessed against *S. mutans* amyloid and biofilm formation. 250 μM AP510md was coupled to a PDA coated 96-well polystyrene plate using the 2 hours at 25°C incubation method (**Figure 4.7A**). The tethered AP510md caused a 32% reduction in ThT as compared to the control, although the value was not statistically significant (*p=0.0796*) (**Figure 4.7B**). However, a reduction in biofilm formation was not observed (**Figure 4.7C**).

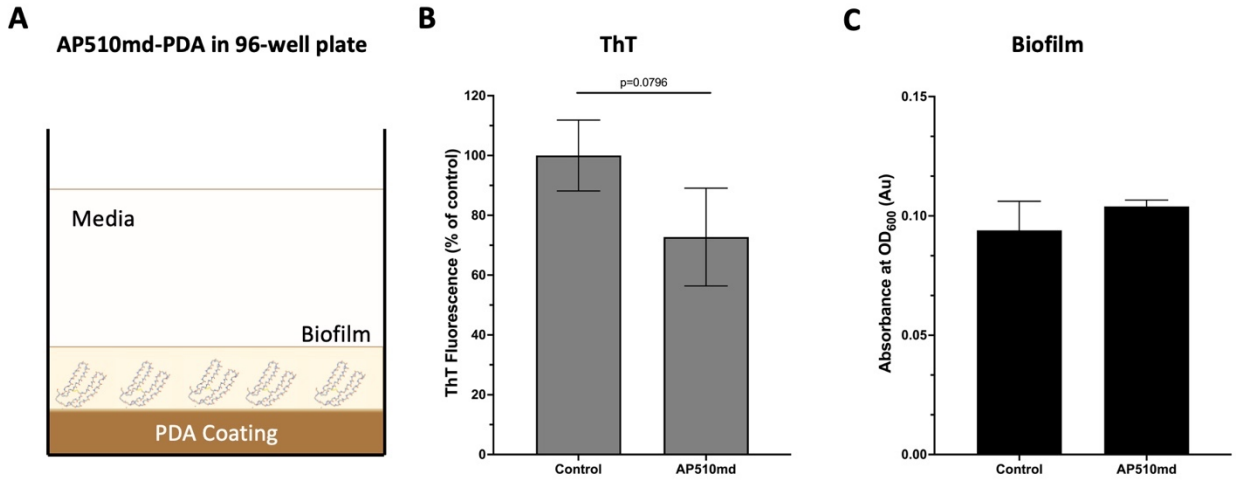

Figure 4.7: PDA-tethered AP510md inhibits amyloid formation. A) Schematic of AP510md tethered to a PDA-coated 96-well polystyrene plate with *S. mutans* biofilms grown for 24 hours. **B)** Tethered AP510-md caused a non-statistically significant reduction in ThT fluorescence (*p=0.0796*). **C)** AP510md did not cause a reduction in biofilm formation as indicated by absorbance at 600 nm. All values are mean ± SD for three replicates.

4.4 Discussion and Future Directions

New strategies are needed to address acute oral biofilm infections. One study showed that 75% of dental infections occurred within two weeks of surgery [188] and a second study showed that 67% of infections developed within the first month [189]. Thus, the goal of this proposal is to prevent initial biofilm infection through attachment of α-sheet peptides.

The first objective was to optimize the growth conditions of *S. mutans*, a facultatively anaerobic, gram-positive coccus found primarily in biofilms on tooth surfaces. We used standard *S. mutans* growth conditions as described in previous work from the Daggett group [10] and observed the expected growth curve profile. A BHI+ medium supplemented with Oxyrase® was selected to ensure an oxygen-limited environment. Plate assays were further provided an oxygen limited environment by wrapping the plates three times with parafilm and placing them in a sealed bag.

The effects of various peptides were then assessed on amyloid and biofilm inhibition in a 48-well plate assay. Here, the peptides were administered in solution and were not tethered to a surface as proposed for dental applications. Greater amyloid and biofilm inhibition was observed from AP90 than from AP401 which corresponds with previous results for gram-positive bacteria [116]. As described, AP90 and AP401 have the same amino acid sequence but with inverse chirality at every position. As such, AP90 has L-amino acids at the hairpin turn and AP401 has D-amino acids at the turn. D-amino acids are frequently incorporated into gram-positive cell walls which are composed of thick peptidoglycan layers [95]. Because gram-positive bacteria, such as *S. mutans*, utilize D-amino acids in their cell wall, the bacteria may also produce proteases that are designed to cleave the peptide bond between D-amino acids. Therefore, we hypothesize that AP401 may be susceptible to cleavage by *S. mutans* proteases, reducing the stability and efficacy of the peptide.

In addition to these monomer peptides, two dimer peptides (AP510md and AP520md) were tested. AP510 was selected due to previous work from the Daggett group where it showed significant amyloid inhibition in *S. mutans* (33% reduction in ThT fluorescence) [10]. Next, AP520 was selected because it has the same sequence as AP90 but with a single residue cysteine substitution so that it can be dimerized. Since we observed significant amyloid inhibition from AP90 but preferred a dimer for PDA coupling efficiency, we were interested in testing AP520 mixed dimer for the PDA experiments.

As previously observed [10], AP510md significantly inhibited amyloid formation as indicated by reduced ThT fluorescence. A significant, though not as large, reduction in fluorescence was also observed for the AP520md. However, both peptides caused a similar reduction in biofilm cell density. A reduction in the total cell density (biofilm, planktonic, and rinse

cells) was also observed, however, the magnitude of this reduction was fairly small. Under these growth conditions, *S. mutans* forms sticky and adherent biofilms. Quantification of planktonic cells can pose challenges as cells can clump and stick to tubes during transfer so these results will be replicated in future assays. Based on these results, both mixed dimer peptides were selected for future assays.

Next, we assessed the coupling efficiency of monomer and dimer peptides to a PDA coated surface and a higher coupling efficiency was observed for the dimer peptide. Synthetic α-sheet peptides contain amino groups (Pep-NH2), which undergo a Michael addition or Michael addition/Schiff base reaction to bind covalently to the PDA surface. For the dimer peptides, the PDA is most likely coupling to the primary amine on the C-terminus. For monomer peptides, PDA is probably coupling to the lysine residue. An additional factor in coupling efficiency is the buffer in which the peptide is solubilized. The dimers were dissolved in DMSO, which raises the pH, whereas the monomers were in solubilized in water.

Finally, in preliminary studies assessing the PDA-tethered AP510md, some inhibition of amyloid formation was observed. However, this did not translate to a reduction in biofilm formation. Further work is required to optimize the peptide coupling for amyloid and biofilm inhibition by adjusting peptide concentration, growth conditions and additional biofilm quantification methods

Future Directions

Future work will focus on optimizing the systems developed in this chapter: *S. mutans* biofilm formation, PDA coated titanium surfaces, and tethered α-sheet peptides. The materials will

be assessed for anti-biofilm properties using broth culture assays as described in **Chapter 4.6.5** including quantification of bacterial growth through colony forming units and SEM imaging.

The developed titanium materials will also be assessed for their mechanical properties and cytocompatibility. Coating thickness is important because the coating lies between the titanium implant and the bone surface. Dental implants are subjected to friction forces, such as that applied by a toothbrush because it is recommended that implants are brushed on a regular basis even during the healing period. This can damage the coating; thus, it is important to determine coating adherence and scratch resistance.

Additionally, cytocompatibility tests are critical for all materials with the potential for clinical applications and provide initial assessments of toxicity or potential irritancy of novel biomaterials. Specifically, cytocompatibility tests will be conducted using Human Embryonic Palatal Mesenchymal cells (ATCC#1486, Manassas, VA) as model osteoblastic cells, as the titanium implants are intended to interact with osseous tissues [168]. Normal human dermal fibroblasts will be used as model fibroblastic cells because some dental and orthopedic implants extend through the mucosal or epidermal tissues. Finally, a basic bacterial suspension test will be conducted, and biofilm formation will be assessed in two ways. We hypothesize that the PDA coated titanium will not demonstrate significant cytotoxicity and that they will inhibit bacterial biofilm formation as demonstrated by less colony forming units as compared to controls.

4.5 Conclusion

This chapter aims to inhibit oral biofilms caused by *S. mutans* and develop a PDA coating for prevention of biofilms on dental implants. These experiments build on previous work from the Daggett group demonstrating the efficacy of α-sheet peptides at inhibiting amyloid fibril formation

for *S. mutans*, the primary bacterial contributor to cavity formation. Here, monomer and dimer peptides demonstrated amyloid inhibition and dimer peptides also prevented biofilm formation. Natural, polymer coatings such as those formed by PDA represent a biocompatible way to improve the antimicrobial properties of oral implants. Thus, the integration of the peptides into a PDA coating represents a significant step forward in functionalizing implants for improved anti-biofilm properties. The proposed studies are highly feasible and will further progress the critical field of novel anti-biofilm treatments. They will also help further demonstrate the versatility of the α-sheet peptides at biofilm inhibition through demonstrated of activity when covalently bound to a surface as compared to when delivered in solution as in **Chapters 2 and 3**.

4.6 Materials and Methods

4.6.1 Peptide Synthesis and Preparation

α-Sheet peptides were synthesized as described in **Chapter 2.5.1** and lyophilized peptide was resuspended in appropriate buffers immediately prior to use. Purified monomer and dimer peptides were resuspended in water. Dimer peptides for PDA binding (referred to as "mixed dimers" as they are a mixture of monomer and dimer peptide without additional HPLC purification) were prepared by adding 4 μL DMSO to a 0.25 mg aliquot of monomer peptide. After thorough mixing, this solution was diluted in 100 μL carbonate buffer (50 mM, pH 9.6). The concentration was then measured by Nanodrop™ instrument (Thermo Fisher Scientific; Waltham, MA) and the concentration was adjusted with dilution in additional carbonate buffer. The mixed dimer peptide solution was incubated at 37°C for 2 hours and then at 4°C overnight.

4.6.2 Streptococcus mutans *Growth Curve*

Streptococcus mutans UA159 [UAB577] (ATCC; Manassas, VA) is a human isolate strain acquired from a child with active caries [10]. *S. mutans* was collected from a Brain Heart Infusion (BHI) medium (Sigma-Aldrich; St. Louis, MO) agar plate and resuspended in BHI medium for overnight growth. BHI medium was prepared by adding 37 g BHI dry power per 1 liter of water. The medium was then autoclaved to sterilize. After autoclaving and immediately before use, the medium was supplemented with sucrose solution to a final concentration of 30 mM (add 1.24 mL of 1M sucrose solution to 40 mL BHI) and with Oxyrase® (Oxyrase, Inc; Mansfield, OH) to a final concentration of 1% v/v (add 400 µL Oxyrase® to 40 mL BHI). This supplemented BHI medium is subsequently referred to a BHI+ medium.

For the growth curve, overnight cultures were grown for 16-18 hours at 37°C without shaking. After 16-18 hours, 1 mL of the overnight culture was then added to 100 mL of fresh medium and allowed to grow at 37°C without shaking. At each time point (0, 2, 4, 6, 8, 11, 26, and 30 hours), 1 mL of culture was removed. The sample was then spun down, resuspended in 1 mL of PBS, ultra-sonicated for 5 seconds on ice, and diluted in tenfold increments. The serial dilutions were then plated on BHI agar plates using the drop plate method [107]. Six replicates were plated per condition. Colonies were grown for 24 hours at 37°C and CFUs were counted. Total CFUs of the suspensions were calculated using the dilution number and the number of CFUs counted in that dilution.

4.6.3 S. mutans Thioflavin T (ThT) and Plate Biofilm Assays

Overnight cultures of *S. mutans* were started as described above and grown for 16-18 hours at 37°C without shaking. Cultures were then “refreshed” by replacing 5 mL of culture with 5 mL

of fresh BHI+ medium and grown for an additional 3 hours. The culture was diluted to an optical density (OD_{600}) of 0.1 (~$8x10^7$ cells/mL) in fresh BHI+ medium. Diluted bacterial culture (180 µL) was plated with 20 µL peptide (or buffer/water control) in triplicate into wells of a sterile, clear 48-well polystyrene plate (Corning; Glendale, AZ). Plates were covered with a lid and wrapped three times with parafilm to create a limited-oxygen environment within the plate. Plates were incubated at 37°C for 24 hours without shaking.

After 24 hours, plates were removed from the incubator. For ThT assays, planktonic cells and medium were then removed and biofilms were rinsed once with 250 µL PBS. Planktonic cells were spun down and resuspended in PBS, and the optical density of both planktonic and rinse samples was determined at 600 nm to estimate "planktonic" and "rinse" cell densities. The PBS rinse solution was removed from the wells and biofilms were resuspended in 200 µL of 20 µM ThT in PBS (Sigma-Aldrich; St. Louis, MO). Biofilms were homogenized by vigorous pipetting (30x per well), 3 minutes of sonication, and 1 minute on a plate shaker. 100 µL of each biofilm suspension was then transferred to a black-walled, clear-bottom 96 well plate for measurements in a plate reader (PerkinElmer; Waltham, MA). ThT fluorescence was measured at 438/495 nm as a proxy for amyloid formation, and biofilm absorbance was measured at 600 nm to estimate bacterial cell density. Fluorescence measurements were corrected for nonspecific fluorescence by subtracting the background intensity of identical samples without bacteria. Biofilm ThT fluorescence values are reported as percent of the average *S. mutans* peptide-free control fluorescence. All values are mean and standard deviation for three replicates.

4.6.4 PDA Coating and Peptide Attachment

For the PDA coating, 2 mg/mL of dopamine HCl (Sigma-Aldrich; St. Louis, MO) was dissolved in 10 mM Tris HCl, pH 8.5. 165 µL of the dopamine-HCl solution was added per well to a 96-well polystyrene plate. The PDA solution was left for 24 hours at room temperature with shaking at 300 RPM. Each well was then rinsed with water five times and dried in a vacuum chamber at 30°C for one hour.

50 µL of the prepared AP dimer solution was then added to each well of the PDA coated plate and left for 2 hours at 25°C. The peptide solution was then removed and each well was gently washed with sterile water (**Figure 4.8**). Peptide coupling efficiency was determined by concentration measurements of the peptide solution before and after the reaction with a Nanodrop™ instrument (Thermo Fisher Scientific; Waltham, MA).

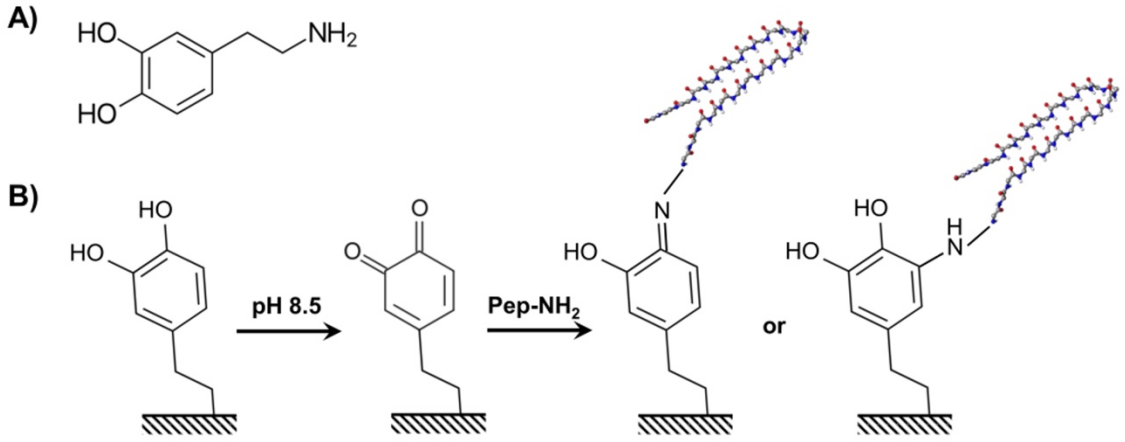

Figure 4.8: Schematic of peptide and PDA coupling. A) Dopamine molecules contain both DOPA (3,4-dihydroxy-L-phenylalanine) and lysine functional groups. **B)** Reaction schematic for PDA coatings. At an alkaline pH, dopamine undergoes self-polymerization to form an adherent coating as well as oxidation of catechol groups to the amine form. α-Sheet peptides can be covalently attached through Michael addition or a Schiff base reaction. Schematic courtesy of Alissa Bleem.

4.6.5 Biofilm PDA-Material Challenge Assays

S. mutans assays were started as described in **Chapter 4.6.3** with the addition of the peptide-tethered, PDA coated 96-well plates as described in **Chapter 4.6.4**. Amyloid and biofilm formation were assessed using a ThT assay with cell density measurements through absorbance readings as in previous sections.

4.6.6 Statistics

All statistical significance values reported are One-Way ANOVA with post-hoc comparisons as shown, and a Bonferroni multiple comparison correction performed in GraphPad Prism. A single asterisk indicates a p-value less than 0.05, which is the cutoff to be considered statistically significant. Two asterisks indicate greater significance, with a p-value less than 0.01. Three asterisks indicate a p-value less than 0.001. Four asterisks indicate a p-value less than 0.0001.

Chapter 5. Designed α-Sheet Peptides Enhance Clearance of Amyloid-β Oligomers by Microglial Cells of the Central Nervous System

5.1 Abstract

Alzheimer's Disease is characterized by the accumulation of insoluble β-amyloid peptide (Aβ) in the brain. However, a growing body of research suggests that soluble, low molecular weight Aβ oligomers are the primary pathogenic agents while amyloid fibrils are relatively benign. Designed synthetic α-sheet peptides that specifically bind toxic Aβ oligomers decrease Aβ levels in both cell and animal models. It was hypothesized that this reduction might be caused by an increased clearance of Aβ oligomers. This study aimed to measure the effect of α-sheet peptides on phagocytosis of Aβ oligomers by macrophages and microglia. All α-sheet peptides tested caused an increase in phagocytosis for the two cell types as measured through Aβ uptake and visualized with confocal microscopy. Furthermore, increased phagocytosis was observed with α-sheet peptides in a modified nonphagocytic HEK293 cell line that was made phagocytic through the co-expression of Triggering receptor expressed on myeloid cells 2 (TREM2) and DNAX activation protein of 12kDa (DAP12). Biolayer interferometry data confirmed a strong interaction between the α-sheet peptides and TREM2 further suggesting that the enhanced phagocytosis is in part mediated via TREM2. Additionally, the α-sheet peptides did not stimulate cytokine production in microglial cells indicating a specific effect on phagocytosis without triggering an inflammatory response. These findings provide a potential mechanism for the α-sheet peptide-mediated reduction in Aβ oligomers previously observed.

5.2 Introduction

As the world population ages, patients and healthcare providers are faced with the growing threat of Alzheimer's Disease (AD). AD is a progressive neurodegenerative disease that primarily affects the elderly and is the leading cause of death in the United States. At present, there is no cure for AD and there are a deficit of early diagnostic tools and sufficient therapies to address the disease biology [190].

The accumulation of the β-amyloid peptide (Aβ) outside of neurons is a hallmark of the disease. Monomeric Aβ is involved with multiple biological functions including memory, learning, and neuroprotection [29-32]. To date, clinical trials have been conducted of potential AD therapeutics that target the monomeric and/or fibrillar forms of Aβ peptide. However, a growing body of research supports the modified amyloid cascade hypothesis, which states that soluble Aβ oligomers are the primary pathogenic agents while amyloid fibrils are relatively benign. There is also evidence that toxic soluble oligomers, not the amyloid burden, are associated with disease progression and that damage begins prior to amyloid plaque deposition [33-37].

Toxic oligomers from various amyloid systems have a shared conformation, not sequence, as indicated by the cross reactivity of the A11 oligomer specific antibody [52]. Atomistic molecular dynamics simulations from the Daggett group revealed a nonstandard secondary structure called α-sheet and demonstrated that unrelated proteins in amyloid diseases form α-sheet structure under amyloidogenic conditions [74, 191, 192]. α-Sheet is similar to β-sheet structure except in α-sheet the carbonyl oxygens align on one strand and the NH groups align along the other, instead of alternating like in β-sheet.

Novel synthetic α-sheet peptides, both monomers (designated "AP#m") and dimers (AP#d), were designed to specifically bind the toxic Aβ oligomers [6, 7]. The Daggett group

demonstrated that multiple APs (AP5, AP90, AP407, and AP421) inhibit Aβ aggregation *in vitro* and protect against toxicity in cells, and that AP5 inhibits Aβ aggregation in two animal models [38]. *In vitro*, incubation of APs with toxic oligomeric Aβ aggregates reduced aggregation by as much as 96% [38]. Additionally, co-incubation with APs neutralized the toxicity of Aβ oligomers as shown through recovered cell viability [38].

The APs were also tested with transgenic APPsw mice that express human Aβ. In an *ex vivo* model, AP5 was applied to coronal brain sections and toxic oligomer levels were measured using the A11 antibody. For AP5 treated sections, a dose-dependent reduction in detectable oligomers was seen with reductions up to 79%. This indicated preferential binding of the toxic oligomers by the APs as seen *in vitro* [38]. Next, a transgenic mouse model was used to assess *in vivo* effects of AP5. The peptide was injected intracranially into the right hemisphere of 103-wk-old Tg APPsw mice. Again, a 40% reduction in Aβ oligomers was observed as compared to the control left hemisphere, as detected with the A11 antibody [38]. Finally, four APs (AP5, AP90, AP407, and AP421) significantly delayed paralysis due to Aβ in a transgenic *C. elegans* model commonly used to assess the effect of exogenous compounds on Aβ toxicity [38].

Based on these findings, it was hypothesized that the AP mediated reduction in toxic Aβ oligomers could be attributed to the APs altering the rate by which toxic Aβ oligomers are phagocytosed, as the APs were not directly impacting Aβ production [17]. Microglia, the primary immune cells of the central nervous system (CNS), are associated with the pathogenesis of AD. Microglia function primarily as phagocytes in the CNS and are involved in tissue maintenance, injury response, and defense against pathogens [40]. In AD, microglial proliferation and activation is concentrated around amyloid plaques [40]. Microglia may prevent the accumulation of Aβ through the clearance of soluble Aβ, phagocytosis of insoluble deposits, and by forming a barrier

around and compacting amyloid plaques [40, 193]. However, Aβ can also trigger an inflammatory response in microglial cells and toxic Aβ and tau proteins activate immune cells (e.g., microglia). Toxic Aβ and tau convert phagocytic microglia to inflammatory microglia resulting in chronic inflammation.

TREM2 (microglial triggering receptor expressed on myeloid cells 2) is a phagocytic receptor that plays a critical role in the clearance of Aβ [194]. TREM2 encodes a receptor that is only expressed on immune cells in the central nervous system, including infiltrating monocytes/macrophages and microglia [194]. TREM2 forms a complex with another protein DAP12; this complex is required to elicit TREM2 mediated phagocytosis and signaling [194]. TREM2 also plays a role in microglial phagocytosis and activation. In a TREM2 knockdown, phagocytosis is inhibited, and the production of inflammatory cytokines is stimulated [195]. The importance of TREM2 in Aβ clearance is highlighted in that loss of function mutations in TREM2 that increase the risk of developing AD and result in impaired Aβ phagocytosis [194, 196]. This underscores the importance of microglia and that their immunoinflammatory response plays a role in the pathobiology of AD [194]. Aβ oligomers also interact with TREM2 with high affinity and induce nuclear factor of activated T cell (NFAT) signaling [194, 196].

In previous work by the Daggett lab, AP5 decreased Aβ oligomers levels *in vivo* and *ex vivo* [38]. Here, we investigated the effect of multiple monomer and dimer APs on phagocytosis by macrophages and microglial cells of *Escherichia coli* bioparticles and toxic Aβ oligomers. Additionally, naturally non-phagocytic Human Embryonic Kidney (HEK293) cells were previously genetically engineered to be phagocytic through the co-expression of TREM2 and DAP12 and used in this study to assess TREM2 mediated phagocytosis [194]. Interactions between

the APs and TREM2 were also measured through biolayer interferometry. Finally, N9 microglial cell activation by APs was measured by cytokine response after 24 hours.

5.3 Results

5.3.1 APs significantly increase the rate of phagocytosis of E. coli *bioparticles in macrophages*

RAW264.7 murine macrophages were first used as a cellular model to assess the impact of AP5 on phagocytosis of *E. coli*. RAW264.7 cells were plated in a 96-well cell culture plate and the cells were treated with *E. coli* and the APs 24 hours after plating. Phagocytosis was then quantified for two hours using pHrodo™ Red *E. coli* BioParticles™ that fluoresce when internalized in the acidic environment of the phagosome. Cytochalasin D (Cyto D), an inhibitor of microfilament-dependent phagocytosis, was used as a positive control. AP5 significantly stimulated the internalization of *E. coli* in RAW264.7 cells at both peptide concentrations, suggesting that AP5 enhances phagocytic activity (**Figure 5.1A**). In contrast, Cyto D significantly limited the uptake of *E. coli* ($p<0.0001$), confirming that the increased fluorescence measured was caused by the phagocytosis of *E. coli*. Additional APs (AP200m, AP202m, and AP202d, where *m* denotes the monomer and *d* denotes the dimer form of the peptide) were then tested (**Figure 5.1B**). The mean velocity (V) of the uptake was quantified (mFU/min) and expressed as a percentage of control cells (i.e., cells treated with fluorescent *E. coli* BioParticles™ in absence of APs). All APs significantly increased the rate of phagocytosis of *E. coli* as compared to the control condition.

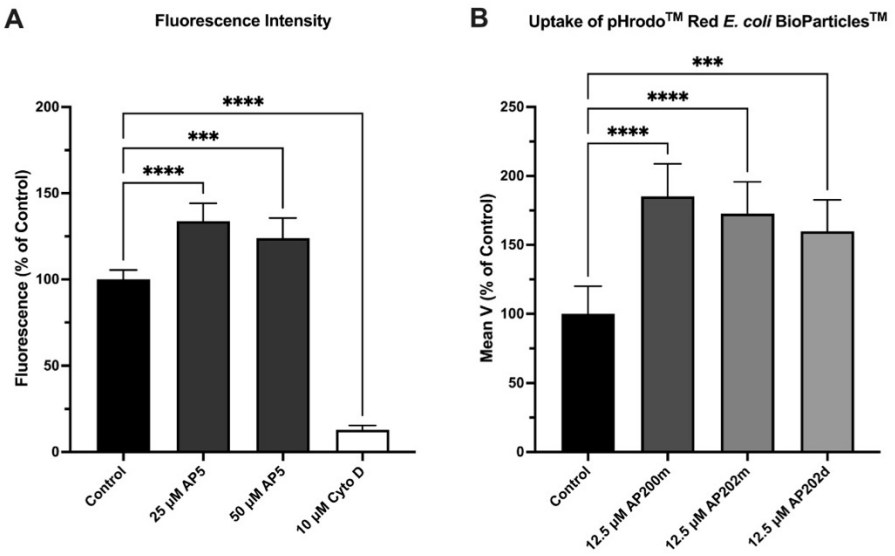

Figure 5.1: α-Sheet peptides increased phagocytosis of pHrodo™ Red E. coli BioParticles™ by RAW264.7 macrophages. A) Addition of AP5 at 25 and 50 µM significantly increased phagocytosis as measured by fluorescence intensity as compared to the cell control (*p<0.0001* and *p=0.*001 for 25 and 50 µM, respectively). **B)** 12.5 µM AP202m, AP202d, and AP200m also significantly increased phagocytosis as quantified by the mean velocity of the uptake (mFU/min) expressed as a percentage of control cells. Significant differences were observed between the uptake of *E. coli* particles between the control and AP conditions with AP202m (*p<0.0001*), AP202d (*p<0.0005*), and AP200m (*p<0.0001*). Values are the mean ± SD for n=5 for **A)** and n=6 for **B)**.

5.3.2 APs significantly enhance the phagocytosis of the Aβ1-42 oligomers in macrophages

We then assessed the effect of the APs on the phagocytosis of toxic Aβ oligomers in RAW264.7 cells using fluorescently labeled Aβ1-42 (FAM-Aβ) peptides. The RAW264.7 cells were co-incubated with FAM-Aβ1-42 oligomers with a range of AP doses (0, 0.78, 1.56, 3.125, 6.25, 12.5, and 25 µM). Six peptides (AP200m, AP201m, AP201d, AP202m, AP202d, and AP203d) were tested. Again, Cyto D (10 µM) was used as a positive control. After four hours of incubation, cells were washed twice with 200 µl of Live Cell Imaging Solution and 100 µl of Live Cell Imaging Solution was added to the cells after the final wash. The fluorescence of surface bound Aβ oligomers was quenched by incubation with 0.4% trypan blue and fluorescence intensities were measured at an excitation/emission of 485/528 nm on a Cytation 3 multimode

plate reader. All six APs significantly enhanced the phagocytosis of the Aβ1-42 oligomers in RAW264.7 cells at a range of concentrations as compared to the no peptide control ($p<0.001$) (**Figure 5.2A**). A non-significant increase in phagocytosis was observed for increasing peptide concentrations up to 3.125 μM, at which point phagocytosis remained constant or decreased.

An additional control of P1, an unstructured random coil peptide, was compared to the APs. There was a significant increase in phagocytosis from AP201m, AP201d, and AP203d as compared to P1 at concentrations of 1.56, 3.125, and 6.25 μM (except for AP201m at 3.125 μM) (**Figure 5.2B**). Comparison of all APs to P1 is shown in **Supplementary Figure 5.1**.

5.3.3 APs enhance phagocytosis of the Aβ1-42 oligomers by microglial cells in vitro

We then repeated these experiments in murine N9 microglial cells and reproduced the effects of the APs first observed in RAW264.7 cells. All six APs significantly stimulated the phagocytosis of the Aβ1-42 oligomers by the microglial cells at all doses tested as compared to the no peptide control ($p<0.001$) (**Figure 5.3A**). Comparison of the APs to the P1 control showed that AP201m and AP203d caused a significant increase in phagocytosis at all concentrations tested (**Figure 5.3B**) while AP201d, AP200m, and AP202d showed a significant increase at some concentrations (**Supplementary Figure 5.2**).

.

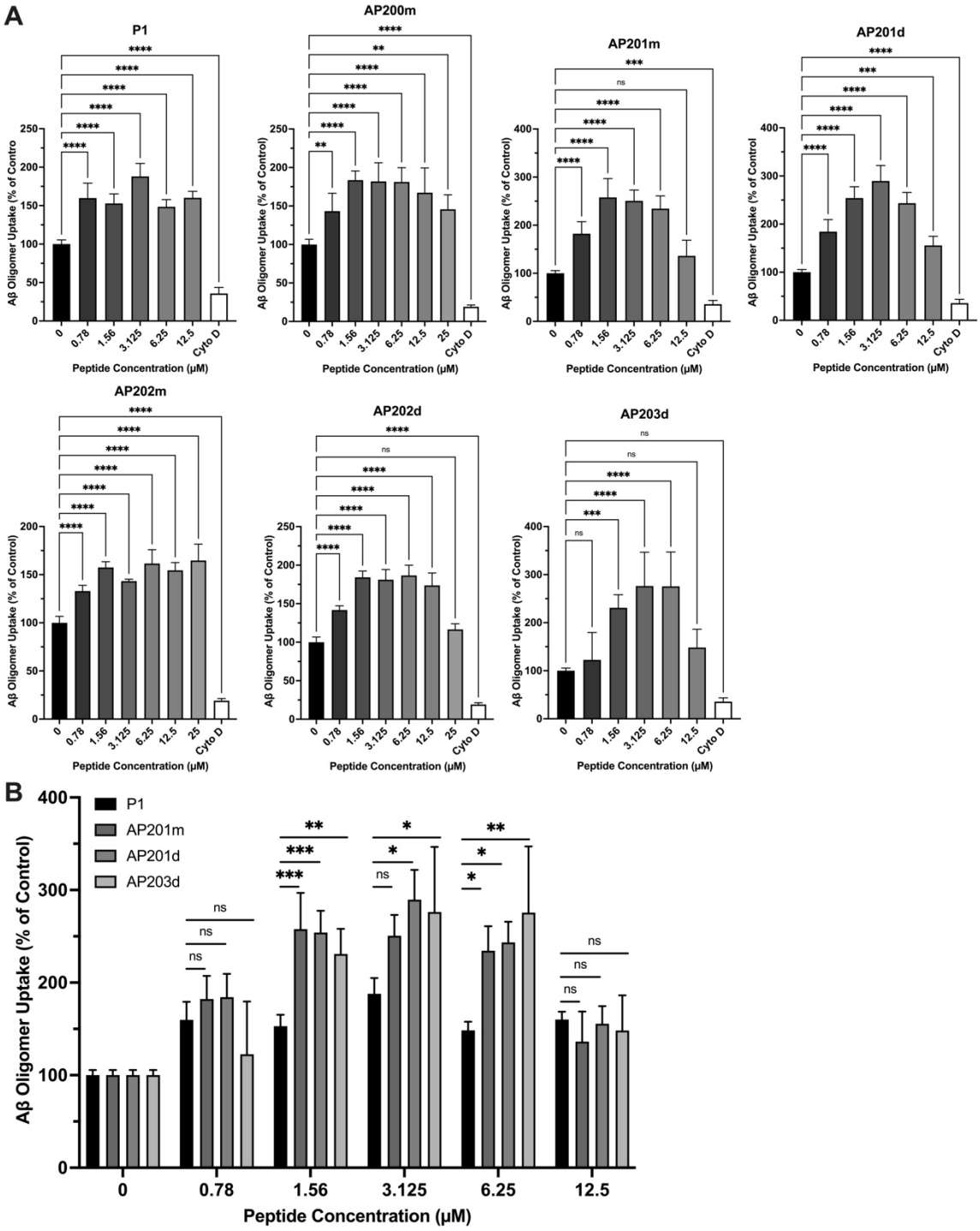

Figure 5.2: APs increased Aβ oligomer uptake by RAW 264.7 murine macrophages. The APs dose-dependently enhance the phagocytosis of Aβ1-42 oligomers in RAW264.7 macrophages. **A)** All APs except for AP203d significantly stimulated phagocytosis as compared to the no-peptide control at concentrations of 0.78 μM. **B)** Comparison of phagocytosis by AP concentration also yielded significantly increased uptake as compared to the P1 control peptide for AP201m, AP201d, and AP203d at concentrations between 1.56 and 6.25 μM. Values are the mean ± SD for n=4 for peptide conditions and n=8 for the control cells.

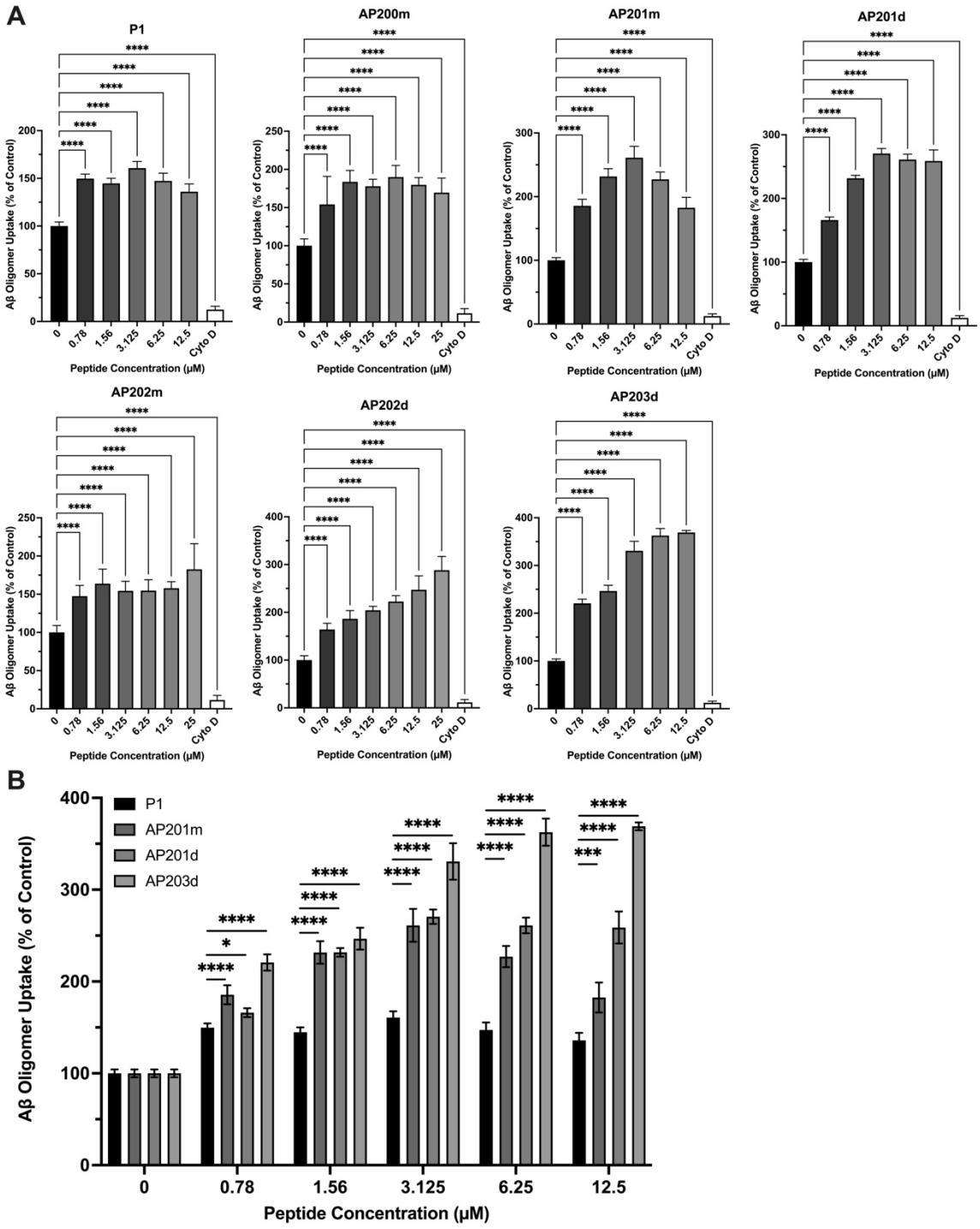

Figure 5.3: APs increased Aβ oligomer uptake by N9 cells. A) Comparison of the APs to the no-peptide control demonstrated that all peptides significantly increased phagocytosis at all concentrations between 0.78 and 25 μM. **B)** Additionally, comparison of AP201m, AP201d, and AP203d to the P1 control showed a significant increased at all concentrations. Values are the mean ± SD for n=4 for peptide conditions and n=8 for the control cells.

5.3.4 APs enhance phagocytosis through interaction with TREM2

After assessing the effect of the APs on phagocytosis by macrophage and microglial cells, we utilized HEK293 cells co-expressing TREM2 and DNAX-activating protein of 12 kDa (DAP12). Four APs (AP200m, AP201m, AP202m, and AP202d) significantly enhanced the phagocytosis of the Aβ oligomers as compared to the no peptide cell control at all concentrations, while AP201d and AP203d enhanced phagocytosis at some concentrations (**Figure 5.4A**). Next, comparison of the APs with the P1 control showed that AP201m, AP201d, and AP203d caused a significant increase in phagocytosis, with AP203d showing the greatest increase in phagocytosis at all but one peptide concentration (**Figure 5.4B**). Of note, the 12.5 μM AP203d condition for the engineered HEK293 cells showed the greatest increase in oligomer uptake of all peptide and cell combinations at 605%. The effect of the APs on toxic Aβ oligomer phagocytosis for all three cell types is summarized in **Table 5.1**. Statistical significance, or lack thereof, is noted for all APs as compared to both the no peptide condition and to the P1 control.

As the APs stimulated phagocytosis of Aβ oligomers in engineered HEK293 TREM2/DAP12 cells, we then investigated whether the peptides were interacting with TREM2 via biolayer interferometry (BLI). Human recombinant TREM2 was immobilized on streptavidin BLI biosensors and tested for direct binding with different APs. Example binding kinetics are shown for AP201d (**Supplementary Figure 5.4A**), which yielded a dissociation constant (K_D) of 190 nM (**Supplementary Figure 5.4A**) showing a high binding affinity of AP201d for TREM2. All additional APs demonstrated an interaction with comparable TREM2 binding affinities (**Table 5.2**) confirming a direct interaction between TREM2 and APs.

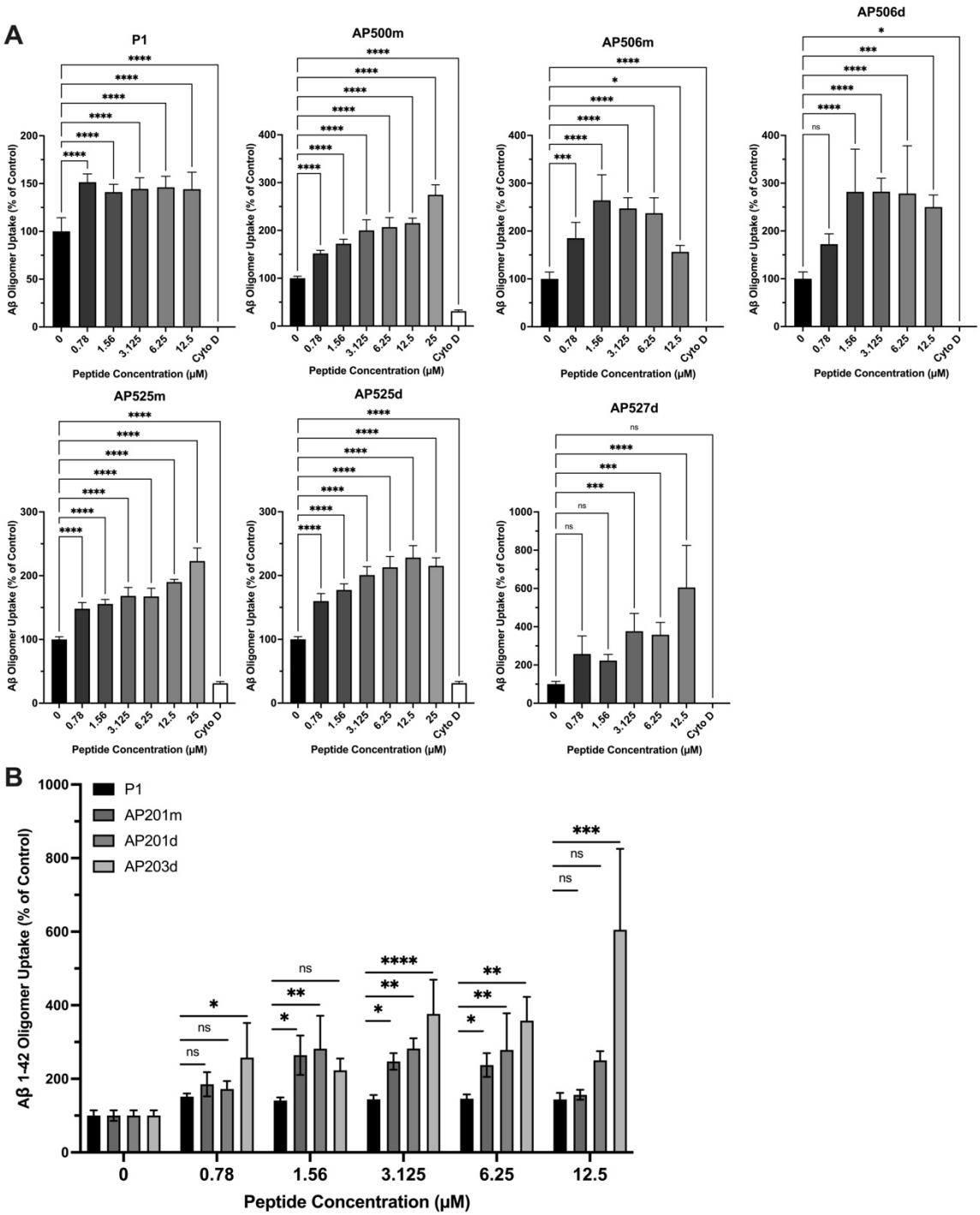

Figure 5.4: APs promoted Aβ oligomer uptake by engineered HEK293 cells. A) AP200m, AP201m, AP202m, and AP202d significantly stimulated the phagocytosis of Aβ oligomers at all concentrations. AP201d and AP203d caused a significant increase at some concentrations. **B)** Comparison of the phagocytic effect of the APs with the P1 control showed that AP203d caused a significant increase in the uptake of Aβ1-42 oligomers at all concentrations while AP201m and AP201d caused a significant increase at concentrations between 1.56 μM and 6.25 μM. Values are the mean ± SD for n=4 for peptide conditions and n=8 for the control cells.

5.3.5 APs do not stimulate pro-inflammatory cytokine expression in microglial cells in vitro

We then tested whether administration of the APs activated microglial cells. N9 microglia were treated with various APs alone or in combination with Aβ oligomers for 24 hours. Lipopolysaccharide (LPS) was used as a positive control for activation of microglial cells. The media surrounding the cells was collected 24-hour after the different treatments and analyzed for cytokine levels (IFNγ, TNFα, IL1β, IL12, IL6, and KC/GRO) by electrochemiluminescence using multiplex ELISA. None of the APs stimulated the production of cytokines. In contrast, LPS significantly enhanced the production of cytokines as expected. Data for IFNγ and IL1β are shown in **Supplementary Figure 5.5** as representative cytokines.

		0.78 µM		1.56 µM		3.125 µM		6.25 µM		12.5 µM		25 µM	
Peptide	Cell Type	0	P1	0	P1	0	P1	0	P1	0	P1	0	P1
AP200m	RAW264.7	**	ns	****	ns	****	ns	****	ns	****	ns	**	
	N9	****	ns	****	**	****	ns	****	***	****	*	****	
	HEK293	****	ns	****	ns	****	ns	****	ns	****	ns	****	
AP201m	RAW264.7	****	ns	****	****	****	ns	****	**	ns	ns		
	N9	****	*	****	****	****	****	****	****	****	**		
	HEK293	***	ns	****	**	****	**	****	ns	*	ns		
AP201d	RAW264.7	****	ns	****	****	****	**	****	**	***	ns		
	N9	****	ns	****	****	****	****	****	****	****	****		
	HEK293	ns	ns	****	***	****	***	****	**	***	ns		
AP202m	RAW264.7	****	ns	****	ns	****	ns	****	ns	****	ns	****	
	N9	****	ns	****	ns	****	ns	****	ns	****	ns	****	
	HEK293	****	ns	****	ns	****	ns	****	ns	****	ns	****	
AP202d	RAW264.7	****	ns	****	ns	****	ns	****	ns	****	ns	ns	
	N9	****	ns	****	**	****	***	****	****	****	****	****	
	HEK293	****	ns	****	ns	****	ns	****	ns	****	ns	****	
AP203d	RAW264.7	ns	ns	****	***	****	**	****	****	ns	ns		
	N9	****	****	****	****	****	****	****	****	****	****	****	
	HEK293	ns	**	ns	ns	***	****	***	****	****	****		

Table 5.1: Summary of effect of APs on phagocytosis of Aβ1-42 oligomers. Results of an ANOVA with post-hoc comparisons and Bonferroni correction are shown for each peptide and cell combination with comparisons to both the cell only control and to the P1 random coil peptide. While all APs caused an increase in phagocytosis, AP201m, AP201d, and AP203d consistently showed the largest effect against the control and P1. P-values are indicated as follows: *ns* = not significant; * $p < 0.05$; ** $p < 0.01$, *** $p < 0.001$, **** $p < 0.0001$.

5.3.6 Immunofluorescence microscopy of Aβ oligomers in microglial cells in vitro

Next, the phagocytosis of fluorescently labelled Aβ oligomers in microglial cells was analyzed by laser confocal microscopy. The N9 cells, with labeled Aβ oligomers as previously described, were washed, fixed in formaldehyde and counterstained with fluorescently labelled phalloidin and DAPI to visualize F-actin to reveal cellular contour and nuclei, respectively. The Aβ oligomers were effectively internalized in the cytosol of N9 microglial cells (**Figure 5.5A**). To address interactions between the oligomers and APs, the uptake of fluorescently labelled Aβ42 oligomers in the presence of CY5-fluorescently labelled AP5 and AP201d peptides by N9 microglia was then monitored. The Aβ42 oligomers and APs were internalized in the cytosol of N9 microglia (**Figure 5.5B**). As expected, Cyto D significantly prevented the internalization of Aβ oligomers and the APs. Furthermore, very good colocalization was observed between Aβ oligomers and the APs.

Sample ID	K_D (M)	k_{on} (1/Ms)	k_{on} Error	k_{dis} (1/s)	k_{dis} Error	k_{obs} (1/s)	Full R^2
AP200m	5.69E-09	116300	5418	0.000662	3.31E-05	0.001798	0.444631
AP201m	3.73E-06	312.6	33.4	0.001165	2.25E-05	0.001168	0.924727
AP201d	1.89E-07	4127	88.37	0.000779	1.72E-05	0.00082	0.927093
AP202m	4.57E-07	2604	98.12	0.00119	3.58E-05	0.001216	0.724712
AP202d	2.93E-07	7460	205.8	0.001781	3.07E-05	0.001854	0.776978
AP203d	8.28E-08	10370	212.8	0.000859	1.48E-05	0.00096	0.922874

Table 5.2: Summary of biolayer interferometry data. Steady-state affinity values determined from BLI experiments indicated strong binding affinity of TREM2 and the APs. A representative binding kinetics curve for AP201d is presented in **Supplementary Figure 5.4**.

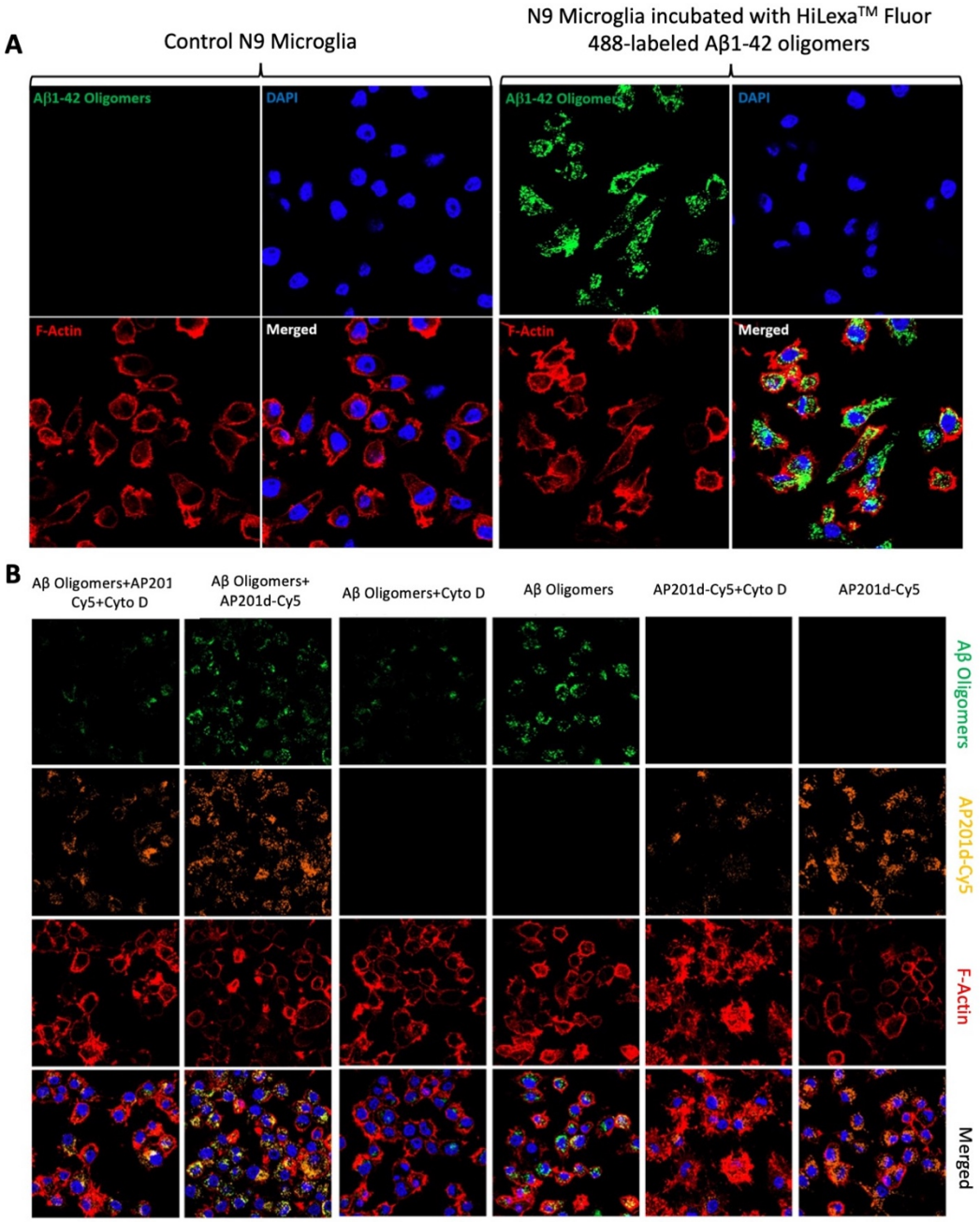

Figure 5.5: Confocal microscopy reveals internalization of Aβ oligomers and colocalization of APs and Aβ oligomers within N9 microglial cells. A) Confocal images of Aβ42 oligomers (green), F-actin (red) and DAPI (blue) are shown. N9 cells were incubated with Aβ oligomers (β-Amyloid (1-42), HiLexa™ Fluor 488-labeled (green). F-actin filaments were labeled with Dylight 554 phalloidin (red) and nuclei were stained with DAPI (blue). The merged images show internalization of Aβ oligomers. **B)** Confocal images of N9 cells incubated with fluorescently labeled Aβ oligomers (green), AP201d-Cy5 (orange), F-actin filaments (red), and nuclei stained with DAPI (blue) are shown for individual channels and merged channels as indicated in the top of the photomicrograph panel. The yellow signal on the merged channels depicts Aβ oligomers that are colocalized with AP201d-Cy5. The phagocytosis inhibitor Cyto D was used as control to verify phagocytic uptake.

Finally, the extensive colocalization between Aβ oligomers and the APs in microglial cells was further examined by 3D confocal microscopy with confocal planes acquired every 0.5 mm along the z-axis of microglial cells (**Figure 5.6**). Green and orange fluorescence indicated localization of Aβ oligomers and the AP, respectively, in the individual FITC and CY5 channels. The confocal planes examined showed that both peptides (AP5 and AP201d) were internalized in the same compartments as the toxic Aβ oligomers, as revealed by yellow fluorescence in the merged channels.

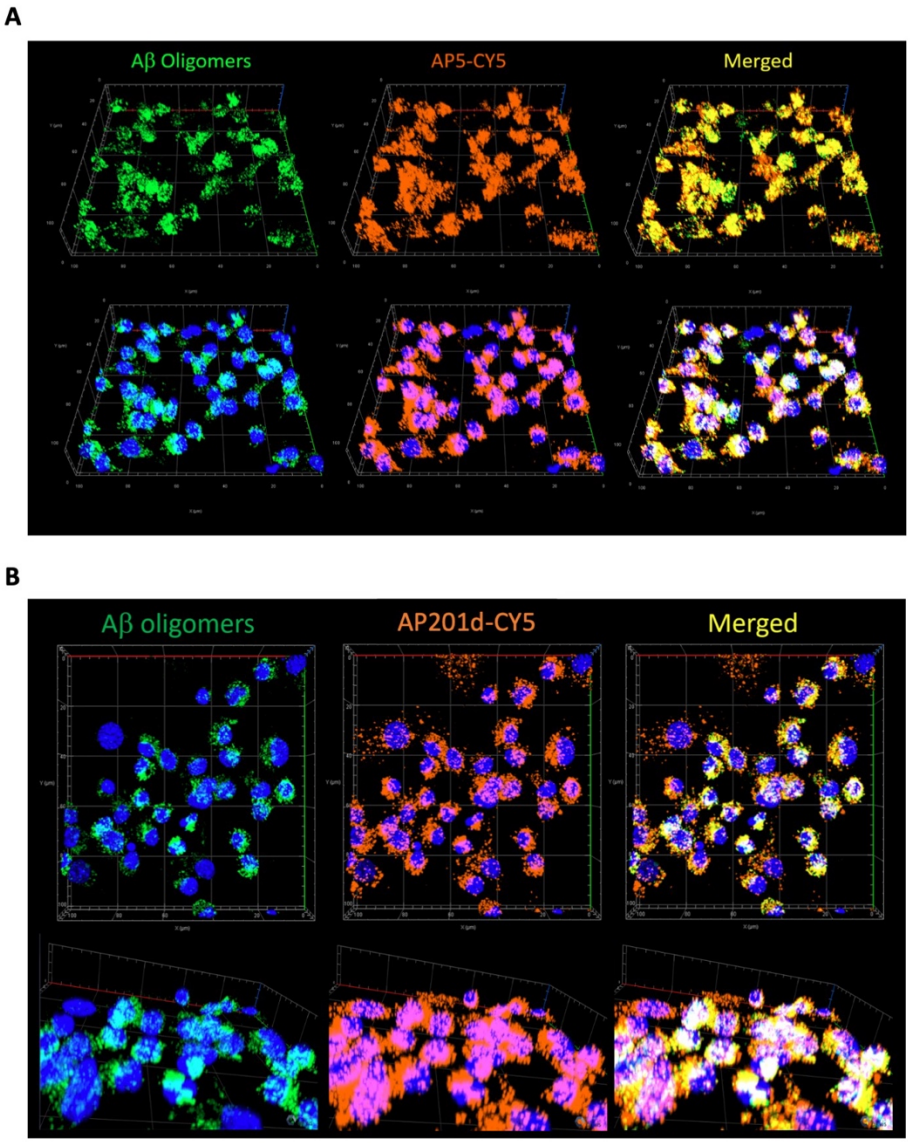

Figure 5.6: 3-Dimensional (3D) confocal microscopy indicates colocalization of Aβ oligomers with APs in N9 microglia cells. N9 microglia were cotreated with Aβ oligomers and **A)** AP5-Cy5 or **B)** AP201d-Cy5 for 4 hours. Laser confocal planes were acquired every 0.5 μm along the z-axis of microglial cells. The top panel (view from the top of the cells) and bottom panel (view from the side of the cells) show 3D images obtained by laser scanning confocal microscopy. Nuclei were stained with DAPI (blue fluorescence). Green and orange fluorescence indicate localization of Aβ oligomers and the AP respectively in the individual FITC and CY5 channels. Yellow fluorescence reveals the colocalization of Aβ oligomers with AP5 or AP201d in the merged channels.

5.4 Discussion

The goal of this study was to investigate the effect of various α-sheet peptides on phagocytosis by two different cell types, macrophages and microglia. An increase in phagocytosis of both *E. coli* particles and Aβ oligomers was observed for all APs tested. Additionally, the APs had a high-affinity interaction with the phagocytic receptor TREM2 and did not activate inflammatory cytokines in microglial cells.

The effect of the APs on phagocytosis was assessed first against *E. coli* particles and then with Aβ oligomers. In both assays, all peptides increased phagocytosis at a range of concentrations. Notably, the enhanced phagocytic effect was seen in three distinct cell types, suggesting the effect is not cell specific and is occurring through common cell surface pathways. In all three cell types, a statistically significant increase in phagocytosis was seen even at the lowest concentration (0.78 μM) for all APs, except for AP201d and AP203d. A dose-dependent increase in phagocytosis was also seen for most AP and cell combinations, although often only up to a concentration of 3.125 μM, suggesting that APs may be phagocytosed and compete with the internalization of Aβ oligomers when used in excessive concentrations. The increase in phagocytosis induced by APs was also statistically significant when compared to the P1 random coil peptide, particularly in the N9 cell type and for AP201m, AP201d, and AP203d.

Additionally, the enhanced phagocytosis was seen across the seven APs tested: four monomers and three dimers. It was hypothesized that the dimeric form of a peptide would

outperform the monomer due to increased α-sheet surface area. In the two cases of direct comparison, between AP201m and AP201d and AP202m and AP202d, the results were comparable, although the dimeric peptides tended to perform better than the monomers at higher concentrations.

Importantly, the engineered HEK293 cells confirmed the hypothesized mechanism for increased phagocytic activity as occurring via interaction between APs and TREM2. The modified cell line does not contain any additional phagocytic receptors. Interestingly, HEK293 cells are non-phagocytic but the co-expression of TREM2 and DAP12 in these cells is sufficient to convert HEK293 cells into phagocytic cells [194]. This provided a unique tool to assess selectively TREM2-dependent phagocytic activity. The increase in phagocytosis triggered by APs in these cells shows that the APs are stimulating TREM2 dependent phagocytosis and may be directly interacting with TREM2.

The high affinity interaction of APs with TREM2 was further substantiated by biolayer interferometry data. This suggests the APs may enhance the phagocytosis of Aβ oligomers by triggering TREM2 signaling as engineered HEK293 cells co-express only the phagocytic TREM12/DAP12 receptor. Additionally, the binding affinity (K_D) of the different APs for TREM2 was comparable to the binding affinity of lipidated Apolipoprotein E, a known ligand for TREM2 [196].

The APs, at concentrations that stimulate Aβ phagocytosis, did not activate N9 microglial cells as quantified by the null values for IFNγ, TNFα, IL1β, IL12, and IL6. This indicates that the mechanisms that regulate microglial activation and phagocytosis are distinct, as we previously described [20]. It is critical that the APs do not activate microglial cells or trigger the release of inflammatory cytokines that could contribute to chronic neuroinflammation, a key aspect of

neurodegenerative diseases [197]. While it was originally thought that sustained inflammatory response in the brains of AD patients was a reaction to the neuronal loss caused by the disorder, there is growing evidence that a chronic immune response also exacerbates AD pathological lesions [197]. Thus, it is crucial that any potential AD therapeutics that enhance Aβ clearance through microglial phagocytosis do not cause additional neuroinflammation by stimulating microglial activation.

5.5 Conclusion

Previous studies demonstrated that α-sheet peptides bind and neutralize toxic Aβ oligomers. Here, we demonstrated that administration of seven APs increased phagocytosis of Aβ oligomers by macrophages and microglial cells. The use of an engineered HEK293 cell line demonstrated that the increased Aβ uptake was mediated by binding of the APs to TREM2, which was further supported by biolayer interferometry data. Critically, inflammatory cytokines were not activated by the APs showing that phagocytic clearance of toxic Aβ oligomers can be enhanced without inducing microglial activation. This work provides a basis for an increased understanding of the mechanisms that contribute to the clearance of toxic Aβ oligomers by APs, highlighting their therapeutic potential in neurodegenerative diseases.

5.6 Materials and Methods

5.6.1 Statistics

All values of statistical significance reported were calculated with one-way ANOVA with post hoc comparisons as shown and a Bonferroni multiple comparison correction performed in GraphPad Prism Version 10.1.0. A single asterisk indicates a *p*-value less than 0.05, which is the

cutoff to be considered statistically significant. Two asterisks indicate greater significance, with a *p*-value less than 0.01. Three asterisks indicate a *p*-value less than 0.001. Four asterisks indicate a *p*-value less than 0.0001.

5.6.2 Synthesis and Preparation of α-Sheet Peptides

Synthetic α-sheet peptide inhibitors were designed *in silico* as previously described [6, 8, 9, 54]**,** using backbone dihedral angle constraints derived from MD simulations [103, 158] and synthesized as previously described by Bleem, et al [9]. Briefly, peptides contain two α-strands of seven residues each, with amino acids alternating sequentially between L-conformation and D-conformation in each of the strands. The α-strands are connected by a five residue turn comprised of all L-amino acids or all D-amino acids, which gives the peptide a hairpin shape. Finally, the tail of each strand consists of a Gly and an Arg residue, followed by acetyl and amide caps at the N- and C-terminus, respectively. Peptides were assembled by solid phase peptide synthesis on Rink amide resin with Fmoc chemistry and HBTU activation using the Liberty Blue Microwave Peptide Synthesizer (CEM Corporation; Charlotte, NC). Peptides were cleaved from the resin and side chain deprotected by TFA/TIPS/H2O (95:2.5:2.5) and precipitated by cold ether. Crude peptides were purified to >95% by RP-HPLC using 5 μM C12 or C18 130 Å columns (Waters Corporation; Milford, MA) and atomic masses were confirmed by electrospray mass spectrometry on a Bruker Esquire Ion Trap (Bruker; Billerica, MA). All peptides were lyophilized after purification and stored at -20 or -80°C until use.

For dimeric peptides, purified and lyophilized monomer was dissolved in 1 mL of DMSO per 100 mg of peptide before resin cleavage.19 mL of carbonate buffer at pH 9.6 was then added per mL of DMSO. The solution was covered in parafilm with holes to allow for airflow and stirred

for 4 hours at 37°C, followed by 48 hours at room temperature. Crude peptides were then purified again to >95% by RP-HPLC using 5 μM C12 or C18 130 Å columns (Waters Corporation; Milford, MA) and atomic masses were confirmed by electrospray mass spectrometry on a Bruker Esquire Ion Trap (Bruker; Billerica, MA). Dimers were lyophilized after purification and stored at -20 or -80°C until use.

5.6.3 Cell Cultures

Murine microglia cell line N9 [198] and RAW264.7 murine macrophage (ATCC RAW 264.7) (ATCC; Manassas, VA) cell lines were maintained in Dulbecco's modified Eagle's medium (DMEM) + GlutaMAX™ (Life Technologies; Carlsbad, CA) with 10% (v/v) fetal calf serum and 100 U/ml penicillin, 100 μg/ml streptomycin. HEK293 TREM2/DAP12 cells were generated as we previously described [194] and were grown in the same medium supplemented with G418 (Thermo Fisher Scientific; Waltham, MA) at 100 mg/ml.

5.6.4 Preparation of Fluorescent Aβ1-42 Oligomers

Lyophilized β-Amyloid (1-42) peptide, HiLexa™ Fluor 488-labeled (AnaSpec Inc.; Fremont, CA) was dissolved with hexafluoro isopropanol (HFIP) (1 mg peptide in 1 mL of ice cold HFIP) and allowed to dry under a fume hood for approximately one hour at room temperature, then completely dried using a Speedvac. 100 μg of HFIP treated Aβ was then dissolved in 50 μL of 0.6 N NaOH. After dissolution in NaOH, Aβ was further diluted with PBS to a concentration of 100 μM and incubated at room temperature for 48 hours to allow the formation of Aβ oligomers.

5.6.5 Phagocytosis Assays

All cells were plated at a density of 100,000 cells in 96-well cell culture plates and cultured for 24 hours after plating prior to start the phagocytosis experiments. pHrodo *Escherichia coli* bioparticles were dissolved in live cell imaging buffer (Invitrogen; Carlsbad, CA) at a concentration of 1 μg/ml and α-sheet peptides and incubated at 37°C with the different cell lines in a Biotek Synergy HT reader. The uptake of *E. coli* bioparticles was measured by quantifying fluorescent emission (Excitation: 560 nm/Emission: 585 nm) every 10 minutes for 2 hours. Phagocytosis was quantified by measuring the average amount of bioparticles uptake in mFU/min during the 2-hour incubation period.

For the measurement of Aβ oligomer phagocytosis in RAW264.7 and N9 cells, cells were incubated with 200 nM 488-Aβ oligomers (β-Amyloid (1-42), HiLexa™ Fluor 488-labeled; AnaSpec Inc.; Fremont, CA) and a range of doses of the different α-sheet peptides for 4 hours in a cell culture incubator (37°C and 5% CO_2). The uptake of fluorescently labelled Aβ oligomers was measured by quantifying fluorescent emission (Excitation: 488nm/Emission: 525nm) after 4 hours of incubation using a Biotek Synergy HT reader. For the measurement of Aβ oligomer phagocytosis in HEK293 TREM2/DAP12. Cells were incubated with 200 nM 488-Aβ oligomers (β-Amyloid (1-42), HiLexa™ Fluor 488-labeled; AnaSpec Inc.; Fremont, CA) and a range of doses of the different α-sheet peptides for 24 hours in a cell culture incubator (37°C and 5% CO_2). The uptake of fluorescently labelled Aβ oligomers was measured by quantifying fluorescent emission (Excitation: 488nm/Emission: 525nm) after 24 hours of incubation using a Biotek Synergy HT reader. Phagocytosis was quantified by measuring the average amount of fluorescent Aβ oligomers uptake in mFU. The fluorescence of the mixture of Aβ oligomers and α-sheet peptides that was added to the culture medium was quantified and used to standardize the fluorescent measurements.

The uptake of fluorescent Aβ oligomers was then expressed as a percentage of the values observed in the control conditions when no α-sheet peptide was added.

5.6.6 Biolayer Interferometry

Kinetic determination of interactions between APs and TREM2 were performed on an Octet RED96 instrument (ForteBio (Pall); Menlo Park, CA). Biotinylated-human TREM2 (Acro Biosystems; Newark, DE) was first loaded near saturation (4000 seconds of loading at a concentration of 3 μg/ml in PBS) on Super Streptavidin sensors (SSA, (ForteBio (Pall); Menlo Park, CA)) which were then washed 3 times in PBS prior to be transferred to fresh PBS for baseline measurement (60 seconds). The SSA sensors were then associated with different concentrations of APs (ranging from 9.77 nM to 10000 nM) for 300 seconds and then transferred to PBS for dissociation for 600 seconds. Binding kinetics were performed at 30°C with a data acquisition rate of 10 Hz. Constant of association (k_{on}), constant of dissociation (k_{dis}) and equilibrium constant of dissociation (K_D) values were determined by global fitting of the binding kinetics applying a 1:1 interaction model using the ForteBio data analysis software (ForteBio (Pall); Menlo Park, CA).

5.6.7 Cytokine Assay

Confluent N9 cells (plated in a 96-well cell culture plate) were treated for 24 hours with different AP5s at a concentration of 2 μM either alone or in combination with 200 nM of Aβ oligomers. LPS 100 ng/mL from *E. coli* (Sigma-Aldrich; St Louis, MO) was used as a positive control to activate N9 microglia. The production of various inflammatory cytokines was analyzed in the culture medium using a V-PLEX Proinflammatory Panel mouse kit (IFNγ, TNFα, IL1β,

IL12, IL6 and KC/GRO) on a MESO QuickPlex SQ120 instrument following the recommendation of the manufacturer (Meso Scale Diagnostics; Rockville, Maryland).

5.6.8 Preparation of N9 Microglial Cells for Laser Confocal Microscopy

N9 cells were incubated with 200 nM Aβ oligomers (β-Amyloid (1-42), HiLexa™ Fluor 488-labeled; AnaSpec Inc.; Fremont, CA), Cy5-AP5 2 μM, Cy5-AP201d 2 μM at 37°C for 4 hours in a cell culture incubator (37°C and 5% CO_2). Cells were also treated with 10 μM cytochalasin D in presence of Aβ oligomers (β-Amyloid (1-42)), HiLexa™ Fluor 488-labeled; AnaSpec Inc.; Fremont, CA), Cy5-AP5 2 μM, Cy5-AP201d 2 μM for 4 hours. Cells were then washed 3 times with PBS and fixed in 4% formaldehyde. F-actin filaments were labeled with Dylight 554 phalloidin (Cell Signaling Technology; Danvers, MA). Stained cells were mounted with ProLong Glass Antifade Mountant with NucBlue stain (Thermo Fisher Scientific; Waltham, MA) and subjected to confocal imaging. Confocal microscopy was carried out using a LSM800 Laser Confocal Scanning Microscope (Carl Zeiss Microscopy; Thornwood, NY) with the ZEN Blue 2.1 software (Carl Zeiss AG; Germany) and a 63x oil differential interference contrast objective (1.40 Oil DIC M27) objective. For 3D confocal microscopy, a z-step size of 0.5 μm was used and around 30 to 35 confocal planes were acquired depending on the volume of the microglial cells.

5.7 Supplementary Information

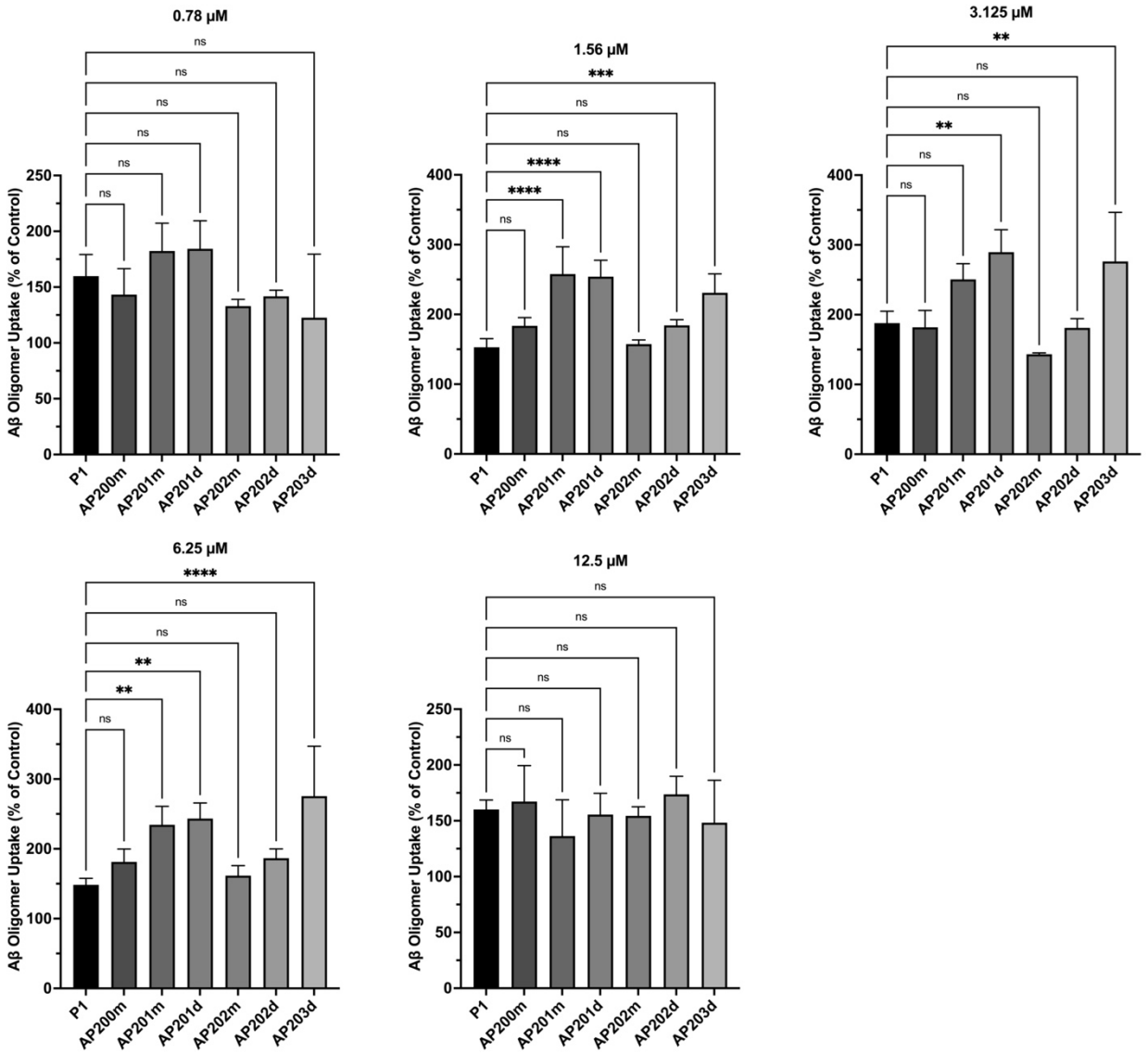

SI Figure 5.1: Aβ oligomer uptake by RAW 264.7 murine macrophages. Comparison of the phagocytic effect of all APs on Aβ1-42 in RAW264.7 macrophages to the P1 random coil peptide control. Values are the mean ± SD for n=4 for peptide conditions and n=8 for the control cells.

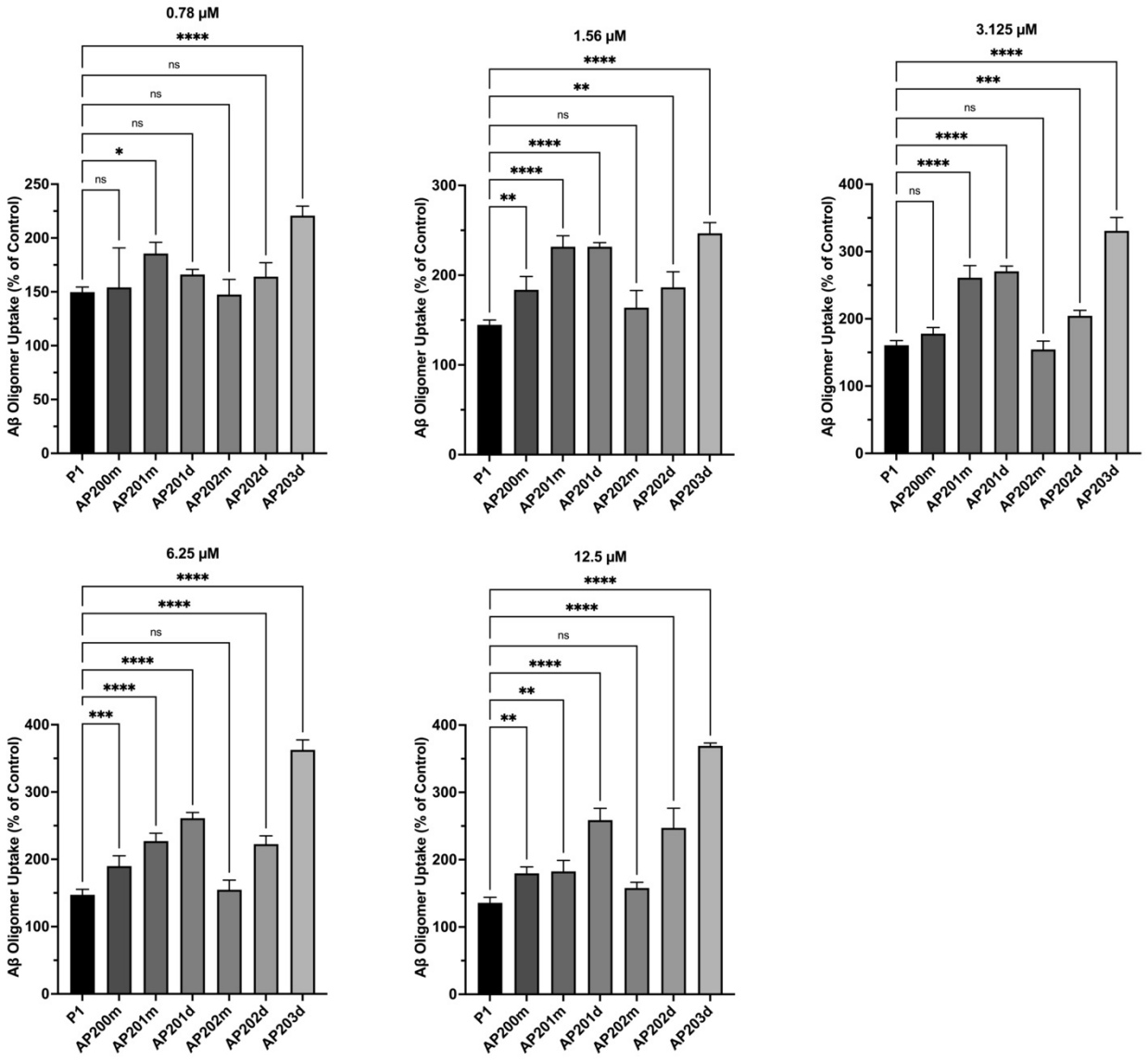

SI Figure 5.2: Aβ oligomer uptake by N9 cells. Comparison of the phagocytic effect of all APs on Aβ1-42 in N9 microglial cells to the P1 random coil peptide control. Values are the mean ± SD for n=4 for peptide conditions and n=8 for the control cells.

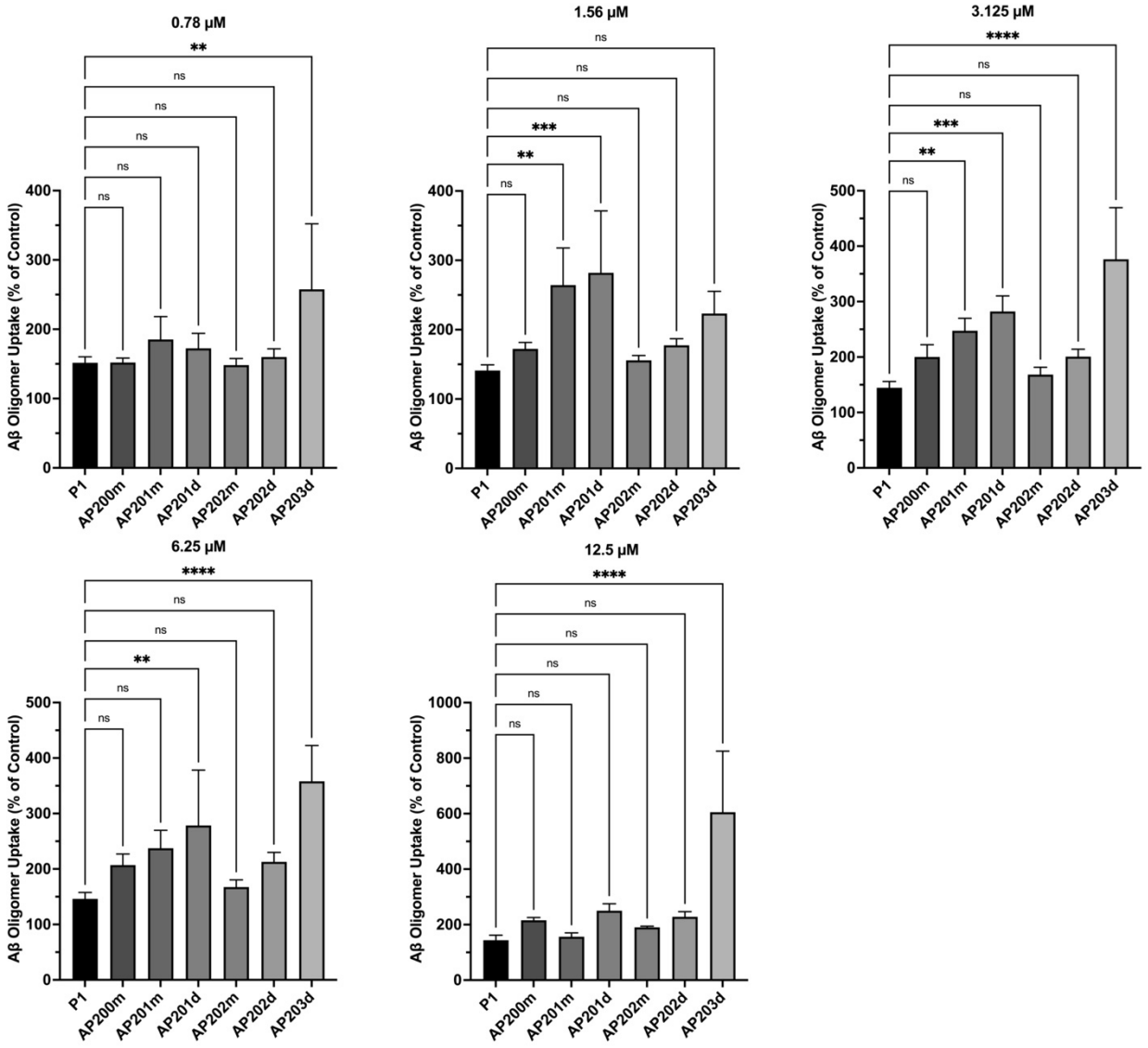

SI Figure 5.3: Aβ oligomer uptake by engineered HEK293 cells. Comparison of the phagocytic effect of all APs on Aβ1-42 in HEK293 cells to the P1 random coil peptide control. Values are the mean ± SD for n=4 for peptide conditions and n=8 for the control cells.

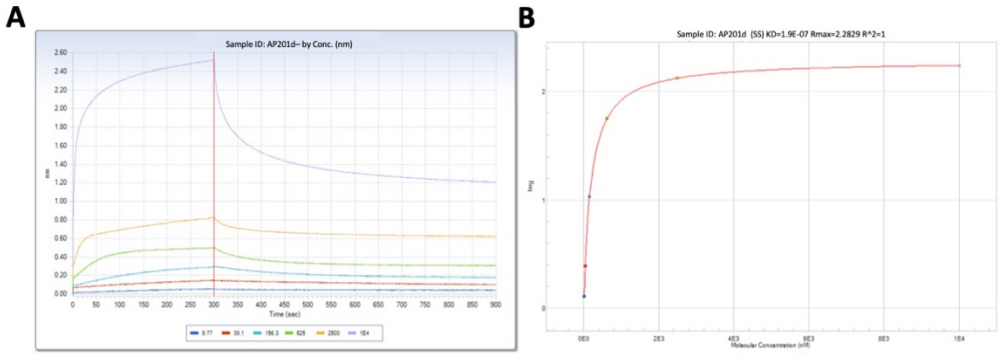

SI Figure 5.4: Biolayer interferometry indicated an interaction between the APs and human recombinant TREM2. Representative biolayer interferometry data for AP201d is shown with additional AP data summarized in **Table 5.2**. **A)** Biotinylated human TREM2 was immobilized on super streptavidin biosensors that were dipped in wells containing a dose range of AP201d from 9.77 nM to 10 μM. The duration of the association was 300 seconds. The sensors were then dipped in PBS to dissociate the AP201d peptide from TREM2 for 600 seconds. **B)** Steady-state affinity values derived from the experiment revealed relatively strong binding affinity of TREM2 to AP201d with a dissociation constant (K_D) of 189 nM.

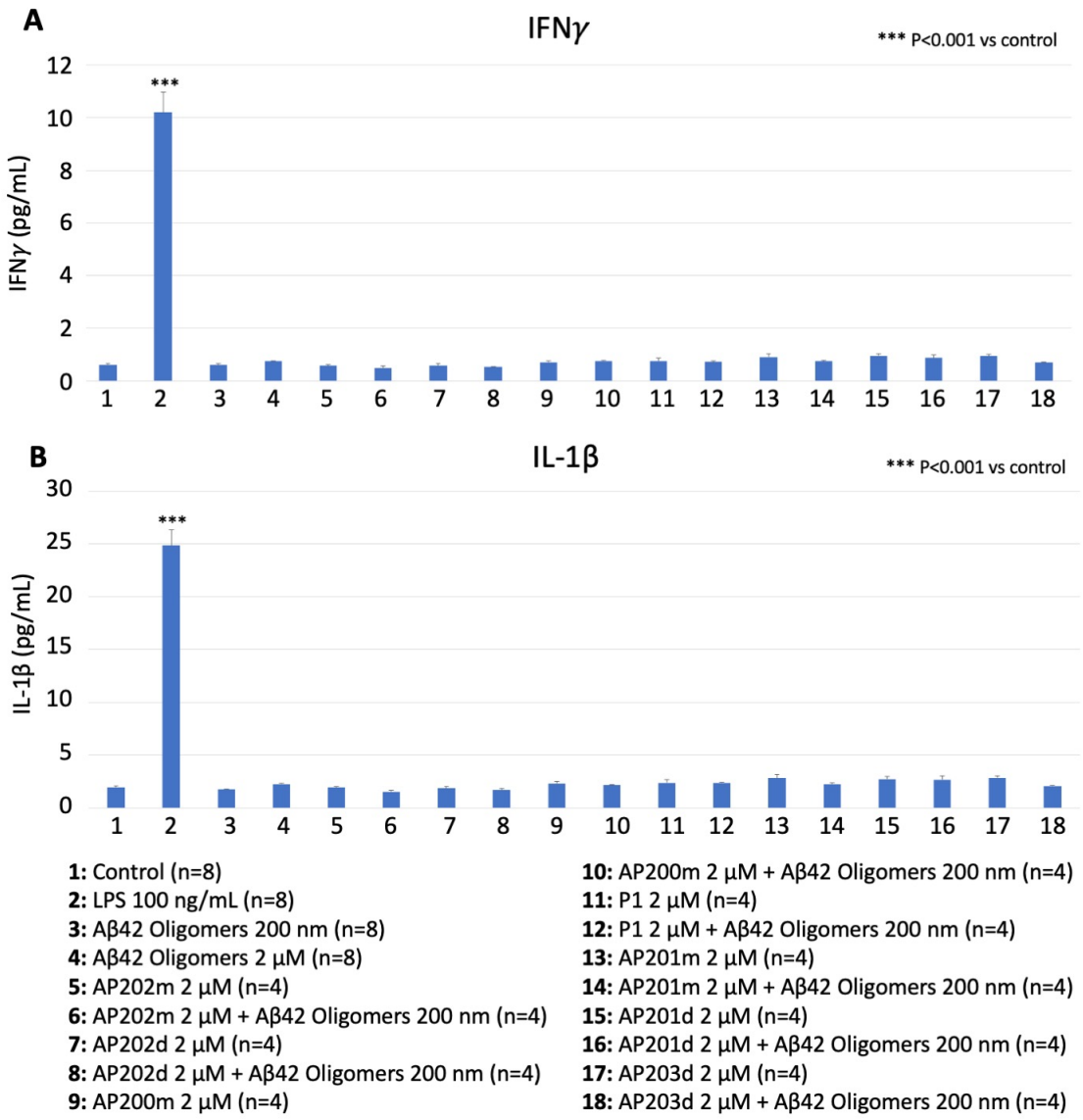

SI Figure 5.5: Cytokine analysis. α-Sheet peptides do not affect the production of **A)** interferon-gamma (IFNγ) and **B)** interleukin-1β (IL-1β) by N9 microglia cells. N9 microglia were treated for 24 hours with the different α-sheet peptides either alone or in combination with Aβ oligomers as indicated in the figure legend of the histograms. Cytokines were quantified by electrochemiluminescence. Analysis by ANOVA showed a significant effect of LPS on cytokine production for all the cytokines (IFNγ, TNFα, IL1β, IL12, IL6 and KC/GRO) tested ($p<0.001$) but no significant effect ($p>0.05$) of the different APs, alone or in combination with Aβ oligomers.

Chapter 6. Effects of Intracranial Injections of α-Sheet Peptides and Aβ Oligomers on the Cognitive Behavior and Soluble Tau Hyperphosphorylation in Tg Tau P301S Mice

6.1 Abstract

Designed α-sheet peptides decrease β-amyloid (Aβ) levels in both *in vitro* and *in vivo* Alzheimer's disease (AD) models through specific binding of low molecular weight toxic Aβ oligomers. The modified AD cascade hypothesis suggests that these toxic oligomers may initiate AD pathogenesis and downstream effects including tau protein hyperphosphorylation. This is highlighted through studies demonstrating that the intracranial infusion of Aβ oligomers affects the propagation of the tau pathology in transgenic mouse models overexpressing tau protein. Tg Tau P301S mice overexpress human tau protein and progressively develop neurodegeneration. Here, we performed bilateral intrahippocampal injections of soluble Aβ1-42 oligomers, of the synthetic α-sheet peptide AP506d, or co-injections of AP506d+Aβ oligomers to study the effects of Aβ oligomers on the propagation of tau pathology and to determine whether AP506d can neutralize the impact of Aβ oligomers in Tg Tau P301S mice. The α-sheet peptide AP506d was well tolerated and did not induce any learning or memory deficit in the mice. However, AP506d had no statistically significant impact on the learning and memory deficits induced by Aβ oligomers, although some positive trends were observed. Western blot analysis of two tau antibodies, PH1 and DA9, showed that co-injections of AP506d+Aβ oligomers resulted in a reduction of tau phosphorylation for both human and murine tau compared to Tg Tau P301S mice intracranially injected with Aβ oligomers only. Finally, neuroinflammation was observed in brain

homogenates from Tg Tau P301S mice as compared to wild-type mice but the intracranial injections of Aβ oligomers and AP506d did not significantly affect cytokine levels.

6.2 Introduction

Alzheimer's Disease (AD) affects over 50 million people worldwide and estimates predict that this number will grow to 150 million by 2050 [28]. AD is characterized by extracellular amyloid plaques and intracellular neurofibrillary tangles in the brain but diagnosed by progressive and irreversible memory loss and cognition changes.

The accumulation of the β-amyloid peptide (Aβ) outside of neurons is a hallmark of AD. Monomeric Aβ is involved with critical biological functions such as memory, learning, and neuroprotection [29-32]. The modified amyloid cascade hypothesis posits that accumulation of soluble Aβ oligomers, not the resultant amyloid fibrils, is the primary trigger of AD pathogenesis as defined by the production of hyperphosphorylated tau tangles, activation of neuronal death, and dementia [33-37]. There is evidence that the toxic soluble oligomers, not the amyloid burden, are associated with disease progression and that damage begins prior to amyloid plaque deposition [33-37].

In conjunction with the accumulation of Aβ plaques, hyperphosphorylation of tau is a major contributor to AD. Tau is a microtubule-associated protein involved in microtubule assembly and stabilization [199]. Precise regulation is required to maintain tau structure and function and there are a wide range of neurodegenerative disorders, called tauopathies, resulting from dysregulated phosphorylation of tau. In AD brains, hyperphosphorylated tau form fibrils in neuronal cell bodies, referred to as neurofibrillary tangles (NFTs), leading to cell damage and inflammation.

Previous data have shown that the intracranial infusion of Aβ oligomers can affect the propagation of the tau pathology in transgenic mouse models overexpressing tau [200]. This suggests that soluble Aβ oligomers could be the toxic peptides responsible for the induction of the tau pathology as posited in the modified amyloid cascade hypothesis of AD. It has been shown that a single intracranial injection of Aβ oligomers in mice is sufficient to activate neuronal GSK3b, one of the main tau kinase responsible for tau phosphorylation [201]. In addition, a single intrahippocampal injection of Aβ42 protofibrils has been shown to cause long term memory deficit and anxiety in rats [202]. Interestingly, intrathecal administration of soluble Aβ oligomers also induces persistent tau hyperphosphorylation and a reduction in hippocampal volume 12 weeks after its administration in non-human primates [203, 204], further highlighting that soluble Aβ oligomers can affect the tau pathology *in vivo*.

Critically, the A11 oligomer-specific antibody binds to the oligomeric form of multiple amyloid systems, including the Aβ oligomer, indicating a shared conformation among amyloid species [52]. Atomistic molecular dynamics simulations from the Daggett group revealed a nonstandard secondary structure called α-sheet and demonstrated that unrelated proteins in amyloid diseases form α-sheet structure under amyloidogenic conditions [74, 191, 192]. α-Sheet structure is defined by the alignment of α-sheet carbonyl oxygens on one strand and alignment of the NH groups along the other, instead of alternating as in β-sheets. Identification of α-sheet structure led to the design of a library of novel synthetic α-sheet peptides of both monomer and dimer structure [6, 7]. These α-sheet peptides are numbered and denoted as “AP#m” for monomer peptides and “AP#d” for dimer peptides.

These APs bind to Aβ oligomeric intermediates and inhibit Aβ aggregation *in vitro*, protect against toxicity and recover viability in cells, and inhibit Aβ aggregation in two animal models

[38]. Additionally, in transgenic APPsw mice that express human Aβ, treatment with AP5 caused a dose-dependent reduction in detectable oligomers, with reductions up to 79% [38]. Four APs (AP5, AP90, AP407, and AP421) significantly delayed paralysis due to Aβ in a transgenic *C. elegans* model commonly used to assess the effect of exogenous compounds on Aβ toxicity [38].

It was hypothesized that this AP mediated reduction in toxic Aβ oligomers could be attributed to the APs altering the rate by which toxic Aβ oligomers are phagocytosed, as the APs do not directly impact Aβ production [17]. Subsequent work demonstrated that the administration of seven APs, including AP506d (a dimer peptide), increased phagocytosis of Aβ oligomers by macrophages and microglial cells (**Chapter 5**).

Here, we used transgenic Tg Tau P301S mice (line PS19) to investigate whether AP506d affects the impact of Aβ oligomers on tau pathology *in vivo*. Tg Tau P301S mice overexpress human tau with the P301S mutation and progressively develop neurodegeneration, intraneuronal tau hyperphosphorylation, and aggregation that closely mimics neurofibrillary tangles [205]. We performed bilateral intrahippocampal injections of soluble Aβ1-42 oligomers in Tg Tau P301S mice to study the effects of Aβ oligomers on the propagation of the tau pathology. To assess the effects of AP506d, we stereotaxically injected AP506d alone in both hippocampi of Tg Tau P301S mice. Finally, some Tau P301S mice were co-injected with AP506d and Aβ oligomers to determine whether AP506d can neutralize the impact of Aβ oligomers in Tg Tau P301S mice.

6.3 Results

Figure 6.1 depicts the timeline for the intracranial experiments. 25- to 26-week-old Tg Tau P301S mice were anesthetized with 3% isoflurane in oxygen and placed on a thermoregulated stereotaxic instrument. Intracranial injections of sterile saline, AP506d, Aβ1-42 oligomers, or

AP506d+Aβ oligomers were performed in both hemispheres in the hippocampus of anesthetized mice.

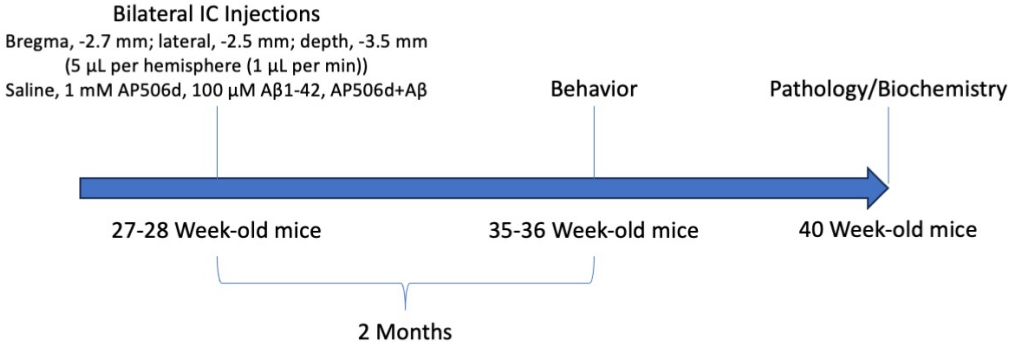

Figure 6.1: Timeline of intracranial injection experiments in Tg Tau P301S mice.

6.3.1 Effects of intracranial injections of AP506d and Aβ oligomers on the behavior of Tg Tau P301S mice

We first examined the cognitive behavior of the mice two months after the intracranial injections. A group of naïve wild-type littermates (WT mice) of the Tg Tau P301S mice (Tg Tau mice) served as a control group. Cognitive behavior was evaluated using the Barnes maze. Acquisition trials were performed during four consecutive days with four trials per day to assess learning behavior with three acquisition measure: primary errors, distance travelled to find target hole, and escape latency. Mice were also subjected to a probe trial 24 hours after the last acquisition trial to investigate possible impairments to memory retention.

A significant effect of time ($p<0.001$) for the number of primary errors was observed for the different treatment groups (**Figure 6.2A**). Thus, all mice learned the task and performed better on Day 4 of the acquisition trials than on Day 1. Analysis across the different days of acquisition did not reveal significant differences between the treatment groups (**Figure 6.2A**). However, a trend for an increased number of primary errors was observed in Tg Tau mice intracranially injected with Aβ oligomers (**Figure 6.2A**), suggesting that this variable is poorly sensitive to

discriminate the different group of mice. A non-significant trend for a reduction of errors was observed in Tg Tau mice intracranially injected with AP506d+Aβ oligomers as compared to Tg Tau mice receiving Aβ oligomers only (**Figure 6.2A**).

Analysis of the distance travelled to find the target hole during the acquisition trials also showed a significant main effect of time ($p<0.001$) (**Figure 6.2B**). Tg Tau mice intracranially injected with Aβ oligomers performed poorly compared to Tg Tau mice intracranially injected with saline or AP506d ($p<0.001$) (**Figure 6.2B**). In contrast, the Tg Tau mice intracranially injected with AP506d performed similarly to Tg Tau mice injected with saline or WT mice (**Figure 6.2B**). A non-significant trend for a reduction in the distance travelled was observed on Day 3 in Tg Tau mice co-injected with AP506d+Aβ oligomers as compared to Tg Tau mice intracranially injected with Aβ oligomers only (**Figure 6.2B**).

Similarly, the cumulative distance, defined as the total sum of the distance of the center point of the mouse to the center of the target hole for each sample of the trials, showed a significant effect of time with a reduction observed for all groups ($p<0.001$) (**Figure 6.2C**). The cumulative distance was significantly higher in Tg Tau mice intracranially injected with Aβ oligomers compared to Tg Tau mice injected with saline or with AP506d ($p<0.001$ for both) (**Figure 6.2C**). No significant effect of the intracranial injection of AP506d was observed (**Figure 6.2C**).

The latency to find the target hole and the velocity of the mice were also significantly reduced as a function of time for all treatment groups ($p<0.001$ and $p<0.02$ for latency and velocity, respectively) (**Figure 6.2D-E**). A significant increase in the escape latency was observed in Tg Tau mice intracranially injected with Aβ oligomers compared to Tg Tau mice injected with saline or AP506d ($p<0.001$) (**Figure 6.2D**). No significant effect of AP506d was observed on the latency to find the target hole (**Figure 6.2D**). Additionally, Tg Tau mice intracranially injected

with Aβ oligomers exhibited a significantly higher velocity as compared to those injected with saline or AP506d (*p<0.001*) (**Figure 6.2E**). No significant effect of the genotype or of AP506d was observed on the velocity of the Tg Tau mice (**Figure 6.2E**).

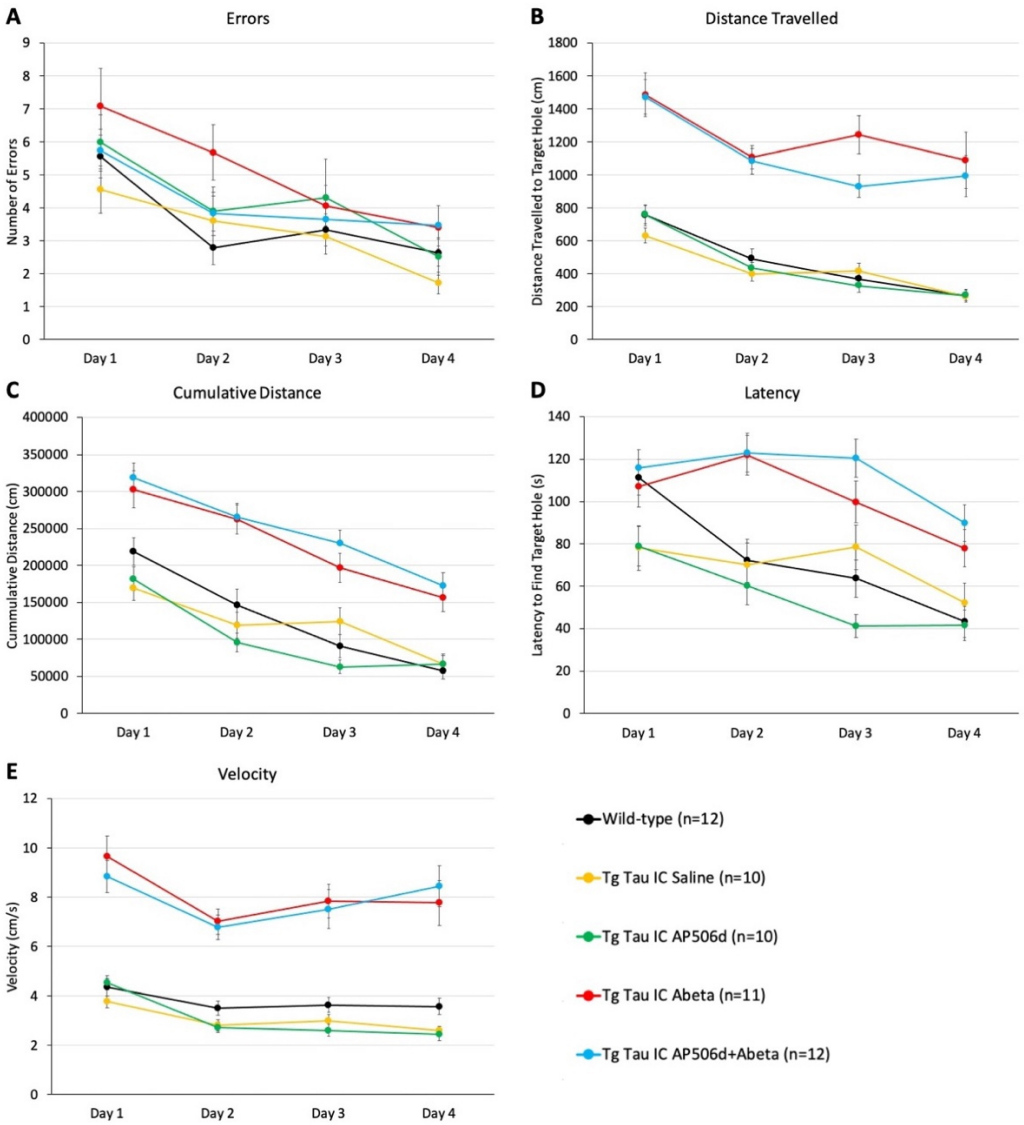

Figure 6.2: Cognitive behavior of the mice in the Barnes maze after IC injections. A) Averaged primary errors in WT and in Tg Tau mice showed a significant effect of time (*p<0.001*). No significant effect of the genotype, Aβ oligomers, or AP506d was seen for the number of errors. **B)** Analysis of the distance travelled showed a significant main effect of time (*p<0.001*) and of the intracranial injection of Aβ oligomers (*p<0.001*). **C)** Cumulative distance also showed a significant effect of time (*p<0.001*) and of the intracranial injections of Aβ oligomers (*p<0.001*). **D)** The measurement of escape latency revealed a significant main effect of time (*p<0.001*) and of the intracranial injection of Aβ oligomers (*p<0.001*) but no significant effect of the genotype or of AP506d. **E)** Finally, the velocity of mice during demonstrated a significant main effect of time (*p<0.02*) and of the intracranial injection of Aβ oligomers (*p<0.001*). Values are mean ± SEM.

A probe test was performed 24 hours after the last acquisition trial in the Barnes maze to assess memory retention. The number of errors made to find the target hole was highly variable, with no statistically significant difference between the different treatment groups (**Figure 6.3A**). The distance travelled by the mice to find the target hole was significantly greater in the probe trial in Tg Tau mice intracranially injected with Aβ oligomers than in those injected with saline (*p=0.02*) or with AP506d (*p=0.007*) (**Figure 6.3B**). Tg Tau mice intracranially injected with AP506d performed similarly to those injected with saline. Tg Tau mice co-injected with AP506d+Aβ oligomers performed similarly to those injected with Aβ oligomers only (**Figure 6.3B**). Escape latency was also quantified during the probe trial but revealed no significant differences between the different treatment groups (data not shown). Finally, there was no statistically significant difference observed for the velocity of the mice between the different treatment groups (**Figure 6.3C**).

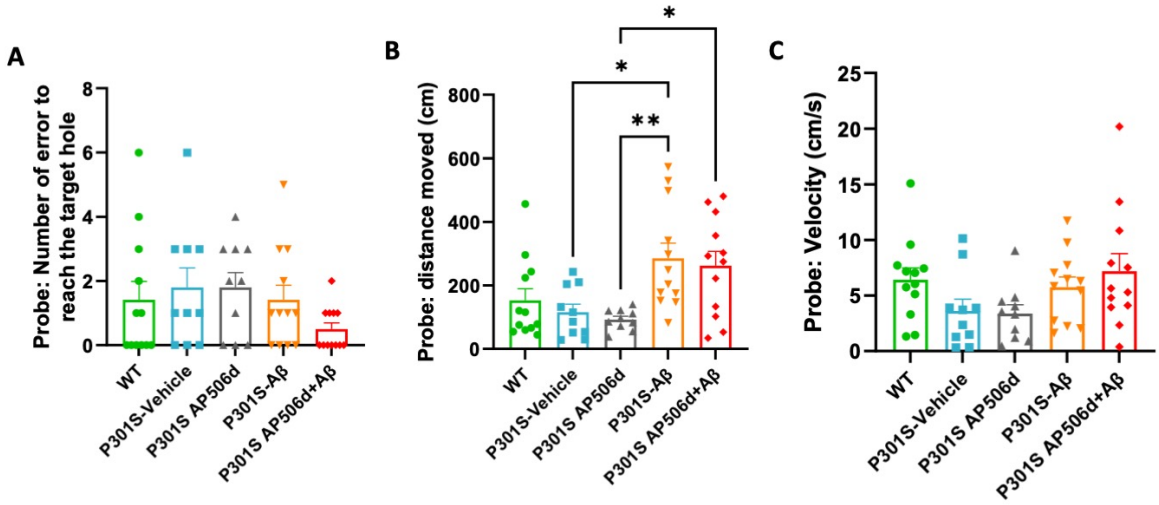

Figure 6.3: Probe test of Barnes maze to assess memory retention. A) The average number of errors by the mice in the probe trial showed no statistically significant difference between the different group of mice. **B)** For the average distance travelled, Tukey's multiple comparison test revealed statistically significant differences between Tg Tau mice injected with Aβ oligomers compared to Tg Tau mice injected with saline (*p=0.02*) and with AP506d (*p=0.007*). **C)** The average velocity of the mice during the probe trial revealed no statistically significant difference between the different groups of mice.

Mice were also tested for anxiety-like behavior in the elevated plus maze (EPM). We observed that the distance and the velocity travelled by the mice in the EPM were similar between groups, with a non-significant trend for an increase in velocity for Tg Tau mice intracranially injected with AP506d (**Figure 6.4A**). The frequency of entry in the closed arms of the EPM was also similar between the different treatment groups (**Figure 6.4B**). However, a statistically significant increase in the frequency of entry in the opened arms was observed in the Tg Tau mice compared to WT mice ($p<0.05$). Tg Tau mice intracranially injected with Aβ oligomers performed similarly to Tg Tau mice injected with saline in the EPM (**Figure 6.4B**), although a trend for a reduction in the exploration of opened arms was observed. The frequency of entry in the opened arms was significantly reduced in Tg Tau mice injected with Aβ oligomers compared to Tg Tau mice injected with AP506d ($p=0.028$) and co-injected with AP506d+Aβ ($p=0.037$) (**Figure 6.4B**). Similar data were obtained by measuring the amount of time spent by the mice in the closed and opened arms of the EPM (**Figure 6.4C**). A trend for a reduction in the amount of time spent in the opened arms was observed in Tg Tau mice intracranially injected with Aβ oligomers, while an increase in opened arm exploration was noted for mice treated with AP506d (**Figure 6.4C**).

6.3.2 Impact of IC injections on soluble Tau hyperphosphorylation in Tg Tau P301S mice

Tg Tau mice were euthanized three months after the bilateral intracranial injections (40-week-old mice) and the brains were collected. One brain hemisphere was fixed in paraformaldehyde for pathological examinations and the other brain hemisphere was snap frozen in liquid nitrogen for biochemical evaluations. Brain homogenates were obtained and a supernatant containing M-PER soluble proteins and a pellet containing insoluble proteins including tau aggregates was collected.

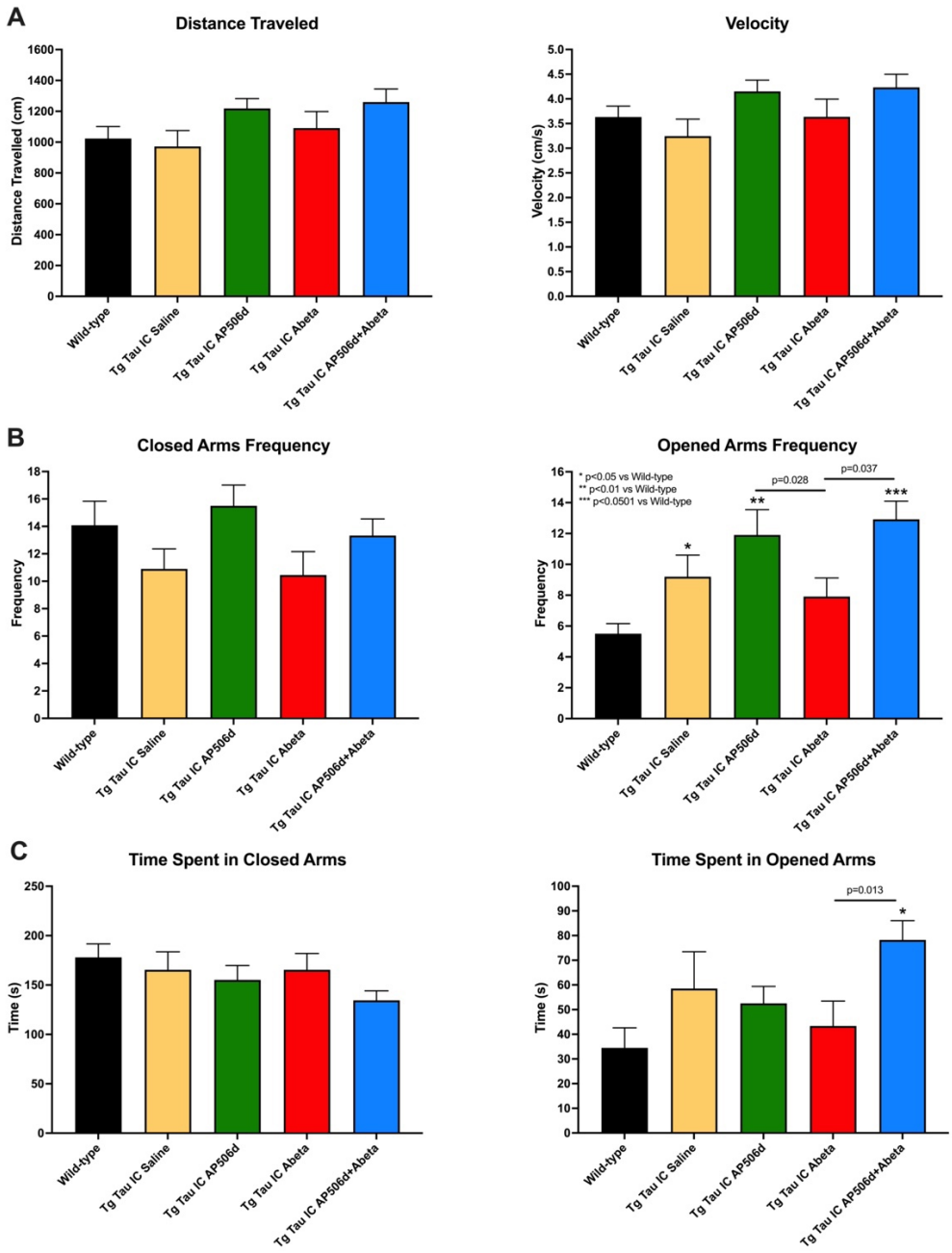

Figure 6.4: Mice were tested for anxiety like behavior in the elevated plus maze (EPM). A) For average distance travelled and velocity, no significant main effect of Aβ oligomers, AP506d, or the genotype was observed. **B)** For closed arm frequency, no differences were observed between treatment groups. For opened arms frequency, a statistically significant difference was observed between the WT and Tg Tau mice ($p<0.05$), WT and Tg Tau mice injected with AP506d ($p<0.01$), and WT and Tg Tau mice co-injected with AP506d+Aβ oligomers. Frequency of entry in the opened arms was significantly reduced in Tg Tau mice injected with Aβ oligomers compared to Tg Tau mice injected with AP506d ($p=0.028$) and to Tg Tau mice co-injected with AP506d+Aβ oligomers ($p=0.037$). **C)** A trend for a reduction in the amount of time spent in the opened arms was observed in Tg Tau mice intracranially injected with Aβ oligomers, while an increase in opened arm exploration was noted for mice treated with AP506d. Values are mean ± SEM.

We analyzed the impact of the intracranial injections with Aβ oligomers and AP506d on tau hyperphosphorylation by western blotting using the soluble fraction of the brain homogenates. Tau hyperphosphorylation was quantified using the PHF1 antibody which recognizes tau that is phosphorylated on serine amino acids 396 and 404 on the C-terminus [206]. PHF1 recognizes neurofibrillary tangles and pre-tangles in various tauopathy models and in AD brains. Western blots were also immunostained with the CP13 antibody which detects tau phosphorylated at serine 202 and DA9 as a measure of total tau.

As shown by Western blot, intracranial injections of AP506d and Aβ oligomers stimulated the phosphorylation of human tau and murine tau in the Tg Tau mice (**Figure 6.5A**) at the PHF1 epitope (S396/S404) in the soluble fraction of brain homogenates. The co-injection of AP506d+Aβ oligomers did not result in additive effects. In contrast, a non-significant trend for a reduction of PHF1 tau phosphorylation for both human and murine tau was observed in Tg Tau mice co-injected with AP506d+Aβ oligomers as compared to Tg Tau mice solely injected with Aβ oligomers (**Figure 6.5B-C**). Interestingly, AP506d did not induce the formation of PHF1 immunoreactive truncated tau species, while the intracranial injection of Aβ oligomers significantly increased the production of these truncated forms of tau (**Figure 6.5**). A non-significant trend for a reduction in PHF1 tau truncated species was observed in Tg Tau mice co-injected with AP506d+Aβ oligomers compared to mice injected with Aβ oligomers only (**Figure 6.5D**).

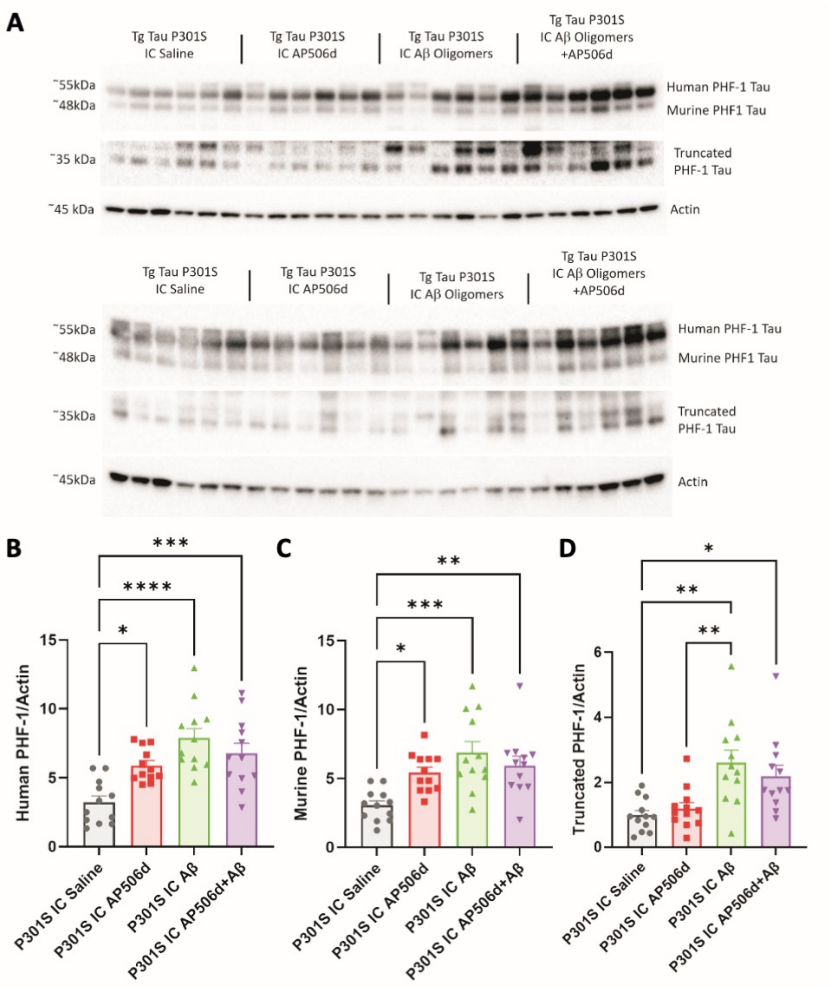

Figure 6.5: The impact of intracranial injections of AP506d and Aβ oligomers on tau phosphorylation at ser396/ser404 (PHF1) and on PHF1 truncated forms of tau in Tg Tau P301S mice (soluble fraction of brain homogenates) was assessed with Western Blot. A non-significant trend for a reduction of PHF1 tau phosphorylation for both human and murine tau was observed in Tg Tau mice co-injected with AP506d+Aβ oligomers as compared to Tg Tau mice solely injected with Aβ oligomers. Values are mean ± SD.

We further analyzed tau phosphorylation at serine 202 using the CP13 antibody. The signal obtained with CP13 was weaker than the chemiluminescent signals observed with PHF1. Only the human tau isoform was measured with this antibody as the murine tau could not be detected. Truncated tau species were only weakly immunopositive with the CP13 antibody, requiring a long exposure time to be revealed on the western blots. We did not detect a significant increase in tau phosphorylation at serine 202 in Tg Tau mice intracranially injected with Aβ or AP506d (**Figure**

6.6A). However, a significant increase in CP13 levels was observed in Tg Tau mice co-injected with AP506d+Aβ oligomers (**Figure 6.6B**). We also did not observe an increase in truncated tau species immunopositive for CP13 in Tg Tau mice intracranially injected with Aβ oligomers and AP506d either alone or in combination (**Figure 6.6C**).

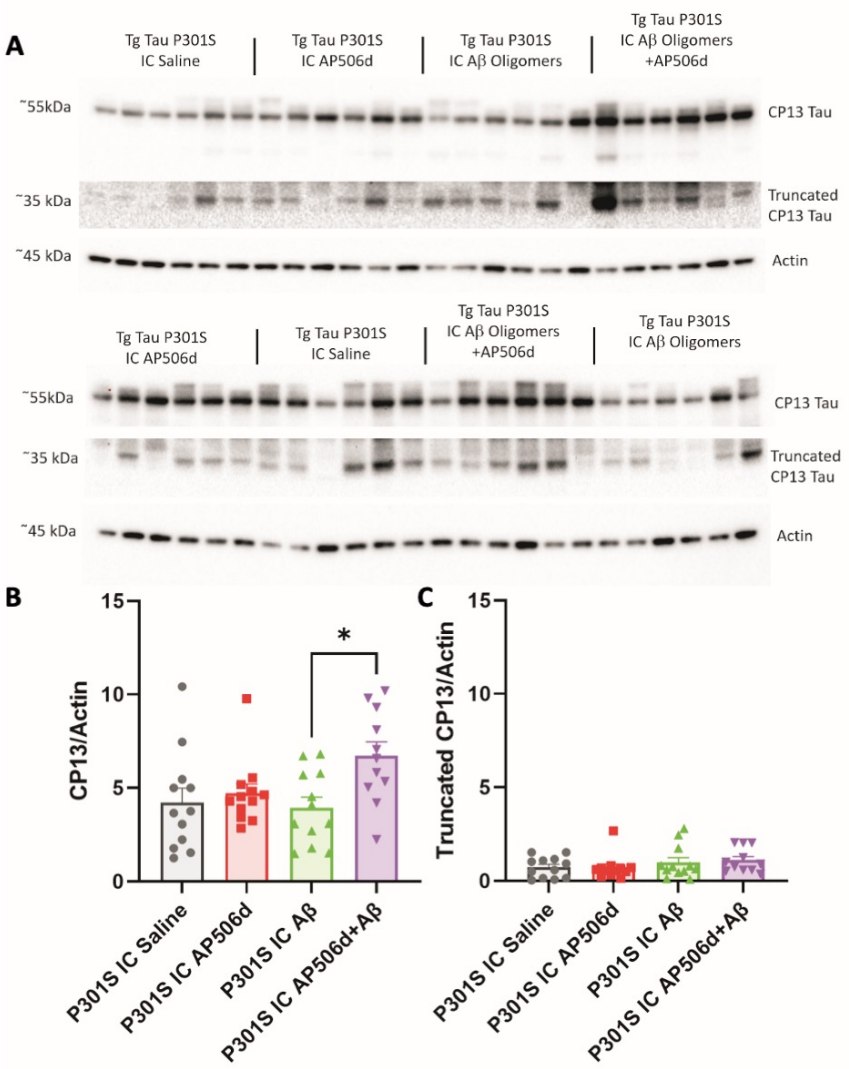

Figure 6.6: Analysis of tau phosphorylation at serine 202 using the CP13 antibody. **A)** We measured the effects of intracranial injections of AP506d and Aβ oligomers on tau phosphorylation at ser202 (CP13) and on CP13 immunopositive truncated forms of tau in Tg Tau P301S mice (soluble fraction of brain homogenates). A significant increase in tau phosphorylation at serine 202 in Tg Tau mice intracranially injected with Aβ or AP506d was not detected. **B)** A significant increase in CP13 levels was observed in Tg Tau mice co-injected with AP506d+Aβ oligomers. **C)** No increase in truncated tau species immunopositive for CP13 was observed in Tg Tau mice intracranially injected with Aβ oligomers and AP506d either alone or in combination. Values are mean ± SD.

We then analyzed the levels of total tau in the soluble fraction of brain homogenates by western blots using the DA9 antibody which recognizes a tau epitope between amino acid 102 and 140. We could not differentiate the murine tau from human tau isoforms on these western blots as the human tau chemiluminescent signal with DA9 was very strong and overlapped with the murine tau band. However, we detected DA9 immunopositive truncated tau species (**Figure 6.7A**). The intracranial injections with AP506d and with Aβ resulted in an increased accumulation of full-length total tau and truncated tau species in the soluble fraction of brain homogenates from Tg Tau mice (**Figure 6.7B-C**). The intracranial injections of Aβ oligomers induced a greater accumulation of total tau and truncated tau species than the intracranial injections of AP506d (**Figure 6.7B-C**). Interestingly, the co-injections of AP506d+Aβ oligomers resulted in a significant reduction in the accumulation of full-length tau and truncated tau species compared to Tg Tau mice intracranially injected with Aβ oligomers only (**Figure 6.7B-C**).

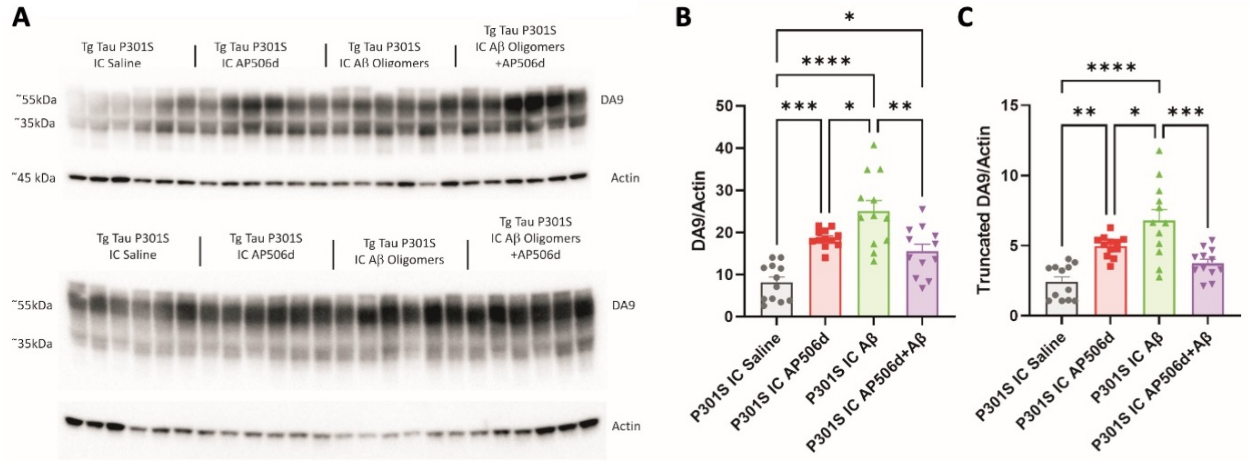

Figure 6.7: Effects of intracranial injections of AP506d and Aβ oligomers on total tau levels (DA9) and DA9 immunopositive truncated forms of tau in Tg Tau mice. Intracranial injections with AP506d and with Aβ resulted in an increased accumulation of full-length total tau and truncated tau species in the soluble fraction of brain homogenates from Tg Tau mice. The intracranial injections of Aβ oligomers induced a greater accumulation of total tau and truncated tau species than the intracranial injections of AP506d. Interestingly, the co-injections of AP506d+Aβ oligomers resulted in a significant reduction in the accumulation of full-length tau and truncated tau species compared to Tg Tau mice intracranially injected with Aβ oligomers only. Values are mean ± SD.

Next, we used a dot-blot approach [207] under native conditions to quantify the amount of tau pathogenic conformers (misfolded tau) in the soluble fractions of the brain homogenates using the MC1 antibody. MC1 is a tau conformational antibody that detects an aberrant conformation of tau shown to be present in a soluble form of the protein and in neurofibrillary tangles. The MC1 antibody recognizes a misfolded conformation of tau containing amino acids 2-10 and 312-342. Importantly, the levels of MC1 appear to correlate with the severity and progression of Alzheimer's disease [208]. The data was standardized with the CP27 antibody which detects total human tau. We observed a reduction in MC1 immunoreactivity in the soluble fraction of brain homogenates obtained from mice that were intracranially injected with AP506d (**Figure 6.8**).

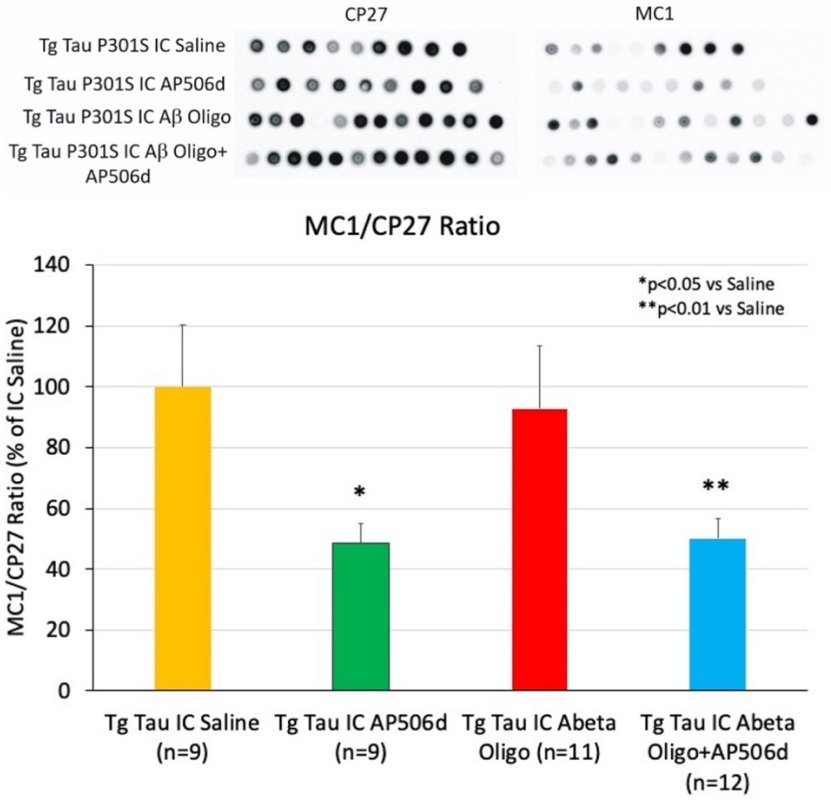

Figure 6.8: Impact of the IC injections on levels of MC1 tau pathogenic conformers/misfolded tau in the soluble fraction of brain homogenates. Dot-blots revealing the amount of total human tau (CP27), and pathogenic tau conformers (MC1) are shown. The histograms represent the average MC1/CP27 ratios of chemiluminescent signals quantified by dot-blots using the soluble fraction of brain homogenates. A reduction in MC1 immunoreactivity in the soluble fraction of brain homogenates was observed in mice that were intracranially injected with AP506d. Values are mean ± SD.

To assess the potential impact of the intracranial Aβ oligomers and AP506d injections on neuroinflammation, we analyzed multiple cytokine levels in the soluble fractions of brain homogenates using a multiplex ELISA (MesoScale Discovery, USA). Levels of interferon-g, interleukin-4 (IL-4), and IL-5 were below the detection level of the ELISA (data not shown). A significant increase in IL-1β and a trend for an increased in KC/GRO and TNFα were observed in brain homogenates from Tg Tau mice as compared to WT mice (**Figure 6.9**). No significant effect of the intracranial injections of Aβ oligomers and AP506d was observed on cytokine levels using brain homogenates (**Figure 6.9**).

6.3.3 Immunofluorescent Staining of Brain Sections

We then analyzed the possible impact of the intracranial injections with Aβ oligomers and AP506d on the intraneuronal accumulation of misfolded tau aggregates via triple immunofluorescent staining of brain sections with MC1, GFAP, and Iba1. Brain section images were acquired by laser confocal microscopy and covered the entire hippocampus. The average fluorescent intensity of the different fluorescent stains was quantified by image analysis with ImageJ for the entire hippocampus. **Figure 6.10** shows a representative laser confocal microscopic field of the CA1 region of the hippocampus for mice of the different groups.

Data revealed a significant increase in MC1 immunopositive misfolded tau aggregates in Tg Tau mice compared to WT mice in the hippocampus ($p<0.001$) (**Figure 6.11A**). A significant decrease in the amount of misfolded MC1 tau aggregates was observed in the hippocampi of Tg Tau mice co-injected with AP506d+Aβ oligomers as compared to Tg Tau mice injected with saline ($p=0.03$) (**Figure 6.11A**). However, no significant impact of the intracranial injections with AP506d or with Aβ oligomers alone was observed on MC1 immunopositive tau aggregates

(**Figure 6.11A**). A significant increase in GFAP and Iba1 immunostaining was observed in the hippocampi of Tg Tau mice compared to WT mice, showing the presence of microgliosis and astrogliosis in the hippocampi of Tg Tau mice (*p=0.007* for GFAP and *p=0.011* for Iba1, respectively) (**Figure 6.11B-C**). We did not observe a significant effect of AP506d and of Aβ oligomer on microgliosis and astrogliosis in Tg Tau mice which aligns with the cytokine data obtained using brain homogenates (**Figure 6.11B-C**).

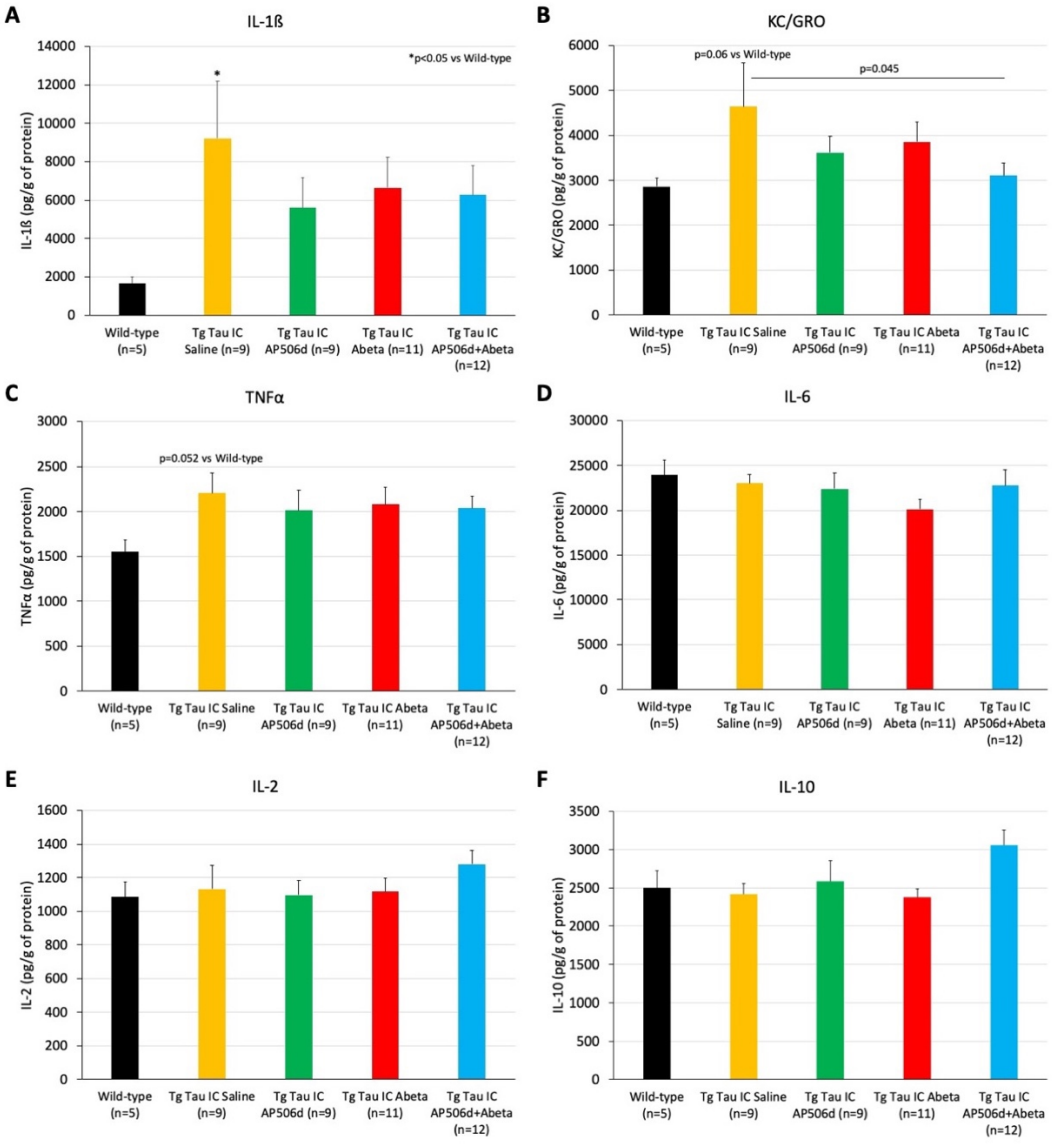

Figure 6.9: Quantification of cytokines in brain homogenates from WT and Tg Tau mice intracranially injected with saline, AP506d, and Aβ oligomers. ANOVA revealed a significant main effect of the genotype on IL-1β and KC/GRO. Values are mean ± SD.

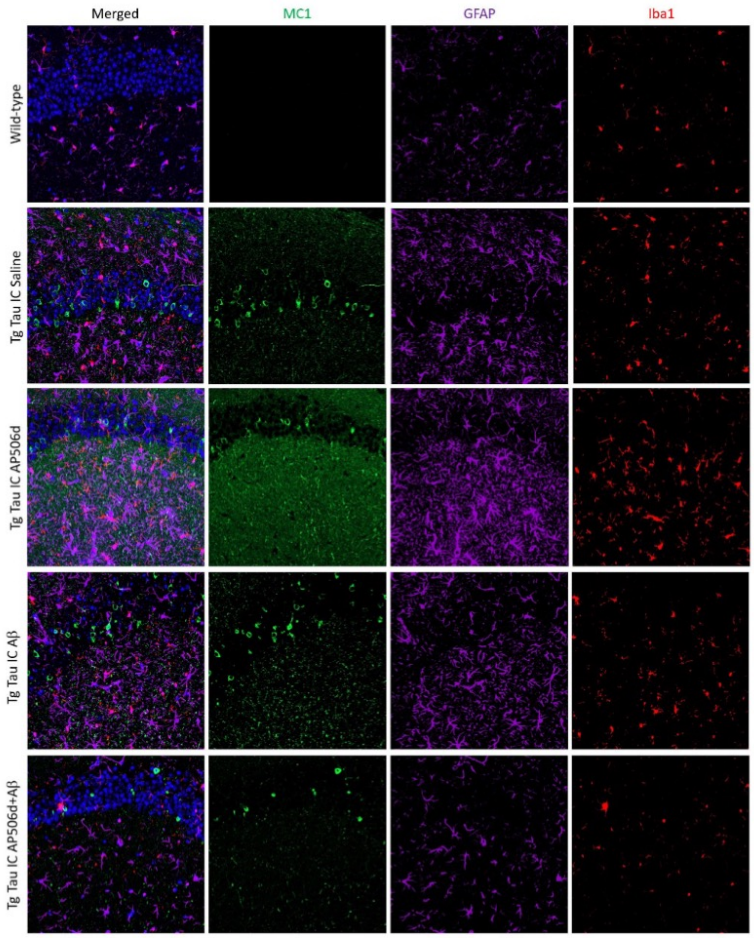

Figure 6.10: Representative laser confocal microscopic images of the CA1 region of the hippocampus following immunostaining of brain sections with MC1, GFAP, and Iba1 antibodies (quantification in **Figure 6.11**). Brain sections were counterstained with DAPI.

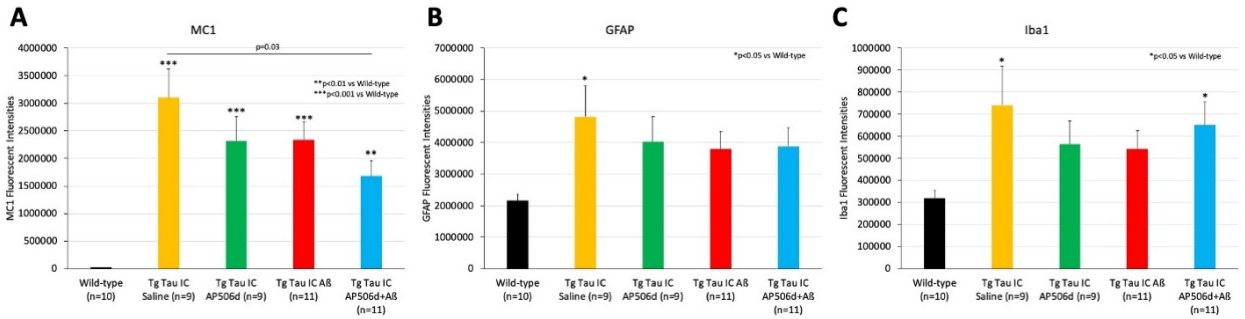

Figure 6.11: Quantification of MC1 antibodies in brain sections. A) Average MC1 intensities in the hippocampus showed a significant main effect of the genotype ($p<0.001$), of the IC injections of Aβ oligomers ($p<0.04$), and of AP506d ($p<0.04$) on MC1 levels. Post-hoc comparisons with Bonferroni's correction showed statistically significant differences between WT and Tg Tau P301S mice and between Tg Tau mice injected with saline and Tg Tau mice injected with AP506d+Aβ oligomers ($p=0.03$). **B-C)** Only a statistically significant main effect of the genotype on GFAP ($p=0.007$) and Iba1 ($p=0.011$) immunoreactivities was noted. Values are mean ± SD.

Brain sections were also stained with PHF-1 to detect tau aggregates immunopositive for PHF-1 (**Figure 6.12**). As expected, imaging of the entire hippocampus by laser confocal microscopy revealed increased levels of PHF-1 tau aggregates in Tg Tau mice compared to WT (**Figure 6.12A**). No significant effect of the intracranial injections of AP506d or Aβ oligomers was found on the amount of PHF-1 tau aggregates, although a trend for a reduction was observed (**Figure 6.12B**).

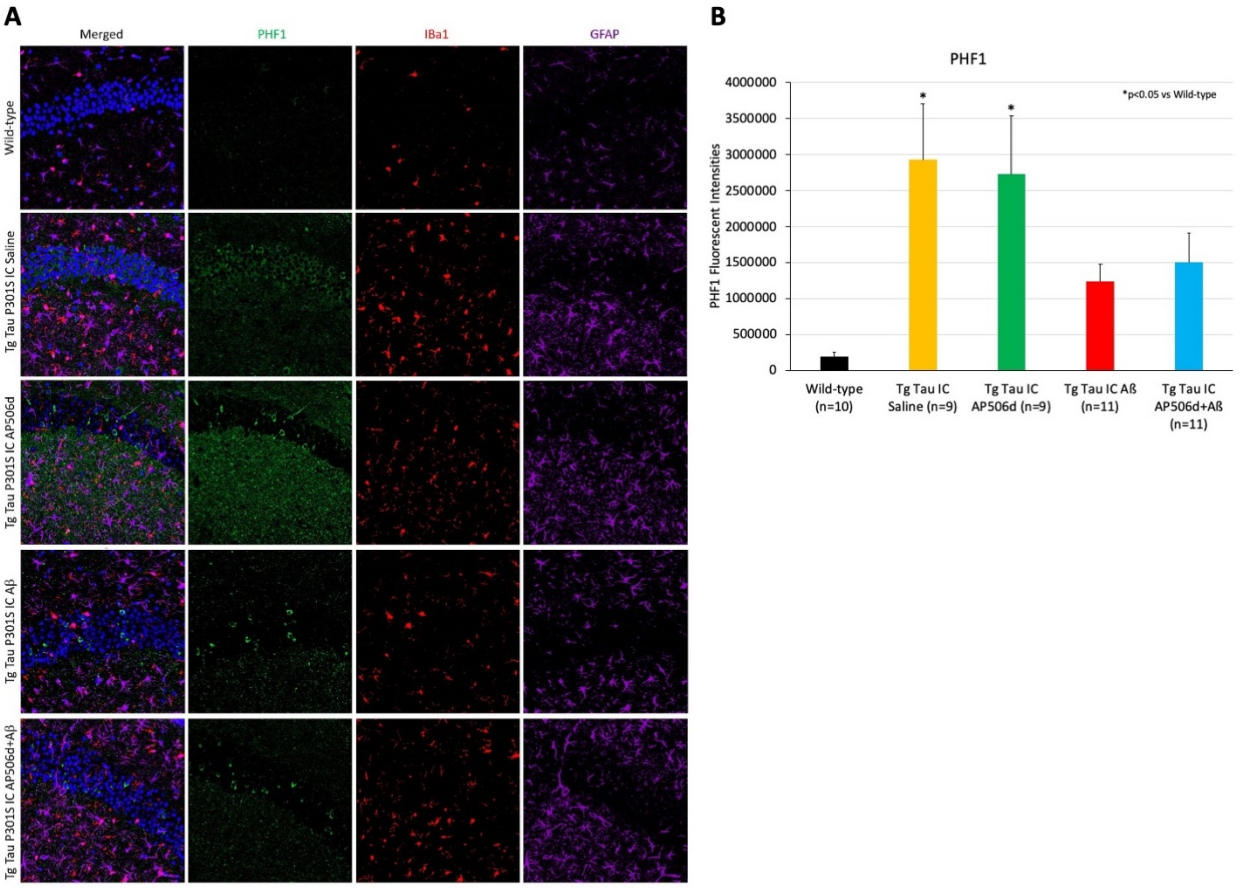

Figure 6.12: Immunostaining of brain sections with PHF-1, GFAP, and Iba1 antibodies. A) Representative laser confocal microscopic images of the CA1 region of the hippocampus following immunostaining. Brain sections were counterstained with DAPI. **B)** Average PHF-1 fluorescent intensities in the hippocampus. A significant main effect of the genotype ($p<0.003$) and of the intracranial injections of Aβ oligomers ($p<0.04$) on PHF-1 fluorescent intensities was observed. Post-hoc comparisons revealed significant differences between WT and Tg Tau mice but no difference between Tg Tau IC saline mice and Tg Tau IC Aβ mice and between Tg Tau IC Saline mice and Tg Tau IC AP506d+Aβ mice. Values are mean ± SD.

We then investigated whether the synaptic loss induced by the tau pathology in Tg Tau mice was affected by the intracranial injections of AP506d and Aβ oligomers, as measured by synapsin-1. Synapsin-1 levels were significantly reduced in the CA1 region of the hippocampus in Tg Tau mice as compared to WT mice ($p<0.02$) (**Figure 6.13**). However, intracranial injections of AP506d or Aβ oligomers did not significantly impact synaptic loss in Tg Tau mice (**Figure 6.13B**).

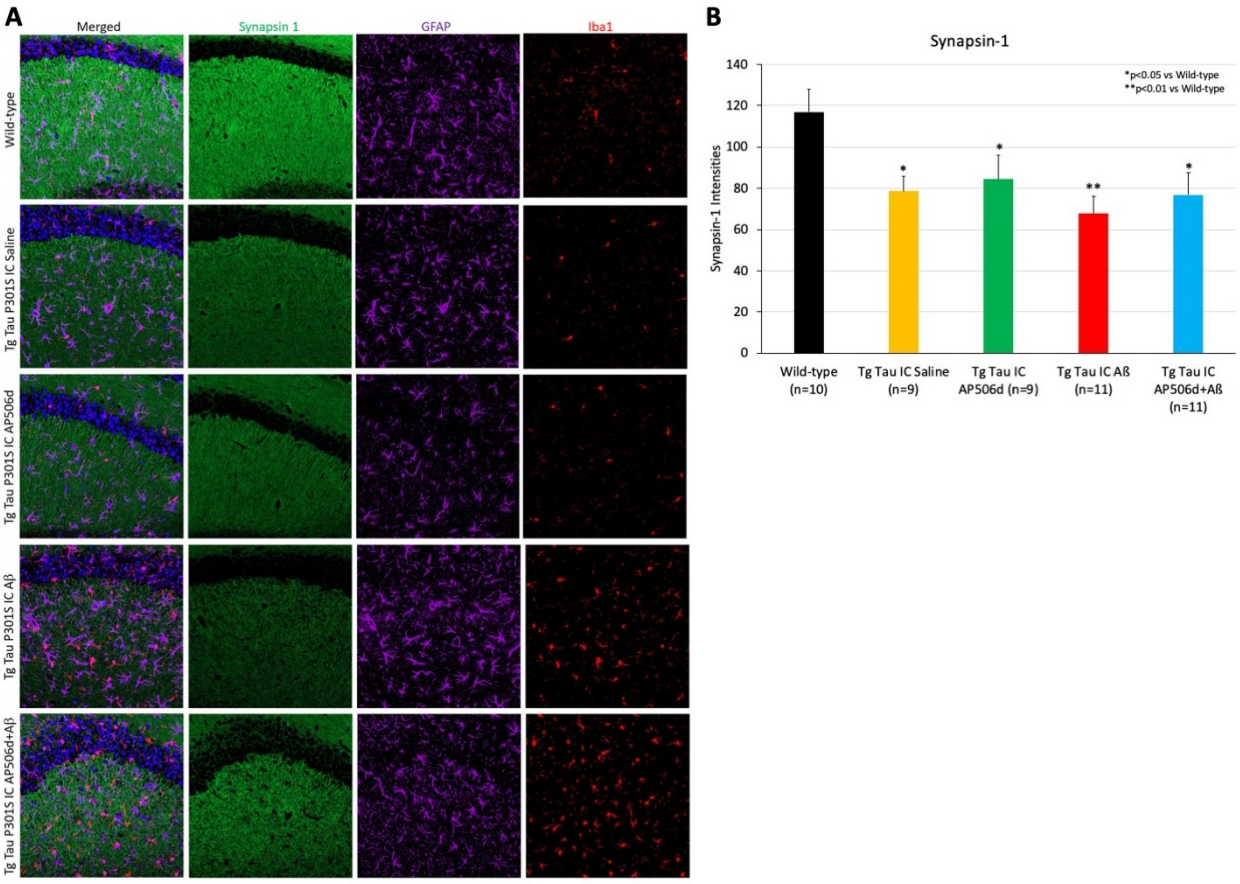

Figure 6.13: Assessment of synaptic loss induced by the tau pathology in Tg Tau mice. A) Representative laser confocal microscopy images of the CA1 regions of the hippocampus depicting synapsin-1 immunofluorescent staining. **B)** Average synapsin-1 intensities in the CA1 region of the hippocampus. ANOVA showed a significant main effect of the genotype on the average synapsin-1 intensity levels ($p<0.02$) but no significant effect of the IC injections of Aβ or AP506d. Values are mean ± SD.

Finally, we observed a very good correlation between the Iba1 and GFAP immunoreactivities in the hippocampi of the mice ($p<0.001$) (**Figure 6.14A**). There was also a

positive correlation observed between the levels of tau aggregates and the amount of astrogliosis and microgliosis, but no correlation with soluble tau species (**Figure 6.14B**). We observed a statistically significant negative correlation between the amount of PHF-1 soluble tau and synapsin-1 levels (*p=0.033*), between the amount of total soluble tau (DA9) and synapsin-1 levels (*p=0.011*), and between total soluble tau truncated species amount and synapsin-1 levels (*p=0.004*) (**Figure 6.14C**).

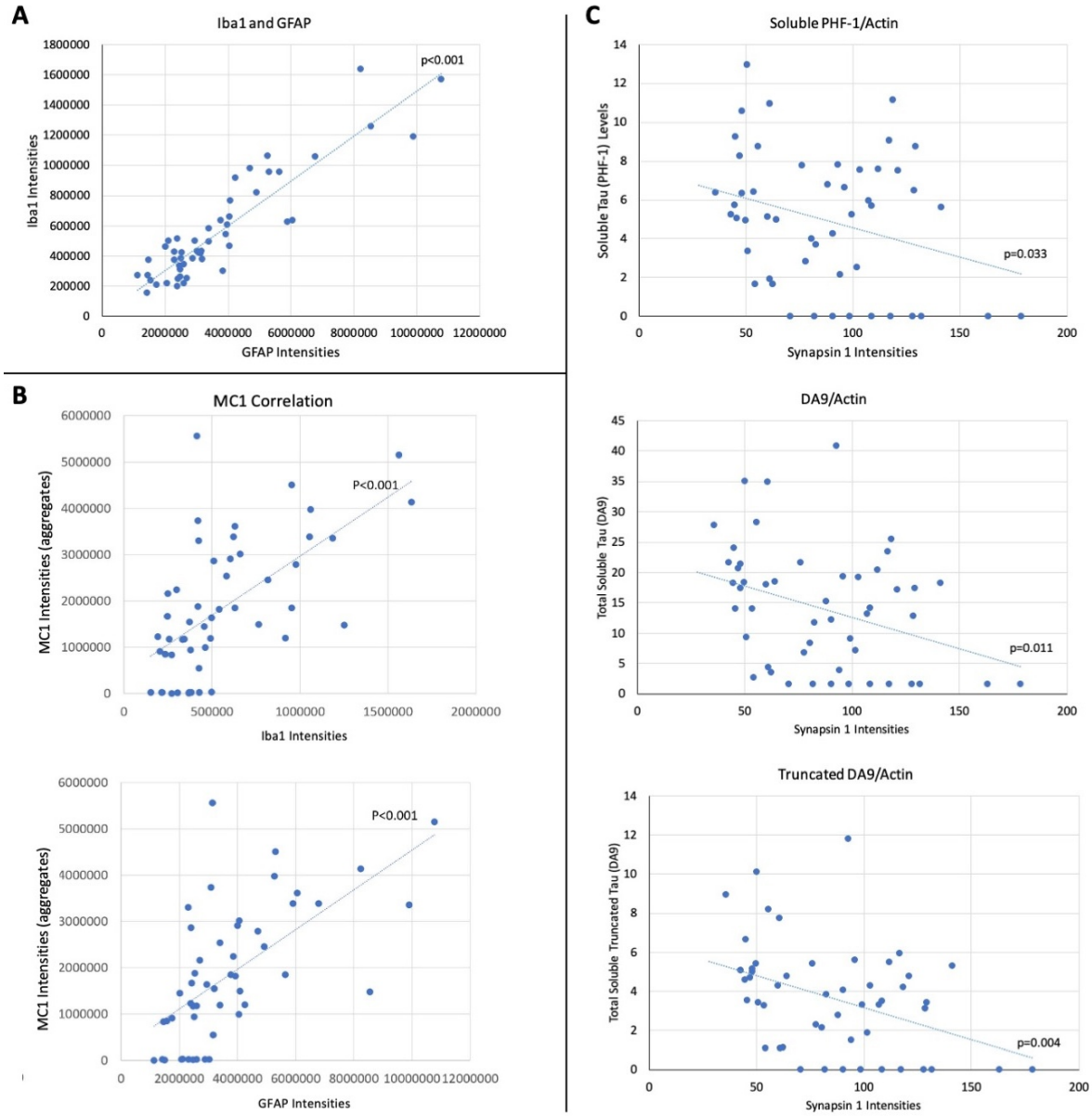

Figure 6.14: Correlation measurements. A) Correlation between Iba1 and GFAP levels in the hippocampus. Each dot represents the average intensities of GFAP and Iba1 for each mouse. Pearson correlation showed a statistically significant correlation ($p<0.001$) between GFAP and Iba1 levels. **B)** Correlation between MC1 immunopositive tau aggregate levels and microgliosis and astrogliosis in the hippocampus of Tg Tau mice. Each dot represents the average amount of MC1 immunopositive tau aggregates, GFAP, and Iba1 intensities for each mouse. Pearson correlation showed a significant correlation ($p<0.001$) between MC1 tau aggregates levels and the amount of microgliosis and astrogliosis in the hippocampus of Tg Tau mice. **C)** Correlations between soluble tau levels and the synaptic loss in the hippocampus. Pearson correlation showed a statistically significant negative correlation between the amount of PHF-1 soluble tau and synapsin-1 levels ($p=0.033$), between the amount of total soluble tau (DA9) and synapsin-1 levels ($p=0.011$) and between total soluble tau truncated species amount and synapsin-1 levels ($p=0.004$). No correlation was observed between insoluble/aggregated PHF-1 or MC1 tau and synapsin-1 levels.

6.4 Discussion

In this study, we used transgenic Tg Tau P301S mice to investigate whether AP506d affects the impact of Aβ oligomers on tau pathology *in vivo*. No cognitive deficit was observed between the WT and Tg Tau mice. The intracranial injections of Aβ oligomers induced long-term learning deficit and memory impairment in Tg Tau mice. The α-sheet peptide AP506d was well tolerated and did not induce any learning or memory deficit in the Tg Tau mice. However, AP506d had no statistically significant impact on the learning and memory deficits induced by Aβ oligomers, although some positive trends were observed with AP506d when the number of errors and the distance travelled to find the target hole were considered.

As shown in **Figure 6.2A-C**, learning over time was apparent across all the groups as measured by each of the three acquisition measures (primary errors, distance travelled to find target hole, and escape latency). All measures tended to be reduced after four days of training as compared to the first day. Specifically, analysis of the distance travelled indicated that the intracranial injection of Aβ oligomers caused learning impairment while the intracranial injection of AP506d did not have a deleterious impact (**Figure 6.2B**). A non-significant trend in distance traveled by in Tg Tau mice co-injected with AP506d+Aβ oligomers suggested that the α-sheet

peptide AP506d may slightly reduce the learning impairment induced by Aβ oligomers. For cumulative distance, all mice progressively learned to find the target hole in the Barnes maze (**Figure 6.2C**). However, the Aβ oligomers caused a learning deficit in the mice as indicated by increased distance traveled from the Tg Tau mice intracranially injected with Aβ oligomers. No effect was observed from the AP506d mice. While AP506d did not reduce the impact of Aβ oligomers on learning in the Barnes maze, it also did not impair learning like the Aβ oligomers.

A reduction in the latency to find the target hole for all groups likewise demonstrated that all animals exhibited learning in the Barnes maze (**Figure 6.2D**). An increase in the escape latency was observed in Tg Tau mice intracranially injected with Aβ oligomers, confirming that Aβ oligomers induced a learning deficit in the mice. In contract, no significant effect from AP506d was observed, showing that AP506d was not able to reverse the learning deficit induced by Aβ oligomers. Finally, the increase in velocity for Tg Tau mice intracranially injected with Aβ oligomers indicated that Aβ oligomers may induce hyperactivity in Tg Tau mice (**Figure 6.2E**).

Next, the number and variability of errors measured by the probe test suggested the variable was not sensitive enough to assess the performance of the mice in the Barnes maze (**Figure 6.3A**). However, the increased distance traveled during the probe trial in Tg Tau mice injected with Aβ oligomers indicated that Aβ oligomers are inducing memory impairment (**Figure 6.3B**). In contrast, AP506d did not appear to have a deleterious impact as the AP506d mice performed similarly to those injected with saline (**Figure 6.3B**). The lack of a rescue effect seen from co-injected mice suggested that AP506d cannot reverse the memory deficit induced by Aβ oligomers (**Figure 6.3B**). Finally, the lack of a difference between treatment groups for the velocity test showed that the locomotor activity of the different group of mice was comparable during the probe test of the Barnes maze.

In the EPM, Tg Tau mice showed disinhibition compared to WT mice. Injection of Aβ oligomers increased anxiety in the Tg Tau mice while AP506d decreased anxiety induced by Aβ oligomers in Tg Tau mice. Specifically, the locomotor activity of the mice in the different treatment groups was comparable as indicated by velocity and distance travelled in the EPM (**Figure 6.4A**). The Tg Tau mice had decreased anxiety, or increased disinhibition, as compared to WT mice as indicated by frequency of entry in the opened arms (**Figure 6.4B**). Additionally, mice co-injected with AP506d+Aβ showed significantly reduced anxiety as indicated by the opened arms frequency (**Figure 6.4B**). Overall, the data further demonstrated that AP506d reduced the anxiety induced by Aβ oligomers in Tg Tau mice, suggesting that AP506d may reduce some of the impact of the intracranial injection of Aβ oligomers in Tg Tau mice.

Next, we analyzed the levels of murine and human tau, truncated and total, with western blot using three antibodies (PHF1, CP13, and DA9). PHF1 recognizes neurofibrillary tangles and pre-tangles in various tauopathy models and in AD brains. As indicated by the PH1 antibody, injection of AP506d increased soluble PHF-1 Tau species but not PHF-1 truncated tau species. Injection of Aβ oligomers increased both full length soluble PHF-1 tau species and PHF-1 truncated tau species. However, AP506d did not significantly affect soluble PHF-1 tau levels induced by Aβ oligomers (**Figure 6.5**). The CP13 antibody, which detects tau phosphorylated at serine 202 and DA9, was used as a measure of total tau. A significant increase in CP13 levels was observed in Tg Tau mice co-injected with AP506d+Aβ oligomers (**Figure 6.6**).

The DA9 antibody also served as a measure of total tau. DA9 levels indicated that the total soluble tau species were increased by AP506d injections and injection of Aβ oligomers increased total soluble tau species and total truncated tau levels. AP506d injection also significantly reduced the total soluble tau and total truncated tau species induced by Aβ oligomers (**Figure 6.7**).

Next, dot blot analysis revealed MC1 tau aggregates in Tg Tau mice but did not detect aggregates in WT mice. It also revealed that AP506d intracranial injections significantly reduced MC1 immunoreactivity in Aβ injected Tg Tau mice (**Figure 6.8**).

It was previously demonstrated that Aβ peptides can promote pathological tau filament assembly in neurons by triggering caspase cleavage of tau and generating a proteolytic product with enhanced polymerization kinetics [209]. These data therefore link Aβ exposure to tau cleavage and argue for a pathogenic role of caspase-cleaved tau in AD as tau truncation promotes its pathological assembly into filaments. The proteolytic cleavage of tau has been shown to induce a toxic gain of function by hindering axonal transport and promoting dendritic atrophy and tau oligomerization [210]. Truncated tau species can be phosphorylated by GSK3b and recognized by the PHF1 antibody, and these truncated tau species are associated with both early and late markers of neurofibrillary tangles and are correlated with cognitive decline in AD [211, 212].

Next, we analyzed cytokine levels as a measure of the effect of injections on neuroinflammation. Neuroinflammation occurred in the Tg Tau mice as indicated by an increase in select cytokines (L-1β, KC/GRO, and TNFα) (**Figure 6.9**). However, there was no increase in cytokine levels in brain homogenates from mice receiving injections, suggesting that the intracranial injections did not exacerbate the neuroinflammation in Tg Tau mice (**Figure 6.9**).

We then performed triple immunofluorescent staining of brain sections with MC1, GFAP, and Iba1 (**Figure 6.10**). MC1 staining revealed a significant increase in tau aggregates in Tg Tau mice compared to WT mice in the hippocampus (**Figure 6.11**). A significant decrease in the amount of misfolded MC1 tau aggregates was observed in the hippocampi of Tg Tau mice co-injected with AP506d+Aβ oligomers as compared to Tg Tau mice injected with saline. For PHF-1 staining, PHF-1 immunoreactivity, insoluble tau species, was largely increased in Tg Tau mice compared to WT

and not affected by AP506d injections (**Figure 6.12**). A non-significant trend for a reduction in PHF-1 immunoreactivity in Aβ and AP506d+ Aβ injected Tg Tau mice was also observed.

For, GFAP and Iba1 immunostaining, a significant increase in GFAP and Iba1 was observed in the hippocampi of Tg Tau mice compared to WT mice, indicating the presence of microgliosis and astrogliosis in the hippocampi of Tg Tau mice (**Figure 6.12**). However, astrogliosis/microgliosis were. not significantly affected by AP506d or Aβ injections (**Figure 6.12**).

Synapsin-1 is a presynaptic protein found in mature synapses and often used as a synaptic marker. It has been shown previously that synapsin-1 levels are reduced in Tg Tau mice and associated with synaptic loss [213]. Here, reduced levels of synapsin-1 in the CA1 region of the hippocampus in Tg Tau mice compared to WT mice confirmed that synaptic densities are decreased in Tg Tau mice (**Figure 6.13**). Additionally, a non-significant trend for more synaptical density reduction was observed in Tg Tau mice injected with Aβ oligomers. Finally, a non-significant trend was noted for increased synaptical density in AP506d injected Tg Tau mice (**Figure 6.13**).

Correlation between the Iba1 and GFAP immunoreactivities in the hippocampi of the mice indicated that the presence of activated microglia is associated with the astrogliosis (**Figure 6.14A**). Additionally, the positive correlation between the levels of tau aggregates, but not soluble tau species, and the amount of astrogliosis and microgliosis, suggested that either the aggregated form of tau contributed to the induction of microgliosis and astrogliosis in Tg Tau mice or that the neuroinflammatory processes exacerbated the accumulation of tau aggregates in Tg Tau mice (**Figure 6.14B**). Finally, the negative correlation between the soluble tau species and the levels of

synapsin-1 suggested that soluble forms of tau, rather than tau aggregates, are implicated in the loss of synapses in Tg Tau mice (**Figure 6.14C**).

6.5 Conclusion

The intracranial injections of Aβ oligomers resulted in long-term behavioral impairments in Tg Tau mice, whereas AP506d intracranial injections appeared to be safe. Interestingly, AP506d reduced the anxiety induced by the intracranial injection of Aβ oligomers in Tg Tau mice, suggesting it opposed some of the impairments induced by Aβ oligomers. Western blot analysis of the PH1 and DA9 antibodies showed that the co-injections of AP506d+Aβ oligomers resulted in a reduction of tau phosphorylation for both human and murine tau and full-length tau and truncated tau species compared to Tg Tau mice intracranially injected with Aβ oligomers only. In dot blots, AP506d intracranial injections also reduced the amount of soluble misfolded tau in Tg Tau mice but had no significant impact on the levels of tau aggregates. Again, the co-injection of AP506d+Aβ oligomers resulted in a significant reduction in the accumulation of full-length tau and truncated tau species as compared to Tg Tau mice intracranially injected with Aβ oligomers only. No significant effect of the intracranial injections of Aβ oligomers and AP506d was observed on cytokine levels using brain homogenates or on synapsin-1 levels. Overall, these data suggest that the AP506d peptide may have some ability to reverse the effects of Aβ oligomers on tau pathology.

6.6 Materials and Methods

6.6.1 Synthesis and Preparation of α-Sheet Peptides

Synthetic α-sheet peptide inhibitors were designed *in silico* as previously described [6, 8, 9, 54]**,** using backbone dihedral angle constraints derived from MD simulations [103, 158] and synthesized as previously described by Bleem, et al [9]. Briefly, peptides contain two α-strands of seven residues each, with amino acids alternating sequentially between L-conformation and D-conformation in each of the strands. The α-strands are connected by a five residue turn comprised of all L-amino acids or all D-amino acids, which gives the peptide a hairpin shape. Finally, the tail of each strand consists of a Gly and an Arg residue, followed by acetyl and amide caps at the N- and C-terminus, respectively. Peptides were assembled by solid phase peptide synthesis on Rink amide resin with Fmoc chemistry and HBTU activation using the Liberty Blue Microwave Peptide Synthesizer (CEM Corporation; Charlotte, NC). Peptides were cleaved from the resin and side chain deprotected by TFA/TIPS/H2O (95:2.5:2.5) and precipitated by cold ether. Crude peptides were purified to >95% by RP-HPLC using 5 μM C12 or C18 130 Å columns (Waters Corporation; Milford, MA) and atomic masses were confirmed by electrospray mass spectrometry on a Bruker Esquire Ion Trap (Bruker; Billerica, MA). All peptides were lyophilized after purification and stored at -20 or -80°C until use.

For dimeric peptides, purified and lyophilized monomer was dissolved in 1 mL of DMSO per 100 mg of peptide before resin cleavage.19 mL of carbonate buffer at pH 9.6 was then added per mL of DMSO. The solution was covered in parafilm with holes to allow for airflow and stirred for 4 hours at 37°C, followed by 48 hours at room temperature. Crude peptides were then purified again to >95% by RP-HPLC using 5 μM C12 or C18 130 Å columns (Waters Corporation; Milford,

MA) and atomic masses were confirmed by electrospray mass spectrometry on a Bruker Esquire Ion Trap (Bruker; Billerica, MA). Dimers were lyophilized after purification and stored at -20 or -80°C until use.

6.6.2 IC Injections

Figure 6.1 depicts the timeline for the intracranial experiments. 25- to 26-week-old Tg Tau P301S mice were anesthetized with 3% isoflurane in oxygen and placed on a thermoregulated stereotaxic instrument. Intracranial injections of sterile saline, AP506d, Aβ oligomers, or AP506d+Aβ oligomers were performed in both hemispheres in the hippocampus of anesthetized mice using the following coordinates: Bregma, -2.7 mm; lateral -2.5 mm; depth, -3.5 mm. The volume injected in each hemisphere was 5 µL at a speed of 1 µL per minute. The concentration of AP506d in saline was 1 mM and the concentration of Aβ1-42 oligomer was 100 mM.

6.6.3 Western Blot and Dot Blot Assays

Tg Tau mice were euthanized three months after the bilateral intracranial injections (40-week-old mice) and the brains were collected. One brain hemisphere was fixed in paraformaldehyde for pathological examinations and the other brain hemisphere was snap frozen in liquid nitrogen for biochemical evaluations. Brain homogenates were obtained by sonication using Mammalian Protein Extraction reagent (M-PER, Thermo Fisher Scientific) containing a cocktail of proteases and phosphatases inhibitors. Following centrifugation at 20,000 g for 30 minutes at 4°C, a supernatant containing M-PER soluble proteins and a pellet containing insoluble proteins including tau aggregates were collected.

Western blotting was then performed using the soluble fraction of the brain homogenates. Tau hyperphosphorylation was quantified using the PHF1 antibody which recognizes tau that is phosphorylated on serine amino acids 396 and 404 on the C-terminus [206]. PHF1 recognizes neurofibrillary tangles and pre-tangles in various tauopathy models and in AD brains. Western blots were also immunostained with the CP13 antibody which detects tau phosphorylated at serine 202 and DA9 as a measure of total tau.

6.6.4 Cytokine Analysis

Multiple cytokine levels were measured in the soluble fractions of brain homogenates using a multiplex ELISA (MesoScale Discovery, USA). Levels of interferon-g, interleukin-4 (IL-4), and IL-5 were below the detection level of the ELISA (data not shown).

6.6.5 Triple Immunofluorescent Staining

The intraneuronal accumulation of misfolded tau aggregates was assessed via triple immunofluorescent staining of brain sections with MC1, GFAP, and Iba1. Brain section images were acquired by laser confocal microscopy and covered the entire hippocampus. The average fluorescent intensity of the different fluorescent stains was quantified by image analysis with ImageJ for the entire hippocampus.

Conclusion

This dissertation investigates the inhibition of amyloid fibrilization by designed α-sheet peptides in the context of both bacterial biofilms and Alzheimer's Disease (AD). Synthetic α-sheet peptides bind to amyloid oligomers and prevent the formation of mature amyloid fibrils, subsequently inhibiting biofilm formation in bacteria or neutralizing toxicity in mammalian cells.

Many bacteria produce functional amyloid as part of their biofilm extracellular matrix. These proteins help the bacteria to resist physical and chemical dispersion of their biofilm and to reduce the efficacy of traditional antibiotics. However, the α-sheet peptides inhibit amyloid and biofilm formation in both gram-negative and -positive species, presenting a novel prevention method for bacterial biofilms. Medical biofilms are a persistent problem as the usage of biomedical devices rises and bacterial resistance to traditional antibiotics increases.

In **Chapter 2**, the effect of the co-administration of two α-sheet peptides and five antibiotics was studied in clinical isolates of gram-negative *E. coli* and gram-positive *S. aureus*. When biofilms were initially treated with α-sheet peptides, they were more susceptible to all antibiotic types, even those with traditionally low efficacy. Interestingly, the two peptides, which have the same sequence but differ in the chirality of each amino acid, showed varying efficacy for the gram-negative versus -positive bacterial species. This suggests that the efficacy of the peptides is somewhat species dependent, likely due to differing bacterial proteases which could cleave the α-sheet peptides. These results suggest that the peptides may be a useful tool for extending the efficacy of existing antibiotics with potential application to a broad range of bacterial species. Future work will focus on testing additional peptide and antibiotic combinations in different bacteria.

In **Chapter 3**, the α-sheet peptides were applied to the problem of bacterial biofilm infection at a wound site. Biofilm formation in a wound exacerbates infection and impairs healing, frequently leading to chronic wounds which require long-term treatment and systemic antibiotic usage. Here, the peptides were incorporated into a cotton gauze functionalized with alternating layers of chitosan and alginate which are natural, biocompatible, and antibacterial polymers. The gauze showed good cytocompatibility with human fibroblasts and demonstrated anti-biofilm activity against clinical isolates of *E. coli* and *S. aureus.* As previously observed, the gauze with synthetic α-sheet peptides also increased the biofilm antibiotic susceptibility for both species of bacteria. Potential future work will focus on additional testing of the biocompatibility of the gauze as well as *in vivo* testing of the gauze anti-biofilm properties in a rat burn model.

In Chapters 2 and 3, the α-sheet peptides were administered to bacterial biofilms in solution or released from a material. In **Chapter 4**, it was proposed that the peptides could be attached to a surface to prevent biofilm formation at an implant site. A polydopamine (PDA) coating was thus investigated for peptide tethering to dental implants to prevent oral biofilm infection. The peptides inhibited amyloid and biofilm formation by *S. mutans* and were effectively coupled to a surface using PDA. Future work will continue material development of the implant coating with additional assessments of anti-biofilm action, material strength and stability, and biocompatibility.

In contrast to bacterial amyloid which functionally support bacterial growth and biofilm formation, mammalian amyloid proteins are associated with over 40 diseases, including AD. AD is characterized by the accumulation of insoluble β-amyloid peptide (Aβ) in the brain. Previous work from the Daggett lab showed that multiple α-sheet peptides inhibit Aβ aggregation in both *in vitro* and *in vivo* AD models. In **Chapter 5**, the effect of the peptides on the phagocytosis of Aβ oligomers was tested in microglia, the primary immune cells of the central nervous system, and in

macrophages. All seven peptides tested increased the phagocytosis of Aβ oligomers by macrophages and microglial cells. This work provides a basis for an increased understanding of the mechanisms that contribute to the clearance of toxic Aβ oligomers by APs, highlighting their therapeutic potential in neurodegenerative diseases.

Finally, in **Chapter 6**, the peptides were further explored in the context of AD progression and disease mechanism. The peptides, along with Aβ oligomers, were injected into transgenic mice that overexpress the human tau protein. The intracranial injections of Aβ oligomers resulted in long-term behavioral impairments in the transgenic mice, whereas AP506d intracranial injections appeared to be safe. Interestingly, AP506d reduced the anxiety induced by the intracranial injection of Aβ oligomers in the transgenic mice, suggesting it opposed some of the impairments induced by Aβ oligomers.

Together, this dissertation work presents a study of designed α-sheet peptides and amyloid inhibition with applications in bacterial and mammalian amyloid systems. Significant work remains to be done to further examine the effect of the peptides on antibiotic susceptibility and to develop materials for peptide delivery to potential biofilm sites in the human body. Likewise, additional work is required to fully understand the effect of the peptides on Aβ phagocytosis and toxicity with critical implications for the understanding and treatment of AD.

References

[1] F. Chiti and C. M. Dobson, "Protein Misfolding, Amyloid Formation, and Human Disease: A Summary of Progress Over the Last Decade," (in eng), *Annu Rev Biochem,* vol. 86, pp. 27-68, Jun 20 2017, doi: 10.1146/annurev-biochem-061516-045115.

[2] A. Bleem and V. Daggett, "Structural and functional diversity among amyloid proteins: Agents of disease, building blocks of biology, and implications for molecular engineering," (in eng), *Biotechnol Bioeng,* vol. 114, no. 1, pp. 7-20, Jan 2017, doi: 10.1002/bit.26059.

[3] J. D. Sipe *et al.*, "Nomenclature 2014: Amyloid fibril proteins and clinical classification of the amyloidosis," (in eng), *Amyloid,* vol. 21, no. 4, pp. 221-4, Dec 2014, doi: 10.3109/13506129.2014.964858.

[4] S. I. Cohen *et al.*, "Proliferation of amyloid-β42 aggregates occurs through a secondary nucleation mechanism," (in eng), *Proc Natl Acad Sci U S A,* vol. 110, no. 24, pp. 9758-63, Jun 11 2013, doi: 10.1073/pnas.1218402110.

[5] T. Prosswimmer and V. Daggett, "The role of α-sheet structure in amyloidogenesis: characterization and implications," (in eng), *Open Biol,* vol. 12, no. 11, p. 220261, Nov 2022, doi: 10.1098/rsob.220261.

[6] G. Hopping *et al.*, "Designed α-sheet peptides inhibit amyloid formation by targeting toxic oligomers," *eLife,* vol. 3, p. e01681, 2014/07/15 2014, doi: 10.7554/eLife.01681.

[7] J. Kellock, G. Hopping, B. Caughey, and V. Daggett, "Peptides Composed of Alternating L- and D-Amino Acids Inhibit Amyloidogenesis in Three Distinct Amyloid Systems Independent of Sequence," *Journal of Molecular Biology,* vol. 428, no. 11, pp. 2317-2328, 2016/06/05/ 2016, doi: https://doi.org/10.1016/j.jmb.2016.03.013.

[8] A. Bleem, R. Francisco, J. D. Bryers, and V. Daggett, "Designed α-sheet peptides suppress amyloid formation in *Staphylococcus aureus* biofilms," (in eng), *NPJ Biofilms Microbiomes,* vol. 3, pp. 16-16, 2017, doi: 10.1038/s41522-017-0025-2.

[9] A. Bleem *et al.*, "Designed α-sheet peptides disrupt uropathogenic *E. coli* biofilms rendering bacteria susceptible to antibiotics and immune cells," *Scientific Reports,* vol. 13, no. 1, p. 9272, 2023/06/07 2023, doi: 10.1038/s41598-023-36343-6.

[10] N. Paranjapye and V. Daggett, "De Novo Designed α-Sheet Peptides Inhibit Functional Amyloid Formation of *Streptococcus mutans* Biofilms," *Journal of Molecular Biology,* vol. 430, no. 20, pp. 3764-3773, 2018/10/12/ 2018, doi: https://doi.org/10.1016/j.jmb.2018.07.005.

[11] W. H. DePas and M. R. Chapman, "Microbial manipulation of the amyloid fold," (in eng), *Res Microbiol,* vol. 163, no. 9-10, pp. 592-606, Nov-Dec 2012, doi: 10.1016/j.resmic.2012.10.009.

[12] A. K. Syed and B. R. Boles, "Fold modulating function: bacterial toxins to functional amyloids," (in English), *Front Microbiol,* Review vol. 5, 2014-August-01 2014, doi: 10.3389/fmicb.2014.00401.

[13] Y. Zhou, D. Smith, B. J. Leong, K. Brännström, F. Almqvist, and M. R. Chapman, "Promiscuous cross-seeding between bacterial amyloids promotes interspecies biofilms," (in eng), *The Journal of biological chemistry,* vol. 287, no. 42, pp. 35092-35103, 2012, doi: 10.1074/jbc.M112.383737.

[14] M. M. Barnhart and M. R. Chapman, "Curli biogenesis and function," (in eng), *Annu Rev Microbiol,* vol. 60, pp. 131-147, 2006, doi: 10.1146/annurev.micro.60.080805.142106.

[15] L. Matilla-Cuenca, A. Toledo-Arana, and J. Valle, "Anti-Biofilm Molecules Targeting Functional Amyloids," (in eng), *Antibiotics (Basel),* vol. 10, no. 7, Jun 29 2021, doi: 10.3390/antibiotics10070795.
[16] K. Schwartz, A. K. Syed, R. E. Stephenson, A. H. Rickard, and B. R. Boles, "Functional amyloids composed of phenol soluble modulins stabilize *Staphylococcus aureus* biofilms," (in eng), *PLoS Pathog,* vol. 8, no. 6, pp. e1002744-e1002744, 2012, doi: 10.1371/journal.ppat.1002744.
[17] C. f. D. C. a. Prevention. "Healthcare-Associated Infections Data Portal." https://www.cdc.gov/hai/data/portal/index.html.
[18] S. S. Magill *et al.*, "Changes in Prevalence of Health Care-Associated Infections in U.S. Hospitals," (in eng), *N Engl J Med,* vol. 379, no. 18, pp. 1732-1744, Nov 1 2018, doi: 10.1056/NEJMoa1801550.
[19] K. Gidey, M. T. Gidey, B. Y. Hailu, Z. B. Gebreamlak, and Y. L. Niriayo, "Clinical and economic burden of healthcare-associated infections: A prospective cohort study," (in eng), *PLoS One,* vol. 18, no. 2, p. e0282141, 2023, doi: 10.1371/journal.pone.0282141.
[20] N. Høiby *et al.*, "ESCMID guideline for the diagnosis and treatment of biofilm infections 2014," (in eng), *Clin Microbiol Infect,* vol. 21 Suppl 1, pp. S1-25, May 2015, doi: 10.1016/j.cmi.2014.10.024.
[21] J. D. Bryers, "Medical biofilms," (in eng), *Biotechnol Bioeng,* vol. 100, no. 1, pp. 1-18, May 1 2008, doi: 10.1002/bit.21838.
[22] K. Lewis, "Multidrug Tolerance of Biofilms and Persister Cells," in *Bacterial Biofilms*, T. Romeo Ed. Berlin, Heidelberg: Springer Berlin Heidelberg, 2008, pp. 107-131.
[23] D. Lebeaux, J.-M. Ghigo, and C. Beloin, "Biofilm-Related Infections: Bridging the Gap between Clinical Management and Fundamental Aspects of Recalcitrance toward Antibiotics," *Microbiology and Molecular Biology Reviews,* vol. 78, no. 3, pp. 510-543, 2014, doi: 10.1128/mmbr.00013-14.
[24] C. von Eiff, C. Heilmann, and G. Peters, "New aspects in the molecular basis of polymer-associated infections due to staphylococci," (in eng), *Eur J Clin Microbiol Infect Dis,* vol. 18, no. 12, pp. 843-6, Dec 1999, doi: 10.1007/s100960050417.
[25] A. Prinzi and R. Rohde. "The Role of Bacterial Biofilms in Antimicrobial Resistance." American Society for Microbiology. https://asm.org/Articles/2023/March/The-Role-of-Bacterial-Biofilms-in-Antimicrobial-Re (accessed.
[26] F. Giorgi, J. M. Curran, and E. A. Patterson, "Real-time monitoring of the dynamics and interactions of bacteria and the early-stage formation of biofilms," *Scientific Reports,* vol. 12, no. 1, p. 18146, 2022/10/28 2022, doi: 10.1038/s41598-022-22669-0.
[27] J. D. Bryers, C. M. Giachelli, and B. D. Ratner, "Engineering biomaterials to integrate and heal: the biocompatibility paradigm shifts," (in eng), *Biotechnol Bioeng,* vol. 109, no. 8, pp. 1898-911, Aug 2012, doi: 10.1002/bit.24559.
[28] "2024 Alzheimer's disease facts and figures," (in eng), *Alzheimers Dement,* vol. 20, no. 5, pp. 3708-3821, May 2024, doi: 10.1002/alz.13809.
[29] J. E. Morley, S. A. Farr, W. A. Banks, S. N. Johnson, K. A. Yamada, and L. Xu, "A physiological role for amyloid-beta protein:enhancement of learning and memory," (in eng), *J Alzheimers Dis,* vol. 19, no. 2, pp. 441-9, 2010, doi: 10.3233/jad-2009-1230.
[30] G. M. Bishop and S. R. Robinson, "Physiological roles of amyloid-beta and implications for its removal in Alzheimer's disease," (in eng), *Drugs Aging,* vol. 21, no. 10, pp. 621-30, 2004, doi: 10.2165/00002512-200421100-00001.

[31] J. S. Whitson, D. J. Selkoe, and C. W. Cotman, "Amyloid beta protein enhances the survival of hippocampal neurons in vitro," (in eng), *Science,* vol. 243, no. 4897, pp. 1488-90, Mar 17 1989, doi: 10.1126/science.2928783.
[32] M. Hiltunen, T. van Groen, and J. Jolkkonen, "Functional roles of amyloid-beta protein precursor and amyloid-beta peptides: evidence from experimental studies," (in eng), *J Alzheimers Dis,* vol. 18, no. 2, pp. 401-12, 2009, doi: 10.3233/jad-2009-1154.
[33] C. Haass and D. J. Selkoe, "Soluble protein oligomers in neurodegeneration: lessons from the Alzheimer's amyloid beta-peptide," (in eng), *Nat Rev Mol Cell Biol,* vol. 8, no. 2, pp. 101-12, Feb 2007, doi: 10.1038/nrm2101.
[34] M. P. Lambert *et al.*, "Vaccination with soluble Abeta oligomers generates toxicity-neutralizing antibodies," (in eng), *J Neurochem,* vol. 79, no. 3, pp. 595-605, Nov 2001, doi: 10.1046/j.1471-4159.2001.00592.x.
[35] R. D. Klein *et al.*, "Structure-Function Analysis of the Curli Accessory Protein CsgE Defines Surfaces Essential for Coordinating Amyloid Fiber Formation," (in eng), *mBio,* vol. 9, no. 4, Jul 17 2018, doi: 10.1128/mBio.01349-18.
[36] M. Sakono and T. Zako, "Amyloid oligomers: formation and toxicity of Abeta oligomers," (in eng), *Febs j,* vol. 277, no. 6, pp. 1348-58, Mar 2010, doi: 10.1111/j.1742-4658.2010.07568.x.
[37] K. R. Zahs and K. H. Ashe, "β-Amyloid oligomers in aging and Alzheimer's disease," (in eng), *Front Aging Neurosci,* vol. 5, p. 28, 2013, doi: 10.3389/fnagi.2013.00028.
[38] D. Shea *et al.*, "α-Sheet secondary structure in amyloid β-peptide drives aggregation and toxicity in Alzheimer's disease," *Proceedings of the National Academy of Sciences,* vol. 116, no. 18, p. 8895, 2019, doi: 10.1073/pnas.1820585116.
[39] T. Yang, S. Li, H. Xu, D. M. Walsh, and D. J. Selkoe, "Large Soluble Oligomers of Amyloid β-Protein from Alzheimer Brain Are Far Less Neuroactive Than the Smaller Oligomers to Which They Dissociate," (in eng), *J Neurosci,* vol. 37, no. 1, pp. 152-163, Jan 4 2017, doi: 10.1523/jneurosci.1698-16.2016.
[40] D. V. Hansen, J. E. Hanson, and M. Sheng, "Microglia in Alzheimer's disease," (in eng), *J Cell Biol,* vol. 217, no. 2, pp. 459-472, Feb 5 2018, doi: 10.1083/jcb.201709069.
[41] T. Prosswimmer, A. Heng, and V. Daggett, "Mechanistic insights into the role of amyloid-β in innate immunity," *Scientific Reports,* vol. 14, no. 1, p. 5376, 2024/03/05 2024, doi: 10.1038/s41598-024-55423-9.
[42] T. P. Knowles, M. Vendruscolo, and C. M. Dobson, "The amyloid state and its association with protein misfolding diseases," (in eng), *Nat Rev Mol Cell Biol,* vol. 15, no. 6, pp. 384-96, Jun 2014, doi: 10.1038/nrm3810.
[43] W. F. Xue, A. L. Hellewell, W. S. Gosal, S. W. Homans, E. W. Hewitt, and S. E. Radford, "Fibril fragmentation enhances amyloid cytotoxicity," (in eng), *J Biol Chem,* vol. 284, no. 49, pp. 34272-82, Dec 4 2009, doi: 10.1074/jbc.M109.049809.
[44] J. L. Tomic, A. Pensalfini, E. Head, and C. G. Glabe, "Soluble fibrillar oligomer levels are elevated in Alzheimer's disease brain and correlate with cognitive dysfunction," (in eng), *Neurobiol Dis,* vol. 35, no. 3, pp. 352-8, Sep 2009, doi: 10.1016/j.nbd.2009.05.024.
[45] J. Hardy and D. J. Selkoe, "The amyloid hypothesis of Alzheimer's disease: progress and problems on the road to therapeutics," (in eng), *Science,* vol. 297, no. 5580, pp. 353-6, Jul 19 2002, doi: 10.1126/science.1072994.

[46] M. Bucciantini *et al.*, "Inherent toxicity of aggregates implies a common mechanism for protein misfolding diseases," (in eng), *Nature,* vol. 416, no. 6880, pp. 507-11, Apr 4 2002, doi: 10.1038/416507a.
[47] M. L. Evans and M. R. Chapman, "Curli biogenesis: order out of disorder," (in eng), *Biochim Biophys Acta,* vol. 1843, no. 8, pp. 1551-8, Aug 2014, doi: 10.1016/j.bbamcr.2013.09.010.
[48] M. Zaman and M. Andreasen, "Cross-talk between individual phenol-soluble modulins in *Staphylococcus aureus* biofilm enables rapid and efficient amyloid formation," (in eng), *Elife,* vol. 9, Dec 1 2020, doi: 10.7554/eLife.59776.
[49] R. M. Donlan, "Biofilms: microbial life on surfaces," (in eng), *Emerg Infect Dis,* vol. 8, no. 9, pp. 881-90, Sep 2002, doi: 10.3201/eid0809.020063.
[50] C. Y. Lin *et al.*, "Toxic human islet amyloid polypeptide (h-IAPP) oligomers are intracellular, and vaccination to induce anti-toxic oligomer antibodies does not prevent h-IAPP-induced beta-cell apoptosis in h-IAPP transgenic mice," (in eng), *Diabetes,* vol. 56, no. 5, pp. 1324-32, May 2007, doi: 10.2337/db06-1579.
[51] L. Haataja, T. Gurlo, C. J. Huang, and P. C. Butler, "Islet amyloid in type 2 diabetes, and the toxic oligomer hypothesis," (in eng), *Endocr Rev,* vol. 29, no. 3, pp. 303-16, May 2008, doi: 10.1210/er.2007-0037.
[52] R. Kayed *et al.*, "Common structure of soluble amyloid oligomers implies common mechanism of pathogenesis," (in eng), *Science,* vol. 300, no. 5618, pp. 486-9, Apr 18 2003, doi: 10.1126/science.1079469.
[53] T. M. Bi and V. Daggett, "The Role of α-sheet in Amyloid Oligomer Aggregation and Toxicity," (in eng), *Yale J Biol Med,* vol. 91, no. 3, pp. 247-255, Sep 2018.
[54] N. L. Maris, D. Shea, A. Bleem, J. D. Bryers, and V. Daggett, "Chemical and Physical Variability in Structural Isomers of an l/d α-Sheet Peptide Designed To Inhibit Amyloidogenesis," (in eng), *Biochemistry,* vol. 57, no. 5, pp. 507-510, 2018, doi: 10.1021/acs.biochem.7b00345.
[55] V. Daggett, "Alpha-sheet: The toxic conformer in amyloid diseases?," (in eng), *Acc Chem Res,* vol. 39, no. 9, pp. 594-602, Sep 2006, doi: 10.1021/ar0500719.
[56] Y. Guo, G. Song, M. Sun, J. Wang, and Y. Wang, "Prevalence and Therapies of Antibiotic-Resistance in Staphylococcus aureus," (in English), *Frontiers in Cellular and Infection Microbiology,* Review vol. 10, 2020-March-17 2020, doi: 10.3389/fcimb.2020.00107.
[57] R. A. Fisher, B. Gollan, and S. Helaine, "Persistent bacterial infections and persister cells," *Nature Reviews Microbiology,* vol. 15, no. 8, pp. 453-464, 2017/08/01 2017, doi: 10.1038/nrmicro.2017.42.
[58] H. A. Khan, F. K. Baig, and R. Mehboob, "Nosocomial infections: Epidemiology, prevention, control and surveillance," *Asian Pacific Journal of Tropical Biomedicine,* vol. 7, no. 5, pp. 478-482, 2017/05/01/ 2017, doi: https://doi.org/10.1016/j.apjtb.2017.01.019.
[59] L. M. Weiner *et al.*, "Antimicrobial-Resistant Pathogens Associated With Healthcare-Associated Infections: Summary of Data Reported to the National Healthcare Safety Network at the Centers for Disease Control and Prevention, 2011-2014," (in eng), *Infect Control Hosp Epidemiol,* vol. 37, no. 11, pp. 1288-1301, Nov 2016, doi: 10.1017/ice.2016.174.
[60] L. M. Weiner *et al.*, "Vital Signs: Preventing Antibiotic-Resistant Infections in Hospitals - United States, 2014," *American journal of transplantation : official journal of the*

American Society of Transplantation and the American Society of Transplant Surgeons, vol. 16, no. 7, pp. 2224-30, 6/28/entrez6/28/pubmed11/29/medline 2016. [Online]. Available: https://www.unboundmedicine.com/medline/citation/27348802/Vital_Signs:_Preventing_Antibiotic_Resistant_Infections_in_Hospitals___United_States_2014_.

[61] CDC, "Antibiotic resistance threats in the United States, 2019," *Atlanta, Georgia.,* 2019.

[62] J. M. Munita and C. A. Arias, "Mechanisms of Antibiotic Resistance," (in eng), *Microbiol Spectr,* vol. 4, no. 2, Apr 2016, doi: 10.1128/microbiolspec.VMBF-0016-2015.

[63] E. Banin, K. M. Brady, and E. P. Greenberg, "Chelator-induced dispersal and killing of *Pseudomonas aeruginosa* cells in a biofilm," (in eng), *Appl Environ Microbiol,* vol. 72, no. 3, pp. 2064-9, Mar 2006, doi: 10.1128/aem.72.3.2064-2069.2006.

[64] S. Singh, S. Datta, K. B. Narayanan, and K. N. Rajnish, "Bacterial exo-polysaccharides in biofilms: role in antimicrobial resistance and treatments," (in eng), *J Genet Eng Biotechnol,* vol. 19, no. 1, p. 140, Sep 23 2021, doi: 10.1186/s43141-021-00242-y.

[65] B. Kot, "Antibiotic Resistance Among Uropathogenic *Escherichia coli*," (in eng), *Pol J Microbiol,* vol. 68, no. 4, pp. 403-415, Dec 2019, doi: 10.33073/pjm-2019-048.

[66] H. I. Al-Talib, C. Y. Yean, K. Al-Jashamy, and H. Hasan, "Methicillin-resistant *Staphylococcus aureus* nosocomial infection trends in Hospital Universiti Sains Malaysia during 2002-2007," (in eng), *Ann Saudi Med,* vol. 30, no. 5, pp. 358-63, Sep-Oct 2010, doi: 10.4103/0256-4947.67077.

[67] S. Yu *et al.*, "PslG, a self-produced glycosyl hydrolase, triggers biofilm disassembly by disrupting exopolysaccharide matrix," (in eng), *Cell Res,* vol. 25, no. 12, pp. 1352-67, Dec 2015, doi: 10.1038/cr.2015.129.

[68] H. Devlin, S. Fulaz, D. W. Hiebner, J. P. O'Gara, and E. Casey, "Enzyme-Functionalized Mesoporous Silica Nanoparticles to Target *Staphylococcus aureus* and Disperse Biofilms," (in eng), *Int J Nanomedicine,* vol. 16, pp. 1929-1942, 2021, doi: 10.2147/ijn.S293190.

[69] M. Okshevsky, V. R. Regina, and R. L. Meyer, "Extracellular DNA as a target for biofilm control," *Current Opinion in Biotechnology,* vol. 33, pp. 73-80, 2015/06/01/ 2015, doi: https://doi.org/10.1016/j.copbio.2014.12.002.

[70] L. Gao *et al.*, "Nanocatalysts promote *Streptococcus mutans* biofilm matrix degradation and enhance bacterial killing to suppress dental caries in vivo," (in eng), *Biomaterials,* vol. 101, pp. 272-84, Sep 2016, doi: 10.1016/j.biomaterials.2016.05.051.

[71] Y. Wang *et al.*, "Anti-Biofilm Activity of Graphene Quantum Dots via Self-Assembly with Bacterial Amyloid Proteins," (in eng), *ACS Nano,* vol. 13, no. 4, pp. 4278-4289, Apr 23 2019, doi: 10.1021/acsnano.8b09403.

[72] L. C. Powell *et al.*, "Targeted disruption of the extracellular polymeric network of *Pseudomonas aeruginosa* biofilms by alginate oligosaccharides," (in eng), *NPJ Biofilms Microbiomes,* vol. 4, p. 13, 2018, doi: 10.1038/s41522-018-0056-3.

[73] L. Cegelski *et al.*, "Small-molecule inhibitors target *Escherichia coli* amyloid biogenesis and biofilm formation," *Nature Chemical Biology,* vol. 5, no. 12, pp. 913-919, 2009/12/01 2009, doi: 10.1038/nchembio.242.

[74] V. Daggett, "α-Sheet: The Toxic Conformer in Amyloid Diseases?," *Accounts of Chemical Research,* vol. 39, no. 9, pp. 594-602, 2006/09/01 2006, doi: 10.1021/ar0500719.

[75] D. Shea *et al.*, "SOBA: Development and testing of a soluble oligomer binding assay for detection of amyloidogenic toxic oligomers," (in eng), *Proc Natl Acad Sci U S A,* vol. 119, no. 50, p. e2213157119, Dec 13 2022, doi: 10.1073/pnas.2213157119.
[76] M. A. Mulvey, J. D. Schilling, and S. J. Hultgren, "Establishment of a persistent *Escherichia coli* reservoir during the acute phase of a bladder infection," (in eng), *Infect Immun,* vol. 69, no. 7, pp. 4572-9, Jul 2001, doi: 10.1128/iai.69.7.4572-4579.2001.
[77] V. García *et al.*, "Genome-wide analysis of fitness-factors in uropathogenic *Escherichia coli* during growth in laboratory media and during urinary tract infections," (in eng), *Microb Genom,* vol. 7, no. 12, Dec 2021, doi: 10.1099/mgen.0.000719.
[78] B. J. Akhavan, N. R. Khanna, and P. Vijhani, "Amoxicillin," in *StatPearls*. Treasure Island (FL) ineligible companies. Disclosure: Niloufar Khanna declares no relevant financial relationships with ineligible companies. Disclosure: Praveen Vijhani declares no relevant financial relationships with ineligible companies.: StatPearls Publishing
Copyright © 2023, StatPearls Publishing LLC., 2023.
[79] D. Sharma, R. P. Patel, S. T. R. Zaidi, M. M. R. Sarker, Q. Y. Lean, and L. C. Ming, "Interplay of the Quality of Ciprofloxacin and Antibiotic Resistance in Developing Countries," (in eng), *Front Pharmacol,* vol. 8, p. 546, 2017, doi: 10.3389/fphar.2017.00546.
[80] J. A. Washington, 2nd and W. R. Wilson, "Erythromycin: a microbial and clinical perspective after 30 years of clinical use (1)," (in eng), *Mayo Clin Proc,* vol. 60, no. 3, pp. 189-203, Mar 1985, doi: 10.1016/s0025-6196(12)60219-5.
[81] B. J. Chaves and P. Tadi, "Gentamicin," in *StatPearls*. Treasure Island (FL) ineligible companies. Disclosure: Prasanna Tadi declares no relevant financial relationships with ineligible companies.: StatPearls Publishing
Copyright © 2023, StatPearls Publishing LLC., 2023.
[82] S. Patel, C. V. Preuss, and F. Bernice, "Vancomycin," in *StatPearls*. Treasure Island (FL) ineligible companies. Disclosure: Charles Preuss declares no relevant financial relationships with ineligible companies. Disclosure: Fidelia Bernice declares no relevant financial relationships with ineligible companies.: StatPearls Publishing
Copyright © 2023, StatPearls Publishing LLC., 2023.
[83] Z. Rafaque *et al.*, "In-vitro Investigation of Antibiotics Efficacy Against Uropathogenic *Escherichia coli* Biofilms and Antibiotic Induced Biofilm Formation at Sub-Minimum Inhibitory Concentration of Ciprofloxacin," (in eng), *Infect Drug Resist,* vol. 13, pp. 2801-2810, 2020, doi: 10.2147/IDR.S258355.
[84] L. Thieme *et al.*, "MBEC Versus MBIC: the Lack of Differentiation between Biofilm Reducing and Inhibitory Effects as a Current Problem in Biofilm Methodology," *Biological Procedures Online,* vol. 21, no. 1, p. 18, 2019/09/13 2019, doi: 10.1186/s12575-019-0106-0.
[85] Y. Okae *et al.*, "Estimation of Minimum Biofilm Eradication Concentration (MBEC) on In Vivo Biofilm on Orthopedic Implants in a Rodent Femoral Infection Model," (in eng), *Front Cell Infect Microbiol,* vol. 12, p. 896978, 2022, doi: 10.3389/fcimb.2022.896978.
[86] J. B. Mandell *et al.*, "Large variations in clinical antibiotic activity against Staphylococcus aureus biofilms of periprosthetic joint infection isolates," (in eng), *J Orthop Res,* vol. 37, no. 7, pp. 1604-1609, Jul 2019, doi: 10.1002/jor.24291.

[87] R. K. Pettit, C. A. Weber, and G. R. Pettit, "Application of a high throughput Alamar blue biofilm susceptibility assay to *Staphylococcus aureus* biofilms," (in eng), *Ann Clin Microbiol Antimicrob,* vol. 8, p. 28, Oct 27 2009, doi: 10.1186/1476-0711-8-28.
[88] P. Castaneda, A. McLaren, G. Tavaziva, and D. Overstreet, "Biofilm Antimicrobial Susceptibility Increases With Antimicrobial Exposure Time," (in eng), *Clin Orthop Relat Res,* vol. 474, no. 7, pp. 1659-64, Jul 2016, doi: 10.1007/s11999-016-4700-z.
[89] C. D. Cruz, S. Shah, and P. Tammela, "Defining conditions for biofilm inhibition and eradication assays for Gram-positive clinical reference strains," *BMC Microbiology,* vol. 18, no. 1, p. 173, 2018/11/03 2018, doi: 10.1186/s12866-018-1321-6.
[90] W. Adamus-Białek *et al.*, "Ciprofloxacin, amoxicillin, and aminoglycosides stimulate genetic and phenotypic changes in uropathogenic *Escherichia coli* strains," (in eng), *Virulence,* vol. 10, no. 1, pp. 260-276, 2019, doi: 10.1080/21505594.2019.1596507.
[91] A. D. Verderosa, J. Harris, R. Dhouib, M. Totsika, and K. E. Fairfull-Smith, "Eradicating uropathogenic *Escherichia coli* biofilms with a ciprofloxacin–dinitroxide conjugate," *MedChemComm,* 10.1039/C9MD00062C vol. 10, no. 5, pp. 699-711, 2019, doi: 10.1039/C9MD00062C.
[92] L. W. Goneau *et al.*, "Selective Target Inactivation Rather than Global Metabolic Dormancy Causes Antibiotic Tolerance in Uropathogens," *Antimicrobial Agents and Chemotherapy,* vol. 58, no. 4, p. 2089, 2014, doi: 10.1128/AAC.02552-13.
[93] M. Biancalana and S. Koide, "Molecular mechanism of Thioflavin-T binding to amyloid fibrils," (in eng), *Biochim Biophys Acta,* vol. 1804, no. 7, pp. 1405-12, Jul 2010, doi: 10.1016/j.bbapap.2010.04.001.
[94] T. J. Silhavy, D. Kahne, and S. Walker, "The bacterial cell envelope," (in eng), *Cold Spring Harb Perspect Biol,* vol. 2, no. 5, p. a000414, May 2010, doi: 10.1101/cshperspect.a000414.
[95] M. M. Alreshidi, R. H. Dunstan, M. M. Macdonald, J. Gottfries, and T. K. Roberts, "The Uptake and Release of Amino Acids by Staphylococcus aureus at Mid-Exponential and Stationary Phases and Their Corresponding Responses to Changes in Temperature, pH and Osmolality," (in eng), *Front Microbiol,* vol. 10, p. 3059, 2019, doi: 10.3389/fmicb.2019.03059.
[96] S. Perov *et al.*, "Structural Insights into Curli CsgA Cross-β Fibril Architecture Inspire Repurposing of Anti-amyloid Compounds as Anti-biofilm Agents," *PLoS Pathog,* vol. 15, no. 8, p. e1007978, 2019, doi: 10.1371/journal.ppat.1007978.
[97] D. Chen, J. Li, T. Pan, R. Wu, Y. Tao, and H. Lin, "The broad-spectrum antibiofilm activity of amyloid-forming hexapeptides," *Microbial Biotechnology,* https://doi.org/10.1111/1751-7915.13721 vol. 14, no. 2, pp. 656-667, 2021/03/01 2021, doi: https://doi.org/10.1111/1751-7915.13721.
[98] D. O. Serra, F. Mika, A. M. Richter, and R. Hengge, "The green tea polyphenol EGCG inhibits *E. coli* biofilm formation by impairing amyloid curli fibre assembly and downregulating the biofilm regulator CsgD via the σ(E) -dependent sRNA RybB," (in eng), *Mol Microbiol,* vol. 101, no. 1, pp. 136-51, Jul 2016, doi: 10.1111/mmi.13379.
[99] M. Pruteanu, J. I. Hernández Lobato, T. Stach, and R. Hengge, "Common plant flavonoids prevent the assembly of amyloid curli fibres and can interfere with bacterial biofilm formation," (in eng), *Environ Microbiol,* vol. 22, no. 12, pp. 5280-5299, Dec 2020, doi: 10.1111/1462-2920.15216.

[100] T. Bikels-Goshen, E. Landau, S. Saguy, and R. Shapira, "Staphylococcal strains adapted to epigallocathechin gallate (EGCG) show reduced susceptibility to vancomycin, oxacillin and ampicillin, increased heat tolerance, and altered cell morphology," *International Journal of Food Microbiology,* vol. 138, no. 1, pp. 26-31, 2010/03/31/ 2010, doi: https://doi.org/10.1016/j.ijfoodmicro.2010.01.011.
[101] C. O'May, A. Ciobanu, H. Lam, and N. Tufenkji, "Tannin derived materials can block swarming motility and enhance biofilm formation in *Pseudomonas aeruginosa*," *Biofouling,* vol. 28, no. 10, pp. 1063-1076, 2012/11/01 2012, doi: 10.1080/08927014.2012.725130.
[102] M. Stenvang *et al.*, "Epigallocatechin Gallate Remodels Overexpressed Functional Amyloids in *Pseudomonas aeruginosa* and Increases Biofilm Susceptibility to Antibiotic Treatment," (in eng), *J Biol Chem,* vol. 291, no. 51, pp. 26540-26553, Dec 16 2016, doi: 10.1074/jbc.M116.739953.
[103] M. W. van der Kamp *et al.*, "Dynameomics: a comprehensive database of protein dynamics," (in eng), *Structure,* vol. 18, no. 4, pp. 423-35, Mar 14 2010, doi: 10.1016/j.str.2010.01.012.
[104] D. A. C. Beck, D. O. V. Alonso, D. Inoyama, and V. Daggett, "The intrinsic conformational propensities of the 20 naturally occurring amino acids and reflection of these propensities in proteins," *Proceedings of the National Academy of Sciences,* vol. 105, no. 34, pp. 12259-12264, 2008, doi: doi:10.1073/pnas.0706527105.
[105] J. Y. Lim, J. M. May, and L. Cegelski, "Dimethyl sulfoxide and ethanol elicit increased amyloid biogenesis and amyloid-integrated biofilm formation in *Escherichia coli*," (in eng), *Appl Environ Microbiol,* vol. 78, no. 9, pp. 3369-78, May 2012, doi: 10.1128/aem.07743-11.
[106] D. A. Blomster-Hautamaa and P. M. Schlievert, "Preparation of toxic shock syndrome toxin-1," (in eng), *Methods Enzymol,* vol. 165, pp. 37-43, 1988, doi: 10.1016/s0076-6879(88)65009-9.
[107] B. Herigstad, M. Hamilton, and J. Heersink, "How to optimize the drop plate method for enumerating bacteria," (in eng), *J Microbiol Methods,* vol. 44, no. 2, pp. 121-9, Mar 1 2001, doi: 10.1016/s0167-7012(00)00241-4.
[108] H. Sorg, D. J. Tilkorn, S. Hager, J. Hauser, and U. Mirastschijski, "Skin Wound Healing: An Update on the Current Knowledge and Concepts," *European Surgical Research,* vol. 58, no. 1-2, pp. 81-94, 2016, doi: 10.1159/000454919.
[109] S. L. Percival, S. M. McCarty, and B. Lipsky, "Biofilms and Wounds: An Overview of the Evidence," (in eng), *Adv Wound Care (New Rochelle),* vol. 4, no. 7, pp. 373-381, 2015, doi: 10.1089/wound.2014.0557.
[110] I. Negut, V. Grumezescu, and A. M. Grumezescu, "Treatment Strategies for Infected Wounds," (in eng), *Molecules,* vol. 23, no. 9, Sep 18 2018, doi: 10.3390/molecules23092392.
[111] S. Darvishi, S. Tavakoli, M. Kharaziha, H. H. Girault, C. F. Kaminski, and I. Mela, "Advances in the Sensing and Treatment of Wound Biofilms," *Angewandte Chemie International Edition,* vol. 61, no. 13, p. e202112218, 2022/03/21 2022, doi: https://doi.org/10.1002/anie.202112218.
[112] M. P. Rowan *et al.*, "Burn wound healing and treatment: review and advancements," (in eng), *Crit Care,* vol. 19, pp. 243-243, 2015, doi: 10.1186/s13054-015-0961-2.

[113] M. R. Parsek and P. K. Singh, "Bacterial Biofilms: An Emerging Link to Disease Pathogenesis," *Annu Rev Microbiol,* vol. 57, no. 1, pp. 677-701, 2003/10/01 2003, doi: 10.1146/annurev.micro.57.030502.090720.
[114] A. Bleem, R. Francisco, J. D. Bryers, and V. Daggett, "Designed α-sheet peptides suppress amyloid formation in *Staphylococcus aureus* biofilms," (in eng), *NPJ Biofilms Microbiomes,* vol. 3, p. 16, 2017, doi: 10.1038/s41522-017-0025-2.
[115] A. Bleem *et al.*, "Protein Engineering Reveals Mechanisms of Functional Amyloid Formation in *Pseudomonas aeruginosa* Biofilms," (in eng), *J Mol Biol,* vol. 430, no. 20, pp. 3751-3763, Oct 12 2018, doi: 10.1016/j.jmb.2018.06.043.
[116] T. Prosswimmer, S. E. Nick, J. D. Bryers, and V. Daggett, "Designed De Novo α-Sheet Peptides Destabilize Bacterial Biofilms and Increase the Susceptibility of *E. coli* and *S. aureus* to Antibiotics," *Int J Mol Sci*, vol. 25, no. 13*,* doi: 10.3390/ijms25137024.
[117] G. Decher, M. Eckle, J. Schmitt, and B. Struth, "Layer-by-layer assembled multicomposite films," *Current Opinion in Colloid & Interface Science,* vol. 3, no. 1, pp. 32-39, 1998/02/01/ 1998, doi: https://doi.org/10.1016/S1359-0294(98)80039-3.
[118] S. Zhao *et al.*, "The Future of Layer-by-Layer Assembly: A Tribute to ACS Nano Associate Editor Helmuth Möhwald," *ACS Nano,* vol. 13, no. 6, pp. 6151-6169, 2019/06/25 2019, doi: 10.1021/acsnano.9b03326.
[119] A. P. Gomes, J. F. Mano, J. A. Queiroz, and I. C. Gouveia, "Layer-by-Layer Deposition of Antibacterial Polyelectrolytes on Cotton Fibres," *Journal of Polymers and the Environment,* vol. 20, no. 4, pp. 1084-1094, 2012/12/01 2012, doi: 10.1007/s10924-012-0507-5.
[120] N. M. Alves, C. Picart, and J. F. Mano, "Self assembling and crosslinking of polyelectrolyte multilayer films of chitosan and alginate studied by QCM and IR spectroscopy," (in eng), *Macromol Biosci,* vol. 9, no. 8, pp. 776-85, Aug 11 2009, doi: 10.1002/mabi.200800336.
[121] G. V. Martins, E. G. Merino, J. F. Mano, and N. M. Alves, "Crosslink effect and albumin adsorption onto chitosan/alginate multilayered systems: an in situ QCM-D study," (in eng), *Macromol Biosci,* vol. 10, no. 12, pp. 1444-55, Dec 8 2010, doi: 10.1002/mabi.201000193.
[122] S. V. Madihally and H. W. T. Matthew, "Porous chitosan scaffolds for tissue engineering," *Biomaterials,* vol. 20, no. 12, pp. 1133-1142, 1999/06/01/ 1999, doi: https://doi.org/10.1016/S0142-9612(99)00011-3.
[123] A. Di Martino, M. Sittinger, and M. V. Risbud, "Chitosan: A versatile biopolymer for orthopaedic tissue-engineering," *Biomaterials,* vol. 26, no. 30, pp. 5983-5990, 2005/10/01/ 2005, doi: https://doi.org/10.1016/j.biomaterials.2005.03.016.
[124] A. Chenite *et al.*, "Novel injectable neutral solutions of chitosan form biodegradable gels in situ," *Biomaterials,* vol. 21, no. 21, pp. 2155-2161, 2000/11/01/ 2000, doi: https://doi.org/10.1016/S0142-9612(00)00116-2.
[125] A. Gomes, Mano, JF., Queiroz, JA., Gouveia, IC., "Incorporation of antimicrobial peptides on functionalized cotton gauzes for medical applications," *Carboyhydrate Polymers,* 2015.
[126] J. A. Rowley, G. Madlambayan, and D. J. Mooney, "Alginate hydrogels as synthetic extracellular matrix materials," *Biomaterials,* vol. 20, no. 1, pp. 45-53, 1999/01/01/ 1999, doi: https://doi.org/10.1016/S0142-9612(98)00107-0.

[127] K. Y. Lee and D. J. Mooney, "Alginate: properties and biomedical applications," (in eng), *Prog Polym Sci,* vol. 37, no. 1, pp. 106-126, Jan 2012, doi: 10.1016/j.progpolymsci.2011.06.003.
[128] M. Otterlei, K. Østgaard, G. Skjåk-Bræk, O. Smidsrød, P. Soon-Shiong, and T. Espevik, "Induction of Cytokine Production from Human Monocytes Stimulated with Alginate," *Journal of Immunotherapy,* vol. 10, no. 4, 1991. [Online]. Available: https://journals.lww.com/immunotherapy-journal/fulltext/1991/08000/induction_of_cytokine_production_from_human.7.aspx.
[129] A. P. Gomes, J. F. Mano, J. A. Queiroz, and I. C. Gouveia, "New biomaterial based on cotton with incorporated Biomolecules," *Journal of Applied Polymer Science,* https://doi.org/10.1002/app.40519 vol. 131, no. 15, 2014/08/05 2014, doi: https://doi.org/10.1002/app.40519.
[130] T. Saito, Y. Okita, T. T. Nge, J. Sugiyama, and A. Isogai, "TEMPO-mediated oxidation of native cellulose: Microscopic analysis of fibrous fractions in the oxidized products," *Carbohydrate Polymers,* vol. 65, no. 4, pp. 435-440, 2006/09/13/ 2006, doi: https://doi.org/10.1016/j.carbpol.2006.01.034.
[131] Z. Dang, J. Zhang, and A. J. Ragauskas, "Characterizing TEMPO-mediated oxidation of ECF bleached softwood kraft pulps," *Carbohydrate Polymers,* vol. 70, no. 3, pp. 310-317, 2007/10/01/ 2007, doi: https://doi.org/10.1016/j.carbpol.2007.04.014.
[132] C. Chung, M. Lee, and E. K. Choe, "Characterization of cotton fabric scouring by FT-IR ATR spectroscopy," *Carbohydrate Polymers,* vol. 58, no. 4, pp. 417-420, 2004/12/07/ 2004, doi: https://doi.org/10.1016/j.carbpol.2004.08.005.
[133] D. Alves, T. Sileika, P. B. Messersmith, and M. O. Pereira, "Polydopamine-Mediated Immobilization of Alginate Lyase to Prevent *P. aeruginosa* Adhesion," (in eng), *Macromol Biosci,* vol. 16, no. 9, pp. 1301-10, Sep 2016, doi: 10.1002/mabi.201600077.
[134] G. Lawrie *et al.*, "Interactions between alginate and chitosan biopolymers characterized using FTIR and XPS," (in eng), *Biomacromolecules,* vol. 8, no. 8, pp. 2533-41, Aug 2007, doi: 10.1021/bm070014y.
[135] T. Mosmann, "Rapid colorimetric assay for cellular growth and survival: Application to proliferation and cytotoxicity assays," *Journal of Immunological Methods,* vol. 65, no. 1, pp. 55-63, 1983/12/16/ 1983, doi: https://doi.org/10.1016/0022-1759(83)90303-4.
[136] H. Ma, E. T. Darmawan, M. Zhang, L. Zhang, and J. D. Bryers, "Development of a poly(ether urethane) system for the controlled release of two novel anti-biofilm agents based on gallium or zinc and its efficacy to prevent bacterial biofilm formation," (in eng), *J Control Release,* vol. 172, no. 3, pp. 1035-44, Dec 28 2013, doi: 10.1016/j.jconrel.2013.10.005.
[137] C. Gallant-Behm, "Comparison of in vitro disc diffusion and time kill-kinetic assays for the evaluation of antimicrobial wound dressing efficacy," *Wound repair and regeneration.,* vol. 13, no. 4, p. 412, 2005.
[138] H. Ma and J. D. Bryers, "Non-invasive method to quantify local bacterial concentrations in a mixed culture biofilm," (in eng), *J Ind Microbiol Biotechnol,* vol. 37, no. 10, pp. 1081-9, Oct 2010, doi: 10.1007/s10295-010-0756-z.
[139] Z. A. Mirani and N. Jamil, "Effect of sub-lethal doses of vancomycin and oxacillin on biofilm formation by vancomycin intermediate resistant *Staphylococcus aureus*," (in eng), *J Basic Microbiol,* vol. 51, no. 2, pp. 191-5, Apr 2011, doi: 10.1002/jobm.201000221.

[140] L. R. Hoffman, D. A. D'Argenio, M. J. MacCoss, Z. Zhang, R. A. Jones, and S. I. Miller, "Aminoglycoside antibiotics induce bacterial biofilm formation," (in eng), *Nature,* vol. 436, no. 7054, pp. 1171-5, Aug 25 2005, doi: 10.1038/nature03912.
[141] B. Boonkaew, M. Kempf, R. Kimble, P. Supaphol, and L. Cuttle, "Antimicrobial efficacy of a novel silver hydrogel dressing compared to two common silver burn wound dressings: Acticoat™ and PolyMem Silver®," *Burns,* vol. 40, no. 1, pp. 89-96, 2014/02/01/ 2014, doi: https://doi.org/10.1016/j.burns.2013.05.011.
[142] G. Han and R. Ceilley, "Chronic Wound Healing: A Review of Current Management and Treatments," (in eng), *Adv Ther,* vol. 34, no. 3, pp. 599-610, Mar 2017, doi: 10.1007/s12325-017-0478-y.
[143] I. Khansa, A. R. Schoenbrunner, C. T. Kraft, and J. E. Janis, "Silver in Wound Care-Friend or Foe?: A Comprehensive Review," (in eng), *Plast Reconstr Surg Glob Open,* vol. 7, no. 8, p. e2390, Aug 2019, doi: 10.1097/gox.0000000000002390.
[144] S. L. Percival and S. M. McCarty, "Silver and Alginates: Role in Wound Healing and Biofilm Control," (in eng), *Adv Wound Care (New Rochelle),* vol. 4, no. 7, pp. 407-414, 2015, doi: 10.1089/wound.2014.0541.
[145] R. Smith, J. Russo, J. Fiegel, and N. Brogden, "Antibiotic Delivery Strategies to Treat Skin Infections When Innate Antimicrobial Defense Fails," (in eng), *Antibiotics (Basel),* vol. 9, no. 2, Feb 1 2020, doi: 10.3390/antibiotics9020056.
[146] M. Tenenhaus, & Rennekampff, H.O. . "Topical agents and dressings for local burn wound care." UpToDate. https://www.uptodate.com/contents/topical-agents-and-dressings-for-local-burn-wound-care (accessed 2020).
[147] M. E. Innes, N. Umraw, J. S. Fish, M. Gomez, and R. C. Cartotto, "The use of silver coated dressings on donor site wounds: a prospective, controlled matched pair study," (in eng), *Burns,* vol. 27, no. 6, pp. 621-7, Sep 2001, doi: 10.1016/s0305-4179(01)00015-8.
[148] M. Malone *et al.*, "The prevalence of biofilms in chronic wounds: a systematic review and meta-analysis of published data," (in eng), *J Wound Care,* vol. 26, no. 1, pp. 20-25, Jan 2 2017, doi: 10.12968/jowc.2017.26.1.20.
[149] S. L. Percival, P. G. Bowler, and D. Russell, "Bacterial resistance to silver in wound care," *Journal of Hospital Infection,* vol. 60, no. 1, pp. 1-7, 2005/05/01/ 2005, doi: https://doi.org/10.1016/j.jhin.2004.11.014.
[150] A. E. M. Hosny, S. A. Rasmy, D. S. Aboul-Magd, M. T. Kashef, and Z. E. El-Bazza, "The increasing threat of silver-resistance in clinical isolates from wounds and burns," (in eng), *Infect Drug Resist,* vol. 12, pp. 1985-2001, 2019, doi: 10.2147/idr.S209881.
[151] A. Panáček *et al.*, "Bacterial resistance to silver nanoparticles and how to overcome it," *Nature Nanotechnology,* vol. 13, no. 1, pp. 65-71, 2018/01/01 2018, doi: 10.1038/s41565-017-0013-y.
[152] K. Woo, C. Dowsett, B. Costa, S. Ebohon, E. J. Woodmansey, and M. Malone, "Efficacy of topical cadexomer iodine treatment in chronic wounds: Systematic review and meta-analysis of comparative clinical trials," (in eng), *Int Wound J,* vol. 18, no. 5, pp. 586-597, Oct 2021, doi: 10.1111/iwj.13560.
[153] D. Angel, P. Morey, J. Storer, and B. Mwipatayi, "The great debate over iodine in wound care continues: a review of the literature," *Wound Practice & Research: Journal of the Australian Wound Management Association,* vol. 16, no. 1, pp. 6-21, 2008.
[154] A. P. Gomes, J. F. Mano, J. A. Queiroz, and I. C. Gouveia, "Layer-by-layer deposition of antimicrobial polymers on cellulosic fibers: a new strategy to develop bioactive textiles,"

Polymers for Advanced Technologies, https://doi.org/10.1002/pat.3176 vol. 24, no. 11, pp. 1005-1010, 2013/11/01 2013, doi: https://doi.org/10.1002/pat.3176.

[155] C.-C. Hsu *et al.*, "Human islet amyloid polypeptide-induced β-cell cytotoxicity is linked to formation of α-sheet structure," *Protein Science,* vol. 33, no. 2, p. e4854, 2024/02/01 2024, doi: https://doi.org/10.1002/pro.4854.

[156] R. Serra *et al.*, "Chronic wound infections: the role of *Pseudomonas aeruginosa* and Staphylococcus aureus," *Expert Rev Anti Infect Ther,* vol. 13, no. 5, pp. 605-613, 2015/05/04 2015, doi: 10.1586/14787210.2015.1023291.

[157] P. G. Bowler, B. I. Duerden, and D. G. Armstrong, "Wound microbiology and associated approaches to wound management," (in eng), *Clin Microbiol Rev,* vol. 14, no. 2, pp. 244-69, Apr 2001, doi: 10.1128/cmr.14.2.244-269.2001.

[158] D. A. Beck, D. O. Alonso, D. Inoyama, and V. Daggett, "The intrinsic conformational propensities of the 20 naturally occurring amino acids and reflection of these propensities in proteins," (in eng), *Proc Natl Acad Sci U S A,* vol. 105, no. 34, pp. 12259-64, Aug 26 2008, doi: 10.1073/pnas.0706527105.

[159] M. J. Gomes AP, Queiroz JA, Gouveia IC., "Incorporation of antimicrobial peptides on functionalized cotton gauzes for medical applications," *Carbohydrate Polymers,* vol. 127:451-461, 2015, doi: 10.1016/j.carbpol.2015.03.089.

[160] C. Lin *et al.*, "Effects of the Conditions of the TEMPO/NaBr/NaClO System on Carboxyl Groups, Degree of Polymerization, and Yield of the Oxidized Cellulose," *BioResources; Vol 13, No 3 (2018),* 06/14/ 2018. [Online]. Available: https://ojs.cnr.ncsu.edu/index.php/BioRes/article/view/BioRes_13_3_5965_Lin_Conditions_Tempo_NaBr_Oxidized_Cellulose.

[161] G. Maurstad, Y. A. Mørch, A. R. Bausch, and B. T. Stokke, "Polyelectrolyte layer interpenetration and swelling of alginate–chitosan multilayers studied by dual wavelength reflection interference contrast microscopy," *Carbohydrate Polymers,* vol. 71, no. 4, pp. 672-681, 2008/03/07/ 2008, doi: https://doi.org/10.1016/j.carbpol.2007.07.019.

[162] M. M. Bradford, "A rapid and sensitive method for the quantitation of microgram quantities of protein utilizing the principle of protein-dye binding," *Analytical Biochemistry,* vol. 72, no. 1, pp. 248-254, 1976/05/07/ 1976, doi: https://doi.org/10.1016/0003-2697(76)90527-3.

[163] N. Carlsson, A. Borde, S. Wölfel, B. Åkerman, and A. Larsson, "Quantification of protein concentration by the Bradford method in the presence of pharmaceutical polymers," *Analytical Biochemistry,* vol. 411, no. 1, pp. 116-121, 2011/04/01/ 2011, doi: https://doi.org/10.1016/j.ab.2010.12.026.

[164] N. Namviriyachote, V. Lipipun, Y. Akkhawattanangkul, P. Charoonrut, and G. C. Ritthidej, "Development of polyurethane foam dressing containing silver and asiaticoside for healing of dermal wound," (in eng), *Asian J Pharm Sci,* vol. 14, no. 1, pp. 63-77, 2019, doi: 10.1016/j.ajps.2018.09.001.

[165] H. Ma, E. T. Darmawan, M. Zhang, L. Zhang, and J. D. Bryers, "Development of a poly(ether urethane) system for the controlled release of two novel anti-biofilm agents based on gallium or zinc and its efficacy to prevent bacterial biofilm formation," (in eng), *Journal of controlled release : official journal of the Controlled Release Society,* vol. 172, no. 3, pp. 1035-1044, 2013, doi: 10.1016/j.jconrel.2013.10.005.

[166] X. Kuang, V. Chen, and X. Xu, "Novel Approaches to the Control of Oral Microbial Biofilms," (in eng), *Biomed Res Int,* vol. 2018, pp. 6498932-6498932, 2018, doi: 10.1155/2018/6498932.
[167] K. E. Fejerskov O, *Dental Caries: The disease and its clinical management.* . Wiley-Blackwell, , 2009.
[168] P. A. Norowski, H. S. Courtney, J. Babu, W. O. Haggard, and J. D. Bumgardner, "Chitosan coatings deliver antimicrobials from titanium implants: a preliminary study," (in eng), *Implant Dent,* vol. 20, no. 1, pp. 56-67, Feb 2011, doi: 10.1097/ID.0b013e3182087ac4.
[169] T. Larsen and N.-E. Fiehn, "Dental biofilm infections – an update," *APMIS,* https://doi.org/10.1111/apm.12688 vol. 125, no. 4, pp. 376-384, 2017/04/01 2017, doi: https://doi.org/10.1111/apm.12688.
[170] R. H. Selwitz, A. I. Ismail, and N. B. Pitts, "Dental caries," (in eng), *Lancet,* vol. 369, no. 9555, pp. 51-9, Jan 6 2007, doi: 10.1016/s0140-6736(07)60031-2.
[171] J. D. Bryers and B. D. Ratner, "Biomaterials approaches to combating oral biofilms and dental disease," (in eng), *BMC Oral Health,* vol. 6 Suppl 1, no. Suppl 1, pp. S15-S15, 2006, doi: 10.1186/1472-6831-6-S1-S15.
[172] R. Liu *et al.*, "Antibacterial effect of copper-bearing titanium alloy (Ti-Cu) against Streptococcus mutans and Porphyromonas gingivalis," *Scientific Reports,* vol. 6, no. 1, p. 29985, 2016/07/26 2016, doi: 10.1038/srep29985.
[173] K. Laosuwan, D. J. Epasinghe, Z. Wu, W. K. Leung, D. W. Green, and H. S. Jung, "Comparison of biofilm formation and migration of *Streptococcus mutans* on tooth roots and titanium miniscrews," (in eng), *Clin Exp Dent Res,* vol. 4, no. 2, pp. 40-47, 2018, doi: 10.1002/cre2.101.
[174] M. W. Oli *et al.*, "Functional amyloid formation by Streptococcus mutans," (in eng), *Microbiology,* vol. 158, no. Pt 12, pp. 2903-2916, 2012, doi: 10.1099/mic.0.060855-0.
[175] R. N. Besingi *et al.*, "Functional amyloids in Streptococcus mutans, their use as targets of biofilm inhibition and initial characterization of SMU_63c," (in eng), *Microbiology,* vol. 163, no. 4, pp. 488-501, 2017, doi: 10.1099/mic.0.000443.
[176] L. Cheng *et al.*, "Developing a New Generation of Antimicrobial and Bioactive Dental Resins," (in eng), *J Dent Res,* vol. 96, no. 8, pp. 855-863, 2017, doi: 10.1177/0022034517709739.
[177] A. E. Pozhitkov *et al.*, "Interruption of Electrical Conductivity of Titanium Dental Implants Suggests a Path Towards Elimination Of Corrosion," (in eng), *PloS one,* vol. 10, no. 10, pp. e0140393-e0140393, 2015, doi: 10.1371/journal.pone.0140393.
[178] D. D. Divakar *et al.*, "Enhanced antimicrobial activity of naturally derived bioactive molecule chitosan conjugated silver nanoparticle against dental implant pathogens," (in eng), *Int J Biol Macromol,* vol. 108, pp. 790-797, Mar 2018, doi: 10.1016/j.ijbiomac.2017.10.166.
[179] R. Bürgers *et al.*, "The anti-adherence activity and bactericidal effect of microparticulate silver additives in composite resin materials," *Archives of Oral Biology,* vol. 54, no. 6, pp. 595-601, 2009/06/01/ 2009, doi: https://doi.org/10.1016/j.archoralbio.2009.03.004.
[180] J. R. Jedrychowski, A. A. Caputo, and S. Kerper, "Antibacterial and mechanical properties of restorative materials combined with chlorhexidines," *Journal of Oral Rehabilitation,* https://doi.org/10.1111/j.1365-2842.1983.tb00133.x vol. 10, no. 5, pp. 373-381, 1983/09/01 1983, doi: https://doi.org/10.1111/j.1365-2842.1983.tb00133.x.

[181] J. D. Bumgardner *et al.*, "The integration of chitosan-coated titanium in bone: an in vivo study in rabbits," (in eng), *Implant Dent,* vol. 16, no. 1, pp. 66-79, Mar 2007, doi: 10.1097/ID.0b013e3180312011.
[182] B. Li *et al.*, "Biological and antibacterial properties of the micro-nanostructured hydroxyapatite/chitosan coating on titanium," *Scientific Reports,* vol. 9, no. 1, p. 14052, 2019/10/01 2019, doi: 10.1038/s41598-019-49941-0.
[183] K. Snauwaert, J. Duyck, D. van Steenberghe, M. Quirynen, and I. Naert, "Time dependent failure rate and marginal bone loss of implant supported prostheses: a 15-year follow-up study," (in eng), *Clin Oral Investig,* vol. 4, no. 1, pp. 13-20, Mar 2000, doi: 10.1007/s007840050107.
[184] M. Esposito, J. M. Hirsch, U. Lekholm, and P. Thomsen, "Biological factors contributing to failures of osseointegrated oral implants. (I). Success criteria and epidemiology," (in eng), *Eur J Oral Sci,* vol. 106, no. 1, pp. 527-51, Feb 1998, doi: 10.1046/j.0909-8836..t01-2-.x.
[185] H. Lee, S. M. Dellatore, W. M. Miller, and P. B. Messersmith, "Mussel-Inspired Surface Chemistry for Multifunctional Coatings," *Science,* vol. 318, no. 5849, p. 426, 2007, doi: 10.1126/science.1147241.
[186] H. Lee, Y. Lee, A. R. Statz, J. Rho, T. G. Park, and P. B. Messersmith, "Substrate-Independent Layer-by-Layer Assembly by Using Mussel-Adhesive-Inspired Polymers," (in eng), *Adv Mater,* vol. 20, no. 9, pp. 1619-1623, May 5 2008, doi: 10.1002/adma.200702378.
[187] H. Lee, J. Rho, and P. B. Messersmith, "Facile Conjugation of Biomolecules onto Surfaces via Mussel Adhesive Protein Inspired Coatings," *Advanced Materials,* vol. 21, no. 4, pp. 431-434, 2009/01/26 2009, doi: 10.1002/adma.200801222.
[188] M. Esposito *et al.*, "Effectiveness of prophylactic antibiotics at placement of dental implants: a pragmatic multicentre placebo-controlled randomised clinical trial," (in eng), *Eur J Oral Implantol,* vol. 3, no. 2, pp. 135-43, Summer 2010.
[189] O. Camps-Font, R. Figueiredo, E. Valmaseda-Castellón, and C. Gay-Escoda, "Postoperative Infections After Dental Implant Placement: Prevalence, Clinical Features, and Treatment," *Implant Dentistry,* vol. 24, no. 6, 2015. [Online]. Available: https://journals.lww.com/implantdent/Fulltext/2015/12000/Postoperative_Infections_After_Dental_Implant.13.aspx.
[190] A. s. Association. "Alzheimer's Disease Facts and Figures." https://www.alz.org/media/Documents/alzheimers-facts-and-figures.pdf (accessed.
[191] R. S. Armen, M. L. DeMarco, D. O. Alonso, and V. Daggett, "Pauling and Corey's alpha-pleated sheet structure may define the prefibrillar amyloidogenic intermediate in amyloid disease," (in eng), *Proc Natl Acad Sci U S A,* vol. 101, no. 32, pp. 11622-7, Aug 10 2004, doi: 10.1073/pnas.0401781101.
[192] R. S. Armen, D. O. Alonso, and V. Daggett, "Anatomy of an amyloidogenic intermediate: conversion of beta-sheet to alpha-sheet structure in transthyretin at acidic pH," (in eng), *Structure,* vol. 12, no. 10, pp. 1847-63, Oct 2004, doi: 10.1016/j.str.2004.08.005.
[193] C. Condello, P. Yuan, A. Schain, and J. Grutzendler, "Microglia constitute a barrier that prevents neurotoxic protofibrillar Aβ42 hotspots around plaques," *Nature Communications,* vol. 6, no. 1, p. 6176, 2015/01/29 2015, doi: 10.1038/ncomms7176.

[194] H. Yao, K. Coppola, J. E. Schweig, F. Crawford, M. Mullan, and D. Paris, "Distinct Signaling Pathways Regulate TREM2 Phagocytic and NFκB Antagonistic Activities," (in eng), *Front Cell Neurosci,* vol. 13, p. 457, 2019, doi: 10.3389/fncel.2019.00457.
[195] K. Takahashi, C. D. Rochford, and H. Neumann, "Clearance of apoptotic neurons without inflammation by microglial triggering receptor expressed on myeloid cells-2," (in eng), *J Exp Med,* vol. 201, no. 4, pp. 647-57, Feb 21 2005, doi: 10.1084/jem.20041611.
[196] C. B. Lessard *et al.*, "High-affinity interactions and signal transduction between Aβ oligomers and TREM2," (in eng), *EMBO Mol Med,* vol. 10, no. 11, Nov 2018, doi: 10.15252/emmm.201809027.
[197] J. W. Kinney, S. M. Bemiller, A. S. Murtishaw, A. M. Leisgang, A. M. Salazar, and B. T. Lamb, "Inflammation as a central mechanism in Alzheimer's disease," (in eng), *Alzheimers Dement (N Y),* vol. 4, pp. 575-590, 2018, doi: 10.1016/j.trci.2018.06.014.
[198] S. B. Corradin, J. Mauël, S. D. Donini, E. Quattrocchi, and P. Ricciardi-Castagnoli, "Inducible nitric oxide synthase activity of cloned murine microglial cells," (in eng), *Glia,* vol. 7, no. 3, pp. 255-62, Mar 1993, doi: 10.1002/glia.440070309.
[199] M. D. Weingarten, A. H. Lockwood, S. Y. Hwo, and M. W. Kirschner, "A protein factor essential for microtubule assembly," (in eng), *Proc Natl Acad Sci U S A,* vol. 72, no. 5, pp. 1858-62, May 1975, doi: 10.1073/pnas.72.5.1858.
[200] J. Götz, F. Chen, J. van Dorpe, and R. M. Nitsch, "Formation of neurofibrillary tangles in P301l tau transgenic mice induced by Abeta 42 fibrils," (in eng), *Science,* vol. 293, no. 5534, pp. 1491-5, Aug 24 2001, doi: 10.1126/science.1062097.
[201] M. L. Selenica *et al.*, "Amyloid oligomers exacerbate tau pathology in a mouse model of tauopathy," (in eng), *Neurodegener Dis,* vol. 11, no. 4, pp. 165-81, 2013, doi: 10.1159/000337230.
[202] S. Sharma, S. Verma, M. Kapoor, A. Saini, and B. Nehru, "Alzheimer's disease like pathology induced six weeks after aggregated amyloid-beta injection in rats: increased oxidative stress and impaired long-term memory with anxiety-like behavior," (in eng), *Neurol Res,* vol. 38, no. 9, pp. 838-50, Sep 2016, doi: 10.1080/01616412.2016.1209337.
[203] D. R. Wakeman *et al.*, "Intrathecal amyloid-beta oligomer administration increases tau phosphorylation in the medial temporal lobe in the African green monkey: A nonhuman primate model of Alzheimer's disease," (in eng), *Neuropathol Appl Neurobiol,* vol. 48, no. 4, p. e12800, Jun 2022, doi: 10.1111/nan.12800.
[204] F. Yue *et al.*, "Synthetic amyloid-β oligomers drive early pathological progression of Alzheimer's disease in nonhuman primates," (in eng), *iScience,* vol. 24, no. 10, p. 103207, Oct 22 2021, doi: 10.1016/j.isci.2021.103207.
[205] Y. Yoshiyama *et al.*, "Synapse loss and microglial activation precede tangles in a P301S tauopathy mouse model," (in eng), *Neuron,* vol. 53, no. 3, pp. 337-51, Feb 1 2007, doi: 10.1016/j.neuron.2007.01.010.
[206] S. G. Greenberg, P. Davies, J. D. Schein, and L. I. Binder, "Hydrofluoric acid-treated tau PHF proteins display the same biochemical properties as normal tau," (in eng), *J Biol Chem,* vol. 267, no. 1, pp. 564-9, Jan 5 1992.
[207] D. Paris *et al.*, "Anatabine Attenuates Tau Phosphorylation and Oligomerization in P301S Tau Transgenic Mice," *Brain Disorders & Therapy,* vol. 03, 06/18 2014, doi: 10.4172/2168-975X.1000126.
[208] G. A. Jicha, B. Berenfeld, and P. Davies, "Sequence requirements for formation of conformational variants of tau similar to those found in Alzheimer's disease," (in eng), *J*

Neurosci Res, vol. 55, no. 6, pp. 713-23, Mar 15 1999, doi: 10.1002/(sici)1097-4547(19990315)55:6<713::Aid-jnr6>3.0.Co;2-g.

[209] T. C. Gamblin *et al.*, "Caspase cleavage of tau: linking amyloid and neurofibrillary tangles in Alzheimer's disease," (in eng), *Proc Natl Acad Sci U S A,* vol. 100, no. 17, pp. 10032-7, Aug 19 2003, doi: 10.1073/pnas.1630428100.

[210] C. Conze *et al.*, "Caspase-cleaved tau is senescence-associated and induces a toxic gain of function by putting a brake on axonal transport," (in eng), *Mol Psychiatry,* vol. 27, no. 7, pp. 3010-3023, Jul 2022, doi: 10.1038/s41380-022-01538-2.

[211] R. A. Rissman *et al.*, "Caspase-cleavage of tau is an early event in Alzheimer disease tangle pathology," (in eng), *J Clin Invest,* vol. 114, no. 1, pp. 121-30, Jul 2004, doi: 10.1172/jci20640.

[212] P. Liu *et al.*, "A soluble truncated tau species related to cognitive dysfunction is elevated in the brain of cognitively impaired human individuals," (in eng), *Sci Rep,* vol. 10, no. 1, p. 3869, Mar 2 2020, doi: 10.1038/s41598-020-60777-x.

[213] J. Z. Xie *et al.*, "P301S-hTau acetylates KEAP1 to trigger synaptic toxicity via inhibiting NRF2/ARE pathway: A novel mechanism underlying hTau-induced synaptic toxicities," (in eng), *Clin Transl Med,* vol. 12, no. 8, p. e1003, Aug 2022, doi: 10.1002/ctm2.1003.

VITA

Sarah Elizabeth Nick was born and grew up in Denver, Colorado. She received her Bachelor of Science in Biomedical Engineering in 2019 from Columbia University in New York, New York. In 2024, she earned her Doctor of Philosophy from the University of Washington in the Department of Bioengineering. Her publications include:

Nick SE, Bryers JD, Daggett V. Layer-by-Layer Functionalized Gauze with Designed α-Sheet Peptides Inhibits *E. coli* and *S. aureus* Biofilm Formation. 2024. *Submitted to* Journal of Biomedical Materials Research: Part A.

Yao H, **Nick SE**, Mullan M, Paris D, Daggett V. Designed α-Sheet Peptides Enhance Clearance of Amyloid-β Oligomers by Microglial Cells of the Central Nervous System. 2024. *In preparation*.

Yao H, **Nick SE**, Mullan M, Paris D, Daggett V. Effects of Intracranial Injections of AP506d and Aβ Oligomers on the Behavior of and Soluble Tau Hyperphosphorylation of Tg Tau P301S Mice. 2024. *In preparation*.

Prosswimmer T*, **Nick SE***, Bryers JD, Daggett V. Designed De Novo α-Sheet Peptides Destabilize Bacterial Biofilms and Increase the Susceptibility of *E. coli* and *S. aureus* to Antibiotics. Int J Mol Sci. 2024 Jun 27;25(13):7024. doi: 10.3390/ijms25137024. PMID: 39000131; PMCID: PMC11241457.

Mravic M, He L, Kratochvil HT, Hu H, **Nick SE**, Bai W, Edwards A, Jo H, Wu Y, DiMaio D, DeGrado WF. De novo-designed transmembrane proteins bind and regulate a cytokine receptor. Nat Chem Biol. 2024 Jun;20(6):751-760. doi: 10.1038/s41589-024-01562-z. Epub 2024 Mar 13. PMID: 38480980; PMCID: PMC11142920.

*These authors contributed equally to this work.

Copyright Permissions

Chapter 2 reproduced in part with permission from:

Prosswimmer T*, **Nick SE***, Bryers JD, Daggett V. Designed De Novo α-Sheet Peptides Destabilize Bacterial Biofilms and Increase the Susceptibility of *E. coli* and *S. aureus* to Antibiotics. Int J Mol Sci. 2024 Jun 27;25(13):7024. doi: 10.3390/ijms25137024. PMID: 39000131; PMCID: PMC11241457.

*These authors contributed equally to this work.